Using human induced pluripotent stem cells to reveal astrocyte-neuron interactions in health and disease

Anne Hedegaard

Thesis submitted for the degree of Doctor of Philosophy

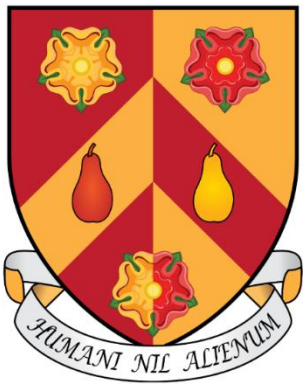

Wolfson College

University of Oxford

Michaelmas Term 2019

Abstract

Interactions between neurons and astrocytes underpin normal brain function. Astrocytes fulfil a variety of essential roles, including regulating synapse formation and maintenance, clearing neurotransmitters, and providing homeostatic regulation of the extracellular ionic environment. Evidence for a more active participation is also emerging, in which astrocytes respond to neuronal signals by influencing synaptic strength through gliotransmission. Most of our knowledge regarding neuron-astrocyte interactions stems from animal models, which have been important in dissecting events at a cellular and molecular level. Yet a major question for experimental neuroscience and drug development is how well findings translate from rodents to the human condition. The recent developments in induced pluripotent stem cell (iPSC) technology are providing a valuable tool with which to answer this question. Furthermore, because iPSCs can be derived from clinically diagnosed patients, this technology affords exciting new opportunities to model human disease processes.

The objective of this thesis was to establish a human co-culture system in which neuron-astrocyte interactions can be investigated. To this end, the first part of the thesis characterises the functionality of cortical human neurons and astrocytes generated using protocols that recapitulate key aspects of corticogenesis. This characterisation establishes that human iPSC-derived astrocytes satisfy many of the hallmarks of rodent astrocytes. Live cell imaging methods are used to investigate intracellular ion dynamics, which are believed to underpin how astrocytes communicate with neurons and regulate the extracellular environment. This reveals that iPSC-derived astrocytes exhibit intracellular Ca^{2+} signalling events both spontaneously and in response to neurotransmitters. Furthermore, through a combination of monoculture and xeno-transplantation models, iPSC-derived astrocytes are shown to respond to neuronal activity and extracellular K^+ by exhibiting similar membrane depolarisation and H^+ dynamics to those observed in rodent astrocytes.

The latter part of the thesis focuses on the use of iPSC co-cultures for studying astrocyte-to-neuron signalling. First, I establish that human astrocytes convey pro-maturational effects in terms of enhancing the intrinsic excitability and synaptic activity of co-cultured human neurons. Next, I develop an optogenetic paradigm for directly eliciting membrane depolarisation and Ca^{2+} events in astrocytes. This leads to glutamate receptor activation in nearby neurons and astrocyte stimulation over a period of days causes a potentiation of the synaptic inputs to co-cultured neurons. Finally, astrocytes are generated from individuals diagnosed with sporadic Alzheimer's disease (sAD), whom are homozygous for the *APOE4* allele - the highest genetic risk factor associated with sAD. Compared to controls, *APOE4* astrocytes are found to secrete less APOE and fail to generate astrocyte-mediated increases in synaptic inputs.

Together, this work advances the use of human iPSC-derived cells for studying neuron-astrocyte interactions. iPSC-derived human astrocytes can recapitulate many of the functional properties of rodent astrocytes and can be used in different co-culture settings to examine multiple forms of astrocyte-to-neuron communication. This represents an important step towards establishing more complex human-based models, which are expected to prove useful for modelling disease processes.

Statement of originality and collaborations

I declare that the work presented in this thesis is entirely my own and I clearly acknowledge where others have made contributions. This work has not previously been submitted for any qualification of degree at this or any other institution.

I would like to thank the following people for assistance with analysis scripts: Joram van Rheede for creating a MatLab script which extracts membrane values for assessment of electrophysiological recording data. Paul Brodersen for coding the Python script used for quantifying the synaptic staining in **Figure 5.7** and **Figure 6.6**. Alexandru Calin for generating the semi-automated MatLab scripts for synchronising the electrophysiological and fluorescence data generated in **Chapter 4**, and for adapting his data analysis script for my purposes.

Alexandru Calin also kindly provided the mouse organotypic slices used in **Chapter 4** and assisted in the transplantations. Tatsiana Waseem had generated the ClopHensorN lentiviral construct used in **Chapter 4** and recorded the data presented in figure 4.3 G and H from cultures which I provided. Lori Dershowitcz, who worked as an MSc student under my supervision, contributed pilot recordings, which are part of the dataset presented on **Figure 5.6**. Emma Whiteley generously let me test the amyloid-β production of my *APOE4/E4* neurons on the MSD assay which she ran, presented in **Figure 7.1**.

Acknowledgements

My experience of the Akerman lab has been that of a friendly, collaborative and stimulating environment, where widely different research interests thrive under the calm and encouraging supervision of Professor Colin Akerman. I thank everyone for making my DPhil experience an overall enjoyable and exciting experience.

I offer my sincerest gratefulness to Colin, who has been a source of guidance, scientific enthusiasm and support throughout my time in his lab. I greatly appreciate how he has helped me grow as a scientist through always constructive recommendations and great generosity with his time. His attitude towards exploring scientific topics and eagerness for tinkering and build things from scratch is inspiring.

I am grateful for the readiness of the members of the Akerman lab to always share skills and expertise, and to Zahid Padamsey for being willing to act as electrophysiology "guru" in hours of desperation. In particular, I would like to thank "Team stem cell" Sarah Newey and Emma Whitely, for being such patient teachers of stem cell culture methods and molecular biology techniques. Without their guidance I could not have kept a single cell alive. Also, my thanks go to Alexandru and Tanya for being great collaborators, for being experts on anything ClopHensorN and for teaching me to master the confocal microscope.

I would like to thank Alzheimer's Research UK for funding this project and for providing me with plenty of opportunities to establish a professional network and to present my work at their conferences, which every time boosted my motivation.

I have felt incredibly supported by friends and family, a word of encouragement and a hug was never far away. Particularly the lovely Oxfordshire acro-yogis have been my weekly "support group". They have cheered me up by letting me stand on their shoulders and helped me forget the stress of a failed lab experiment, by making me giggle as we fail at our acrobatic experiments.

Last, but by no means least, my partner Thomas deserves the warmest most heartfelt thanks I can give. He has been unwavering in his belief in my ability to complete this DPhil marathon, and has done all within his power to see me through it. I have been able to share my excitement with him, and he has had an uncanny ability to turn my tears of frustration into a smile. Thank you for loving me and hugging me when I have needed it the most. You are awesome.

Table of Contents

List of abbreviations

Aβ	amyloid beta
AD	Alzheimer's Disease
AMM	astrocyte maintenance media
AMPAR	α-amino-3-hydroxy-5-methyl-4 isoxazolepropionic acid receptor
AP	action potential
AQP4	aquaporin4
ATP	adenosine triphosphate
BMP	bone morphogenic protein
CatCh	Ca^{2+}-translocating channelrhodopsin
Cm	membrane capacitance
CNS	central nervous system
CNTF	ciliary neurotrophic factor
CRISPR	clustered regularly interspaced short palindromic repeats
CTIP2	COUP-TF-interacting protein-2
CT-1	cardiotrophin-1
Cx	connexin
DNA	deoxyribonucleic acid
DREADD	designer receptors exclusively activated by designer drugs
EAAT	excitatory amino acid transporters
Emx1/2	empty spiracles homeobox 1/2
ER	endoplasmic reticulum
ESC	embryonic stem cell
fAD	familial Alzheimer's Disease
FGF-2	fibroblast growth factor 2
FOV	fields of view
Foxg1	forkhead box protein G1
GABA	gamma-aminobutyric acid
GFAP	glial fibrillary acidic protein
GLAST	glutamate aspartate transporter
GLT-1	glutamate transporter-1
Gpc	glypicans
HEK	human embryonic kidney
iPSC	induced pluripotent stem cell
IP_3	inositol 1,4,5-trisphosphate
JAK-STAT	janus kinase-signal transducer and activator of transcription
LDLR	low-density lipoprotein receptor
LIF	leukaemia inhibitory factor

LiGluR	light-gated glutamate receptor 6
LTP	long-term potentiation
MAP2	microtubule associated protein-2
mEPSC	miniature excitatory post-synaptic current
mGluR	metabotropic glutamate receptor
NCX	Na^+/Ca^{2+} exchanger
NE	network events
NF1A	nuclear factor 1A
Ngn2	neurogenin-2
Nkx2.1	NK2 Homeobox 1
NMDAR	N-methyl-D-aspartate receptor
NMM	neuronal maintenance medium
NPC	neural progenitor cell
Otx2	orthodenticle homeobox 2
Pax6	paired box protein-6
PCR	polymerase chain reaction
pHH3	phospho-histone H3
PKC	proteinase kinase C
PSCs	post-synaptic currents
Ra	access resistance
Rm	membrane resistance
RNA	ribonucleic acid
sAD	sporadic Alzheimer's Disease
SatB2	special AT-rich sequence-binding protein-2
sEPSC	spontaneous excitatory post-synaptic current
SHH	sonic hedgehog
sIPSC	spontaneous inhibitory post-synaptic current
SVZ	subventricular zone
Tbr1	T-box brain-1
Tbr2	T-box brain protein-2
TGF-β	transforming growth factor beta
TNF-α	tumour necrosis factor alpha
TTX	tetrodotoxin
Tuj1	neuron-specific class III β-tubulin
VGLUT	vesicular glutamate transporters
$VGNa^+$	voltage-gated sodium
Vm	membrane potential

Chapter 1

1 General introduction

The human brain is one of the most complex structures known to us, and neuroscience the tool with which we try to tease apart this complexity. We know that brain function relies on the intricate interactions between assemblies of cell types, but much still remains to be understood about the relations, interplay and communication between sub-types of cells, particularly in the context of the human brain. Two very different brain cell types that have evolved to interact particularly closely are neurons and astrocytes (Verkhratsky and Nedergaard, 2016). In fact, they interact so closely that dysfunctions in the relationship between neurons and astrocytes are thought to contribute to, and in some cases underlie, neuropathological diseases including schizophrenia and epilepsy, and neurodegenerative diseases such as amyotrophic lateral sclerosis, Parkinson's disease and Alzheimer's Disease (AD) (Khakh and Sofroniew, 2015; Schitine *et al.*, 2015; Almad and Maragakis, 2018; Dossi, Vasile and Rouach, 2018).

Most of our knowledge regarding neuron-astrocyte interactions stems from animal models, which have been particularly important in advancing our understanding at a molecular and cellular level, as experimental access to human brain tissue has been limited. Yet humans and rodents differ considerably, and a major outstanding question for experimental neuroscience is how well findings from rodents translate to the human condition. The development of induced pluripotent stem cell (iPSC) technology just over a decade ago has provided neuroscience with a valuable tool with which to answer this question. iPSC technology offers the potential to validate and re-evaluate established knowledge gained from

rodent models and importantly, it provides exciting opportunities to test hypotheses in a human disease context.

1.1 The importance of neuron–astrocyte interactions

A specialisation of brain cell functions took place during mammalian evolution, with neurons becoming responsible for fast information transfer and glial cells taking on the role of homeostatic regulators. In phylogenetically old species such as the *Caenorhabditis elegans* worm, astrocytes share many properties with neurons, and if the astrocytes are ablated the animal is impaired, but able to survive (Oikonomou and Shaham, 2011). In contrast, the specialisation of cell types in the mammalian brain has progressed to such a point that a nervous system without glia is unviable (Verkhratsky, Rodríguez and Parpura, 2012). It is argued that the high-precision, high-energy consuming functions of neurons have evolved at the expense of "outsourcing" the homeostatic house-keeping functions to glial cells. Astrocytes keep neurons alive and in a functional state by regulating the extracellular environment via various homeostatic mechanisms, by being a source of energy-substrates and by aiding remodelling and repair after activity or injury (Chandrasekaran *et al.*, 2016).

Historically, the distinct morphology of mammalian astrocytes was first observed by Otto Deitner in 1865, and Camillo Golgi and Ramón y Cajal contributed detailed drawings in 1872, but the name "astrocyte" is attributed to Mihály Lenhossék in 1893 (Chandrasekaran *et al.*, 2016). Astrocytes are parts of the wider family of neuroglia - a very diverse population of cells, which traditionally have been viewed as largely passive, supportive "glue" between neurons. This traditional view is evident from Rudolf Virchow's definition from 150 years ago, stating that neuroglia are a "substance ... which lies between the proper nervous parts, holds

them together and gives the whole its form in a greater or less degree" (Lalo *et al.*, 2011). Whilst still being regarded as important for brain structure, more recent views on astrocytic functions emphasise their supportive homeostatic roles and key contributions to information processing through their integration with neural circuitry.

To be able to fulfil their multitude of homeostatic functions, astrocytes require mechanisms for monitoring and sensing changes in the extracellular environment, mechanisms for reacting to and compensating for changes, and mechanisms for coordinating astrocytic networks to solve these tasks (Verkhratsky, Rodríguez and Parpura, 2012). Insights into how astrocytes have evolved to meet these challenges can again be found by considering the ancestry that astrocytes share with neurons. By evolving from neuronal cells in the primitive nervous systems, astrocytes have "inherited" many of the same receptors, channels and exocytotic machinery found in neurons. It is these features that enable astrocytes to sense their environment (Verkhratsky and Steinhäuser, 2000; Lalo *et al.*, 2011; Verkhratsky, Rodríguez and Parpura, 2012). In fact, astrocytes display regionality through the differential expression of neurotransmitter receptors, which vary between different brain areas and are likely determined by the most prevalent transmitter used by the surrounding neurons (Verkhratsky, 2010). Furthermore, physical intercellular coupling via gap-junctions provides astrocytes with a mechanism to quickly distribute molecules that they remove from the extracellular space, and enables astrocytes to act in a coordinated fashion (Sutor and Hagerty, 2005).

The homeostatic functions of astrocytes have been studied for over half a century and represent the "passive", supportive roles played by astrocytes. However, new found

interest in astrocytes was sparked about 20 years ago, when active astrocytic modulation of neural communication was proposed (Cornell-Bell *et al.*, 1990; Nedergaard, 1994; Parpura *et al.*, 1994; Bezzi *et al.*, 1998). Viewing astrocytes as active participants in neural networks has elevated their status from "non-excitable nerve glue", to being influential partners in shaping cognition (Bellot-Saez *et al.*, 2017). The ways in which astrocytes participate in information processing are varied and a topic of ongoing research. However, intracellular calcium (Ca^{2+}) dynamics are thought to be central to the processes by which astrocytes integrate neuronal signals from their surroundings (Fellin and Carmignoto, 2004; Di Castro *et al.*, 2011; Araque *et al.*, 2014). Indeed, one concept that has gained a lot of attention is the idea that these Ca^{2+} dynamics enable astrocytes to feed signals back to neurons, a process referred to as gliotransmission. In fact, the idea that neurons "talk" to astrocytes and that astrocytes are able to "listen" in a passive capacity was well-established, but gliotransmission captures the idea that astrocytes possess mechanisms to actively "talk back" to neurons.

Having adopted a neuron-centric view in the past, discoveries concerning the physiology and functions of astrocytes are advancing our appreciation of the importance of glia within neuroscience. With so many important functions being accredited to astrocytes, it is now much easier to imagine how astrocyte dysfunction can be so significant for the nervous system. In this regard, disease modelling that incorporates multiple cell types is essential for studying phenomena that are the result of cellular interactions. This thesis represents a body of work that strives to study neuron-astrocyte interactions in a human context. In particular, iPSC technologies are used to develop new experimental systems for studying neuron-astrocyte interactions. Therefore, a running theme of this introductory chapter will be to reflect on our

current understanding of astrocyte biology and the current state-of-the-art in terms of the use of iPSCs to study neuron-astrocyte interactions.

1.2 Astrocytes as synaptic regulators

Networks of neurons relay information to each other via their synapses, and it would seem that astrocytes have evolved to particularly specialise in supporting synapses, both in terms of their formation during development, their pruning to form precise networks and their maintenance in adulthood (Clarke and Barres, 2013). Traditionally, synaptogenesis was viewed as an intrinsic property of neurons (Stevens, 2008), but experiments comparing enriched neuronal cultures and neuron-astrocyte co-cultures have challenged this view. Interestingly, the timing of gliogenesis in rodent cortex corresponds to the excitatory synaptogenic window, occurring around the first to the third postnatal week. This timing is generally believed not to be a coincidence (Johnson *et al.*, 2007; Chung, Allen and Eroglu, 2015; Krencik, van Asperen and Ullian, 2016; Allen and Eroglu, 2017), because of the varied synaptogenic roles attributed to astrocytes.

Synaptogenic effects of astrocytes are exhibited both through contact mediated cues and secreted factors (**Figure 1.1A**). Evidence suggests that physical contact with astrocytes is essential for initiating synapse formation, as pure cultures of embryonic retinal ganglion cells have been shown to be unable to receive synapses in the presence of known synaptogenic secreted factors, until they have been contacted by an astrocyte (Barker *et al.*, 2008).

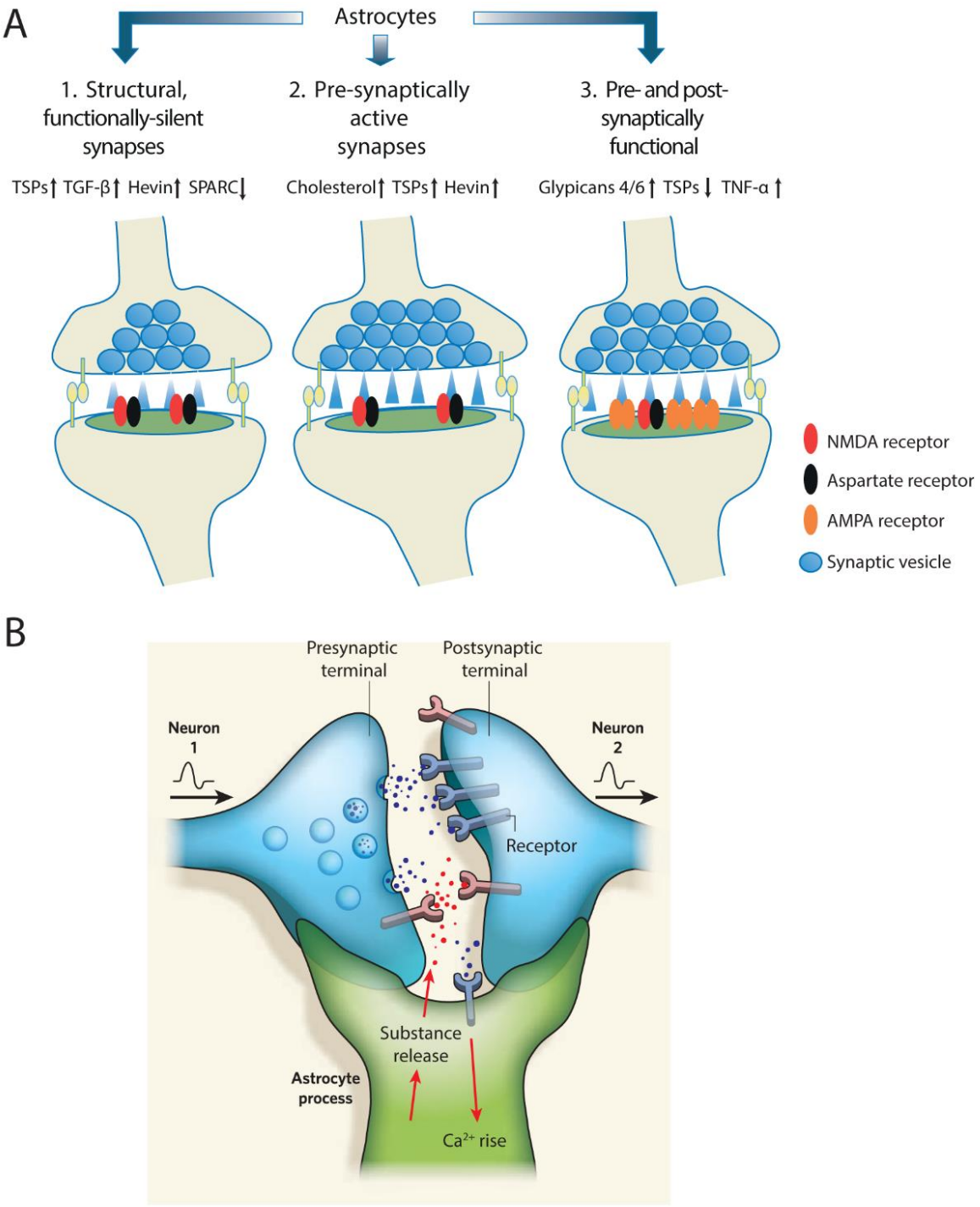

Figure 1.1 Astrocytic regulation of synapses

(A) Astrocytes are implicated in the functional maturation of synapses. Illustration shows astrocyte-secreted factors that have been implicated in the functional maturation of glutamatergic synapses. Factors have been linked to an increase structural synapse formation (left), the induction of pre-synaptic vesicle release (middle), and un-silencing post-synaptically via insertion of AMPA receptors (right). TSPs: thrombospondins. Adapted from Chung et al (2015). **(B)** An astrocyte end-foot enwraps a pre- and post-synaptic structure to form a "tripartite synapse". Spill-over of neurotransmitters can elicit an astrocytic Ca^{2+} response as astrocytes express some of the same receptors as neurons. The rise in intracellular Ca^{2+} has been proposed as a mechanism for coordinating the release of neuroactive substances from astrocytes. Adapted from Allen & Barres (2009).

Indeed, it was previously demonstrated that physical contact between astrocytes and hippocampal neurons activates integrin and protein kinase C (PKC) signalling, which subsequently allows neurons to form synapses (Hama *et al.*, 2004). The importance of vesicle-released factors was demonstrated in an elegant study, where lower densities of synaptic spines were detected xclusively on segments of neuronal dendrites traversing a subset of astrocytes in which vesicular release was blocked (Sultan *et al.*, 2015). Secreted synaptogenic factors thrombospondins, hevin and transforming growth factor-beta (TGF-β), all seem to aid structural synapse formation, as measured by increases in synaptic puncta when these factors were added (Christopherson *et al.*, 2005; Kucukdereli *et al.*, 2011; Diniz *et al.*, 2012). Astrocytes also possess a mechanism for balancing synapse formation, through the secretion of the hevin antagonist: secreted protein acidic, rich in cysteine (SPARC) proteins (Kucukdereli *et al.*, 2011).

In line with the timing of gliogenesis, thrombospondins were found to only be expressed by immature astrocytes in the rodent cortex during the first postnatal week, which coincides with synaptogenesis (Christopherson *et al.*, 2005). Pre-synaptically, thrombospondins and hevin have been shown to induce active vesicle release, but leave post-synapses silent (Christopherson *et al.*, 2005), and astrocytic delivery of cholesterol has been reported to enhance pre-synaptic efficacy (Mauch, Na and Schumacher, 2001; Christopherson *et al.*, 2005). However, to obtain fully functional and mature synapses, the co-action of factors like tumor necrosis factor alpha (TNF-α) and glypicans 4 and 6 (Gpc4 and 6) appear necessary for the un-silencing of post-synaptic structures via the insertion of α-amino-3-hydroxy-5-methyl-4-isoxazolepropionic acid receptors (AMPAR) (Stellwagen *et al.*, 2005; Allen *et al.*,

2012). This literature illustrates that the coordinated action of astrocytic factors and contact cues are paramount to synaptogenesis, but astrocytes also exert control over synaptic pruning. The process of synaptic pruning employs the phagocytic abilities of astrocytes, which are either directly activated through Mertk and Megf10 pathways (Chung *et al.*, 2013), or indirectly serve to tag synapses for subsequent degradation by microglia (Bialas and Stevens, 2013). This process of synapse elimination is thought to be a crucial stage in refining and ultimately shaping the adult neural network (Clarke and Barres, 2013; Chung, Allen and Eroglu, 2015).

In adulthood, single astrocytes have been shown to interact directly with the synapses belonging to 4-8 neurons in the local environment (Halassa *et al.*, 2007). Interestingly, individual synapses appear to only be enveloped or enwrapped by one astrocyte, as astrocytic domains have been described as largely non-overlapping (Bushong *et al.*, 2002; Halassa *et al.*, 2007), with the exception of the primate-specific subtype of interlaminar astrocytes (Oberheim *et al.*, 2009). Such enwrapment of a pre- and post-synaptic pair by an astrocyte process has been termed "the tri-partite synapse" (Araque *et al.*, 1999; Allen and Barres, 2009) (**Figure 1.1B**). A single rodent astrocyte has been estimated to contact between 20,000 and 140,000 synapses (Bushong *et al.*, 2002; Halassa *et al.*, 2007), whereas the much more highly branched human protoplasmic astrocytes have been estimated to contact between 270,000 and 2 million synapses, an estimate which is based on astrocytic volume and synaptic density in the human brain (Oberheim *et al.*, 2009). The impact of isolating each synapse by astrocyte envelopment is believed to be an increase in the precision of synaptic transmission, which includes minimizing the spill-over of neurotransmitter to neighbouring synapses

(Nedergaard and Verkhratsky, 2012; Murphy-Royal *et al.*, 2017). This compartmentalised segregation allows neurons and astrocytes to function as a glio-neuronal processing unit, which can monitor, integrate and ultimately modify a set of synapses (Oberheim *et al.*, 2009).

One of the most important and fundamental roles of astrocytes is to maintain signal transduction at synapses, by dealing appropriately with concentration changes of ions and neurotransmitters. Following action potential (AP) propagation and release of neurotransmitter from the pre-synaptic terminal, the neurons repolarise by the voltage-gated efflux of K^+. A single AP can elevate the local extracellular K^+ concentration by as much as 1 mM (Adelman and Fitzhugh, 1975) and extracellular levels of K^+ have been measured as high as 10 mM during periods of intense network activity (Heinemann and Lux, 1977). Meanwhile, concentrations of the most common excitatory neurotransmitter, glutamate, have been shown to increase transiently within the synaptic cleft from <20 nM up towards 1 mM, of which 160-190 µM was reported to reach the perisynaptic glial membrane (Dzubay and Jahr, 1999). Given these concentration changes, the synaptic cleft requires clearing by the enveloping astrocyte, which efficiently removes excess K^+ and transmitter. K^+ can enter the astrocytes both via gradient-driven co-transport through the Na^+/K^+ ATPase, and through voltage-gated K^+ channels such as K^+ inward rectifiers like $K_{ir}4.1$ (Cheung *et al.*, 2015). Meanwhile, the uptake of glutamate is mainly achieved through the astrocytic excitatory amino acid transporters EAAT1 and EAAT2, which are the human equivalents of the rodent glutamate aspartate transporter (GLAST) and glutamate transporter-1 (GLT-1) respectively, and they are responsible for 90% of glutamate uptake in the brain (Kim *et al.*, 2011). Clearance of glutamate and K^+ is essential for preparing the synapse for subsequent signalling by

preventing receptor desensitisation, which would otherwise lead to loss of signal fidelity (Marcaggi and Attwell, 2004; Kim *et al.*, 2011). Clearance also prevents neuronal excitotoxicity, as terminating glutamate receptor activation prevents an excessive influx of Ca^{2+}, which would activate cell-degradation enzymes (Rothstein *et al.*, 1996; Cheung *et al.*, 2015).

Interestingly, astrocytes have the potential to influence the size and duration of the post-synaptic signal via their K^+ and neurotransmitter uptake dynamics (Grewer and Rauen, 2005). Less efficient clearance of both substances can serve to increase the post-synaptic response and vice versa. In addition, decreased synaptic clearance would increase spill-over of neuroactive substances, which at ~175 µM (as measured at glial cell membranes) or above, is regarded as sufficient to activate extra-synaptic receptors (Dzubay and Jahr, 1999). Further to their clearance of glutamate, astrocytes contribute to the recycling of glutamate, which reduces the need to synthesise new neurotransmitter (Allen, 2014), thereby conveying a metabolic benefit.

Synapse-targeted interactions between neurons and astrocytes are now beginning to be investigated in human iPSC-derived cell cultures. Over the last 7 years, the first reports have indicated that human astrocytes can engage in glutamate transport and promote presumptive synaptic contacts, as evaluated through increases of synaptic proteins (Krencik *et al.*, 2011; Serio *et al.*, 2013; Shaltouki *et al.*, 2013; Lischka *et al.*, 2017; VanderWall *et al.*, 2019). However, quantified maturation of functional synapses has so far only been reported when human neurons are co-cultured with rodent astrocytes (Tang *et al.*, 2013; Prè *et al.*, 2014; Lischka *et al.*, 2017). The potential for human astrocytes to regulate processes at

synapses, including glutamate uptake, K^+ buffering and aspects of functional maturation will be the focus of the experiments described in **Chapter 3** and **Chapter 5** of this thesis.

1.3 Astrocytes as homeostatic regulators

Maintaining homeostasis is vital to a biological system, as it allows the system to function under optimal conditions and to respond to challenges that may otherwise disrupt normal function. The efficiency of the homeostatic processes can therefore determine the amount of damage caused by a particular challenge. Astrocytes are viewed as a key cellular component in maintaining homeostasis in the brain, and these cells operate in collaboration with microglia and oligodendrocytes. Central to this role is the fact that astrocytes bridge multiple cell types (Tyzack, Lakatos and Patani, 2016), giving them the potential to react to the need of one cell type by coordinating the response of others. Astrocytes form a connected syncytium amongst themselves, envelop neuronal synapses, contact the vasculature and act as an intermediate between oligodendrocytes, which are otherwise very sparsely connected with each other (Nagy, Dudek and Rash, 2004). Furthermore, astrocytes are specialised in surveying their surroundings and often have multiple interchangeable mechanisms for responding to an environmental challenge (Nedergaard and Verkhratsky, 2012).

Several categories of homeostasis that are regulated by astrocytes have been described: 1) cellular 2) molecular and 3) metabolic (Verkhratsky, Rodríguez and Parpura, 2012). Cellular homeostasis refers to inter-cellular communication and the exchange of ions and small molecules, both among homogeneous and heterogeneous cell populations. Astrocytes contribute to cellular homeostasis at a brain-wide level at the blood brain barrier (BBB), which provides a selective shield between the brain and the blood stream by only allowing

certain molecules like oxygen and nutrients through. Astrocytes extend so-called end-feet, which enwrap the vasculature, contributing to the physical barrier (Kimelberg and Nedergaard, 2010). In addition, the end-feet carry water-permeable aquaporins (AQP4), with which astrocytes regulate osmotic homeostasis, and the end-feet can also mediate vasodilation (Simard and Nedergaard, 2004). Both osmotic regulation and vasodilation are important reactions to neural activity, and the latter has been shown to be mediated by astrocytic Ca^{2+} elevations initiated by synaptic activity (Takano *et al.*, 2006).

Astrocytes contribute to local cellular homeostasis by facilitating the exchange of ions and small molecules. This is achieved through gap-junctions, which are channels formed by assemblies of transmembrane proteins called connexins (Cx) that serve to link the cytoplasm of adjacent cells (Sutor and Hagerty, 2005; Theis *et al.*, 2005). An assembly of 6 connexins make up a hemichannel, which is located on the membrane of each cell and the complete gap-junction channel is formed by two opposed hemichannels (Sutor and Hagerty, 2005). Gap-junctions provide a nonselective form of communication between connected cells by allowing a passive spread of ions and small molecules of up to ~1 kDa via diffusion. The connexin proteins involved in gap-junctions differ between astrocytes and neurons. Cx36 is primarily present in neurons (Söhl, Maxeiner and Willecke, 2005) at very early stages of development (first 2 postnatal weeks in rodents (Connors, Benardo and Prince, 1983; Peinado, Yuste and Katz, 1993)), during which time they inform the later formation of chemical synapses (Maher, McGinley and Westbrook, 2009; Yu *et al.*, 2012). Cx43 and Cx30 are the most abundant connexins found in astrocytes (Nagy, Dudek and Rash, 2004; Theis *et al.*,

2005), which contribute to the propagation of Ca^{2+} increases between astrocytes (Bennett *et al.*, 2003).

At a molecular level, astrocytes exert homeostatic control over the extracellular environment by carefully regulating concentrations of ions, neurotransmitters and trophic factors. In particular, their aforementioned K^+ buffering and glutamate uptake has great importance for neuronal signalling and health. Early patch-clamp experiments in perisynaptic astrocytes demonstrated that they readily uptake K^+ ions, which are dispersed through the astrocytic syncytium (Kuffler, Nicholls and Orkand, 1966). These experiments preceded the discovery of gap-junctions, but the coupled nature of astrocytes is believed to largely enable accelerated K^+ clearance (Wallraff *et al.*, 2006) as well as glutamate uptake (Theis *et al.*, 2005).

Astrocytes are specialised at sensing changes to their environment and regulating extracellular ion concentrations such as K^+, Na^+, Ca^{2+} and Cl^-, which determines the respective reversal potentials of these ions in different cell populations. Altered reversal potentials impact cell excitability, as well as the action of gradient driven transporters (Annunziato, Boscia and Pignataro, 2013), which ultimately affects cell physiology. The contribution astrocytes make to the regulation of H^+ and HCO_3^- is also hugely important, as these ions determine intracellular and extracellular pH levels, which influence many dynamic cellular processes including enzymatic activity, metabolism and network excitability (Opie, 1965; Drapeau and Nachshen, 1988; Tabb *et al.*, 1992; Raimondo *et al.*, 2015). The pH regulatory mechanisms in astrocytes are particularly sensitive to the activity of surrounding neurons (Chesler and Kraig, 1989; Brookes and Turner, 1994; Pappas and Ransom, 1994; Rose and Deitmer, 1994) and,

during periods of intense network activity, astrocytic intracellular pH changes are typically opposite to those that occur in neurons (Raimondo *et al.*, 2016).

Astrocytes are also regarded as metabolic regulators, as they are believed to provide energy substrates for neurons, as well as reduce the metabolic demands of neurons by recycling neurotransmitters via the glutamate-glutamine cycle. Astrocytes are well suited for the transfer of energy substrates from the bloodstream to neuronal synapses via their end-feet, which contact blood vessels and enwrap synapses (Harris, Jolivet and Attwell, 2012). The astrocyte-neuron "lactate shuttle hypothesis" describes how glucose taken up from the bloodstream might be converted first to glutamine, then to pyruvate and subsequently to lactate, before being shuttled to neurons (Pellerin and Magistretti, 1994). While it is agreed upon that lactate levels increase during neuronal activity (Prichard *et al.*, 1991), it is debated whether lactate can replace glucose within neurons for their adenosine triphosphate (ATP) production (Chih, Lipton and Roberts, 2001; Jolivet *et al.*, 2010; Mangia *et al.*, 2011), which powers transporters like the Na^+/K^+ ATPase that are crucial for maintaining synaptic signalling (Allen, 2014).

Aside from supplying energy, astrocytes also save neurons energy by reducing their neurotransmitter production through recycling of glutamate. This recycling is initiated when glutamate is taken up by astrocytes through EAATs and subsequently converted to the intermediate product glutamine via the astrocyte specific enzyme glutamine synthase (Martinez-Hernandez, Bell and Norenberg, 1977). Glutamine is then transported across the extracellular space without activating receptors, whereupon it is taken up by neurons, converted back to glutamate via glutaminase (Laake *et al.*, 1999; Marcaggi and Attwell, 2004),

and packaged into synaptic vesicles by vesicular glutamate transporters (VGLUTs) (Fremeau *et al.*, 2004).

Our appreciation of the homeostatic properties of astrocytes has mainly been derived from experiments using rodents. These models continue to be powerful as they offer access to various degrees of intact brain networks, which can include the key interacting cell types. When attempting to establish iPSC-based models, it is important that these homeostatic properties are validated in the human cells, as they are seen as fundamental to astrocyte function. Dysregulation in homeostasis is perceived as a loss of normal function, likely leading to neurodegeneration (Sidoryk-Wegrzynowicz *et al.*, 2011; Phatnani and Maniatis, 2015). Certain resting ion concentrations have been measured in iPSC-derived astrocytes (e.g. pH by (Yao *et al.*, 2018)) and in iPSC-derived neurons (e.g. Cl^- by (Livesey *et al.*, 2014)), but the dynamic regulation of these intracellular ion species has not been examined. In **Chapter 4** I will explore whether our current understanding of astrocytic pH and Cl^- homeostasis holds true for iPSC-derived human astrocytes, and how their dynamics behave compared to human neurons.

1.4 Astrocytic Ca^{2+}-signalling

Astrocytes have been historically regarded as electrophysiologically passive, in the sense that unlike neurons, astrocytes are unable to generate fast Na^+-dependent depolarising action potentials with millisecond precision. Yet the discovery that astrocytes exhibit rapid intracellular Ca^{2+} dynamics, has led to a wealth of studies describing both evoked and spontaneous astrocytic Ca^{2+}-signalling. This work has revealed that a variety of ligands are able to elicit Ca^{2+} increases by activating receptors on the surface of astrocytes. These include

the most prevalent neurotransmitters of the central nervous system (CNS), including glutamate, gamma-aminobutyric acid (GABA), ATP and acetylcholine, but also less common signalling molecules, such as histamine, cannabinoids, epinephrine/adrenalin and opioids (Agulhon *et al.*, 2008). Being equipped with such a wealth of receptors enables astrocytes to sense many types of signal transmission in their vicinity, and they appear to consistently respond with Ca^{2+} elevations. Indeed, neuron-targeted stimulation has routinely been shown to trigger Ca^{2+} increases in astrocytes in dissociated culture and in slices (reviewed in (Agulhon *et al.*, 2008; Lalo, Verkhratsky and Pankratov, 2011; Volterra, Liaudet and Savtchouk, 2014; Bazargani and Attwell, 2016)). In efforts to prove the physiological relevance of astrocytic Ca^{2+}-fluxes, multiple groups have reported astrocytic Ca^{2+} elevations in intact brain preparations, in response to physiological stimuli. For example, simple visual stimuli have been shown to evoke astrocytic Ca^{2+} increases in the retina (Newman, 2005) and visual cortex (Schummers, Yu and Sur, 2008); as has whisker stimulation in sensory barrel cortex (Wang *et al.*, 2006).

There is general consensus that the main pathway responsible for the initiation of astrocytic Ca^{2+}-signalling involves the detection of neurotransmitter spill-over. In the well-studied case of glutamate, activation of astrocytic metabotropic glutamate receptors (mGluRs) subsequently stimulates the production of inositol 1,4,5-trisphosphate (IP_3) via phospholipase C activation. IP_3 reliably stimulates release of Ca^{2+} into the cytosol from intracellular stores such as the endoplasmic reticulum (ER) (Pasti *et al.*, 1997; Nash *et al.*, 2002; Agulhon *et al.*, 2008; Verkhratsky, Rodríguez and Parpura, 2012; Volterra, Liaudet and Savtchouk, 2014; Gundersen, Storm-Mathisen and Bergersen, 2015). Alternatively, there is

evidence that neurotransmitter spill-over can activate ionotropic receptors on the astrocytic membrane, allowing a direct influx of cations, including Ca^{2+}, down their concentration gradients (Lalo *et al.*, 2006; Palygin *et al.*, 2010; Lalo, Verkhratsky and Pankratov, 2011). Furthermore, the reversed action of the Na^{+}/Ca^{2+} exchanger (NCX), which in forward mode transports Ca^{2+} out of the cell, could account for intracellular Ca^{2+} increases in astrocytes. The direction of the NCX can be reversed by increases in intracellular Na^{+} or membrane depolarisation (Kirischuk, Kettenmann and Verkhratsky, 1997; Paluzzi *et al.*, 2007; Volterra, Liaudet and Savtchouk, 2014). Furthermore, astrocytic fluxes in intracellular Ca^{2+} can also arise spontaneously, without an apparent initiating neuronal signal. Such spontaneous astrocytic Ca^{2+} fluxes have been found to occur both in rodent acute slices (Nett, Oloff and McCarthy, 2002; Parri and Crunelli, 2003), *in vivo* (Hirase *et al.*, 2004; Nimmerjahn *et al.*, 2004) and was recently detected in human foetal and iPSC-derived astrocytes (Tcw *et al.*, 2017).

Ca^{2+} dynamics are regarded as a principal mode of signal transduction within individual astrocytes; however, the propagation of Ca^{2+} signals between astrocytes has previously been a source of contention in the field. It was debated whether astrocytes can propagate Ca^{2+} waves between them via gap-junctions, as was indicated by experiments where the Ca^{2+} signals disappeared if gap-junctions were blocked (Charles *et al.*, 1991; Iwabuchi *et al.*, 2002; Parri and Crunelli, 2003; Tian *et al.*, 2006). On the other hand, experiments in physically isolated astrocytes suggested that individual astrocytes rather propagate Ca^{2+} signals between them by releasing an intermediate signal (Hassinger *et al.*, 1996), found later to be ATP (Guthrie *et al.*, 1999; Stout *et al.*, 2002; Fiacco and McCarthy, 2004; Schummers,

Yu and Sur, 2008). The debate over the physiological plausibility of Ca^{2+}-wave behaviour may have been settled by more recent analysis methods (Fanelli *et al.*, 2009) and *in vivo* experiments, where Ca^{2+}-wave propagation was demonstrated over much larger fields of view and to be dependent both on gap-junctions as well as purinergic receptors (Kuga *et al.*, 2011).

Overall, astrocytes can be considered as possessing a broad repertoire of Ca^{2+}-signalling mechanisms that they use in response to several types of stimuli, a diversity which some argue represents different ways in which astrocytes may integrate information (Fellin and Carmignoto, 2004; Araque *et al.*, 2014). Regarding Ca^{2+}-signalling in human astrocytes, responsivity to the classical neurotransmitters glutamate and ATP has recently been demonstrated in adult astrocytes purified from brain samples (Zhang *et al.*, 2016). Intriguingly, responsivity to glutamate was at the same time shown to be absent in human foetal astrocytes, which distinguished the human astrocytes from highly responsive rat foetal astrocytes. Another dissimilarity between human and rodent astrocytes has been detected in terms of Ca^{2+}-signalling, as human astrocytes were surprisingly found to propagate Ca^{2+}-waves across a field of view (triggered by Ca^{2+}-uncaging) ~5 times faster than mouse astrocytes (Oberheim *et al.*, 2009). Studies in human iPSC-derived astrocytes, or astrocytes derived from human NT2 cells (a carcinoma stem cell line), have used imaging methods to demonstrate intracellular Ca^{2+} events in response to mechanical injury (Krencik *et al.*, 2011; Roybon *et al.*, 2013; Serio *et al.*, 2013; Li *et al.*, 2018), the neurotransmitters ATP and glutamate (Hill *et al.*, 2012; Serio *et al.*, 2013), as well as spontaneous Ca^{2+} transients (Tcw *et al.*, 2017). As the human astrocytes presented in this thesis were generated using a novel protocol, an important

aim of **Chapter 4** was to describe the spontaneous and evoked Ca^{2+}-signalling properties of the iPSC-derived astrocytes.

1.5 Gliotransmission

A central idea in the field is that intracellular Ca^{2+} elevations are a key step in the process by which astrocytes release neuroactive substances, termed gliotransmitters. Indeed, the concept of gliotransmission offers an explanation of how astrocytes might actively participate in and influence neuronal signalling (Volterra and Meldolesi, 2005) (**Figure 1.2**). The notion of a feedback loop between neurons and astrocytes was sparked by a series of influential studies in the 1980's and early 1990's. These studies discovered that astrocytes could sense neural transmission and responded with intracellular Ca^{2+} events (Bowman and Kimelberg, 1984; Kettenmann, Backus and Schachner, 1984; Cornell-Bell *et al.*, 1990; Porter and McCarthy, 1996), and provided the first evidence that glutamate-triggered Ca^{2+}-activity in astrocytes could trigger Ca^{2+} increases in co-cultured neurons (Nedergaard, 1994; Parpura *et al.*, 1994).

By the late 1990's, several studies had reported glial modulation of synaptic activity (e.g. (Hassinger *et al.*, 1995; A Araque *et al.*, 1998; Alfonso Araque *et al.*, 1998; Bezzi *et al.*, 1998; Kang *et al.*, 1998; Sanzgiri, Araque and Haydon, 1999)) and crucially, the study by Bezzi and colleagues linked neuronal transmission to a meaningful astrocytic output. These authors found that activation of ionotropic and metabotropic glutamate receptors on astrocytes stimulated a Ca^{2+}-dependent glutamate release from the astrocytes, thereby providing a potential mechanism for a feedback loop from neuron to astrocyte, and back to the neuron (Bezzi *et al.*, 1998).

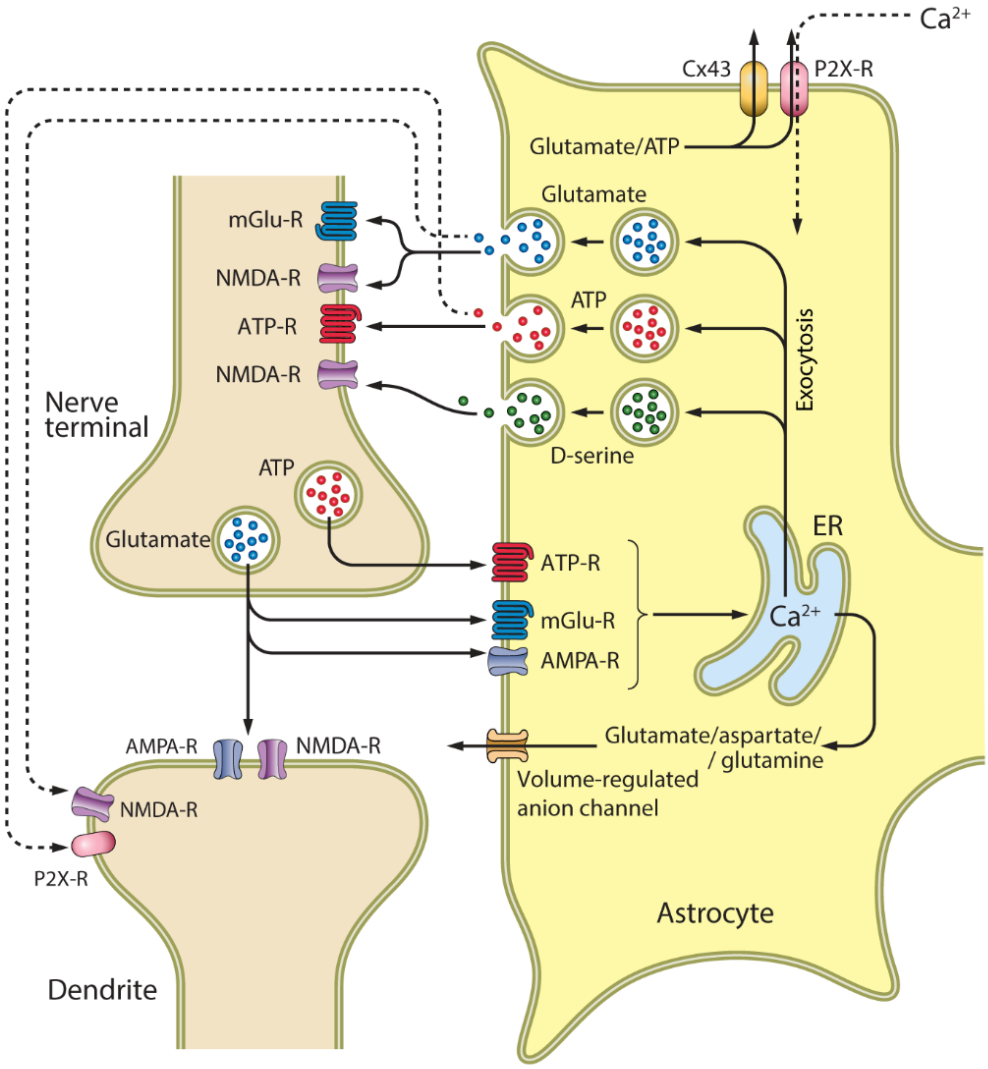

Figure 1.2 Mechanisms implicated in gliotransmission
Schematic overview of the mechanisms that have been implicated in intracellular increases in Ca^{2+} in astrocytes, the release of gliotransmitters, and the effects of gliotransmitters on synaptic activity. Pre-synaptically released glutamate and ATP can activate AMPARs and metabotropic glutamate and ATP receptors on nearby astrocytic processes. This receptor activation leads to Ca^{2+} release from the endoplasmic reticulum (ER). Alternatively, Ca^{2+} can enter astrocytes from the extracellular space via P2X receptors, although there is greater evidence for intracellular store involvement. Increases in the cytosolic Ca^{2+} concentration may trigger exocytotic release of gliotransmitters (e.g., glutamate, D-serine, ATP). Gliotransmitters are also hypothesised to be released through the opening of volume-regulated anion channels, P2X ATP receptors or Cx43 hemichannels. When released, the gliotransmitters can activate receptors on the pre-synaptic membrane or on post-synaptic dendrites. Adapted from Gundersen (2015).

Despite the often non-specific mechanical and electrical stimulation methods utilized in early experiments, the concept of Ca^{2+}-mediated gliotransmission was subsequently shown to operate at a finer synaptic scale. In elegant experiments by both Di Castro et al. (2011) and Panatier et al. (2011), astrocytic processes were proven to be capable of sensing neuronal signalling down to a scale of single synapses, as they responded to miniature excitatory post-synaptic events with focal Ca^{2+} increases (Di Castro *et al.*, 2011; Panatier *et al.*, 2011). Furthermore, both studies showed that local astrocytic Ca^{2+}-activity regulated basal synaptic transmission, as chelating Ca^{2+} in an astrocyte increased the synaptic failure rate in nearby neurons.

Whilst the neurotransmitter-evoked astrocytic Ca^{2+} increases and modulation of neuronal transmission are widely accepted, the proposed Ca^{2+}-dependent mechanism of exocytosis in gliotransmission is the source of current debate (Perea and Araque, 2010; Nedergaard and Verkhratsky, 2012; Araque *et al.*, 2014; Sloan and Barres, 2014; Bazargani and Attwell, 2016; Fiacco and McCarthy, 2018; Savtchouk and Volterra, 2018). As many experiments reporting gliotransmission have been conducted in cultured astrocytes, concerns regarding the physiological relevance of gliotransmission have also been raised. Recently, a select number of experiments employing more sophisticated transgenic mice, acute brain slices and *in vivo* techniques, have failed to detect gliotransmission (Fiacco *et al.*, 2007; Petravicz, Fiacco and McCarthy, 2008; Agulhon, Fiacco and McCarthy, 2010). This has fuelled a debate concerning whether gliotransmission occurs under physiological circumstances and in response to physiological stimuli (Hamilton and Attwell, 2010; Fiacco and McCarthy, 2018; Savtchouk and Volterra, 2018). One view is that previously employed methods for detecting

gliotransmission have been too crude, non-physiological and/or not astrocyte-specific (Fiacco and McCarthy, 2018). Indeed, it has been suggested that Ca^{2+}-dependent release of gliotransmitters is associated only with disease states and reactive astrocytes, rather than being a feature of the healthy brain (Agulhon *et al.*, 2012). The alternative view argues for a more nuanced view of astrocytic Ca^{2+}-signalling; that we do not fully understand the intricacies of astrocytic Ca^{2+}-signalling, such as the role of different sub-cellular compartments (Bazargani and Attwell, 2016). Advocates of Ca^{2+}-dependent exocytosis also rebut that the few experiments in which gliotransmission was not detected might reflect special cases, and that it is too simplistic to claim that gliotransmission is absent from all circuits and brain areas (Savtchouk and Volterra, 2018).

Whether or not astrocytes possess the necessary machinery for vesicular release is also a point of contention. Evidence from electron microscopy, immunogold labelling and single cell reverse transcription and quantitative polymerase chain reaction (RT- and qPCR) have supported the presence of key exocytotic components: small synaptic-like vesicle structures, vesicle loading VGLUT's and vesicle fusion proteins SNAREs, VAMPs and synaptobrevin-2 within astrocytic processes that are facing neuronal synapses (Araque *et al.*, 2000; Bezzi *et al.*, 2004; Crippa *et al.*, 2006; Jourdain *et al.*, 2007; Bergersen *et al.*, 2012; Chai *et al.*, 2017). This is countered by a lack of transcriptomic evidence for VGLUT's and the Ca^{2+}-sensing synaptotagmin mRNA (Cahoy *et al.*, 2008; Chai *et al.*, 2017), as well as whether the estimated 6-fold lower concentration of glutamate in astrocytic vesicles (Bramham *et al.*, 1990) is sufficient to activate neuronal NMDA and AMPA receptors (Barres, 2008; Hamilton and Attwell, 2010). Lastly, opponents of astrocytic Ca^{2+}-dependent exocytosis highlight that

glutamate release can occur in several other ways, for example as a response to swelling or depolarisation, which can open unopposed hemichannels to allow the exit of small cytoplasmic molecules, including glutamate and ATP (Theis *et al.*, 2005; Sloan and Barres, 2014).

The common ground at the moment appears to be that gliotransmission in terms of neuroactive substances released by astrocytes is not controversial, but that the relative importance of Ca^{2+}-mediated vesicular release is unclear (Sloan and Barres, 2014; Fiacco and McCarthy, 2018; Savtchouk and Volterra, 2018). Much of the controversy and contradictory results may stem from a fundamental issue in glia research, which is a shortage of glia-specific tools that offer cell-specific and temporally precise manipulations. Perturbing astrocytes alone without affecting any neuronal or synaptic processes is challenging and, as the existence of gliotransmission is based on neuronal readouts, measurements of astrocytic activity are often the result of indirect inferences (Nedergaard and Verkhratsky, 2012).

1.6 Genetic tools for stimulating astrocytes

Genetic tools promise to be the most direct way of manipulating astrocytes, but care must be taken regarding the specificity of targeting and ensuring that astrocytes still function as expected, given their multiple roles. Astrocytes can be targeted independently of neurons by expressing optogenetic and chemogenetic tools like the cation-permeable opsin Channelrhodopshin-2 (ChR2) or designer receptors exclusively activated by designer drugs (DREADDS) under astrocyte-specific promoters. Recently, modulation of a variety of astrocytic functions has been achieved by utilising such tools in a cell-targeted and temporally-controlled manner in rodent models.

Astrocytic functions influenced by ChR2 stimulation range in scale from cellular interactions to brain-wide and behavioural changes. Among the latter are promotion of sleep when hypothalamic astrocytes in mice were stimulated through ChR2 (Pelluru *et al.*, 2016), but conversely also disturbance of sleep when instead astrocytes in the anterior cingulate cortex was stimulated (Yamashita *et al.*, 2014). If ChR2 was used in its capacity to induce astrocytic acidification through its permeability to H^+, it was shown both to stimulate respiration *in vivo* (Gourine *et al.*, 2010), as well as lead to increased glutamate release and exacerbation of ischemic damage (Beppu *et al.*, 2013). Interestingly, Beppu and colleagues employed another optogenetic tool, Archaerhodopsin, which acts by pumping H^+ out of the cell, to create the reverse effect of alkalinisation and cessation of glutamate release, which ultimately reduced ischemic brain damage (Beppu *et al.*, 2013). Direct cellular interaction with vasculature was detected when astrocyte-targeted ChR2 stimulation was found to transiently increase cerebral blood flow in a K^+-dependent manner (Masamoto *et al.*, no date); similar gliovascular coupling was reported to be capable of evoking BOLD fMRI responses (Takata *et al.*, 2018).

Of particular interest to this thesis are reports of astrocyte-neuron interactions. Several groups have reported intracellular Ca^{2+} increases and associated glutamate release (Sasaki *et al.*, 2012; Berlinguer-Palmini *et al.*, 2014; Ono *et al.*, 2014; Perea *et al.*, 2014; Shen *et al.*, 2017a) or L-lactate release (Tang *et al.*, 2014) when astrocytes were stimulated with ChR2 or light-gated Ca^{2+}-permeable ionotropic glutamate receptor 6 (LiGluR) (D. Li *et al.*, 2012). By providing temporally-controlled activation with brief pulses of light, a subset of these groups have been able to observe short-term effects upon the synaptic signalling between

nearby neurons (D. Li *et al.*, 2012; Sasaki *et al.*, 2012; Berlinguer-Palmini *et al.*, 2014; Perea *et al.*, 2014; Shen *et al.*, 2017a), with most equating these effects to gliotransmission. Excitingly, astrocyte-specific effects on long term potentiation (LTP) and behavioural performance on memory tasks have very recently been demonstrated in mice both via DREADDs and two different optogenetic constructs (Adamsky *et al.*, 2018; Mederos *et al.*, 2019). Adamsky and colleagues reported firstly that activation of the astrocyte-targeted DREADDs was sufficient to induce LTP, which was found to be dependent on NMDARs and D-serine. Secondly, *in vivo* stimulation of astrocytes via DREADDS or light activation of the Opto-α1AR opsin before and during T-maze and fear conditioning memory tasks improved the performance of the mice. Similarly, Mederos et al. stimulated astrocytes using melanopsin and detected induction of LTP, which in their experiments was dependent on ATP, as well as enhanced episodic-like memory when mice performed a novel object recognition task (Mederos *et al.*, 2019).

Newer optogenetic tools like LiGluR and the Ca^{2+}-translocating channelrhodopsin (CatCh) have been reported to produce more reliable intracellular Ca^{2+} elevations in astrocytes (D. Li *et al.*, 2012) than ChR2. Interestingly, LiGluR triggers Ca^{2+} release from internal stores, whereas the Ca^{2+} elevations generated by CatCh are independent of internal store release, which makes these tools interesting for investigating different astrocytic Ca^{2+} signalling pathways (Li, Agulhon, *et al.*, 2013). In addition, recently developed G-protein coupled receptor-based opsins opto-α1AR (Gq-coupled), opto-β2AR (Gs-coupled) and melanopsin, derived from a G-protein-coupled photopigment, could allow for initiation of astrocytic Ca^{2+} events via more physiological routes than traditional opsins. While it is early

days in terms of the routine application of opto-ARs and melanopsin, they have been tested in astrocytes (Figueiredo *et al.*, 2014; Adamsky *et al.*, 2018; Mederos *et al.*, 2019), yet ChR2 and its derivatives are still the most predominantly used optogenetic tool for both neuronal and glial cell types.. In **Chapter 5**, I will capitalise on the optogenetic strategies developed in rodent models for temporally-controlled stimulation of astrocytes using ChR2. I will apply and modify astrocyte-specific optogenetic stimulation in cultures derived from human iPSCs to explore the reciprocal communication between astrocytes and neurons in a human cellular context.

1.7 The translational challenge of animal models

Our knowledge of neuron-astrocyte interactions originates overwhelmingly from studies conducted in rodents. With the advance of transgenic technology, mouse models have become an invaluable tool in neuroscience, in part because they enable the tracking of disease progression throughout their lifespan, but also because of the limited access to human brain tissue (Merkle and Eggan, 2013). Although excised human brain tissue can be regarded as the gold standard model of human brain function, it is important to take into consideration that it is almost always obtained from a disease state, which means that there is no true control condition (Marchetto, Winner and Gage, 2010). Human brain tissue is most often available post mortem, where the tissue is typically aged and generally represents the later stages of the disease. This results in limited information about earlier phases of both normal and diseased states (Marchetto, Winner and Gage, 2010). For studying age-related neurodegenerative diseases in particular, animals with shorter life-spans have made it feasible to model disease progression. Yet, the most widely used animals for studying

neurodegeneration, mice and rats, conspicuously do not naturally develop pathological hallmarks of diseases such as AD during their short life time; whereas these hallmarks are detected in other species (Youssef *et al.*, 2016; Gunn-Moore *et al.*, 2018).

A series of AD mouse models exist, which have been used to elucidate many aspects of both familial and sporadic AD (Cavanaugh, Pippin and Barnard, 2014; Dawson, Golde and Lagier-Tourenne, 2018). However, despite being immensely valuable in leading discoveries into fundamental disease mechanisms and drug development, there have been significant issues with the translation of therapeutics from animal models into clinical practice (Cavanaugh, Pippin and Barnard, 2014; Dawson, Golde and Lagier-Tourenne, 2018). Regrettably, no new drug for AD has been approved since 2003, and the clinical trial failure rate between 2002 and 2012 was a staggering 99.6% (Cummings, Morstorf and Zhong, 2014). This would suggest that there is a species gap between humans and rodents, who notably diverged ~75 million years ago (Sayed, Liu and Wu, 2016), a gap substantial enough that translation is not trivial (Merkle and Eggan, 2013; Cavanaugh, Pippin and Barnard, 2014; Mungenast, Siegert and Tsai, 2015; Sayed, Liu and Wu, 2016).

In particular, transgenic animal models are subject to limitations, for example in terms of genomic differences, dissimilar cellular and molecular environments, and how the disease phenotype is achieved. In transgenic or viral-based models, an exogenous, often human, gene is overexpressed under a strong promoter in all tissues in order for the disease phenotype to be apparent. This requirement makes these models prone to artefacts associated with overexpression and random integration effects. Targeted knock-in and knock-out models help alleviate some of these issues, however phenotypes tend to be either mild, or in many cases

lethal in knock-outs (Dawson, Golde and Lagier-Tourenne, 2018). There is a possibility that human genes and proteins have different functions in mice, such that transgenic mutations might not have the same effect outside of a human context. For example, the sequence of the mouse gene producing endogenous α-synuclein corresponds to the disease-causing A53T mutation in humans (Dawson, Golde and Lagier-Tourenne, 2018). Although the coding regions of murine and human genomes share an 85% similarity, the alignment between human and mouse genomes is limited in the non-coding regions, where similarity is 50% or less (NIH, 2010). This is a particular issue, as many genetic variants associated with human disease are located in these non-coding regions of DNA, which makes it less likely that an animal model expressing these particular genetic variants will replicate the human phenotype (Merkle and Eggan, 2013).

The failures of clinical drug trials, particularly for AD, has led many to consider experimental approaches that could help to bridge the species gap between the popular rodent models and human physiology (Cavanaugh, Pippin and Barnard, 2014; Mungenast, Siegert and Tsai, 2015; Crompton, Cordero-Llana and Caldwell, 2017). The advances achieved in the field of iPSC technology over the last decade have offered some optimism for just such a bridge, and there has been a wave of enthusiasm for taking advantage of iPSC technology in an effort to expedite clinical drug trials (Merkle and Eggan, 2013; Cavanaugh, Pippin and Barnard, 2014; Cummings, Morstorf and Zhong, 2014; Sayed, Liu and Wu, 2016). It is argued that this can be achieved through testing drug candidates in a relevant human cellular context, prior to clinical trials. Using iPSC-derived human cells it would be possible to gage toxicity,

establish potential effective dose ranges and even identify subsets of patients who might be more responsive to a particular drug (Sayed, Liu and Wu, 2016).

In terms of modelling human neurological conditions, it is interesting to note that while neuronal properties appear to be relatively well-conserved between species, interspecies differences in astrocytes are being increasingly recognised (Oberheim *et al.*, 2009; Chandrasekaran *et al.*, 2016; Zhang *et al.*, 2016; Crompton, Cordero-Llana and Caldwell, 2017). The work in this thesis was in part motivated by this translational issue, and represents efforts to establish a purely human co-culture model in which interactions between neurons and astrocytes can be investigated. A number of assays were designed to test whether phenomena and mechanisms described in the extensive rodent literature, can or cannot be recapitulated in human iPSC-derived astrocytes.

1.8 Induced pluripotent stem cell technology

Induced pluripotent stem cell technology was invented just over 10 years ago in the lab of Shinya Yamanaka. This ground-breaking research into somatic reprogramming was inspired by the extraordinary discovery that cell differentiation is not irreversible, as a central dogma of developmental biology had otherwise claimed. Yamanaka and Takahashi wondered if they could identify central genes that are capable of reversing differentiation and inducing pluripotency, as Wilmut and colleagues had shown was possible by transferring a nucleus from an already differentiated somatic cell into an oocyte (Wilmut *et al.*, 1997). Starting off with a selected list of 24 candidate genes, Takahashi and Yamanaka proceeded to narrow down their list by retrovirally transducing combinations of these genes into mouse fibroblast cells and assessing iPSC colony production (Takahashi and Yamanaka, 2006). No single factor

produced colonies, but by transducing cells with all factors barring one at a time, the factors crucial to colony-formation were narrowed down to a combination of just 4 genes: *Sox2*, *Oct3/4*, *c-Myc* and *Klf4*. These are genes involved in maintaining pluripotency in embryonic stem cells (ESCs) or with tumorigenesis. Like ESCs, iPSCs were shown to be able to form teratomas containing differentiated cells from all three germ layers when transplanted into nude mice (Takahashi and Yamanaka, 2006). iPSCs were concluded to be similar, although not identical to, ESCs through examining global gene expression with DNA microarrays. Excitingly, Takahashi and colleagues repeated their success just one year later by using their 4 factors to generate iPSCs from human skin fibroblasts (Takahashi *et al.*, 2007).

Until the invention of iPSC technology, ESCs were the best candidates for transplantation-based cell therapies, but there are certain difficulties associated with their use. Firstly, where ESCs are ethically controversial, in that they are derived from human embryos, iPSCs can be derived from simple skin or blood samples (Zhang, 2013). Secondly, the foetal state of ESCs limits their use in disease modelling, as only developmental monogenic diseases or ones that can be introduced via gene editing can be modelled (Mateizel *et al.*, 2006; Ding *et al.*, 2013). iPSCs on the other hand can be generated from adults where clinical diagnoses have been established, meaning that diseases with later onset can also be modelled (**Figure 1.3**). This is particularly valuable for modelling sporadic and polygenic disorders, where no single mutation determines the disease outcome, but where maintaining the full genetic background is more likely to reveal the interplay between risk factors.

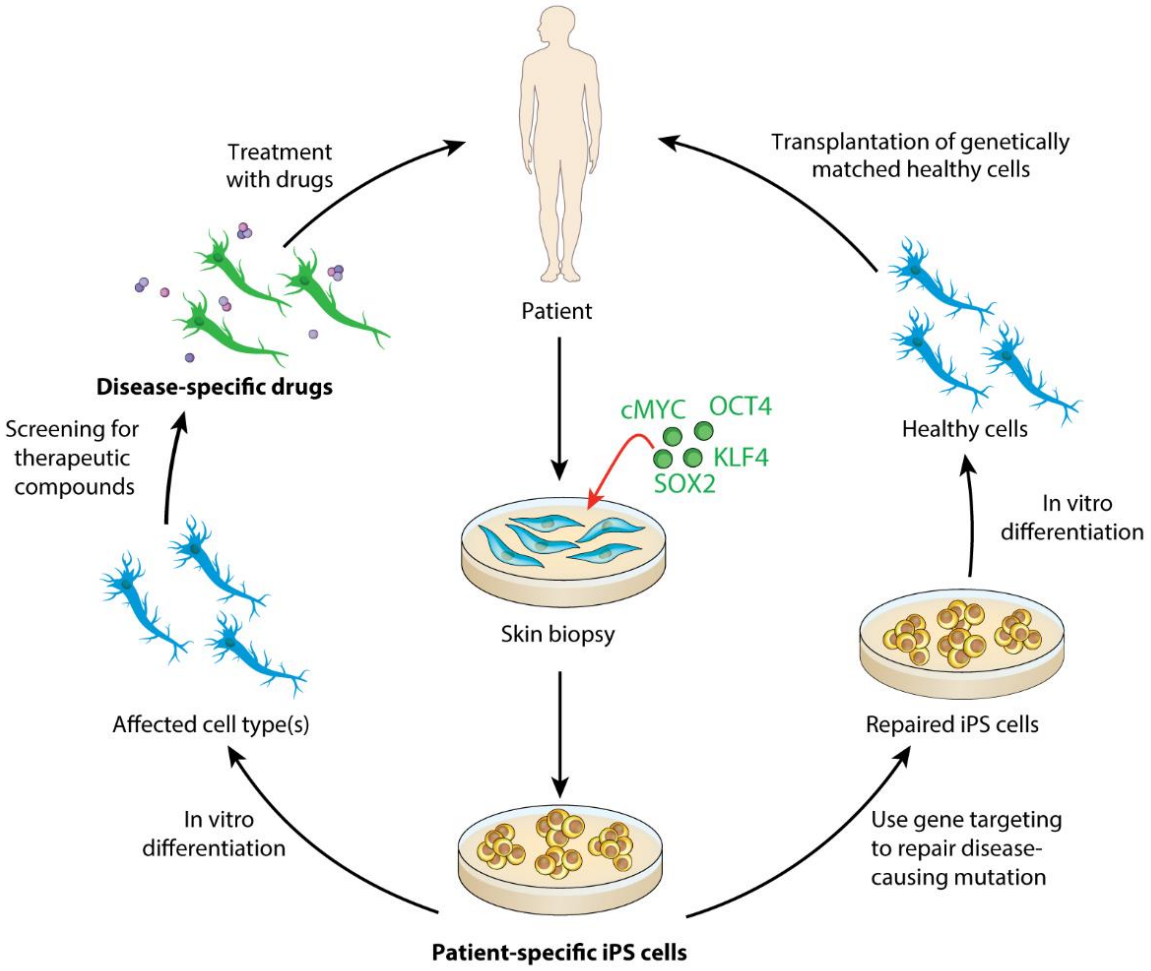

Figure 1.3 Potential medical applications of induced pluripotent stem cell technology

Illustration of how iPSC technology may be used both to model and treat human diseases. A patient skin biopsy is reprogrammed to iPSCs by expressing the four "Yamanaka factors": cMYC, OCT4, KLF4 and SOX2. The patient-specific iPSCs can either be differentiated *in vitro* to specific cell types (left-hand side) and used as a model system to study disease mechanisms and ultimately screen drugs prior to clinical trials. Or, in the context of a neurodegenerative disease for example, the patient-specific iPSCs can be gene-edited to repair a disease-causing mutation (right-hand side), after which the iPSCs can be differentiated *in vitro* to the desired cell type for cell-replacement therapy. Adapted from Robinton & Daley (2012).

To this end, the combination of iPSC and gene editing techniques like clustered regularly interspaced short palindromic repeats (CRISPR) is well-placed to uncover the influence of sporadic mutations, as it allows for studying the effect of altering one isolated mutation, whilst keeping the remaining genetic background constant (Robinton and Daley, 2012). Thirdly, because ESCs will always be derived from a donor, cell transplantation therapy includes the risk of tissue rejection, whereas iPSC technology is more compatible with the idea of individualised medicine, where an individual can have their own cells reprogrammed and transplanted after differentiation (Sayed, Liu and Wu, 2016).

1.9 Recapitulating mammalian cortical development with iPSC models

An important starting point for this thesis is the iPSC differentiation protocols that have been developed for generating specific CNS cell types. One area where stem cell based protocols have found success in recapitulating aspects of *in vivo* developmental biology, is in the generation of cortical neurons (Watanabe *et al.*, 2005; Eiraku *et al.*, 2008; Gaspard *et al.*, 2008; Shi *et al.*, 2012a; Kadoshima *et al.*, 2013). This has represented an important achievement for the iPSC field, as many neurodegenerative and neuropsychiatric disorders are associated with changes at the level of the cortex, including AD (Braak and Braak, 1991; Thompson *et al.*, 2010; Arendt *et al.*, 2015; Gan *et al.*, 2018). Corticogenesis *in vivo* is a remarkably self-governed process, which protocols using iPSCs have attempted to mimic. The germ-layer of importance for nervous system development is the ectoderm, which during the *in utero* process of neurulation folds up and forms the neural tube. The ectoderm can both become skin and central nervous system, but differentiation towards skin is inhibited by

signals from the underlying notochord, inhibiting bone morphogenic protein (BMP) an nodal/activin signalling (Levine and Brivanlou, 2007; Reichert, Randall and Hill, 2013). This inhibition sets progenitors on the default pathway towards telencephalon differentiation (Wilson and Houart, 2004; Levine and Brivanlou, 2007; Anderson and Vanderhaeghen, 2014).

Commonly used iPSC protocols recapitulate this process by employing dual SMAD inhibition, which converges on the BMP and nodal/activin pathways (Chambers *et al.*, 2009). Neuroepithelial cells at the rostral end of the neural tube become the brain, whilst the spinal cord is formed from the caudal end (Stiles and Jernigan, 2010). Around the time of the closure of the neural tube, the anterior/rostral regions undergo rapid expansion, creating neural progenitors that will give rise to the cells of the hindbrain, midbrain and forebrain, the most anterior part of which will make up the cortex (Stiles and Jernigan, 2010). A striking feature of iPSC-based directed neural differentiation protocols is the seemingly inherent propensity of the cells to form so-called rosette structures, reminiscent of transverse sections of a neural tube (Kelava and Lancaster, 2017). In the pre-neurogenic phase, the neuroepithelial cells within the telencephalon divide symmetrically and expand their population, forming the highly proliferative ventricular zone (VZ) (Florio and Huttner, 2014). Remarkably, the rosette structures arising spontaneously during iPSC neural differentiation display features reminiscent of ventricular and sub-ventricular zones (SVZ) in terms of proliferation patterns and marker expression (Edri *et al.*, 2015; Kelava and Lancaster, 2017).

At the onset of the neurogenic phase, the neuroepithelial cells undergo a morphological transformation to radial glia progenitor cells, which are the originators of additional cortical glutamatergic neuronal progenitor types (Paridaen and Huttner, 2014;

Manuel *et al.*, 2015). Radial glia are characterised by their apical process that extends to the pial surface, and by the expression of transcription factors: paired box protein-6 (PAX6), forkhead box protein G1 (FOXG1) and empty spiracles homeobox 1 and 2 (EMX1/2) (Bystron, Blakemore and Rakic, 2008; Jiang and Nardelli, 2016). Radial glia initially also self-renew at the ventricular surface via symmetric divisions, but gradually switch to asymmetric divisions that produce neurons (**Figure 1.4**). These asymmetric divisions can produce a radial glia daughter cell and either an intermediate progenitor cell, characterised by T-box brain protein-2 (TBR2) but not PAX6 expression (Florio and Huttner, 2014), or a neuron. Intermediate progenitors and newly born neurons then migrate along the apical processes of radial glia to populate the SVZ and the cortical plate, respectively (Florio and Huttner, 2014). Lastly, the radial glia can produce an intermediate progenitor cell, along with an outer radial glial cell (Bystron, Blakemore and Rakic, 2008; Jiang and Nardelli, 2016). Outer radial glia will renew themselves and produce intermediate progenitors, whereas the intermediate progenitors only divide once to give rise to two neurons (Paridaen and Huttner, 2014).

Interestingly, important species differences in terms of progenitor-pool composition and the neuronal output associated with each progenitor sub-type have been reported, with the apparent abundance of intermediate progenitors being highlighted as a potentially important driver of evolutionary differences in cortical expansion between the rodent and primate brain (Lodato, Shetty and Arlotta, 2014; Paridaen and Huttner, 2014; Kelava and Lancaster, 2017). As cortical complexity of neuronal subtypes is thought to arise from a

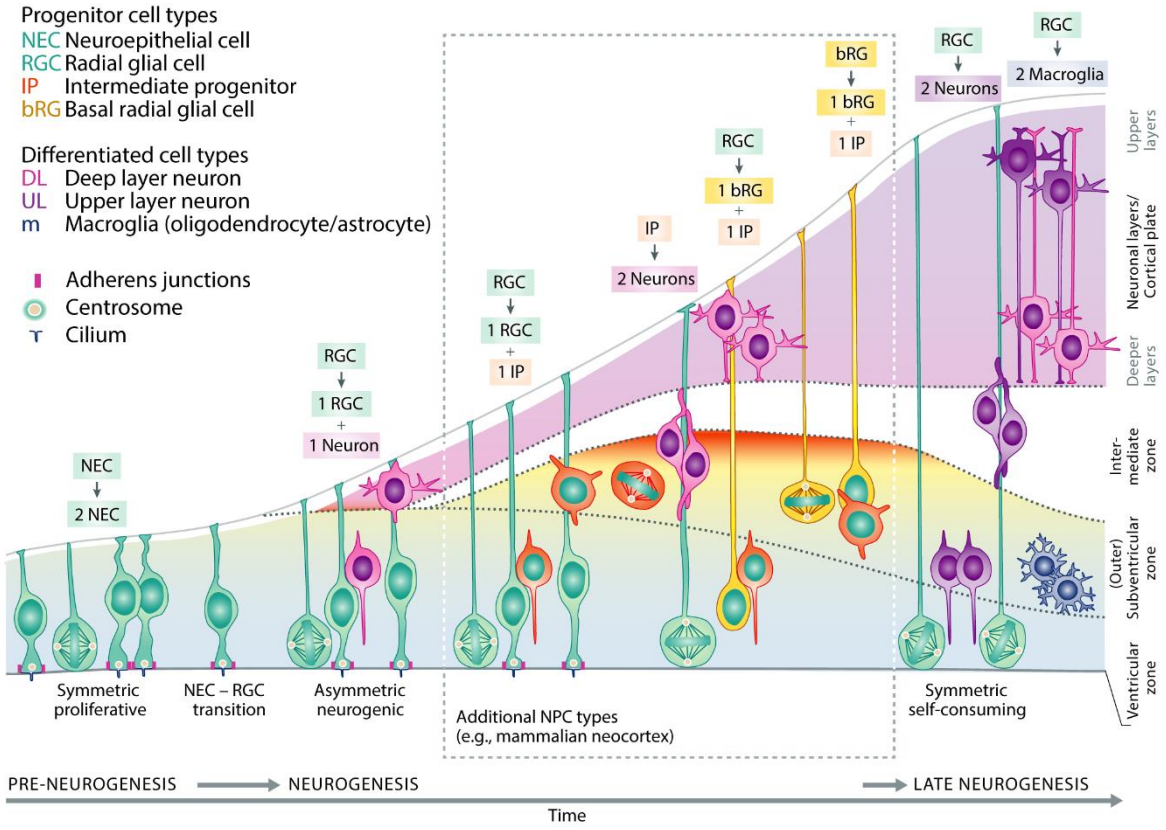

Figure 1.4 Embryonic neurogenesis and gliogenesis
Schematic overview of central nervous system development in vertebrates, with mammalian-specific progenitor subtypes highlighted in the dashed box. The possible outcomes of neural progenitor divisions are indicated above the illustration. Note that outer radial glia are referred to as "basal radial glial cells" and that astrocytes are represented under the term "macroglia". Adapted from Paridaen & Huttner (2014).

diversity of neuronal progenitors (Gaspard *et al.*, 2008; Shi, Kirwan and Livesey, 2012), it has been seen as important for iPSC cortical differentiation protocols to demonstrate the generation of these different progenitor pools (Shi *et al.*, 2012a).

Another remarkable example of self-organisation during *in vivo* corticogenesis is the formation of the cortical layers. The mammalian cortex consists of six layers that are generated in an "inside-out" fashion, with deeper layer neurons arising first, and upper layer neurons being born later and migrating from the VZ through the deeper layers before reaching their destination (Manuel *et al.*, 2015; Suzuki and Vanderhaeghen, 2015; Kelava and Lancaster, 2017). As such, the layer-identity of a cortical neuron depends on the time during

corticogenesis at which the neuron was generated. Notably, the protocol utilized in this thesis for generating iPSC-derived cortical neurons has been shown to recapitulate this general phenomenon of time-dependent layer formation (Shi *et al.*, 2012a; Shi, Kirwan and Livesey, 2012). Nevertheless, this and other protocols have reported a skewing of neuronal populations towards deeper layers, rather than upper layers (Gaspard *et al.*, 2008; Espuny-Camacho *et al.*, 2013; Kindberg *et al.*, 2014; Van den Ameele *et al.*, 2014) This is in contrast to the situation *in vivo*, and may be caused by the low-density non cell-aggregate culture methods employed (Anderson and Vanderhaeghen, 2014; Van den Ameele *et al.*, 2014). Accelerated neuronal maturation and skewing towards upper layer neuronal fates was achieved in protocols forcing expression of the neuronal differentiation factor, Neurogenin-2 (Ngn2), via an inducible lentiviral system, either starting from iPSCs (Zhang *et al.*, 2013) or neural progenitor cells (NPCs) (Ho *et al.*, 2015).

The adult mammalian cortex is reported to consist of ~80% excitatory neurons and ~20% inhibitory neurons (Hendry *et al.*, 1987; Markram *et al.*, 2004), with interneurons most commonly reported as originating from the ventral ganglionic eminences and migrating tangentially into cortex during later stages of development (Wonders and Anderson, 2006). In an iPSC-based system, ventralisation can be achieved by activation of sonic hedgehog (SHH) signalling (Liu and Zhang, 2011), which leads to the presumption that a protocol lacking morphogens will only generate glutamatergic neurons (Shi *et al.*, 2012a). However, published protocols, similar to the one utilized in this thesis, also lacking ventralising morphogens, have reported small proportions of interneurons or interneuron progenitors (Weick *et al.*, 2013; Floruta *et al.*, 2017), and contrary to the general consensus, interneuron

progenitors have in fact been detected within the developing human cortex (Jakovcevski, Mayer and Zecevic, 2011; Zecevic, Hu and Jakovcevski, 2011).

For the above reasons, in generating iPSC-derived cortical neurons to study neuron-astrocyte interactions, a portion of **Chapter 3** is devoted to characterising a published cortical differentiation protocol. The protocol is assessed in terms of its ability to recapitulate aspects of *in vivo* corticogenesis, including the formation of different progenitor-pools, self-organisation into neural-tube-like rosettes, inside-out layer formation and the emergence of functional excitatory and inhibitory neuron types.

1.10 Mammalian gliogenesis and implications for iPSC differentiation

The neurogenic period of corticogenesis is followed by a period of gliogenesis, where radial glial cells begin to preferentially give rise to astrocytes (Barnabé-Heider *et al.*, 2005; Kessaris, Pringle and Richardson, 2013; Tyzack, Lakatos and Patani, 2016) (**Figure 1.4**). In humans, this switch occurs around 7 months of gestation (Roessmann and Gambetti, 1986; Van den Ameele *et al.*, 2014) and based on rodent research, gliogenesis is thought to include two proliferative progenitor stages (Molofsky and Deneen, 2015). First, astrocyte progenitors arise from asymmetric divisions of proliferating radial glia. These astrocyte progenitors then migrate to their final destinations throughout the brain and there is evidence to suggest that their migration pattern is primarily radial, such that the progenitors tend to be restricted to a cortical column (Jacobsen and Miller, 2003). The second proliferative stage involves the local symmetric divisions of the astrocyte progenitors at their final destination. These divisions produce immature astrocytes (Molofsky and Deneen, 2015; Schitine *et al.*, 2015), which will

go on to fully differentiate into mature astrocytes at later stages (Ge *et al.*, 2012). Additionally, some evidence suggests that a separate pool of non-radial glia astrocyte-restricted precursors may arise from neuro-epithelial stem cells after neurogenesis (Y. Liu *et al.*, 2004; Kessaris, Pringle and Richardson, 2013), but the distinction between this astrogenic pathway and the one involving radial glia is poorly defined. Regional diversity is thought to be acquired during these later stages and to be regulated by local extrinsic cues to match the need of the surrounding neuronal tissue (Freeman, 2010). Finally, subsets of astrocytes are believed to retain their proliferative potential throughout adulthood, as they have been shown to be capable of dividing in response to physical injury and to contribute to the formation of a glial scar (Mohn and Koob, 2015; Dossi, Vasile and Rouach, 2018). If these astrocytes subsequently revert to their quiescent state, such a reaction is viewed as tissue protective (Mohn and Koob, 2015). However, astrocytes that remain in a reactive state have been implicated in pathological states, including neurodegenerative conditions (Dimou and Götz, 2014; Crompton, Cordero-Llana and Caldwell, 2017).

Much remains to be discovered regarding how local patterning affects the functional diversity of astrocytes (Molofsky and Deneen, 2015), but in terms of human cortex, four morphologically distinct astrocytic subtypes have been identified (**Figure 1.5**): a) Projection astrocytes, which reside in cortical layer I but send tortuous processes through layers II-IV; b) Protoplasmic astrocytes, which reside within cortical layers II-VI and exhibit a "bushy" morphology that reflects their involvement in synapse monitoring; c) Varicose projection astrocytes, which reside in layers V-VI and are characterised by varicosities on their processes; and d) Fibrous astrocytes, which reside in the white matter (Oberheim *et al.*, 2009). Of these,

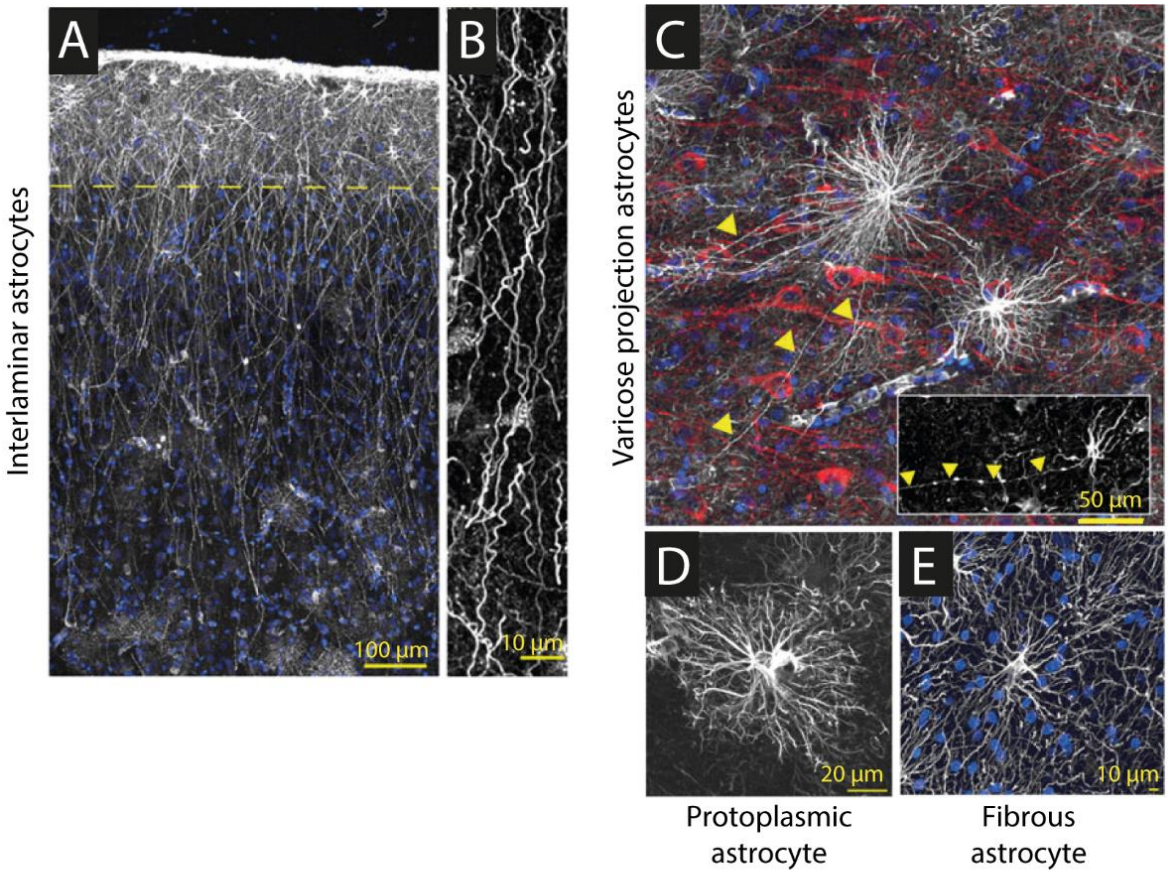

Figure 1.5 Morphologies of human astrocytes
Astrocytes labelled with DAPI (blue) and GFAP (white) from post-mortem brain tissue. **(A)** Interlaminar astrocytes in layers I-II of cortex. The layer distinction is indicated by the dashed line. **(B)** Characteristic tortuous projections of interlaminar astrocytes. **(C)** Varicose projection astrocytes in layer V-VI, inset showing the regularly spaced varicosities, MAP labelling of neurons (red). **(D)** Highly branched protoplasmic astrocytes in layers II-VI. **(E)** White matter fibrous astrocytes. Adapted from Oberheim et al. (2009).

a) and c) have so far only been observed in humans and higher order primates, and both human protoplasmic and fibrous astrocytes were found to be larger and more highly branched than their rodent counterparts (Oberheim *et al.*, 2009). Furthermore, human and rodent astrocytes also differ significantly in their gene expression profiles, with over 600 genes found to be active in human astrocytes, but not detected in rodents (Zhang *et al.*, 2016). Excitingly, transcriptomic methods for distinguishing subclasses of astrocytes across different brain

regions have recently been developed both for mouse (Chai *et al.*, 2017) as well as human brain (John Lin *et al.*, 2017).

In human iPSC-derived neuronal cultures, the gradual appearance of astrocytes has been reported after prolonged culture periods (Shi *et al.*, 2012a). This so-called 'gliogenic switch' is controlled by Notch signalling, which at an epigenetic level induces the de-methylation of glial genes such as glial fibrillary acidic protein (*GFAP*) (Namihira *et al.*, 2009) and, at a signalling level, influences both pro-neural basic helix loop helix factors as well as activating the astrogliogenic Janus kinase-signal transducer and activator of transcription (JAK-STAT)-pathway (Tyzack, Lakatos and Patani, 2016). Secreted cytokines that influence the JAK-STAT-pathway, such as leukaemia inhibitory factor (LIF), ciliary neurotrophic factor (CNTF) and cardiotrophin-1 (CT-1), have been utilised in protocols for differentiating stem cells into astrocytes in an effort to activate the gliogenic switch (Krencik and Zhang, 2011; Emdad *et al.*, 2012; Serio *et al.*, 2013; Shaltouki *et al.*, 2013).

The protocols mentioned here are based on the re-capitulation of a neurogenic expansion stage, which over varying time frames make the transition from neurogenesis to gliogenesis. However, an accelerated strategy for generating human astrocytes via an inducible system was recently reported (Li *et al.*, 2018). This protocol uses inducible expression of nuclear factor 1A (NF1A) and SOX9 in iPSCs via CRISPR/Cas9 gene editing and, is suggested to allow for regional subtypes of astrocytes to be produced. The subtypes of astrocytes that have been achieved with iPSC technology to date represent large-scale regions such as the spinal cord (Roybon *et al.*, 2013), ventralised forebrain and cortex (Li *et al.*, 2018),

but efforts towards deriving more morphologically sophisticated human astrocytes are ongoing (Krencik *et al.*, 2017).

More generally, there are challenges associated with assessing whether an astrocyte has been generated. No single characteristic defines a mature functional astrocyte, and although their differentiation during development is steadily being uncovered, the processes governing their morphological, molecular and functional maturation remain poorly understood (Yang, Higashimori and Morel, 2013). To this end, protocols that attempt to generate astrocytes from iPSCs must go beyond mere marker expression as a method of cell classification. For these reasons, **Chapters 3**, **4** and **5** of this thesis investigate iPSC-derived human astrocytes by examining a combination of basic marker expression, biophysical properties, buffering capacity, ion homeostatic processes and their potential to support synaptically-connected networks of neurons.

1.11 Challenges of generating physiologically relevant cell cultures

From its outset, a major goal of the iPSC field has been to produce mature human brain cell types for studying particular neurological disease states. Yet, in terms of iPSC-derived neurons and astrocytes, studies have found that their gene-expression profile tends to be mainly foetal, and many functional properties resemble those of immature cells (Mariani *et al.*, 2012; Brennand *et al.*, 2015; Lischka *et al.*, 2017). A clear challenge for the field is therefore how to encourage maturational processes in cell types, but in a manner that maintains physiological relevance. In this regard, it is becoming generally recognised that co-culturing iPSC-derived human neurons with rodent astrocytes can advance the maturational state, in terms of both

the intrinsic electrical and synaptic properties of the neurons (Johnson *et al.*, 2007; Tang *et al.*, 2013; Odawara *et al.*, 2014; Lischka *et al.*, 2017), which allow for more sophisticated spiking patterns (Kayama *et al.*, 2018; Tukker *et al.*, 2018). However, similar benefits, particularly with respect to action potential generation and synaptic activity, have not been observed when iPSC-derived neurons were co-cultured with human astrocytes (Lischka *et al.*, 2017). Nevertheless, given the close relationship between neurons and astrocytes during development and in adulthood, co-cultures of the two cell types seems to make good sense, particularly for studying synapse-relevant interactions (Johnson *et al.*, 2007; Chung, Allen and Eroglu, 2015; Krencik, van Asperen and Ullian, 2016; Allen and Eroglu, 2017).

Animal models are still currently the most intact and physiologically representative model systems available to neuroscience. To take full advantage of this emerging technology and to start bridging the species gap, the iPSC field has begun to take steps towards better representing the cell type diversity that is found in intact tissues. The brain contains many more cell types and sub-types than neurons and astrocytes, and opportunities for co-culturing defined cell populations are increasing, as more differentiation protocols are published (e.g. oligodendrocytes (Wang *et al.*, 2013; Ehrlich *et al.*, 2017), microglia (Abud *et al.*, 2017; Haenseler *et al.*, 2017), motoneurons (Sances *et al.*, 2016; Bianchi *et al.*, 2018), and dopaminergic neurons (Kikuchi *et al.*, 2017; Sandor *et al.*, 2017)).

Another approach that has been used to examine iPSC-derived cells in a context of greater cellular diversity and physiologically relevance has been to perform transplantation studies. This provides an opportunity for iPSC-derived cells to integrate into a physiologically relevant environment, featuring anatomically defined structures and cellular networks,

relevant levels of neural activity, and in the case of *in vivo* transplantation, natural nutrient-delivery. Studies implementing this technique have shown that iPSC-derived neurons seem to respond appropriately to regional clues (Hiragi *et al.*, 2017), and transplanted human astrocytes have been reported to contact blood vessels (Krencik *et al.*, 2011). Building upon this rationale, **Chapter 4** will employ a xenotransplantation approach using organotypic rodent brain slices, in order to examine the capacity of human iPSC-derived neurons and astrocytes to detect and respond to the homeostatic challenge imposed by defined periods of synaptically-generated network activity.

1.12 Sporadic Alzheimer's disease and iPSC modelling

The neurodegenerative disorder known as Alzheimer's disease (AD) is the leading cause of dementia, accounting for two thirds of all cases (Alzheimer's Research UK, 2018). Currently, around 46 million people live with dementia worldwide, and with an increasingly ageing population, this number is estimated to rise to 131.5 million by 2050 (Prince *et al.*, 2015). Age remains the greatest risk factor for developing AD, with the incidence increasing exponentially between the ages of 65 and 90 (Jorm and Jolley, 1998). This tendency has been found to continue, such that the rate of incidence doubles approximately every 5 years, even after the age of 90 (Corrada *et al.*, 2010). AD presents itself in two subtypes, a familial early onset type (fAD) that accounts for 1-6% of cases, and a late onset sporadic type (sAD) that accounts for the overwhelming majority. The first published case of AD described the post-mortem brain of a 56-year old woman who had suffered from severe memory loss, and the physician Aloysius Alzheimer found her brain to be characterised by severe atrophy and dense extracellular and intracellular aggregates (Alzheimer, 1911). These aggregates were later molecularly identified

as amyloid plaques and tau neurofibrillary tangles (Glenner and Wong, 1984; Grundke-Iqbal *et al.*, 1986; Kosik, Joachim and Selkoe, 1987), and particularly the accumulation of amyloid beta (Aβ) proteins has been proposed to be the primary driver of AD pathogenesis under the so-called "amyloid cascade hypothesis" (Hardy and Selkoe, 2002).

Studies of fAD have provided strong support for the idea that Aβ accumulation initiates a toxic cascade that results in AD pathology, including tau tangles, synaptic dysfunction, inflammation, and neuronal death, as well as associated cognitive problems. Such studies have provided insights into disease mechanisms, revealing that the penetrant mutations in the amyloid precursor protein (APP) and presenilin-1 and 2 (PSEN1 and 2) affect toxic Aβ species production (Weggen and Beher, 2012). The longer Aβ peptides ($A\beta_{42}$ and $A\beta_{43}$) have been hypothesised to be the pathogenic forms of Aβ, with $A\beta_{40}$ representing the normal, healthy variant (Jarrett, Berger and Lansbury, 1993). The fAD mutations exert their action on Aβ peptides in the following fashion: APP mutations result in Aβ production being skewed towards $A\beta_{42}$, as the cleavage site on APP is altered. Meanwhile, PSEN1 and 2 are components of the γ-secretase complex that cleaves APP, and thus affects the ratio of toxic to non-toxic Aβ species that are produced (Weggen and Beher, 2012). The amyloid cascade hypothesis has however been criticised for being too simplistic in its linearity and neuro-centricity (De Strooper and Karran, 2016).

Intriguingly, fAD and sAD look phenotypically alike, in terms of Aβ and tau protein tangle pathology, brain atrophy and clinical symptoms (Weggen and Beher, 2012). However, the sAD cases do not exhibit penetrant mutations that increase toxic Aβ production, and disease severity in terms of cognitive decline does not correlate well with Aβ pathology; as

Aβ load reaches its peak up to 10-15 years before clinical symptoms are established (De Strooper and Karran, 2016). Loss of synapses correlates much better with cognitive decline (Terry *et al.*, 1991), and it has been suggested that AD pathogenesis rather represents an attack on synapses, causing first synaptic failure, followed by neuronal death (Small, Mok and Bornstein, 2001; Selkoe, 2002). This viewpoint calls for shifting the focus to synapses. In addition to Aβ being toxic to synapses (Mucke *et al.*, 2000), any detriment to homeostatic support from astrocytes would also have harmful effects on synaptic function (Sidoryk-Wegrzynowicz *et al.*, 2011; Khakh and Sofroniew, 2015; Phatnani and Maniatis, 2015; Schitine *et al.*, 2015; Almad and Maragakis, 2018; Dossi, Vasile and Rouach, 2018). Of particular interest to sAD is the genetic risk, which is mediated by the E4 allele of apolipoprotein E (APOE) - a protein mainly secreted by astrocytes (Mahley, 1988). *APOE4* has been repeatedly identified in genome wide association studies (GWAS) (Harold *et al.*, 2009; Lambert *et al.*, 2013) to convey an increased risk of developing sAD and decreased age of onset, amounting to a 47% risk with one allele, and up to 90% if the individual harbours two alleles (E. H. E. Corder *et al.*, 1993; Huang, 2010; Liu *et al.*, 2013).

The mechanisms by which APOE4 exerts its modulation of AD pathogenesis is a topic of ongoing investigation. Evidence connecting APOE4 to Aβ-dependent processes have been reported, including evidence that APOE4 can influence the production, aggregation and clearance of the toxic molecule (Strittmatter *et al.*, 1993; Castellano *et al.*, 2011; Huang *et al.*, 2017). However, Aβ-independent mechanisms have also been implicated, and these focus on the normal functions associated with APOE, which concerns lipid and cholesterol delivery from astrocytes to neurons (Mahley, 1988). Lipid and cholesterol delivery is known to be

important for membrane biosynthesis, for neurite outgrowth, and for synapse formation, repair and plasticity (Mahley, Nathan and Pitas, 1996; Kim *et al.*, 2014; Xue-Shan *et al.*, 2016), so sAD-related suboptimal function of APOE4 is hypothesised to impact the maintenance of neuronal networks and synapses (Ji *et al.*, 2003; Koffie *et al.*, 2012; Chung *et al.*, 2016).

Where the mutations causing fAD are regarded as mediating toxic gains of function with respect to enhancing Aβ production, the *APOE4* genotype is mainly considered as being associated with a loss of protective function. There has been great interest in modelling AD using iPSCs, with most attention given to cell lines from patients with fAD (Yagi *et al.*, 2011; Israel *et al.*, 2012; Kondo *et al.*, 2013; Muratore *et al.*, 2014; Sproul *et al.*, 2014; Moore *et al.*, 2015), which have generally been successful in demonstrating increased $A\beta_{42}$:$A\beta_{40}$ ratios, and in some cases tau aggregates. For iPSC-modelling of sAD, a combination of cell lines from sAD patients both with and without the *APOE4* allele have been used, as well as cell lines from healthy control individuals, genome edited to express *APOE4* (Israel *et al.*, 2012; Kondo *et al.*, 2013; Huang *et al.*, 2017; Zhao *et al.*, 2017; Lin *et al.*, 2018; Wang *et al.*, 2018). The detection of Aβ phenotypes in these sAD cell lines has been variable, which is perhaps unsurprising as sAD represents a complex interplay between genetic risk, environmental factors and age. Furthermore, the studies were performed using enriched neuronal cultures, which does not take into account how astrocyte-secreted APOE influences Aβ levels.

Excitingly, several aspects of the AD phenotype were recently demonstrated by Lin and colleagues (2018), particularly altered Aβ-related processing in neurons, astrocytes and microglia respectively. These researchers compared iPSC-derived cells harbouring *APOE3/E3* and isogenic *APOE4/E4* alleles (Lin *et al.*, 2018). Also notable, Wang et al. (2018) recently

demonstrated a range of AD-related biochemical changes in their *APOE4* iPSC-derived neurons, including tau phosphorylation and GABAergic neuron degradation, which were rescued by gene editing the *APOE4* cell line to *APOE3* (Wang *et al.*, 2018). Overall, iPSC-models of sAD are still in their infancy and structural synapses have been assessed in only a small number of studies (Israel *et al.*, 2012; Zhao *et al.*, 2017; Lin *et al.*, 2018), and synaptic function in only one case (Lin *et al.*, 2018). Synaptic health and functionality represent important aspects of AD pathophysiology that are yet to be systematically investigated and replicated in an iPSC-model. This will therefore be a focus in **Chapter 6**, where I will vary the *APOE* genotype of human astrocytes and assess their ability to influence synaptic signalling amongst human cortical neurons.

1.13 Aims of this thesis

As reviewed above, neuron-astrocyte interactions are incredibly important for normal brain function, with astrocytes fulfilling a variety of dynamic roles, supporting synapses and regulating extracellular homeostasis. The notion of astrocytes as active participants in network signalling has gained traction over the past two decades, and much effort has gone into elucidating a neuron-to-astrocyte-to-neuron reciprocal feedback loop. The vast majority of evidence for both the basic functions of astrocytes and their precise interactions with neurons has been obtained from animal models, but iPSC technology now offers a means to make human astrocytes more easily accessible for experimental study. With this opportunity comes the demand for well-characterised iPSC-derived astrocytes, which may assist in bridging the potential species gap, in terms of translation from rodent to human. A challenge however, is

to assess the multiple functional properties of astrocytes, including their potential to interact with neuronal cell types.

The great advantage of iPSC technology is the ability to derive cells from individuals clinically diagnosed with neurological disorders, which enables unprecedented ways in which sporadic and non-developmental diseases can be studied at the cellular and molecular levels. A sporadic disease that is predicted to increase substantially in the coming decades is late-onset sAD. The disease mechanisms involved are multi-faceted and, in addition to problems caused by Aβ, synaptic dysfunction is viewed increasingly as a target for intervention. Considering that sAD can take decades to manifest in patients, signs from recent studies that aspects of this disease can be modelled with iPSC technology are promising, although the implications of astrocyte-neuron signalling in synaptic health has received little attention. Astrocytes are thought to influence sAD phenotypes through APOE secretion and potential homeostatic dysfunction. Therefore, the establishment of more complex co-cultures that can capture interactions and compensatory mechanisms between cell types when modelling sAD using iPSCs would be highly advantageous.

To that end, the aims of this thesis are:

1) To generate iPSC-derived human neurons and astrocytes from the same cortical progenitor pool, and characterise them according to cell type.

2) To examine ion homeostasis in human iPSC-derived astrocytes and neurons during network activity.

3) To develop an assay for investigating reciprocal signalling between human neurons and astrocytes and its potential influence on synaptic transmission.

4) To assess the influence of astrocytic *APOE* genotypes on astrocyte-mediated synaptic enhancement.

Chapter 2

2 Materials and methods

2.1 Materials

2.1.1 Human cells lines

HEK293T cells used for lentivirus production were kindly gifted from Mariolina Salio, (Weatherall Institute of Molecular Medicine, University of Oxford). All reprogramming of skin fibroblasts and quality control of human iPSC lines was conducted through the IMI EU sponsored StemBANCC consortium, who used the CytoTune iPS 2.0 Sendai virus reprogramming kit (Thermo Scientific, cat# A16517). Human iPSC lines used for this thesis were obtained through their cell repository (http://stembancc.org/). All healthy control cell lines were derived from individuals with no history of dementia, mental health problems, diabetes or migraine. The *APOE* genotype of iPSC lines was only described for a subset of cell lines at the outset of this project, so I tested this (see section 2.3.4); this information is now available on the repository website and corresponds to my results. The *APOE* knockout line was generated using CRISPR/Cas9 genome editing of an *APOE3/E4* parent line and was provided by a StemBANCC industry collaborator (Bioneer).

Diagnose	**Genotype**	**Cell line**	**Clone**	**Sex (M/F)**	**Age**
Healthy control	*APOE2/E3*	SBAd03	01	Female	31
	APOE2/E3	SBAd03	05	Female	31
	APOE3/E3	SBAd02	01	Male	51
Genome edited	*APOE K.O.*	Bioni-010	C3	Male	46
Sporadic AD	*APOE4/E4*	SFC042-03	01	Female	67
Sporadic AD	*APOE4/E4*	SFC140-04	01	Female	70

All cell lines were regularly tested for mycoplasma by PCR in accordance with (Young *et al.*, 2010) and were at all times found to be negative.

2.1.2 Animals

All animal work was carried out in accordance with the Animals (Scientific Procedures) Act, 1986 (United Kingdom) and under project and personal licenses approved by the UK Home Office. Rat cortical astrocytes were generated from P1 Wistar rats, bought from Charles River Laboratories. Mouse organotypic hippocampal brain slice cultures were prepared from P7 male or female C57BL/6 mice obtained from The Jackson Laboratory, bred and maintained in the lab by Alexandru Calin.

2.1.3 Lentiviral vectors

Vector	Virus	Source	Reference
pMD2.G	Encodes VSV-G viral envelope, 2nd generation lentivirus	pMD2.G was a gift from Didier Trono (Addgene plasmid # 12259)	
pCMV delta 8.91	Encodes Gag, Pol, Rev and Tat viral packaging, 2nd generation lentivirus		
pLenti-CAG-hChR2(H134R)-EYFP-WPRE	LV-CAG-ChR2-YFP	A gift from Karl Deisseroth (Addgene plasmid # 20945)	(Zhang *et al.*, 2007)
pLenti-CAG-EYFP	LV-CAG-YFP	Developed by Yuan Ting in the Akerman lab	
pLenti-CaMKIIa-mKate2-WPRE	LV-CamKIIa-mKate2	A kind gift from Ricardo Dolmetsch.	(Shcheglovitov *et al.*, 2013)
FUdeltaGW-rtTA	LV-Ubiq-rtTA	A gift from Konrad Hochedlinger (Addgene plasmid # 19780)	(Maherali *et al.*, 2008)
pTet-O-Ngn2-puro	LV-TetO-mNgn2-T2A-Puro	A gift from Marius Wernig (Addgene plasmid # 52047)	(Zhang *et al.*, 2013)

2.1.4 Cell culture media

Media components were purchased from ThermoFisher Scientific (includes: Gibco, Invitrogen and Life Technologies), unless otherwise stated.

mTeSR1: Used for maintaining human iPSC cultures, mTeSR1 media with supplement (STEMCELL Technologies).

NMM: Neuronal Maintenance Media. Used for neural induction, containing: 50% vol/vol Neurobasal, 50% vol/vol DMEM/F12 Glutamax medium with 1x N2, 1x B27 + Vitamin A, 2.5 µg/mL insulin (Sigma), 1 mM L-glutamine, 0.5x non-essential amino acids (NEAAs), 0.5 mM Sodium Pyruvate (Sigma), 55 µM β-mercaptoethanol, 50 U/mL penicillin and 50 mg/mL streptomycin.

NMM-A: Used for maturing neurons, Neurobasal was substituted for Neurobasal-A in the NMM recipe in an attempt to improve glucose levels and external osmolarity.

Ngn2-media: Used for induced neurogenin-2 neurons: Neurobasal A medium containing 1x B27 + Vitamin A, 1 mM L-glutamine, 50 U/mL penicillin and 50 mg/mL streptomycin, 10 ng/mL BDNF (Peprotech), 10 ng/mL NT-3 (Peprotech), 1 µg/mL doxycycline (Sigma), 200 nM ascorbic acid (Sigma), 200 ng/mL laminin.

Glial media A: Used for freshly isolated rat glia: MEM containing 0.6% wt/vol D-Glucose (Sigma), 50 U/mL penicillin and 50 mg/mL streptomycin, 10% vol/vol horse serum.

Glial media B: Used for glia after thawing, prior to co-culture: DMEM with 15% vol/vol filtered foetal bovine serum (FBS).

Glial media C: 78.8% vol/vol Minimum Essential Media + GlutaMAX-I, 20% vol/vol heat-inactivated horse serum, 1% vol/vol B27, 30 mM HEPES (Sigma), 26 mM D-glucose (Sigma), 5.8 mM $NaHCO_3$ (Sigma), 1 mM $CaCl_2$ (Sigma), 2 mM $MgSO_4 \cdot 7H_2O$ (Sigma).

AstroDiff/AstroMature: Used for differentiation of human astrocytes from iPSCs: Basal media with Supplements A, B and C (STEMCELL Technologies).

AMM: Astrocyte Maintenance Media. Used for maturing astrocytes, consisting of: 45% vol/vol Neurobasal, 45% vol/vol DMEM/F12 Glutamax containing 1 mM L-glutamine, 50 U/mL penicillin and 50 mg/mL streptomycin and 10% filtered FBS.

2.1.5 Recording solutions

All components were purchased from Sigma.

Solution	Composition (mM)
ACSF 1	126 NaCl, 2.5 KCl, 1.2 NaH_2PO_4, 26 $NaHCO_3$, 3 $CaCl_2$, 1 $MgCl_2$ and 10 glucose
ACSF 2	120 NaCl, 3 KCl, 0.5-1.5 $MgCl_2$, 2 $CaCl_2$, 1.2 NaH_2PO_4, 23 $NaHCO_3$, 11 glucose, 0.2 ascorbic acid
ACSF 3	123 K^+-gluconate, 23 HEPES, 11 D-glucose, 1.2 NaH_2PO_4, 2 $MgSO_4$ and 2 Ca^{2+}-gluconate
HEPES ACSF	140 NaCl, 5 KCl, 2 $CaCl_2$, 10 HEPES and 10 glucose
Internal (1)	140 K^+ or Cs^+-gluconate, 6 NaCl, 1 EGTA, 10 HEPES, 4 MgATP and 0.4 Na_3GTP
Internal (2)	145 K^+-gluconate, 6 NaCl, 10 HEPES, 4 MgATP and 0.4 Na_3GTP
Internal (3)	134 K^+-gluconate, 2 NaCl, 10 HEPES, 2 MgATP, 2 Na_2ATP and 0.3 NaGTP

All ACSF solutions were adjusted to pH 7.35 with NaOH, and to an osmolarity of 290 mOsm. For ACSF 1, 2 and 3 oxygen and pH levels were stabilized by continuously bubbling the ACSF with 95% O2 and 5% CO2. ACSF 1 was used for initial electrophysiology experiments

shown in **Chapter 3**. In **Chapter 4** the high K^+ ACSF 3 was used for generating calibration curves for the ratiometric ClopHensorN construct and all subsequent experiments involving ClopHensorN were recorded in ACSF 2. The recording solution was switched to the HEPES based ACSF for experiments in **Chapter 5** and **6**.

All internal solutions were adjusted to pH 7.35 with either KOH or CsOH, and to an osmolarity of 290 mOsm. The Cs^+ version of internal (1) contained the use-dependent $VGNa^+$ channels blocker QX314 to enable spike-free depolarisation of the patched cell to a holding potential of 0 mV for recordings of inhibitory currents. Internal (2) is without the Ca^{2+} chelator EGTA and was used for Ca^{2+} imaging experiments of patched astrocytes. Internal (3) was used for patching mouse neurons in organotypic slices.

2.1.6 Drugs

All drugs were purchased from Tocris, unless stated otherwise.

Drug	**Function**	**Final Concentration (µM)**
TTX	Voltage gated Na-channel blocker	1
QX314 (Alomone Labs)	Use-dependent voltage gated Na^+-channel blocker	5000
Picrotoxin	$GABA_A$ receptor blocker	100
S0859 (Sigma)	Sodium bicarbonate inhibitor	50
MCPG	mGluR blocker	800
Y-27632	ROCK inhibitor	10
SB431542	inhibitor of the TGF-β/Activin/NODAL pathway	10
Dorsomorphin	inhibitor of the BMP pathway	1
AraC	Cell cycle inhibitor	4

2.1.7 Primary antibodies

Antibody	Raised in	Concentration	Supplier	Catalogue #
CTIP2	Rat	1:250	Abcam	ab18465
GFAP	Mouse IgG1	1:1000	Millipore	MAB360
Homer1	Rabbit	1:500	Synaptic Systems	160003
Ki67	Mouse IgG1	1:600	BD bioscience	550609
MAP2A	Mouse IgG1	1:1000	Millipore	MAB378
Nkx2.1	Mouse IgG1	1:500	Millipore	MAB5460
Otx1/2	Rabbit	1:500	Abcam	ab9566
Pax6	Rabbit	1:500	Covance	PRB-278P
pHH3	Rabbit	1:500	Millipore	06-570
SatB2	Mouse IgG1	1:200	Abcam	ab51502
Synaptophysin	Guinea Pig	1:1000	Synaptic Systems	101004
S100β	Rabbit	1:800	Abcam	ab868
Tbr1	Rabbit	1:500	Abcam	ab31950
Tbr2	Rabbit	1:500	Abcam	ab23345
Tuj1	Mouse IgG2a	1:2000	Biolegend	B199846

2.1.8 Secondary antibodies

Antibody	Conjugate	Raised in	Concentration	Supplier	Catalogue #
Anti-mouse	Alexa Fluor 350	Goat	1:1000	Life Tech.	A21049
Anti-mouse	Alexa Fluor 488	Goat	1:1000	Life Tech.	A11029
Anti-mouse IgG1	Alexa Fluor 488	Goat	1:500	Life Tech.	A21121
Anti-mouse	Alexa Fluor 568	Goat	1:1000	Life Tech.	A11031
Anti-mouse IgG2a	Alexa Fluor 568	Goat	1:500	Life Tech.	A21134
Anti-mouse	Alexa Fluor 633	Goat	1:500	Life Tech.	A21052
Anti-mouse IgG1	Alexa Fluor 680	Goat	1:500	Life Tech.	A31562
Anti-rabbit	Alexa Fluor 488	Goat	1:1000	Life Tech.	A11034
Anti-rabbit	Alexa Fluor 568	Goat	1:1000	Life Tech.	A11036
Anti-rabbit DyLight	Alexa Fluor 680	Goat	1:1000	Thermo Scientific	35569
Anti-guinea pig	Alexa Fluor 488	Goat	1:400	Life Tech.	A11073
Anti-rat	Alexa Fluor 488	Goat	1:1000	Life Tech.	A11006

2.1.9 Chemicals and calcium dyes

Name	Function	Supplier (catalogue#)	Final concentration (µM) or dilution
DAPI	Nuclear stain	Gibco (D1306)	1:5000
Propidium iodide	Cell death stain	Life Technologies (P3566)	1:20
Strepavidin	Recognises biocytin, conjugated to Alexa-Fluor 568	Invitrogen (S11226)	1:1000
Rhod-2 AM	Red shifted Ca^{2+} dye, membrane permeable	Life Technologies (R1245MP)	5 µM
OGB-1 AM	Oregon Green BAPTA Ca^{2+} dye, membrane permeable	Life Technologies (06807)	10 µM
OGB-2 K^+ salt	Oregon Green BAPTA Ca^{2+} dye, membrane impermeable	Life Technologies (06808)	200 µM

2.1.10 *APOE* genotyping primers

Forward: 5′-TCCAAGGAGCTGCAGGCGGCGCA

Reverse: 5′-GCCCCGGCCTGGTACACTGCCA

Designed by (Zivelin *et al.*, 1997), yields a 218-bp DNA fragment which includes both *APOE* polymorphic sites.

2.1.11 Assay kits

Glutamate uptake: colorimetric enzyme assay (Sigma, cat# MAK004)

APOE ELISA: Standard sandwich enzyme-linked immunosorbent assay for detection of secreted human APOE (Thermo Scientific, cat# EHAPOE)

Aβ detection: V-PLEX Plus Aβ Peptide Panel 1 (6E10) meso-scale-discovery kit (MSD, cat# K15200G-1)

BCA: bicinchoninic acid colorimetric protein detection assay (Thermo Scientific, cat# 23227)

MinElute: PCR purification kit (Qiagen, cat# 28004)

2.2 Cell culture methods

All cells, cultures and organotypic slices were grown in humidified 5% CO2 tissue culture incubators, at 37°C.

2.2.1 Human iPSC cell culture

Feeder-free human iPSCs were grown on 9.5 cm^2 wells of 6-well plates (Corning) coated with Geltrex (Gibco) and maintained in mTeSR1 medium (STEMCELL Technologies). Geltrex was diluted with cold K.O. DMEM (Gibco) at 1:100 and plates incubated for ~1 hour at 37°C before immediate use, or stored overnight at 4°C. 100% media changes were conducted every day and when cells reached ~90% confluency, they were passaged at a ratio of 1:3 as follows: Cells were washed with PBS (Gibco), followed by a quick wash with Versene-EDTA (Gibco) and then incubated with Versene-EDTA at 37°C for 6-8min until cells had loosened. Versene-EDTA was carefully removed and cells washed off using pre-warmed mTeSR before distribution onto coated plates. The mTeSR1 medium was supplemented with 10 µM Y-27632 (Tocris) overnight, following each passage.

2.2.2 Induction of human cortical neurons from iPSCs

In preparation for neural induction, following a modified Shi et al. (2012) protocol (Shi, Kirwan and Livesey, 2012), the iPSCs were passaged (see section 2.2.1) at a ratio of 2:1 to ensure 100% confluency. The next day (Induction day 0), the culture medium was changed to neural induction medium (NIM) consisting of NMM supplemented with dual SMAD inhibiting factors: 10 µM SB431542 (Tocris) and 1 µM dorsomorphin (Tocris). NIM was changed daily for 12 days as the cells were forming a dense neuroepithelial sheet. To lift the sheet on day 13, it was scored into a grid using a sterile needle and incubated at 37°C with

200 µL freshly filtered 10 mg/mL Dispase (Gibco) added to the media. Lifting was encouraged by frequently tapping the plates over 10-15 min of incubation and cells were collected using a stripette to gently transfer them without breaking up the sheet too much into 10 mL of NMM. To wash out the Dispase, cells were allowed to pellet by gravity, media removed and this wash-step repeated. Cell clumps were plated in NIM supplemented with 10 µM Y-27632 (Tocris) onto plates pre-coated for >4 hours with 15 µg/mL laminin (Life Technologies) and left to adhere overnight. The medium was changed 24 hours later to NMM supplemented with 20 ng/mL FGF2 (Peprotech) and changed every day for 4 days to promote/encourage rosette formation.

Rosettes were then maintained in NMM over the next 10-15 days, during which they were expanded onto laminin-coated wells and cleaned up 2-5 times by selective lifting with Dispase as described above, but without the needle-scoring. Onset of neurogenesis occurred around day 20-25, at which point cultures were dissociated to single cells using Accutase (Sigma) and plated onto laminin-coated wells at a ratio of 1:2 in the following manner: cells were washed with PBS and subsequently incubated with 500 µL Accutase solution at 37°C for 5-10 min. To loosen all cells and split up clumps, gentle trituration and collection of cells into 9 mL NMM was performed using a P1000. This cell-suspension was centrifuged at 300 g for 5 min (Heraeus Megafuge 8 centrifuge (Thermo Scientific)), the supernatant removed and the pellet re-suspended in NMM with 10 µM Y-27632 for plating. The next day, cells were given fresh NMM. The resulting neural progenitor cells (NPCs) were generally expanded a second time using Accutase, before being frozen down between days 28-32 post initiation of neural induction. Freezing involved lifting with Accutase, and re-suspending the centrifuged

cell-pellet in ice-cold freezing media consisting of: 90% vol/vol NMM, 10% vol/vol dimethylsulfoxide (DMSO) (Sigma) and 20ng/mL FGF2 (Peprotech), quickly aliquoting in cryovials at 1.5x10^6 cells/vial and storing them overnight in a CoolCell freezing container (Corning) at -80°C to facilitate slow freezing, and moving them to liquid nitrogen (LiN_2) storage the following day.

2.2.3 Induced Ngn2 expression applied to human cortical NPCs

The inducible Ngn2 method (Zhang *et al.*, 2013; Ho *et al.*, 2015) relies on the co-transduction of 2 lentiviral constructs: 1) LV-Ubiquitin-rtTA, which expresses the transcriptional activator rtTA under the constitutive promoter Ubiquitin and enables transcription in all cells that take up this construct, and 2) LV-TetO-mNgn2-P2A-$puro^R$, consisting of the tetracycline-controlled Tet-On operator, which controls the transcription of mouse Ngn2 fused to puromycin resistance, such that transcription of Ngn2 ensures equimolar amounts of puromycin-resistance. A cell needs to be successfully transduced with both constructs in order for Ngn2 expression to be 'turned on', as the TetOn operator depends on the binding of rtTA to initiate transcription. However, nothing is turned on before the addition of doxycycline, which is required for rtTA to bind to TetO, thus making the system inducible. The Ngn2 constructs were employed as described in Ho et al. (2015), such that Ngn2 expression could be induced in cortical NPCs, generated as described in section 2.2.2, prior to co-culture.

Cryostored NPCs were fast-thawed in a 37°C water bath and re-suspended in NMM-A, centrifuged at 300 g for 5 min. The cell-pellet was re-suspended in NMM-A supplemented with 10 µM Y-27632 (Tocris) and FGF2 (Peprotech) then plated onto 10 µg/mL laminin (Life Technologies) coated wells. The day after plating, LV-Ubiq-rtTa and LV-TetO-mNgn2-T2A-

Puro lentiviral supernatants (generated as described in section 2.3.3), were added to the NPC cultures, each at a dilution of 1:3-1:5. Virus-containing media was changed ~12 hours later. The next day, Ngn2 was induced (day 0) by switching to doxycycline (Sigma) containing Ngn2-media. On day 2, 2µg/mL puromycin (Sigma) was added, along with transduction with LV-CamKIIa-mKate2 lentivirus supernatant at 1/5 dilution. CamKIIa-mKate2 virus was removed on day 3 while keeping puromycin present at 2 µg/mL. Puromycin was withdrawn on day 4 and cells were left to recover for 1-3 days before lifting with Accutase (Sigma) and finally plating onto human astrocytes at 100,000-150,000 cells/coverslip in Ngn2-media with 10 µM Y-27632 overnight. Co-cultures were maintained in Ngn2-media supplemented with 1 % vol/vol horse serum (Gibco) and 50 % media changes were carried out every 2-3 days. On day 10 cultures were treated with 4 µM Ara-C (Sigma).

2.2.4 Induction of human astrocytes from iPSCs

The protocol accompanying the astrocyte differentiation and maturation kits from STEMCELL technologies was adapted to start from a neural rosette stage. Neural rosettes were generated (see section 2.2.2) and grown on laminin and the AstroDiff media was applied around day 20-25 of neural induction. Astrocyte progenitors were kept in AstroDiff for 20 days (until day 40-45) and underwent 3 expansions, every time when cells reached ~90% confluency. Cells were lifted with Accutase (Sigma), washed in AMM, centrifuged at 300 g for 5 min and re-suspended in AstroDiff for re-plating at $1x10^5$ cells/cm^2. At the 3rd passage, the majority of cells were frozen down as progenitor stock in 90% vol/vol AstroDiff media with 10% vol/vol DMSO (Sigma). Media was then changed to AstroMature for a further 15 days (until day 55-60), during which astrocyte precursors also underwent 3 passages with Accutase.

Similarly, at the 6th passage, cells could be frozen down as astrocyte precursor stock in 90% vol/vol AstroMature media with 10% vol/vol DMSO. To maintain astrocytes beyond the manufacturer's protocol (see Appendix A), I devised the astrocyte maintenance media (AMM), which was optimised in terms of long-term cell survival, adhesion to coverslips and maintenance of S100β and GFAP expression. Final maturation was thus conducted in AMM media for 20-30 days (until day 75-90) and if cells were still proliferating, further passages were conducted, but using Trypsin/EDTA (Gibco) and washing in serum-containing AMM. Media was changed every 2-3 days throughout the differentiation protocol. Cryo-stored stocks of astrocyte progenitors and precursors could be thawed and the protocol resumed from the point they were frozen down.

2.2.5 Cortical rat astrocyte cultures

Cortical rat astrocytes were either obtained from Gibco and grown in glial medium or produced in house, following standard procedures: P1 Wistar rat pups were killed by decapitation (schedule 1 procedure), their brains extracted into ice-cold CMF-HBSS containing: 10x Hanks Balanced Salt Solution (HBSS) (without: $CaCl_2$, $MgCl_2$, $NaHCO_3$) (Gibco), made to 1x by dilution with filter-sterilised dH_2O and addition of 10 mM HEPES (Sigma). All meningeal tissue carefully removed to prevent subsequent microglial growth in the culture. Clean cortical heimispheres were transferred to another HBSS-containing Petri dish and physically dissociated with scissors before undergoing trypsin-treatment in CMF-HBSS with 10% trypsin (2.5% stock, Gibco) and 10 % DNAse (1% stock, Sigma), while incubating in a water bath at 37°C with occasional swirling and trituration to dissolve tissue clumps. Cell-suspension was poured through a 70 µm mesh cell-strainer (VWR) into ice-cold

glial media before centrifugation to pellet cells. Cells were then re-suspended in warmed glial media and plated in T75 flasks (corning) at $7.5x10^6$ cells/flask.

These cultures were left to proliferate until confluent with bi-weekly media changes and occasional firm tapping to loosen any potential microglial cells. Confluent cells were lifted with Accutase (Sigma), washed and centrifuged before being frozen down as stocks in 70% vol/vol glial media, 20% vol/vol horse serum (Gibco) and 10% vol/vol DMSO (Sigma) and stored in LiN_2.

2.2.6 Coverslip preparation

Glass coverslips (13mm, thickness 0, VWR) were pre-treated to improve their hydrophilicity and enhance adherence of cells during long-term culture. Coverslips were soaked for a minimum of 48 hours in 70% nitric acid, washed 5x in dH_2O before sterilisation in 100 % ethanol for 30 min and dried overnight in an oven to ensure complete evaporation of ethanol.

Poly-L-ornithine and laminin (P+L): coating used for enriched neuronal cultures. Coverslips were incubated with 200 µL/coverslip of 0.01% wt/vol poly-L-ornithine (Sigma) for at least 4 hours at 37°C, followed by replacement with 200 µL/coverslip of 15 µg/mL laminin (Life Technologies), diluted from stock in DPBS (with $CaCl_2$ and $MgCl_2$) and incubated for minimum 4 hours at 37°C with. The coating solution was aspirated off immediately before seeding of neurons.

Poly-D-lysine (PDL): coating used both for enriched rat astrocyte cultures and co-cultures. Coverslips were incubated for 1 hour at 37°C with 200 µL/coverslip of 0.1 mg/mL poly-D-lysine (Sigma), diluted from stock with sterile dH_2O. Then coverslips were

rinsed with sterile dH_2O, which was fully aspirated off and coverslips left to dry for 30 min before addition of rat astrocytes.

Matrigel: coating used for enriched human astrocyte cultures and co-cultures. Matrigel (Scientific Lab Supplies) was diluted in K.O. DMEM (Gibco) to a concentration of 0.1 mg/mL immediately prior to addition to coverslips and incubation at 37°C for 1 hour prior to seeding of human astrocytes.

2.2.7 Co-cultures

Co-cultures of astrocytes and cortical neurons were always established with astrocytes seeded onto the plates or glass coverslips and neurons subsequently seeded on top, allowing access to neurons for patching. Frozen cells were fast-thawed in a water bath at 37°C, washed in K.O. DMEM and centrifuged at 300 g for 5 min before plating. Coverslips were coated as described in section 2.2.6, and cells were seeded in their respective growth media at ~200,000-250,000 cells/coverslip for astrocytes and ~100,000-150,000 cells/coverslip for neurons.

For optogenetic experiments, astrocytes were transduced with LV-CAG-ChR2-YFP or LV-CAG-YFP lentiviral constructs 1 day after plating onto coverslips and left to grow confluent and express the constructs for ~ 1 week before the addition of neurons. To facilitate selective patching in co-cultures of neurons derived via the neurogenic protocol, NPCs were brought up onto a plastic tissue culture plate before seeding onto astrocytes and transduced with a LV-CamKIIa-mKate2 construct 1 day later. Once expression was detected, neurons were lifted with Accutase (Sigma), washed, centrifuged at 300 g for 5 min and seeded onto astrocytes. Co-cultures were maintained in either NMM-A (Shi et al. (2012) derived NPCs)

or Ngn2-media (induced Ngn2 NPCs), with media changes every 2-3 days, supplemented with laminin at 10 µg/mL once a week.

2.2.8 Long-duration optogenetic stimulation

ChR2-expressing astrocytes in co-cultures with human neurons were stimulated over several days while growing inside the tissue culture incubator. For this purpose, a custom-built setup was constructed which featured Rebel Star LEDs in Royal Blue (447.5nm wavelength, Luxeon) fitted on a heat-sink. Each LED was covered with a Carclo 8° 20mm optic beam concentrator (Luxeon), and encased in a light-impenetrable tube (Thorlabs), containing a biconvex lens with a 40 mm focal length (Comar). LEDs were suspended above the culture plates to maximise the effect of the heat-sink and minimize the heat-transfer to the illuminated cells, see illustration of the setup on **Figure 5.5A**). Earlier experimentation with cell-culture plates placed directly on top of LEDs resulted in cell death which made cultures unviable for electrophysiological experiments.

Test of LED intensity linearity was conducted using a power meter (Thorlabs, PM100D) placed at the level where the cells would sit and by gradually increasing the LED power. The linear relationship was experimentally determined until driving the LED with 500 mA, where R^2=0.999. Above 500 mA the LED intensity (mW/mm^2) was described by the linear equation: y = 0.0049x + 0.0194 obtained from the experimental data. These intensity measures were repeated at the electrophysiology rig in order to match the stimulation with what was delivered in the incubator. A stimulation intensity of 1mW/mm^2 was selected, as it is sufficient for near maximal activation of the ChR2-H134R variant used (Mattis *et al.*, 2012). Furthermore, H134R's slightly slower kinetics compared to wild type ChR2 was not considered

an issue, as using it in astrocytes alleviates the need for rapid membrane repolarisation for the precise induction of successive APs.

The LED pulse stimulation paradigm was controlled by a Grass S48 stimulator (Grass Technologies), which in turn was connected to a custom-built LED output box from which the LED intensity was controlled. Cells were positioned beneath the optogenetic LED setup inside the tissue culture incubator for a minimum of 2 days and a maximum of 7 days, and were exposed to a paradigm of 250 ms pulses of 450 nm light with either 50 or 100 s intervals. At the end of the stimulation protocol cells were either used for electrophysiology or fixed for immunolabelling. For experiments with ChR2 lentivirus in both control and stimulated condition, equivalent expression levels were assessed manually before experimentation but also via fluorescent images taken on the rig during whole-cell patch clamping. Mean grey levels of these images taken for each condition within each experiment were calculated using Fiji (Image J), and if they differed more than 33% the experiment was excluded.

2.2.9 Mouse organotypic hippocampal slice culture

Organotypic hippocampal slices were generated and maintained by Alexandru Calin, who sacrificed mice at P7, excised the hippocampi and grew the slices on a semi-porous membrane in glial media C (section 2.1.4), in accordance with (Călin *et al.*, 2018). 100% media changes were performed every 2-3 days and cultures were maintained at 37°C.

Human neurons and astrocytes were cultured separately and transduced with LV-CMV-ClopHensorN on the same day as hippocampal slices were made. 7 days later, human cells were lifted and dissociated to single-cell suspensions. Neurons and astrocytes were

separately transplanted into the mouse organotypic slices either by placing a 15 µL droplet of cell-suspension on top of the slice, or by injecting a concentrated volume of ~0.5 µL cell-suspension along the Cornu Ammonis 1 (CA1) region of the slice, using a bevelled borosilicate glass pipette, driven by a Picospritzer® II (General Valve Corporation). These transplants were carried out in collaboration with Alexandru Calin. For optimisation purposes, neurons were transplanted at concentrations of 10,000, 25,000 and 50,000 cells/slice and astrocytes at 25,000, 50,000 and 100,000 cells/slice. Integration was found to be best with the injection method, and integrated cell numbers were often most optimal for imaging at 25,000 cells/slice. ClopHensorN$^+$ cells were left to integrate within the mouse slices for a minimum of 10 days and recordings were performed up until 22 days post transplantation for astrocytes and 53 days for neurons.

In the majority of the transplants, organotypic slices displayed spontaneous seizure-like events, during which ClopHensorN responses were measured. On 2 occasions, network activity was induced by replacing the usual ACSF (listed in section 2.1.5) with a 0 Mg^{2+} ACSF (as described in (Raimondo *et al.*, 2013)).

2.3 Molecular biology methods

2.3.1 Immunolabelling

Human cells on coverslips and organotypic slices were prefixed in 2% wt/vol paraformaldehyde/sucrose (PFA) in PBS for 10 min, followed by fixation in 4% PFA for 10 min, then washed 3x in PBS and stored at 4°C in PBS with 0.02% wt/vol sodium azide.

General protocol: Cells were permeabilised in PBS with 0.3% vol/vol Triton-X (TX) for 3x5 min and blocked in PBS with 1.5% vol/vol TX and 10% normal goat serum

(NGS, Sigma) for at least 1 hour at room temperature. Cells were subsequently incubated for either 1 hour at room temperature or overnight at 4°C with primary antibodies made up in PBS with 0.15% TX and 2% NGS. Primary antibodies were washed off with PBS with 0.3% vol/vol TX for 3x5 min before secondary antibodies were added, made up in PBS with 0.15% TX and 2% NGS and centrifuged at 13,200 RPM at 4°C to remove aggregates. Cells were incubated with secondary antibodies at room temperature for 1-2 hours before washing with PBS 3x5min and addition of nuclear stain DAPI, diluted to 1:5000 in PBS with 0.3% vol/vol TX. Lastly, salt solutions were rinsed off in dH_2O and coverslips mounted onto glass slides (VWR) with ProLong Gold or Diamond antifade mountant (Life Technologies).

For synaptic markers: an extended protocol was used. The procedure was the same as above, but with the Triton-X concentration increased to 0.4% for permeabilisation, and cells were incubated with primary antibodies at 4°C for 2 days and with secondary antibodies overnight.

2.3.2 Immunolabelling quantifications

All image quantification was performed using plug-ins for Image J (Fiji), apart from the quantification of synaptic puncta, for which a Python script was developed in-house by Dr. Paul Brodersen. All images were taken on **an epifluorescent microscope (BX40, Olympus) with cubes optimised for the excitation and emission spectra of each fluorophore.**

Tbr2/pHH3 distance: Images of rosettes taken both at 10x and 20x magnification were analysed using the "cell counter" plug-in. The length of the radius of each rosette

was determined by obtaining the xy-coordinates of the lumen and a point on the apical perimeter, and subsequently using the Pythagorean theorem:

$r = \sqrt{(x_2 - x_1)^2 + (y_2 - y_1)^2}$. The apical perimeter was determined by drawing a circle which encompassed the full rosette structure, centred on the lumen. The distance of $Tbr2^+$ or $pHH3^+$ cells from the lumen of a rosette was likewise found by calculating the radial distance of a positively labelled cell from the lumen via their respective xy-coordinates, and expressing the distance as a percentage of the total radius: $$Distance\ of\ labelled\ cell\ (\%) = \frac{radius\ length_{(Cell)}}{radius\ length_{(Rosette)}} \cdot 100$$

Cortical layer markers: Images of dissociated cell-cultures taken both at 10x and 20x magnification were analysed using the "analyse particles" function. First, an image was converted to a binary mask by thresholding, and individual cells in close proximity distinguished from each other by applying the "watershed" function. The total number of cells in a given composite image was determined from the DAPI-image alone, and likewise for the cortical markers, such that a percentage of cells labelling positive for a given marker could be calculated:

$$Positive\ cells\ (\%) = \frac{\#\ marker^+}{\#\ DAPI^+} \cdot 100$$

Astrocytic markers: the relative percentages of GFAP, S100β and Tuj1 were determined from images at 20x magnification. Quantification was performed using the "cell counter" plugin to manually place a counter on each DAPI nuclei (from this image only), and subsequently on DAPI nuclei NOT surrounded by positive labelling (from a combined image of that given marker and DAPI). The numbers of GFAP and

S100β positive cells were calculated from the total number of DAPI nuclei, subtracting non-staining associated nuclei and Tuj1$^+$ cells.

Induction inclusion criteria: Inductions were screened for excessive/disproportionate ventralisation via Nkx2.1 interneuron progenitor expression. The criteria for inclusion was set at maximum 20% Nkx2.1 expression calculated at the rosette stage, as this matches the predicted proportion of interneurons in the mature cortex (Hendry *et al.*, 1987; Markram *et al.*, 2004). As no inductions expressed more than 20% Nkx2.1$^+$ cells, none were excluded from subsequent experimentation.

Synaptic markers: All images processed for quantification of synaptic markers were taken at 100x magnification using an oil-submersible objective**. Gain and exposure settings were initially optimised for each fluorophore and kept consistent throughout. Furthermore, imaging regions were selected on the basis of keeping the density of neuronal processes consistent between images and five fields of view were obtained per coverslip.** The Python script was kindly developed in collaboration with Paul Brodersen and identifies neurites and calculates their length from images of MAP2 staining, as well as classifying pre-and post-synaptic markers which satisfy criteria of brightness threshold (97.5%) and size range (16-144 pixels, which corresponds to 0.1-1 µm). In short, the script generates a 'neurite mask' from the MAP2 image by first enhancing the contrast via local histogram equalisation, then pieces of neurites found via phase-symmetry are connected and any unconnected line-segments cleaned away. Lastly, the image is thresholded and converted into the binary neurite mask. The synaptic marker images

went through a process of thresholding, size-selection and were lastly matched up with the neurite mask. Only synaptic puncta overlapping with the identified neurites are quantified, and if their location overlapped, they were counted as dual labelled.

2.3.3 Lentivirus production

HEK293T cells for transfection were plated in a T75 flask (Corning) at a density of 6.5x10^6 cells/flask in growth medium consisting of: 90% vol/vol DMEM (Gibco) and 10% vol/vol FBS (Gibco). Cells were grown to 60% confluency and media supplemented with 1x NEAAs (Gibco) prior to transfection. Cells were transfected according to the protocol by (Tashiro *et al.*, 2015) with 100 µL Lipofectamine 2000 (Invitrogen), 9.375µg vector DNA, 3.125µg VSVg envelope DNA and 8.75µg Δ8.91 packaging DNA made up in Opti-MEM (Gibco) in the following way: Lipofectamine was added to 1 mL Opti-MEM and incubated at room temperature for 5 min. Separately, DNA was added to 1 mL Opti-MEM and then transferred to the Lipofectamine solution, inverting to mix solutions. The mixture was incubated for a further 25-30 minutes before addition to HEK cells. Transfection medium was replaced with fresh growth medium 5 hours later.

Media containing the viral particles was harvested after 48 hours, centrifuged at 1000 g for 3 minutes to remove cell debris, and then passed through a 0.45 µm filter before aliquoting. If cells had not detached significantly, a second harvest could be obtained by adding media and collecting it 48 hours later. Supernatant was either stored at -80 ^{0}C or further processed by ultracentrifugation to concentrate the viral particles. For ultracentrifugation, 8 mL supernatant was transferred into conical bottomed, heat sealed tubes (Beckman Coulter) and ultracentrifuged at 30,000 rpm in a SW41TI swinging bucket

rotor at 4°C for 3 hours (Beckman L8-70M Ultracentrifuge). The supernatant was subsequently extracted and each viral pellet was re-suspended in 20 µL Opti-MEM with 1:100 DNase I (1 U/µL stock concentration, Sigma), left overnight at 4 ^{0}C, and lastly aliquoted and stored at -80 ^{0}C.

2.3.4 Crude DNA extraction

Extraction of DNA from human cell cultures for the purpose of *APOE* genotyping (see section 2.3.5) was conducted as follows: cells were washed once in ice-cold PBS before 300 µL ice-cold PBS was used to dislodge the cells by spraying it onto the well. Cells were centrifuged at 10,000 RPM at 4°C for 5 min, after which the supernatant was carefully removed without disturbing the pellet. Cell lysis was performed by adding 400 µL DNA extraction buffer (1.0 M Tris-HCl (pH 7.5), 0.5M EDTA (pH 8.0), 10% vol/vol SDS, 10 mg/mL RNAse, 200 µg/mL proteinase K, made up in ddH_2O) to each pellet and incubating them at 65°C for 30 min, followed by a gradual heating to 96°C and a 2 min incubation at this temperature. Approximate DNA concentrations were measured using a NanoDrop spectrophotometer (Thermo Scientific). If not used directly, samples were frozen and stored at -20°C.

2.3.5 *APOE* genotyping

Genotyping of cell lines with unknown A*POE* genotype was conducted by PCR amplification of a 218 bp DNA fragment spanning the 2 *APOE* polymorphic sites and subsequent restriction digestion, as described in (Zivelin *et al.*, 1997), but certain technical aspects were optimised. DNA samples extracted according to section 2.3.4 were PCR amplified using a Platinum Taq (Invitrogen) mixture containing: 10% 10x PCR buffer (without Mg^{2+}), 10mM dNTP mix, 1.5mM $MgCl_2$, 25 µM Forward primer, 25 µM Reverse primer, 0.4% Platinum Taq polymerase,

10% DMSO, 66% dH_2O, 10% DNA, for each sample. Thermocycling conditions were optimized from (Zivelin *et al.*, 1997) to 40 cycles consisting of: 30 s of denaturing at 94°C, 30 s of annealing at 55°C and 60 s of extension at 72°C, then held at 4°C. Before performing the restriction digestion, confirmation of PCR product was obtained by running 5 µL of PCR sample by gel electrophoresis on a 3% wt/vol agarose gel in 1xTAE buffer (40 mM Tris acetate, 1 mM EDTA) containing 0.1 µg/mL ethidium bromide at 80 V. A 1 kb DNA ladder (Invitrogen) was run alongside DNA fragments and visualised using a UV trans-illuminator.

PCR samples were then purified using a MinElute PCR purification kit (Qiagen), following the manufacturers protocol (see Appendix B), ending with DNA elution in ~30 µL EB buffer per sample. Restriction digestion took place in a 30 µL reaction volume using 10 units HaeII enzyme, 5 units AflIII and CutSmart buffer (all from New England Biolabs) according to manufacturer's instructions (see Appendix C) and the mixture was incubated overnight at 37°C. 15 µL of the digested samples were run on a 4% wt/vol agarose gel in order to increase the separation between small similar sized fragments; together with an undigested PCR sample as positive control for the 218 bp *APOE* fragment, a sample where DNA was substituted for dH_2O but had undergone the PCR protocol and a 1 kb DNA ladder. Gel electrophoresis was run at 80 V for 45 min to create separation between small fragments.

2.3.6 Protein extraction and quantification

Protein extraction and quantification for normalisation of cell numbers in APOE ELISA (section 2.3.7) and glutamate uptake (section 2.3.8) assays were performed using the colorimetric Pierce BCA assay (Thermo Scientific). Cell samples were washed in cold PBS before being incubated on ice for 15 min in cold treatment buffer containing: 75 mM Tris-HCl

(pH 6.8), 3.8% SDS, 4 M Urea, 20% Glycerol, 5% (all from Sigma), made up in dH_2O. Cells were scraped off from the plate and collected in protein low-bind Eppendorf tubes (Sigma) and subsequently snap-frozen and stored at -80°C.

Protein assays were conducted according to the manufacturer's instructions (see Appendix D), but in summary, 100 µL of BCA working reagent was added to 12.5 µL of cell sample in triplicate on a 96 well plate, which was incubated for 30-60 minutes at 37 ^{0}C, and read at 595 nm on a Sunrise F039300 plate-reader (Tecan). Serial dilutions of bovine serum albumin in treatment buffer were used to generate a standard curve ranging from 0-2000 µg/mL).

2.3.7 APOE ELISA assay

Cultures of human iPSC-derived astrocytes from a confirmed *APOE3/E3*, an *APOE4/E4* and an *APOE* knockout cell line were maintained in AMM to an age of 90 days. At this point media was collected (48 hours since last feed) and cells simultaneously lysed for protein normalisation as described in section 2.3.6. Media samples were kept in Protein LowBind tubes (Eppendorf) and stored at -80°C. The APOE ELISA assay was conducted according to manufacturer's instructions (see Appendix E), with the addition of more points at the lower end of the standard curve to increase precision, as a test run suggested my samples would fall in the range below 25 µg/mL. In short, 100 µL standard and media samples (in triplicate) was added to each well of a 96 well plate and incubated for 2.5 hours, then 100 µL biotinylated antibody for 1 hour, followed by 100 µL horse-radish peroxidase for 45 min. The plate was washed 5x with wash buffer between each addition. Lastly, wells were incubated with 100 µL TMB substrate for 30 min while protected from light, after which stop-solution was added

and plate was read at 450 nm on a Sunrise F039300 plate-reader (Tecan). All samples were normalised to protein content by dividing the APOE content readout with the quantification of protein from an accompanying BCA assay.

2.3.8 Meso-scale discovery assay for Aβ detection

This assay was run by Emma Whitely and I contributed neurons with *APOE4/E4* background. In short, the procedure involved growing NPCs (generated according to section 2.2.2) on poly-L-ornithine and laminin coated 12 well plates (Corning) at 100,000 cells/cm^2, until harvesting at 50 days post final plating. Media was changed 48 hours prior to harvest and on collection day was centrifuged at 1000 g at 4°C for 5 minutes to remove cell debris. 1:100 Halt combo inhibitor and EDTA (ThermoFisher) and 1:200 protease inhibitor cocktail (P8340 Sigma) were added, and samples stored at -80 ^{0}C.

Cells were washed and collected in 4°C PBS and pelleted at 5000 g for 5 minutes. Cell pellets were lysed for 20 minutes on ice in RIPA buffer (50 mM Tris pH 8, 150 mM NaCl, 1 % NP-40, 0.5 % NaDeoxycholate, 0.1 % SDS) containing 1:100 Halt combo inhibitor and EDTA (ThermoFisher) and 1:200 protease inhibitor cocktail (P8340 Sigma). Lysates were transferred to a QIAshredder column (Qiagen) and spun at 4°C at 16000 g for 10 minutes. Supernatants were snap frozen and stored at -80°C. A Pierce BCA assay (Thermo Fisher) was used to determine sample protein concentration, as described in section 2.3.6.

Amyloid-β measurements were performed with undiluted media using the V-PLEX Plus Aβ Peptide Panel 1 (6E10) Kit (Meso Scale Discovery) according to manufacturer's instructions (see Appendix F). $A\beta_{40}$ blocker was omitted. Total Aβ concentration was normalised to total protein amount. Four separate wells of cells for each neuronal

differentiation were plated and analysed for the MSD assay, representing four technical replicates.

2.3.9 Glutamate uptake assay

An enzymatic glutamate detection kit (Sigma) was used to assess glutamate uptake capability from iPSC-derived human astrocytes, compared to HEK293T cells. Both cell types were grown to confluency, and on the day of experiment cells were equilibrated with HBSS for 10 min, before the addition of 50 µM L-glutamate containing HBSS. Samples from their media were taken at 10, 30 and 60 minutes and kept on ice. After the last sample, cells were lifted with trypsin/EDTA, washed in AMM and centrifuged at 300g for 5 min. The pellet was subsequently lysed in 500 µL ice-cold RIPA buffer (Thermo Fisher Scientific) containing phosphatase- and proteinase inhibitors (Sigma). Cell debris was removed by centrifuging the lysate at 13,500 RPM for 5 min at 4°C and keeping the supernatant.

The glutamate detection assay was conducted according to manufacturer's instructions (see Appendix G). Briefly in summary: 50 µL sample and standard were added to a 96 well plate in duplicate, followed by 100 µL of reaction mix and 30 min incubation at 37°C protected from light. The absorbance was measured at 450 nm on a Sunrise F039300 plate-reader (Tecan). The amount of glutamate taken up by the astrocytes was calculated as a difference between time-points, by subtracting the concentration of glutamate detected in each sample from the concentration measured at the 10 min time point. All values were then normalised to protein content, quantified by running an accompanying BCA assay on the protein samples.

2.4 Electrophysiological methods

Whole-cell patch clamp recordings were performed with thin-wall borosilicate glass pipettes (resistances of 5-8 MΩ for neurons, and 7-12 MΩ for astrocytes), back-filled with intracellular solution (see section 2.1.5), produced using a Sutter P-97 Flaming-Brown puller (Sutter Instrument Company). Neurons were patched using standard techniques of applying positive pressure to create a dimple in the soma membrane, which helped form a giga-seal once pressure was released. Negative holding current was applied at the giga-seal stage prior to break-through. For astrocytes, this procedure had to be performed in a much gentler fashion, due to their flatter morphologies and more delicate membranes. Astrocytes rarely had an obvious soma, so an edge of membrane was often chosen for patching. Reduced amounts of positive pressure was applied and if the giga-seal did not form instantly once pressure was released, cells were left for a couple of minutes or very gentle negative pressure was applied. Breaking through also required much gentler application of negative pressure.

Cultures were constantly perfused with external solution at a rate of ~2 mL/min, heated to 33-35^{0}C using a combination of water bath and in-line heater. Drugs were dissolved in dH_2O where possible, or DMSO if necessary, and were made up to final concentration in external solution for bath application. To prevent mixing of solutions, 10 mL of perfusate was allowed to flow through before recycling solutions, when changing to or from a drug-containing solution.

2.4.1 Acquisition and analysis

Rig setup 1: Recordings from human iPSC-derived neuron or astrocyte enriched cultures and co-cultures were made with a Multiclamp 700B amplifier (Molecular Devices)

and the accompanying software Clampex version 10.5. Signals were digitized with an Axon digidata 1550 (Molecular devices), filtered at 2 kHz (Bessel filter) and sampled at 20 kHz. Cultures were viewed using a FV3-290 microscope (Olympus) through a 60x/0.90NA w LUMPlanFI objective (Olympus) with a 1.3x magnifier and DFK 41BU02 camera (ImagingSource) through the accompanying IC Capture v2.2 software. CamKIIa-mKate2^{+} cells were identified and visualized under epifluorescence (RFP: 543/22 nm excitation filter, 562 nm dichroic, 593/40 nm emission filter). The headstage was controlled with an MP-225 Intracel micromanipulator (Sutter Instrument Company).

Rig setup 2: Recordings from rat astrocytes and patched human astrocytes in combination with Ca^{2+}-imaging were performed on another electrophysiology setup, where cells were viewed using a BX51WI microscope (Olympus) through a 20x/1.00NA XLUMPlanFL-N objective (Olympus) and iXon camera (Andor Technologies) with a 4x magnifier. Recordings here were made with a Multiclamp 700B amplifier, an Axon digidata 1322A and Clampex version 9.0 software (all from Molecular Devices). Signals were filtered at 2 kHz (Bessel filter) and sampled at 10 kHz. Rhod-2 and OGB fluorescence was visualized under epifluorescence. The headstage was controlled with an MP-225 Intracel micromanipulator (Sutter Instrument Company).

Rig setup 3: Recordings of human iPSC-derived cells transplanted into mouse organotypic slices were recorded on a LSM 880 confocal microscope setup, equipped with an argon laser (for excitation at 488 and 458 nm) and a diode-pumped solid-state laser (for 561 nm excitation), a 20x water-immersion objective (W Plan-Apochromat, NA

1.0), all controlled with ZEN black software (Zeiss, Germany). Simultaneous electrophysiology was carried out using a Multiclamp 700B amplifier (Molecular devises) and digitizer (National Instruments). For patching, cells were visualised using a DFK 41BU02 camera (ImagingSource) and the IC Capture v2.1 software and recordings made with WinWCP v5.1.6 (Strathclyde) software. The headstage was controlled with an MP-225 Intracel micromanipulator (Sutter Instrument Company).

Electrophysiological data collected using Clampex was analysed using the accompanying Clampfit software (version 10.5, Molecular Devices), whereas data collected on the confocal setup was analysed through a combination of the open-source WinWCP v5.1.6 software, (Strathclyde) and MatLab, version 2016b (MathWorks).

To be included for analysis, cells required an access resistance below 50 MΩ at all times. Automated measurements of access resistance (Ra), membrane capacitance (Cm) and membrane resistance (Rm) were generated through the Clampex membrane test function. For a recorded trace to be accepted for analysis, Ra, Cm and Rm values preceding and following should not deviate by more than 40% from the maximum or minimum throughout the recording period.

2.4.2 Intrinsic properties

Cells were voltage-clamped at -70 mV for the assessment of voltage-gated currents which were elicited with a voltage step protocol from -90 to +20 mV (neurons) or -140 to 30 mV (astrocytes) in increments of 10mV. The leak subtracted trace was used for analysis and the

maximum sodium (Na^+) current was taken as the largest negative voltage-gated current, whereas the maximum potassium (K^+) current was measured as the largest positive current (including both A-type and delayed rectifier K^+ channels). Resting membrane potential (Vm_{rest}) was noted upon entry to current clamp mode in the absence of current injection and junction potential corrected values were reported. Junction potential for the combination of external and internal was calculated via Clampex's (Molecular devices) liquid junction potential function to be +14 mV. Current was injected to adjust cell Vm to -70 mV in current clamp mode, such that action potentials (APs) were always elicited from the same baseline.

To induce AP firing in neurons, current was injected in 5 pA steps from -20 to +35 pA. On occasions steps were increased to 10 pA or more steps were added if depolarization was not sufficient to reach AP threshold. For astrocytes, it was ensured that depolarisation reached 0 mV to rule out AP initiation capacity. The number of consecutive APs reported for each neuron was the maximum number of overshooting APs peaking over -10 mV, fired during one current step. Spike threshold was the lowest membrane voltage which triggered an AP across the current-steps.

2.4.3 Spontaneous synaptic activity

Spontaneous post-synaptic currents (sPSPs) were recorded in voltage-clamp near the respective theoretical reversal potentials of GABA and glutamate receptors for the combination of internal and external solutions used, to minimise contamination between GABAergic and glutamatergic inputs. Accounting for the liquid junction potential of +14 mV, sEPSCs were recorded at -70 mV ($E_{GABA} = \frac{R \cdot T}{z \cdot F} \cdot \ln\left(\frac{149}{6}\right) = -84.7\ mV$) and IPSCs at 0 mV ($E_{Glut} = \frac{R \cdot T}{z \cdot F} \cdot \ln\left(\frac{140+5}{7.2+140}\right) = -9.6\ mV$), where R (ideal gas constant) = 8.314 J/(mol*K);

T (temperature) = 306 K; z (valence of ion species) = +1 for Na^+ and K^+ and -1 for Cl^-; and F (Faraday's constant) = 96,485 C/mol. In **Chapter 3** recordings of sEPSCs and sIPSCs were interleaved and performed with the Cs^+ based version of Internal 1 (section 2.1.5). In subsequent chapters sEPSCs were recorded in the presence of picrotoxin (PTX). Miniature excitatory post-synaptic currents (mEPSCs) were recorded in both PTX and tetrodotoxin (TTX). Separate gap-free 1 min voltage clamp traces were recorded for each neuron and averaged if more than 1 trace fulfilled the recording inclusion criteria (see section 2.4.1).

For automated event detection, a template was generated in Clampfit by manual selection of 50-100 events for averaging. Templates were generated independently for excitatory and inhibitory events as required for the differing kinetics. Events were detected in Clampfit by running the template across a recording, setting a match-criterion of 4-6. Subsequent post-hoc filtering was applied using criteria for amplitude: >7 pA, half width: <4 ms and rise time 10-90%: <1.2 ms, which were designed to exclude false-positive events and were determined through comparison against manual detection. The PSC amplitude was calculated by averaging all included events per neuron. Cells with a PSC frequency of <0.017 Hz (corresponding to having less than 1 synaptic event per min) were regarded as having a frequency of 0.

2.4.4 Biocytin filling of cells

To reveal gap-junction connected astrocytes, ~5 µg/mL biocytin (Sigma) was dissolved in the internal patching solution, aided by slight heating and sonication to reduce the chance of blocking the pipette. After whole-cell configuration was achieved, biocytin was left to fill the cell for at least 5 min while recordings took place.

2.4.5 Glutamate induced currents from patched astrocytes

L-glutamate for bath application was first diluted in NaOH to 100 mM, then further diluted to a stock concentration of 10 mM in dH_2O and used at a final concentration of 100 µM by dilution in ACSF. The biophysical properties of patched cells were first confirmed to correspond to putative astrocytes in terms of limited $VGNa^+$ current and lack of AP initiation. Astrocytes were held at -70 mV while a 6 min gap-free recording was started simultaneously with glutamate wash in, which was switched back to ACSF after 1-1.5 min.

2.4.6 Acute LED stimulation

Acute, short-term stimulation of ChR2 expressing astrocytes and simultaneous patch-clamp recordings of spontaneous EPSCs from co-cultured neurons was performed using a movable LED on the electrophysiology rig. From each neuron, a 2 min baseline was recorded, then a 50 s train of 245 ms LED pulses was delivered at 2-4 Hz straight underneath the cultures, followed by a post-stimulation recording of 2 min. LED intensities used ranged from ~0.3-2.7mW/mm^2, because of optimisation attempts to minimise heat from the LED, but maximise stimulation intensity. Neurons were all held at -70 mV in voltage clamp in the presence of PTX. In the cases when MCPG was bath applied, stimulation was first confirmed to convey a sEPSC increase and then stimulation was repeated in the presence of MCPG.

2.4.7 Puff application of substances

High concentration KCl and neurotransmitters ATP and glutamate were applied locally to human astrocytes. Patch-pipettes were back-filled with the relevant solution and were attached to a Picospritzer® II (General Valve Corporation), on which the pressure was set to 1-2 psi to minimise movement artefacts. The pipette-holder was mounted on an MP-225 Intracel micro-manipulator (Sutter Instrument Company) to ensure fine control of placement

near target cells. Substances could be applied in precisely controlled puffs as the picospritzer can be triggered from the Clampfit (Molecular devices) software.

2.5 Imaging methods

2.5.1 Calcium imaging

Calcium signals were recorded from both rat and human astrocyte cultures both under spontaneous and evoked conditions, which included ChR2 activation and local application of neurotransmitters.

Membrane permeable AM-ester forms of Ca^{2+} dyes (see section 2.1.9) were used for assessing Ca^{2+} behaviours at a population level, while the membrane impermeable K^{+}-salt form was used for filling individual cells via whole-cell patching. Stock solutions were made up in DMSO to 2 mM and vortexed to mix thoroughly. When loading whole astrocyte populations grown on glass coverslips, the amount of dye needed to achieve the final working concentration was first mixed with the same amount of the detergent Pluronic F-127 (20% solution in DMSO, Invitrogen), before being diluted in media (AMM) and vortexed. This final mixture of dye, pluronic and media was added to the astrocytes and incubated for 60 min at 37°C. Following this initial loading, dye-containing media was removed and cells were incubated in normal, indicator-free media for ~30 min.

A xenon-lamp where the shutter was controllable without touching the microscope was used for imaging. The red-shifted dye Rhod-2 was imaged using a 535/50 nm excitation filter, 565 nm dichroic mirror and 590 nm emission filter. Green Ca^{2+} dyes OGB-1 and 2 were imaged using 480/40 nm excitation filter, 505 nm dichroic and 520 nm emission filter.

The size of Ca^{2+} events was calculated as $\Delta F/F$ according to: $\frac{\Delta F}{F} = \frac{F_t - F_{t=0}}{F_{t=0}}$ where $F_{t=0}$ is an average of at least the first 5 frames of a movie. An astrocyte was counted as displaying an event if $\Delta F/F$ during the imaging time frame surpassed a limit of 1.05.

2.5.2 Spontaneous events

Astrocytes were loaded with 10 µM OGB-1 AM ester as described above (section 2.5.1) and 2 minute movies were recorded from different fields of view around cultures, generally at framerates of 2-4 Hz. Spontaneously arising events were categorised as synchronous if their initiation was within 1 s of another spontaneous event recorded within the same field of view. Because the frame rate was often 2 Hz, a 1 s gap means that synchronicity was determined as events starting within 2 frames of the first event.

2.5.3 Neurotransmitter-evoked events

Populations of astrocytes were loaded with 10 µM OGB-1 AM, whereas single astrocytes were patched and filled through the pipette with 0.2 mM OGB-2 K^+-salt, dissolved in the EGTA-free internal solution (2). In both cases, local application of 100 µM glutamate or 1 mM ATP was achieved through a Picospritzer® II (General Valve Corporation), controlled by Clampex (see section 2.4.7).

2.5.4 LED-evoked events

ChR2-expressing rat astrocytes were loaded with 5 µM Rhod-2 AM, while human astrocytes were loaded with 10 µM OGB-1 AM. Rhod-2 allowed for separation of ChR2-expression and dye loading, whereas both signals were green for OGB-1. After identifying an appropriate field of view, the LED was put between the condenser and the recording chamber and the LED

was triggered from a protocol in Clampfit, where the duration of the pulse could be adjusted. The light intensity was controlled by a custom-built LED controller.

2.5.5 Movie analysis

Brightness and contrast was adjusted on all imaging files in Image J, along with histogram correction via the plugin from EMBL tools: Bleach correction. ROIs were placed over cell bodies or parts of cell membranes that could be clearly defined, and lastly a square ROI placed on a piece of background. Data from all ROIs was extracted as mean grey values from every image via the multimeasure function and exported to Excel. First, background was subtracted, after which $\Delta F/F$ was calculated as described in section 2.5.1.

2.5.6 ClopHensorN imaging

All ratiometric ClopHensorN data presented in **Chapter 4** was captured on the confocal rig setup 3 described in section 2.4.1, featuring an argon laser for excitation at 488 and 458 nm and a diode-pumped solid-state laser for 561 nm excitation. Emitted fluorescence was collected by one photomultiplier tube (PMT) in the 635-700 nm range when ClopHensorN was excited at 561 nm, and by a second PMT in the 500-550 nm range during 458 nm and 488 nm excitation. Fluorescence readouts were always collected by drawing regions of interest (ROIs) over the cell body, such that no overexposed pixels were part of the selection, and background fluorescence was subtracted. Data was then exported and processed using custom-made Matlab scripts (developed in collaboration with Alexandru Calin). Exposure thresholds were used to exclude regions of interest that had signal-to-noise ratio lower than 2.

ClopHensorN is a fusion protein comprising a pH and Cl^- sensitive E^2GFP linked to a pH and Cl^- insensitive tdTomato. The binding of H^+ to E^2GFP increases its fluorescence,

whereas binding of Cl^- has the opposite effect, as Cl^- quenches E^2GFP fluorescence in a concentration dependent manner. The binding affinity of Cl^- to E^2GFP depends on the presence of H^+, and thus on pH because the ion-binding pocket of E^2GFP is negatively charged, so it binds H^+ independently of Cl^-, whereas Cl^- can only bind in the presence of H^+ due to electrostatic repulsion (Arosio *et al.*, 2010). Raimondo and colleagues who developed ClopHensorN verified that the pH readout was indeed unaffected by $[Cl^-]$ (Raimondo *et al.*, 2013), whereas the $[Cl^-]$ readout heavily depended on pH because of the necessary co-binding of H^+ to overcome the negative repulsion. This relationship means that a low, acidic pH promotes Cl^- binding, as ClopHensorN is in a very protonated state, and thus acidity produces more effective Cl^- -dependent quenching.

The distinction between H^+ and Cl^- arises from the specific ion sensitivity of the fluorophores when excited at defined wavelengths: 1) E^2GFP at 488 nm: the signal is sensitive to pH and Cl^-, 2) E^2GFP at 458 nm: the pH isosbestic point where the signal is only sensitive to Cl^- (Arosio *et al.*, 2010), and 3) tdTomato at 561 nm: the signal is insensitive to both pH and Cl^- changes, which means it is used as normalisation for brightness changes due to inadvertent effects like bleaching and tissue movement. All recordings were corrected for bleaching effects by fitting an exponential decay to each wavelength signal, which approximated the bleaching rate and was subsequently used to stabilise the optical signals. For recordings of fluorescence of transplanted cells during network events (NEs), NEs were first detected and fluorescence data during NEs was excluded from the exponential decay function fitting. Following bleach correction, ion selective readouts were obtained by computing ratios between the signals:

$$\frac{488\,nm}{458\,nm} = \frac{pH + Cl^{-}\ sensitive}{Cl^{-}\ sensitive} = pH\ ratio$$

$$\frac{458\,nm}{561\,nm} = \frac{Cl^{-}\ sensitive}{pH + Cl^{-}\ insensitive} = Cl^{-}\ ratio$$

These ratios were used to infer the pH and Cl^- concentration according to experimentally determined calibration curves (see section 2.5.7). Measurements were excluded if their pH or Cl^- ratios were not within the respective calibration curve ranges. Furthermore, Cl^- values above 200 mM were considered artefacts and excluded from analysis.

2.5.7 Calibration

ClopHensorN calibration was performed in collaboration with Tatsiana Waseem and Alexandru Calin, following the previously described method of Raimondo et al. 2013, which is a technique previously employed for other fluorescent reporters or dyes (Boyarsky *et al.*, 1988; Arosio *et al.*, 2010). HEK239 cells were lentivirally transduced with ClopHensorN 3-5 days prior to recording. Intra- and extracellular pH and Cl^- concentration were equilibrated by using a mixture of ionophores: the K^+/H^+ exchanger nigericin (20 µM), the Cl^-/OH^- exchanger tributyltin chloride (40 µM) and the Cl^- ionophore I (1 µM) in high K^+ buffer solution (ACSF 3, see section 2.1.5). Cells were incubated with ionophores for 30 min prior to recording initiation. Separate calibration curves were obtained by monitoring the pH and Cl^- ratios emitted by ClopHensorN expressing HEK293 cells, while systematically clamping their pH and Cl^- through changing the extracellular pH or Cl^- concentration.

For pH: The intracellular pH was controlled by titrating KOH or HNO_3 to the HEPES-based buffer solution containing the ionophore cocktail described above. Following each pH adjustment, the intra- and extracellular compartments were left to equilibrate at

least 15 min before the pH ratio was measured by imaging ClopHensorN. According to the Grynkiewicz equation (Grynkiewicz, Poenie and Tsien, 1985), the binding of a proton to ClopHensorN in a 1:1 proton:ClopHensorN complex would lead to the following relationship:

$$pH_i = pK_A + \log\left(\frac{R_{pH} - R_{Acid}}{R_{Base} - R_{pH}}\right) + \log\left(\frac{F_{458}{}_{Acid}}{F_{458}{}_{Base}}\right) \quad (1)$$

Where pH_i represents the intracellular pH, pK_A denotes the acid dissociation constant of ClopHensorN, R_{pH} is the measured pH ratio, R_{Acid} is the theoretical ratio for ClopHensorN in its most acidic form and likewise, R_{Base} is the ratio for the most alkaline form of ClopHensorN. $F_{458,Acid}$ and $F_{458,Base}$ represent the fluorescence of ClopHensorN when excited at 458 nm in its most acidic and basic form, respectively. Given that the fluorescence of E^2GFP is insensitive to changes in pH when the fluorophore is excited at 458 nm (pH isosbestic point), the equation above can be simplified to:

$$pH_i = pK_A + \log\left(\frac{R_{pH} - R_{Acid}}{R_{Base} - R_{pH}}\right) \quad (2)$$

Calibration data consisting of measured R_{pH} was fitted to the following re-arranged version of the equation:

$$R_{pH} = \frac{R_{Base} \cdot 10^{pH - pK_A} + R_{Acid}}{1 + 10^{pH - pK_A}} \quad (3)$$

The fitted sigmoidal curve was determined using 6 pH calibration values between pH 6 and 8.5, and pH ratio data within one standard deviation of the mode for each pH value was used. This allowed for pK_A, R_{Acid} and R_{Base} to be calculated; with R_{Acid} being determined from the asymptote at pH $-\infty$, R_{Base} from the asymptote at pH $+\infty$, and pK_A as the pH at which half

of ClopHensorN is in protonated (acidic) form, so the pH corresponding to the ratio halfway between R_{Acid} and R_{Base}.

For chloride: The intracellular Cl^- concentration was controlled by systematically adjusting the extracellular pH to a set value (as described above, with KOH and HNO_3) and varying the Cl^- concentrations, achieved by replacing determined amounts of K-gluconate from the HEPES-based buffer solution containing the ionophore cocktail with KCl. Following each adjustment of pH and/or Cl^- concentration, the intra- and extracellular compartments were left to equilibrate for at least 15 min before the Cl^- ratio was measured by imaging ClopHensorN. Again, according to the Grynkiewicz equation, the binding of Cl^- and the formation of a 1:1 Cl^--ClopHensorN complex would result in the following relationship:

$$[Cl^-]_i = K_{d,\ pH}^{Cl^-} \cdot \left(\frac{R_{Cl^-} - R_{free}}{R_{bound,pH} - R_{Cl^-}}\right) \cdot \left(\frac{F_{561,free}}{F_{561,bound}}\right) \quad (4)$$

In this equation, $[Cl^-]_i$ denotes the intracellular Cl^- concentration, $K_d^{Cl^-,\ pH}$ signifies the Cl^- dissociation constant which is dependent on pH, R_{Cl^-} is the measured Cl^- ratio, R_{free} is the theoretical Cl^- ratio of ClopHensorN in its Cl^- free form (in the absence of Cl^- in the solution) and $R_{bound,pH}$ is the Cl^- ratio of ClopHensorN in its fully Cl^- saturated form, for a given pH. $F_{561,free}$ and $F_{561,bound}$ represent the fluorescence of ClopHensorN when excited at 561 nm in its Cl^- free and Cl^- bound form, respectively. Given that the fluorescence of tdTomato is insensitive to changes of both pH or Cl^- when the fluorophore is excited at 561 nm, the equation above simplifies to:

$$[Cl^-]_i = K_{d,\ pH}^{Cl^-} \cdot \left(\frac{R_{Cl^-} - R_{free}}{R_{bound,pH} - R_{Cl^-}}\right) \quad (5)$$

Calibration data consisting of measured R_{Cl^-} was fitted to the following re-arranged version of the equation:

$$R_{Cl^-} = \left(\frac{[Cl^-]_i \cdot R_{bound,pH} + K_{d,\ pH}^{Cl^-} \cdot R_{free}}{K_{d,\ pH}^{Cl^-} + [Cl^-]_i}\right) \quad (6)$$

As separate sets of Cl^- calibrations were performed at different pH values, it allowed for the calculation of $K_d^{Cl^-,\ pH}$, R_{free} and $R_{bound,pH}$ for each pH. R_{free}, representing the ratio for ClopHensorN in its completely unquenched form when $[Cl^-] = 0$ mM, was inferred at the point where all calibration curves intersected. However, the 0 mM Cl^- solution was unlikely to create a completely Cl^- free intracellular environment due to imperfect permeabilization, therefore calibrations used for calculations were bounded at a nominal $[Cl^-]$ of 4 mM. $R_{bound,pH}$ was assumed to relate linearly with pH and was determined from the asymptote at $[Cl^-]$ $+\infty$, and $K_d^{Cl^-,\ pH}$ relates to pH according to the following relationship:

$$K_{d,\ pH}^{Cl^-} = {}^1K_d^{Cl^-} \cdot \left(\frac{1+10^{pK_A - pH_i}}{10^{pK_A - pH_i}}\right) \quad (7)$$

Where ${}^1K_d^{Cl^-}$ represents the dissociation constant for Cl^- in the most acidic (fully protonated) form of ClopHensorN. The calibration curves for inferring Cl^- concentrations were experimentally determined for pH 6 and 7, which were subsequently used for generating the appropriate calibration curve for a given pH by fitting to equation (6).

2.5.8 Monitoring of network events in organotypic slices

For the detection of NEs in organotypic hippocampal slices, mouse pyramidal neurons were whole-cell patched clamped, using borosilicate glass pipettes (resistances 4-7 MΩ), backfilled with internal solution (3) (see section 2.1.5). The slice was continuously perfused with O_2 bubbled ACSF 2 (see section 2.1.5). Neuronal identity was confirmed by eliciting successive APs via current injection (typically 100-400 pA in steps of 100 pA). Gap-free continuous

recording of neuronal membrane potential was carried out in current clamp in the I=0 mode. Neurons with initial Vm_{rest}> -50 mV were rejected. Initiation of confocal imaging could be triggered through the electrophysiology software via a specially built trigger box to ensure simultaneous electrophysiological recording and imaging. Electrophysiology and imaging files were synchronised using a custom-built matlab-script and individual NEs detected.

2.5.9 Measures

Baseline pH and $[Cl^-]_i$: was determined from an average generated from the 5 s of trace immediately preceding the start of an NE and averaged for all NEs per cell.

pH and $[Cl^-]_i$ dynamics: The dynamic measures were all calculated and presented per NE, the duration of which were set to represent 100%, such that any measure is expressed relative to a normalised % of NE duration.

Peak change in pH/$[Cl^-]_i$: (Δ pH/$[Cl^-]_i$ peak) was measured as amplitude at the maximal deflection from baseline.

Area under the curve (AUC): was calculated as an integral over the inferred pH/Cl^- trace, where baseline was subtracted from the pH/$[Cl^-]_i$ trace prior to integration. The AUC integral was extracted between 50% and 250% of time relative to each NE duration to avoid artefacts at the beginning of NEs, which the Δ peak measure is more sensitive to.

Time to peak and time to 75% return: were determined between the baseline and 1) the maximal deflection in either direction (peak) or 2) the point at which the signal had returned 75% of the way towards baseline after the peak; 75% was chosen instead

of 100% return to rescue the cases where 100% return was not achieved for reasons such as drift in the baseline or rapid initiation of the next spontaneous NE.

Data where chloride was inferred to be above 200 mM or pH changes exceeded 6 units were excluded as artefacts. For network dynamics, only chloride traces that recovered within 40 mM from resting level were considered.

2.6 Statistical analysis

All statistical analysis was performed using the Prism software, version 6 (GraphPad). Bars on graphs represent means and error bars indicate ± standard error of the mean (SEM). Non-parametric statistical tests were employed on all data-sets, as ranks and medians are more robust to outliers, and because several data-sets have tails of zero-values. Data-sets were regarded as un-paired and two-tailed tests were performed, unless otherwise stated, and the appropriate type of test was indicated after each reported p-value. Results were corrected for multiple comparisons. Statistical significance was reported at the following levels:

* $p < 0.05$, ** $p < 0.01$, *** $p < 0.001$.

Chapter 3

3 Generation and characterisation of iPSC-derived human neurons and astrocytes

3.1 Introduction

Together, neurons and astrocytes comprise the majority of brain tissue and they are known to interact closely in order to maintain normal brain function. Whilst neurons are regarded as the excitable, information carrying cells, they cannot function without the support of astrocytes. This reliance upon astrocytes is illustrated by the lethality of mice in which gliogenesis is prohibited (X. Li *et al.*, 2012) or where key astrocytic genes are knocked out (Djukic *et al.*, 2007; Tanaka *et al.*, 2009). The majority of what is known regarding neuronal and astrocytic function and their interactions stems from rodent models, and although these have been invaluable to neuroscience, potential species differences should be considered, especially when attempting to model human diseases (Cavanaugh, Pippin and Barnard, 2014; Youssef *et al.*, 2016; Gunn-Moore *et al.*, 2018). iPSC technology enables the generation of human-relevant *in vitro* model systems, where cells of the same kind and from the same individual can be derived continuously and in a manner that facilitates reproducibility and scalability of experiments. In addressing the central aim of studying interactions between human iPSC-derived cortical neurons and astrocytes, the first step of this thesis was to reliably generate the two cell types and confirm their functionality.

A rational strategy for deriving cortical neurons and astrocytes is to attempt to recapitulate key aspects of cortical neuro- and glio-genesis that occur *in vivo*. Corticogenesis has been considered the default pathway of the developing brain (Wilson and Houart, 2004;

Levine and Brivanlou, 2007) and key aspects of the process has been recapitulated by iPSC differentiation protocols, including an extended neurogenic time period over several weeks (as compared to days in mouse brain development), a sequential formation of cortical layers in an inside-out fashion, and a delayed switch to gliogenesis (Shi *et al.*, 2012b; Anderson and Vanderhaeghen, 2014). The polarised rosette structures that form spontaneously during iPSC neural induction are thought to recapitulate aspects of the VZ and SVZ, where excitatory cortical neurogenesis occurs in the embryonic brain (Lodato, Shetty and Arlotta, 2014; Manuel *et al.*, 2015). Several pools of human glutamatergic cortical progenitors have been described (Florio and Huttner, 2014), and progenitor pool diversity is considered fundamental for enabling the recapitulation of excitatory neuron diversity found in the adult cortex using iPSCs (Gaspard *et al.*, 2008; Shi, Kirwan and Livesey, 2012).

Neurogenesis is followed by gliogenesis *in vivo*, which is characterised by a decrease in neurogenic potential and switch to glia production. By attempting to influence the important gliogenic JAK-STAT pathway, iPSC-based differentiation protocols have achieved human astrocyte generation over varying time frames (Krencik and Zhang, 2011; Emdad *et al.*, 2012; Serio *et al.*, 2013; Shaltouki *et al.*, 2013). Despite varying in the technical details of differentiation and media composition, these protocols all rely on the principle that astrocyte subtype specificity is governed by regional patterning imposed during the preceding neurogenic stage (Hochstim, Deneen, Lukaszewicz, Zhou and David J. Anderson, 2008; Liu and Zhang, 2011). This chapter reflects my efforts to re-capitulate key aspects of cortical neuro- and glio-genesis when deriving both neurons and astrocytes from human iPSCs.

A crucial stage in verifying the successful generation of cortical neurons and astrocytes is an assessment of their functional properties. Neurons have excitable cell membranes due to high densities of ion-selective voltage-gated channels, which enable them to fire fast and precisely timed APs. These APs are used by neurons to initiate the release of synaptic vesicles from their pre-synaptic structures, which affords fast chemical communication with other post-synaptic neurons within the network. Conversely, astrocytic membranes are largely non-excitable under physiological conditions and owe this state to a combination of factors, which includes: 1) a much lower density of voltage-gated Na^+ ($VGNa^+$) channels compared to neurons (Sontheimer, Black and Waxman, 1996), 2) a high permeability for K^+ (Du *et al.*, 2015), and 3) gap-junction connectivity (Sutor and Hagerty, 2005). The latter two factors act to lower the membrane resistance, as any current injected can both leak out of the cell and be dispersed to neighbouring cells. This gap junctional connectivity allows for specialised homeostatic functions, particularly in the case of glutamate uptake and K^+ buffering, as the cell-to-cell coupling of astrocytes enables the dispersion of these excitotoxic molecules via inter-cellular diffusion (Ozog, Siushansian and Naus, 2002; Wallraff *et al.*, 2006). Whether the human cortical neurons and astrocytes generated from iPSCs display these differences in terms of biophysical properties and intercellular signalling will be investigated in this chapter.

More specifically, the aims of this chapter are to:

1) Establish methods for the reliable generation of human cortical neurons and astrocytes from a common progenitor pool.

2) Verify that the human neurons recapitulate aspects of corticogenesis and develop functional properties.

3) Confirm that the human astrocytes are biophysically distinct from the neurons and develop the capacity for homeostatic support of neuronal synapses.

3.2 Results

In order to study interactions between human iPSC-derived cortical neurons and astrocytes, I modified both published and unpublished protocols for generating the two cell types of interest. For deriving cortical neurons, I made use of an established protocol (Shi, Kirwan and Livesey, 2012), which is based on the dual SMAD inhibition strategy, known to promote ectoderm while inhibiting endoderm and mesoderm (Gaude *et al.*, 2005; Chambers *et al.*, 2009). The protocol reports the generation of three subtypes of cortical neural progenitors identified in human (radial glia, intermediate progenitors and outer radial glia), the sequential appearance of cortical layer markers, and the appearance of astrocytes beyond 90 days of culture. Although some degree of gliogenesis was observed by Shi and colleagues, I wanted to more efficiently and rapidly generate an enriched astrocyte population from the same cortical progenitor pool. To achieve this, I subjected iPSCs to the first ~3 weeks of the Shi et al. (2012b) cortical neuron induction protocol (see section 2.2.2) and subsequently split the induction into two streams, one continuing the cortical neuron differentiation, the other being driven towards astrocytic differentiation using a proprietary media kit (see section 2.2.4) (**Figure 3.1A**). A proprietary kit was selected based on the proposed short differentiation time frame and the evidence from the Brennand lab, who screened 11 different astrocyte differentiation protocols and found that the commercial kits were the most robust (Tcw *et al.*, 2017).

iPSCs were set on a neurogenic path by selectively growing neural ectoderm via dual SMAD inhibition using the drugs SB431542 and Dorsomorphin (**Figure 3.1B**). A dense neuroepithelial sheet was achieved after 12 days of dual SMAD inhibition, and the transition

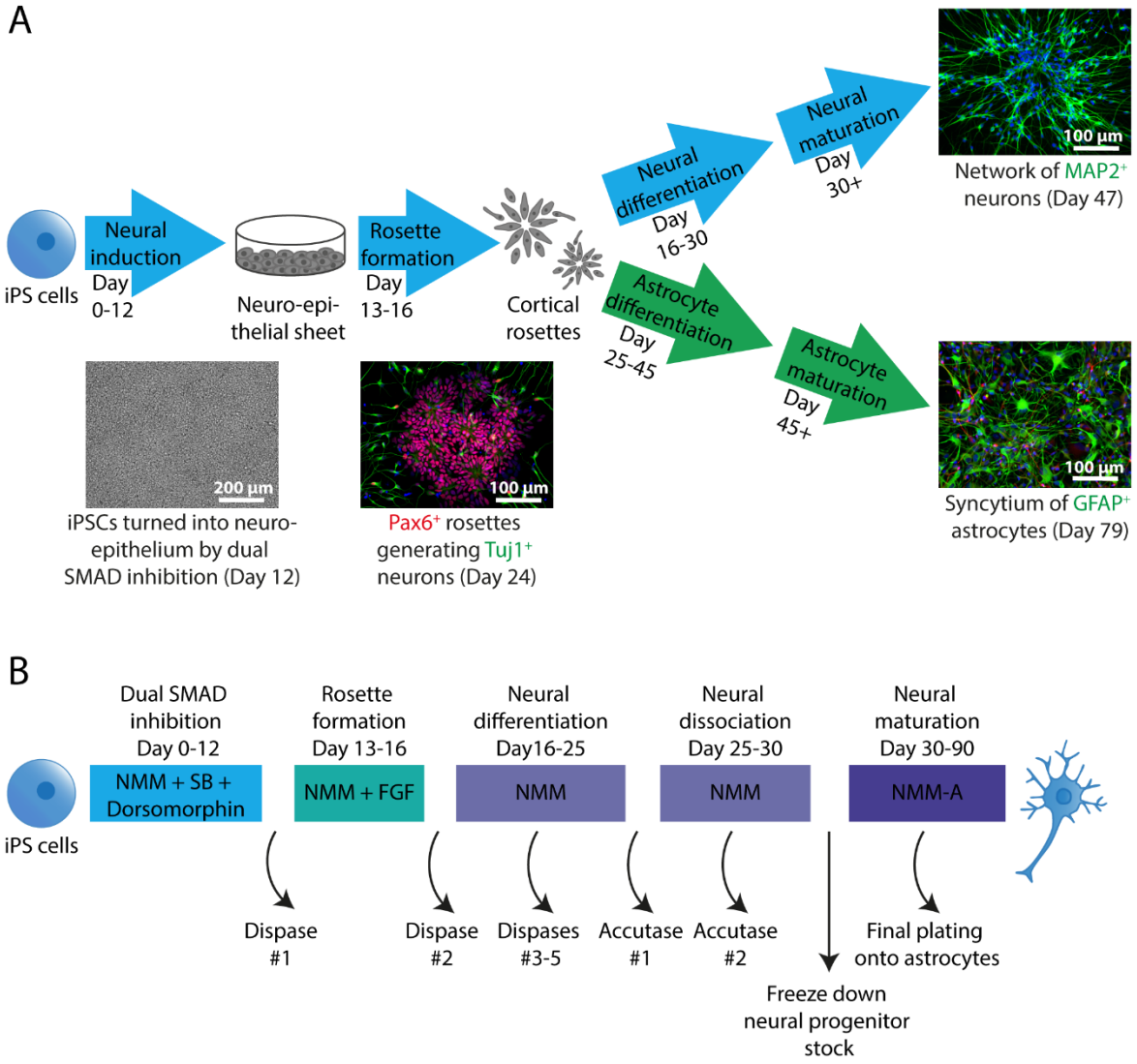

Figure 3.1 Human neurons and astrocytes can be generated from a common progenitor pool
(A) Schematic showing the different stages of differentiation from iPSCs towards Pax6⁺ cortical radial glia progenitors, which can be driven towards either a neuronal or astrocytic fate. This protocol allows for the generation of Tuj1⁺ and MAP2⁺ neurons, as well as GFAP⁺ astrocytes from the same vial of iPSCs. **(B)** Detailed outline of the neuronal differentiation protocol, based on Shi et al. (2012b). Dual SMAD inhibition for 12 days, using SB431542 and dorsomorphin, causes the iPSCs to form a neuro-epithelial sheet. On day 13, the neuro-epithelial sheet is broken up with the first dispase treatment, whereupon rosette formation is stimulated with the addition of FGF for 4 days. On day 17, the second dispase is performed, which is followed by further selective lifts with dispase to yield a clean population of rosettes. Around day 25, rosettes are dissociated to single cells by 1-2 accutase treatments, after which the neural progenitors can be frozen and cryostored in liquid nitrogen. Individual vials of frozen progenitor stocks can be thawed, further matured and plated onto astrocytes for experimentation. NMM: Neuronal Maintenance Media, NMM-A: same recipe as NMM but with neurobasal exchanged for neurobasal-A.

to NPCs was stimulated by breaking up the sheet. The resulting dissociated clumps of cells possess the ability to self-organise into polarised rosette-structures with a lumen, around which neural progenitors were distributed in a radial fashion (Wilson and Stice, 2006; Mertens *et al.*, 2016). Rosette-formation was aided by the addition of fibroblast growth factor 2 (FGF-2) and selective lifts and expansions of rosettes yielded neuron-producing cultures. Dissociation to single cells promoted the switch from highly proliferative radial glial cells towards final differentiation, where the neural progenitor might undergo one or two further divisions, before giving rise to post-mitotic neurons (Florio and Huttner, 2014; Paridaen and Huttner, 2014). Using this protocol, I managed to reliably generate stocks of human cortical NPCs from several iPSC lines, which could be thawed out and go through a period of maturation in preparation for experimentation.

Since cortical differentiation is thought to be a default pathway in the absence of caudalising and ventralising morphogens (Wilson and Houart, 2004; Li *et al.*, 2009; Lupo *et al.*, 2014), the Shi et al. (2012b) protocol does not include any patterning factors. To verify that the cells generated were indeed following a cortical neural pathway, cells at the rosette-stage of every induction were subjected to a series of quality control checks using immunostaining (see section 2.3.1). These controls also served to ensure comparability across cell lines and different inductions. Commitment to a forebrain fate was confirmed by orthodenticle homeobox 2 (Otx2) positive staining (**Figure 3.2A**), as Otx2 is important for the specification of neural ectoderm into fore- and midbrain regions (Simeone, 1998). At this stage, cells are expected to still be highly proliferative, which was confirmed by the abundance of $Ki67^+$ cells. The Ki67 protein has been shown to be present in cycling cells at all active

phases (G1, S, G2, and M) of cell-division (Scholzen and Gerdes, 2000). From the pattern of Ki67 staining, it was observed that the majority of cell divisions occurred at the lumen of rosettes, consistent with this region resembling the VZ *in vivo*.

The near 100% expression of Pax6 within rosettes signified the dominant presence of the radial glia progenitor subtype, which is known to be essential for normal corticogenesis (Götz, Stoykova and Gruss, 1998; Manuel *et al.*, 2015). The neuron-specific class III β-tubulin (Tuj1) marked immature post-mitotic neurons migrating outwards from the rosettes (**Figure 3.2B**). The fact that Pax6 was not detected in the nuclei of $Tuj1^{+}$ cells demonstrated that when a neuron was produced from a radial glia division, the progenitor identity was lost. The same staining conducted at a later time point also revealed that Pax6 expression is gradually reduced as neurons mature in culture (data from day 45 staining, not shown). The specific mitosis-marker phospho-histone H3 (pHH3) allows for easy detection and quantification of cells in M-phase of the cell cycle (Hendzel *et al.*, 1997). This marker revealed a predominantly apical location of cells undergoing mitosis in rosettes (**Figure 3.2C**). The intermediate progenitor subtype can be distinguished from the radial glia and outer radial glia progenitor subtypes by their expression of the transcription factor Tbr2 (Florio and Huttner, 2014; Manuel *et al.*, 2015) (**Figure 3.2D**). Therefore, when considered together, the Pax6 and Tbr2 positive labelling in rosettes indicated that the cultures produced at least two subtypes of cortical neural progenitors that have the potential to give rise to excitatory cortical neurons.

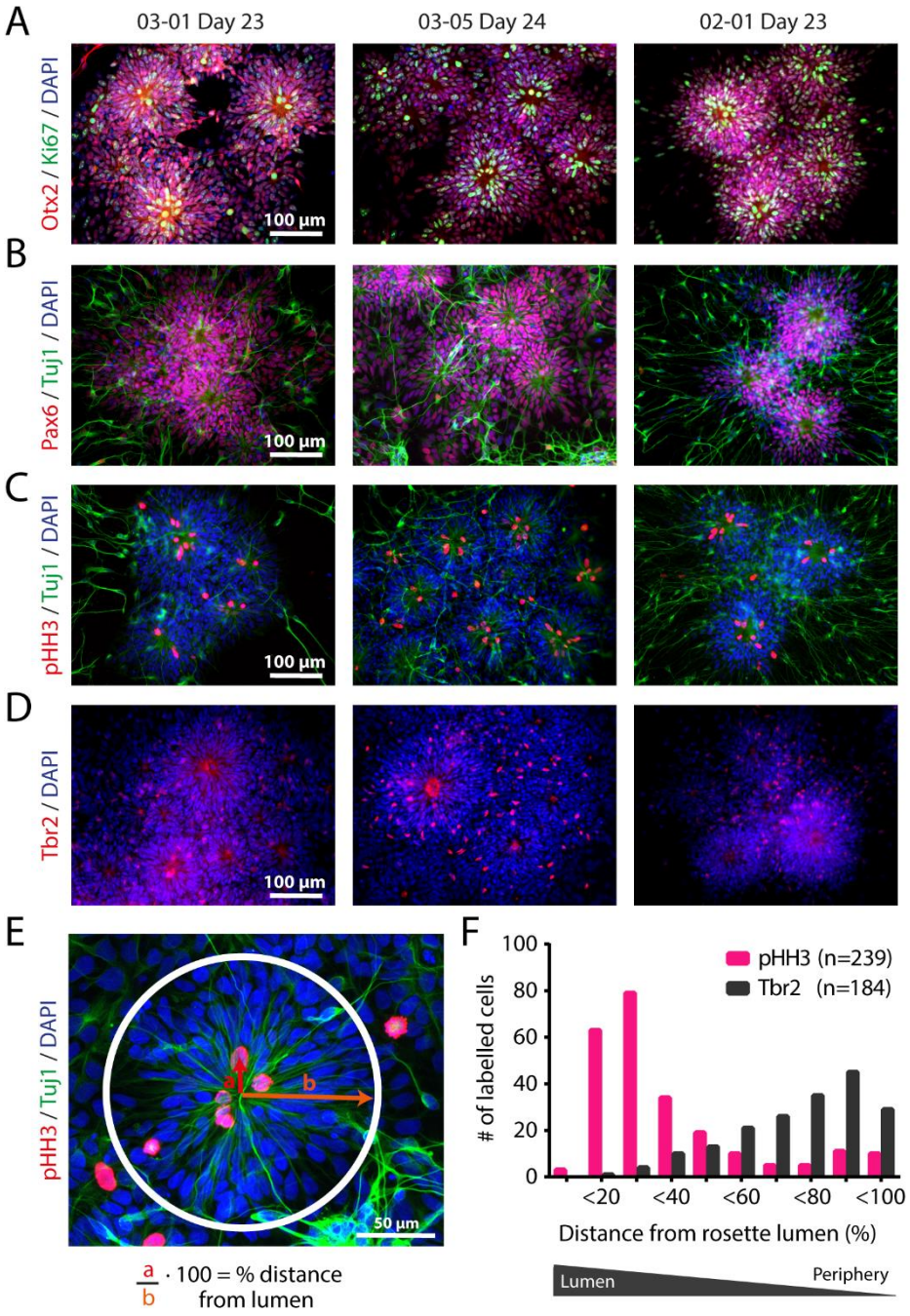

Figure 3.2 Cortical differentiation captures aspects of embryonic progenitor behaviour *in vivo*

(A) Rosettes derived from three healthy control iPSC lines (03-01, 03-05 and 02-01) were immunolabelled at approximately day 25 after induction. All cell lines formed polarised rosettes of cortical neural progenitors (Otx2$^+$), many of which were undergoing proliferation (Ki67$^+$). **(B)** Rosettes were predominantly comprised of the main cortical progenitor-subtype, radial glia (Pax6$^+$), and neurons (Tuj1$^+$) migrating away from the rosette. **(C)** Most mitoses occurred close to the lumen of rosettes (pHH3$^+$). **(D)** Rosettes also contained a population of intermediate cortical progenitors (Tbr2$^+$). All nuclei were stained with DAPI. **(E)** The locations of cell soma were defined as a percentage distance from the lumen of their rosette. **(F)** The majority of pHH3$^+$ mitoses occurred close to the lumen of rosettes, whereas the Tbr2$^+$ intermediate progenitors were mainly located towards the periphery of rosettes (n=239 pHH3$^+$ cells from 60 rosettes, n=184 Tbr2$^+$ cells from 41 rosettes).

Mitosis amongst radial glia has been reported to take place in the VZ of the embryonic brain, whereas intermediate progenitors and outer radial glia have been reported to divide within the SVZ (Paridaen and Huttner, 2014). These zones can be equated to the apical lumen and basal outer edge of rosettes, respectively (Kelava and Lancaster, 2017), and I was able to capture a similar arrangement of mitosis by quantifying the distribution of $pHH3^+$ and $Tbr2^+$ nuclei from the rosette lumen (see section 2.3.2) (**Figure 3.2E** and **F**). This analysis was conducted from two separate inductions, each from a different cell line. The results show that the vast majority of $pHH3^+$ mitoses occurred within 10-30% of the distance from the lumen to the outer edge of rosettes, consistent with the reported ventricular zone location of radial glia in M-phase. Conversely, $Tbr2^+$ cells were dispersed throughout the area between 30-100% from the lumen, with a peak at 80-90%. Although this more basal location of Tbr2 staining does not directly demonstrate that the intermediate progenitors also divide here, previous work has indicated that these progenitors remain within the SVZ, whereas radial glia are known to perform interkinetic nuclear migration in order to divide at the VZ surface (Florio and Huttner, 2014; Paridaen and Huttner, 2014).

The diverse progenitor pool of the developing cortex is believed to give rise to the neuronal populations of six cortical layers in a characteristic inside-out sequential manner (Rakic, 1975; Kadoshima *et al.*, 2013; Livesey *et al.*, 2015). To investigate if cortical neurons derived from iPSCs recapitulate this time-dependent layer formation, cultures were immunolabelled for cortical markers at different time points. Transcription factors T-box brain-1 (Tbr1) and COUP-TF-interacting protein-2 (CTIP2) are regarded as markers of layers VI and V, respectively (Molyneaux *et al.*, 2007), and were detected in the cultures at ~45

days after the initiation of neural induction (**Figure 3.3A**). Tbr1 and CTIP2 staining was quantified from images taken of dual-labelled cultures, using image thresholding (see section 2.3.2) (Tbr1: 30 ± 7%, n=10 fields of view (FOV); CTIP2: 41 ± 6%, n=10 FOV; from 3 inductions, 3 cell lines) (**Figure 3.3B**). The deeper cortical layer markers did indeed appear first, as the upper layer marker special AT-rich sequence-binding protein-2 (SatB2) (Molyneaux *et al.*, 2007), was barely detected at this time point (SatB2: 1 ± 0.1%, n=11 FOV; CTIP2: 40 ± 7%, n=11 FOV; from 4 inductions, 3 cell lines) (**Figure 3.3C** and **D**). Instead, distinct SatB2^{+} labelling was observed at ~70 days (SatB2: 8 ± 1%, n=12 FOV; CTIP2: 37 ± 4%, n=12 FOV; from 3 inductions, 3 cell lines) (**Figure 3.3E** and **F**). Spatial layer organisation is not expected in 2D dissociated cultures due to the lack of juxtacrine signals from surrounding cells. Consistent with this idea, the layer markers typically displayed a 'salt-and-pepper' like distribution where cells were intermixed, with low levels of dual expression of different markers. Although some areas of cultures did appear to be organised in a layer-like fashion, with layer markers located in distinct opposition to each other (see labelling from 03-05 and 02-01 on **Figure 3.3A** and 02-01 on **3.3E**). In summary, these observations demonstrate that cortical neurons derived from iPSCs undergo a sequential differentiation, reminiscent of the *in vivo* inside-out formation of cortex.

The cortical induction and differentiation protocol adopted here has been reported as producing exclusively glutamatergic neurons (Shi, Kirwan and Livesey, 2012). However, the traditional view that interneurons migrate into the cortex from their birthplace in the ganglionic eminences (Molyneaux *et al.*, 2007; Hansen *et al.*, 2013; Mertens *et al.*, 2016) has been challenged by the detection of interneuron progenitors within neocortical ventricular and

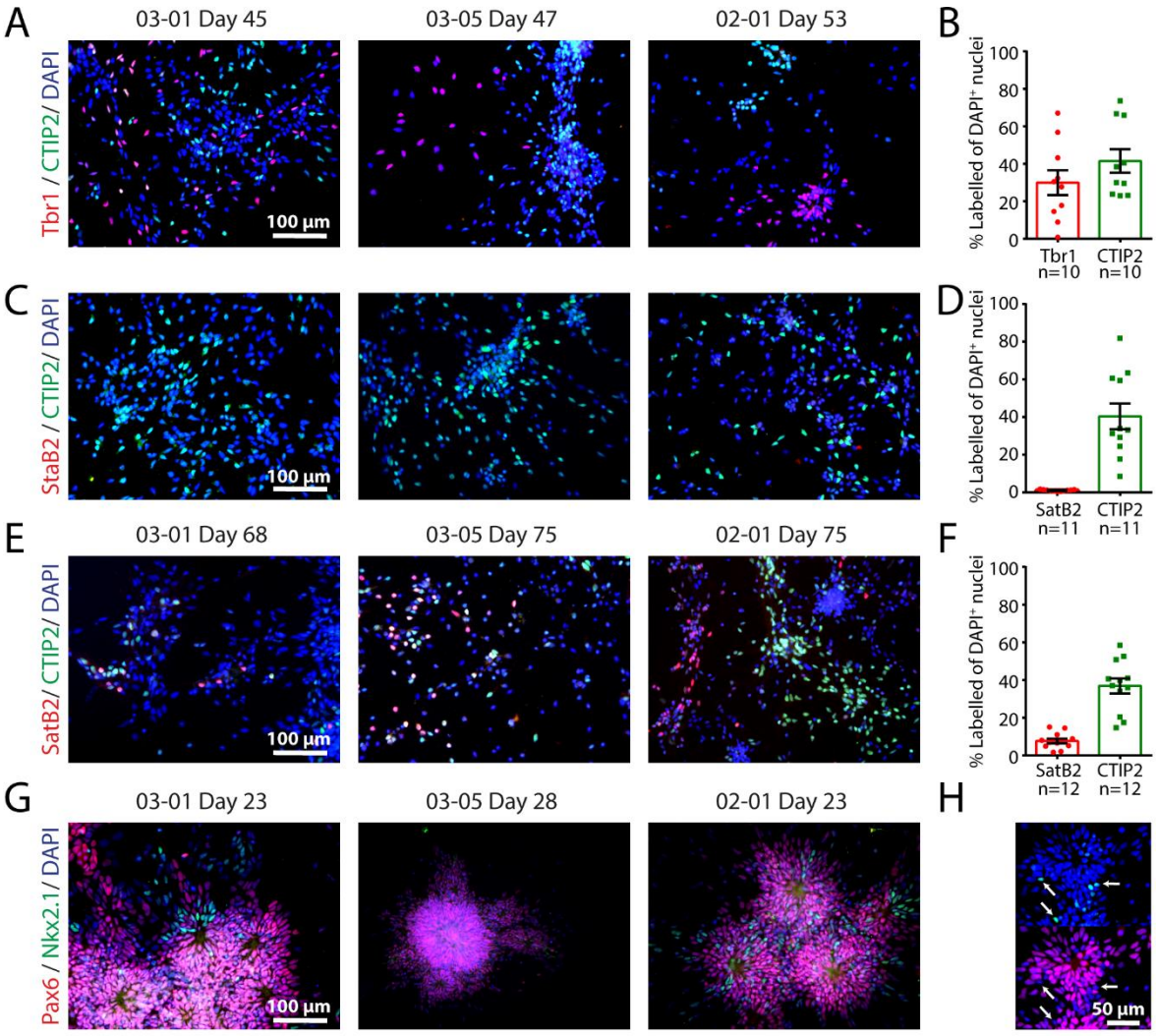

Figure 3.3 iPSC-derived neurons display appropriate markers of cortical development
Markers of cortical layers appeared in a time-dependent manner, consistent with the inside-out formation of the cortex *in vivo*. Dissociated cortical neuronal cultures were immunolabelled at different time points during maturation. **(A)** Deeper layer markers Tbr1 (layer VI) and CTIP2 (layer V) were detected at day ~45 from neural induction. **(B)** Quantification of the proportions of Tbr1$^+$ and CTIP2$^+$ cells, relative to DAPI nuclei at day ~45 (n=10 FOV). **(C)** Conversely, the upper layer marker SatB2 (layers II-IV) was rarely observed in the same cultures. **(D)** Quantification of the proportions of CTIP2$^+$ and SatB2$^+$ cells, relative to DAPI nuclei at day ~45 (n=11 FOV). **(E)** The upper layer marker SatB2 was detected from day ~70, alongside CTIP2 staining. **(F)** Quantification of the proportions of CTIP2$^+$ and SatB2$^+$ cells, relative to DAPI nuclei at day ~70 (n=12 FOV). **(G)** In some inductions (e.g. 03-01, 02-01), a proportion of Nkx2.1$^+$ interneuron progenitors was detected amongst Pax6$^+$ radial glia in rosettes at day ~25, whereas other inductions were Nkx2.1 negative (e.g. 03-05). **(H)** Nkx2.1 labelling (arrows) appeared to be mutually exclusive from Pax6 labelling.

subventricular zones of human embryonic brains (Letinic, Zoncu and Rakic, 2002; Jakovcevski, Mayer and Zecevic, 2011; Zecevic, Hu and Jakovcevski, 2011). I was therefore interested in investigating whether this protocol might also generate interneuron progenitors. By staining rosettes for the interneuron progenitor marker NK2 Homeobox 1 (Nkx2.1), I indeed detected the presence of small numbers of interneuron progenitors in some inductions (**Figure 3.3G**). Nkx2.1 and Pax6 staining was mutually exclusive, such that Nkx2.1 was only detected in Pax6-negative progenitor cells, and vice versa (**Figure 3.3H**). The expression of Nkx2.1 was not cell-line dependent, but rather induction dependent, with some inductions displaying expression in a subset of rosettes, and other inductions being completely devoid of Nkx2.1 (for example the 03-05 induction shown in **Figure 3.3G**). As no inductions expressed more than 20% Nkx2.1$^+$ interneuron progenitors, none were excluded from subsequent experimentation.

The data shown so far has confirmed that iPSCs can be reliably driven towards a cortical fate, that different progenitor pools can emerge, and that aspects of the inside-out layer formation are re-capitulated. I next set out to assess the functional properties of the human iPSC-derived cortical neurons generated, using electrophysiological recordings performed on single cells (see section 2.4.1 and 2.4.2). Hallmarks of neuronal excitability are the initiation of fast, inward VGNa$^+$ currents and all-or-none APs (Chinchalongporn *et al.*, 2015). I used measures of maximum VGNa$^+$ current size, the ability to sustain APs and AP initiation threshold to assess basic neuronal functionality and maturity. In addition, passive membrane properties can also provide an indication of neuronal maturity. In particular, membrane capacitance (Cm) offers a proxy measure for membrane surface area, with higher

values indicating more dendritic branches, lower membrane resistances (Rm) reflecting greater levels of ion channels within the membrane, and lower resting membrane potentials (Vm_{rest}) have been associated with maturity in human neurons (Westerlund *et al.*, 2003; Prè *et al.*, 2014; Bardy *et al.*, 2016).

Prior to experimentation, NPCs were seeded onto poly-L-ornithine and laminin (P+L) coated glass coverslips and matured for a further 50-80 days (see section 2.2.6). Whole-cell patch-clamp recordings were performed at an average age of 92 ± 3.3 days (range 79-117 days) from the time that dual SMAD inhibition was initiated (**Figure 3.4A**). This age was selected based on evidence that electrophysiological properties of iPSC-derived neurons mature with time in culture (Prè *et al.*, 2014). The depolarising phase of APs require the opening of rapidly inactivating $VGNa^+$ channels, whereas the re- and hyper-polarising phases rely on a combination of fast and slowly inactivating K^+ channels. These inward $VGNa^+$ and outward K^+ currents were initiated in iPSC-derived neurons using the voltage-clamp configuration and $VGNa^+$ currents could be blocked by tetrodotoxin (TTX) (**Figure 3.4B**). Initiation of $VGNa^+$ and integrated at its soma. This integration of inputs was imitated by the injection of series currents, and ultimately APs, occur as a function of the synaptic inputs received by a neuron of depolarising current steps in the current-clamp configuration, and APs were initiated if the spike threshold was reached (**Figure 3.4B**). All of the recorded neurons possessed functional $VGNa^+$ channels, as all displayed $VGNa^+$ currents of varying magnitude (mean maximal $VGNa^+$ current: -1.7 ± 0.2 nA, n=21 neurons; from 3 cell lines, 4 inductions) (**Figure 3.4C**).

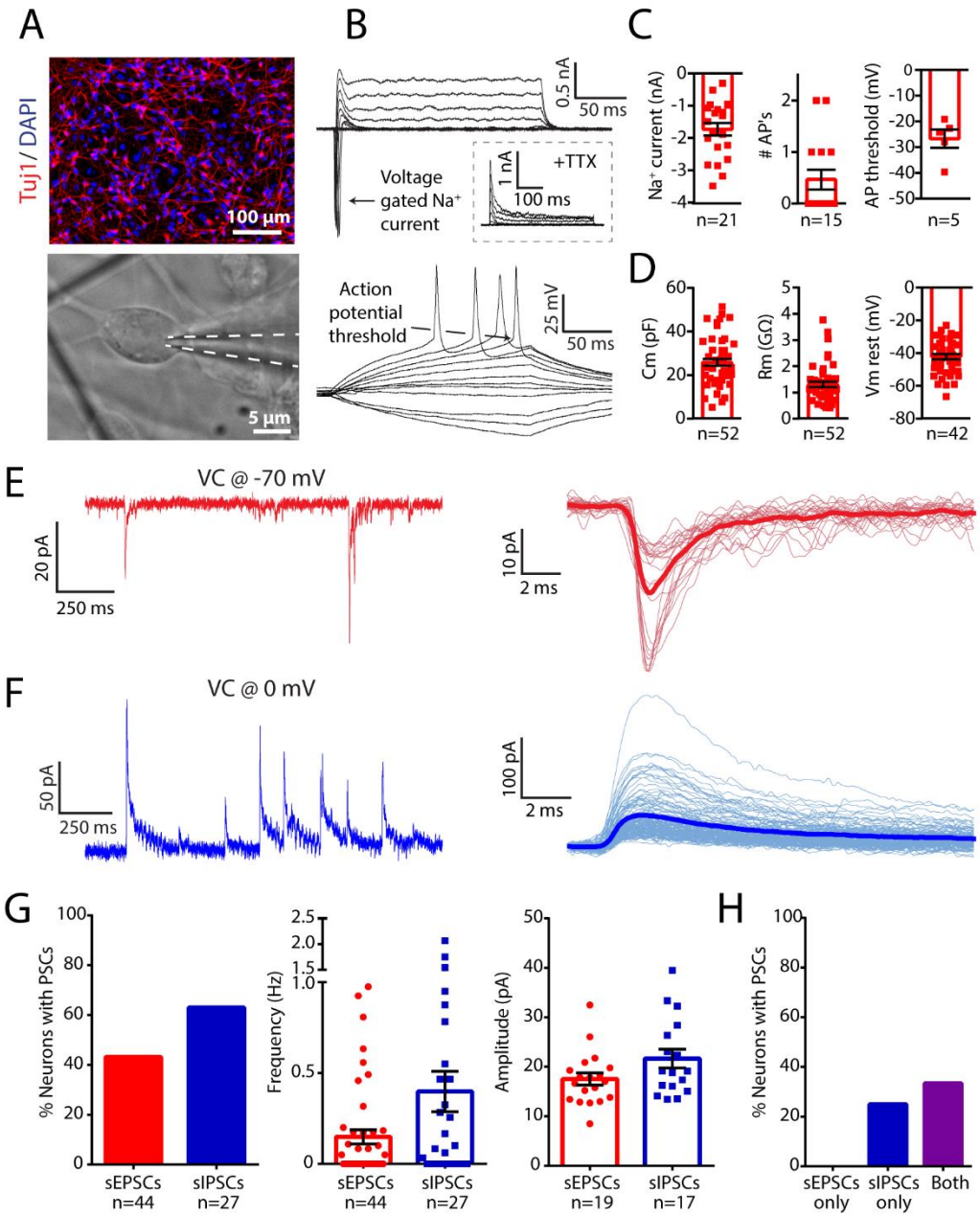

Figure 3.4 iPSC-derived neurons are electrophysiologically functional but immature

(A) Monocultures of human iPSC-derived cortical neurons (top) in which electrophysiological properties were assessed using whole-cell patch clamp recordings (bottom). **(B)** A series of voltage steps delivered from a holding potential of -70 mV elicited inward $VGNa^+$ currents (top), that were blocked by TTX (inset). The ability to fire APs was assessed in current clamp by injecting current steps (bottom). **(C)** Quantification of the active membrane properties: $VGNa^+$ currents, AP generation and AP threshold. **(D)** Quantifications of the passive membrane properties: membrane capacitance (Cm), membrane resistance (Rm) and resting membrane potential (Vm rest). **(E)** Spontaneous excitatory postsynaptic currents (sEPSCs) were assessed at a holding potential of -70 mV in voltage clamp mode. Traces show excerpts from a 1 min recording (left) and all detected events in that recording (right), with the average EPSC in bold. **(F)** Spontaneous inhibitory postsynaptic currents (sIPSCs) were assessed at a holding potential of 0 mV. Convention as in 'E'. **(G)** Proportion of neurons receiving sEPSCs and sIPSCs, the frequency of events within individual neurons, and the mean sEPSC amplitudes. **(H)** Breakdown of the proportions of neurons, in which recordings at both -70 mV and 0 mV were performed (n=24).

Nevertheless, only 33% (5 out of 15) of neurons recorded were capable of AP generation, exhibiting a maximum of 2 consecutive spikes per 200 ms (# APs: 0.5 ± 0.2 APs, n=15 neurons; from 3 cell lines, 3 inductions) (**Figure 3.4C**). The membrane potential threshold for AP initiation was measured at the inflection of the first AP generated by the cell (AP threshold: -26.7 ± 3.5 mV, n=5 neurons; from 2 cell lines, 2 inductions) (**Figure 3.4C**). The passive membrane properties of the neurons displayed values across rather wide ranges, as can be appreciated from the spread of data points and the interquartile range (IQR) reported below in addition to SEM, potentially reflecting neurons at different maturational stages within the cultures (Cm: 25.7 ± 1.6 pF, IQR=16.3, n=52 neurons; Rm: 1.3 ± 0.1 GΩ, IQR=0.7, n=52 neurons; Vm_{rest}: -42.1 ± 1.7 mV, IQR=17, n=42 neurons; from 3 cell lines, 5 inductions) (**Figure 3.4D**).

To assess the ability of the neurons to establish a functional, synaptically-connected network, spontaneous post-synaptic events were also recorded and quantified (see section 2.4.3). As the neurons were generated with a protocol tailored towards producing cortical glutamatergic neurons, assessing excitatory transmission was the main focus. However, switching the K^+ based internal solution to a Cs^+ based internal (see section 2.1.5) for a subset of recordings made it possible to assess both spontaneous inhibitory and excitatory post-synaptic currents (sIPSCs and sEPSCs, respectively) in the same cell (**Figure 3.4E** and **F**). In addition to being detected at each other's reversal potential, the faster kinetics of sEPSCs make them easily distinguishable from the slower sIPSCs (compare overlays in **Figure 3.4E** and **F**). To be classified as a cell that receives synaptic input from the network, a neuron had to average >1 post-synaptic current (PSC) per minute.

Quantification of the proportion of neurons receiving PSCs revealed that the majority of iPSC-derived cortical neurons (assessed from 3 cell lines, 5 inductions throughout) were synaptically immature in terms of excitatory transmission (sEPSCs: 43%, n=44; sIPSCs: 63%, n=27 neurons) (**Figure 3.4G**). The detection of a substantial proportion of neurons that received sIPSCs means that functional interneurons were present in the cultures, consistent with the Nkx2.1^{+} interneuron progenitors observed at the neural rosette stage. Across the population, the frequency of sIPSCs and sEPSCs was similar (sEPSCs: 0.15 ± 0.04 Hz, n=44 neurons; sIPSCs: 0.40 ± 0.11 Hz, n=27 neurons; p=0.054, un-paired Mann-Whitney test) (**Figure 3.4G**), and exhibited similar amplitudes (sEPSCs: 17.5 ± 1.2 pA, n=19 neurons; sIPSCs: 21.7 ± 1.9 pA, n=17 neurons; p=0.107, un-paired Mann-Whitney test) (**Figure 3.4G**). Interestingly, from the subset of 24 neurons where recordings were obtained both at -70 mV and at 0 mV within the same cell, it was observed that none of these cells received only sEPSCs, whereas a quarter received only sIPSCs, and a third displayed both sEPSCs and sIPSCs (sEPSCs only: 0%, sIPSCs only: 25%, Both: 33%, n=24 neurons) (**Figure 3.4H**). This suggests that at this stage of maturation, GABAergic synapses can be more common or active than glutamatergic synaptic connections.

Having established a protocol that generates functional, albeit immature cortical neurons, the derivation of human astrocytes from iPSCs was investigated. Cortical astrocytes arise from the same radial glia progenitors as neurons, but at a later stage in development when neurogenesis switches to gliogenesis (Kessaris, Pringle and Richardson, 2013; Paridaen and Huttner, 2014; Takouda, Katada and Nakashima, 2017). To recapitulate this aspect of *in vivo* corticogenesis, a common progenitor-pool of Pax6^{+} radial glia was used as the starting

point for the generation of iPSC-derived human cortical astrocytes (as depicted in **Figure 3.1**). As there is no specific marker of cortical astrocytes, I was forced to make the assumption that the regional patterning that applies to the cortical neuronal differentiation would also apply to astrocytes (Hochstim, Deneen, Lukaszewicz, Zhou and David J Anderson, 2008; Krencik *et al.*, 2011; Liu and Zhang, 2011). To first obtain a radial glia progenitor pool from which both an induction of neurons and of astrocytes could originate, the iPSCs were treated exactly as during the neuronal differentiation protocol, modified from Shi et al. (2016b), up until day 17-25, when NPC-producing rosettes had formed (**Figure 3.5A**). The media fed to the population of $Pax6^+$ rosette-organised radial glia was then switched to AstroDiff (Stemcell technologies) (see section 2.2.4). A change in morphology of the cells arising from the rosettes was observed within a few days in AstroDiff, such that flatter, more amorphous cells became evident.

However, the markers S100β and GFAP, which are known to be expressed by astrocytes (Ludwin, Kosek and Eng, 1976), were sparsely expressed at these early astrocyte progenitor stages (<40 days; **Figure 3.5B**). These morphological changes became more obvious as the rosettes were dissociated to single cells and plated at lower density. Lower plating density, along with trituration of the cell suspension, served to gradually select for astrocytic cells, consistent with reports that a lower density is tolerated by astrocyte progenitors but promotes apoptosis in NPCs (Barnabé-Heider and Miller, 2003), and that trituration reduces the neurogenic potential of the cultures undergoing transition from neuro- to glio-genesis (Krencik and Zhang, 2011).

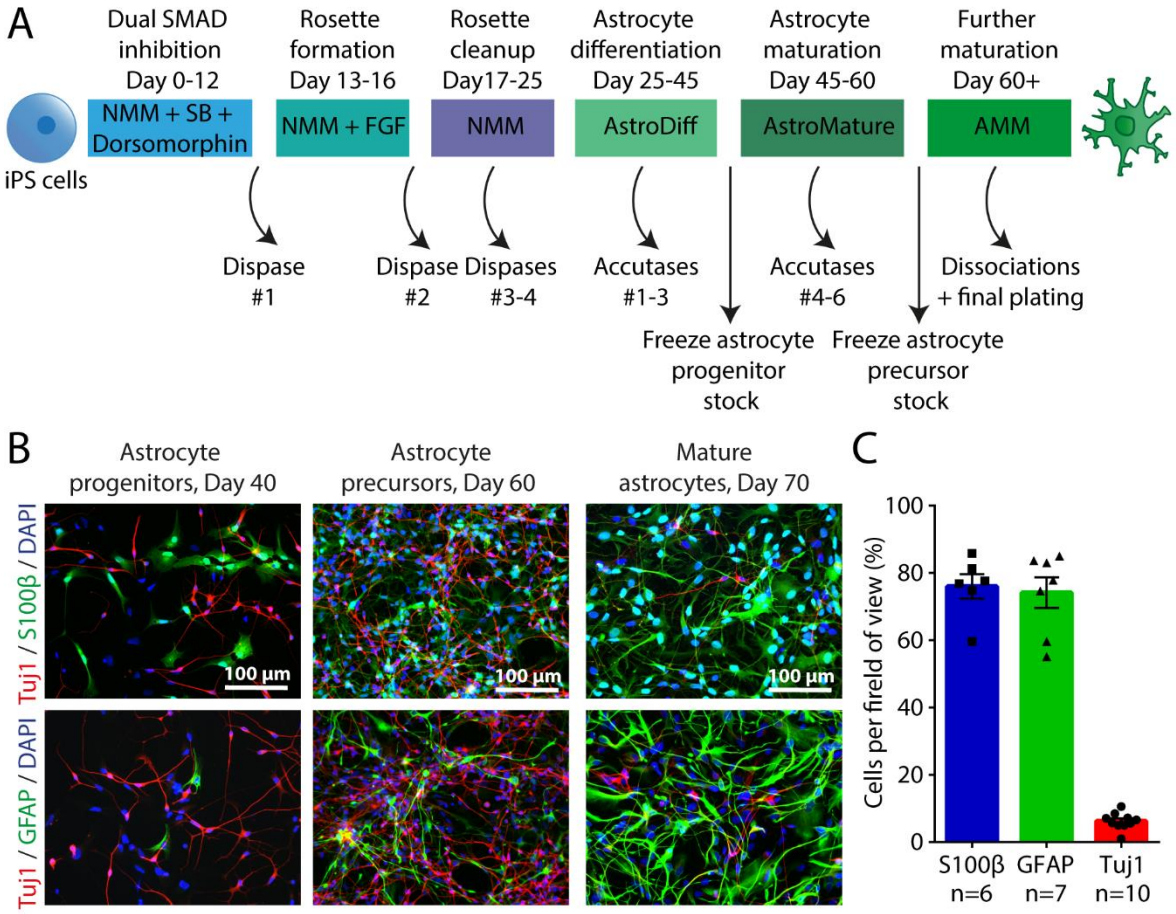

Figure 3.5 Protocol for generating mature human astrocytes from iPSCs
(A) Astrocyte differentiation protocol, modified from the proprietary "Astrocyte Differentiation" and "Astrocyte Maturation" protocols from Stem Cells Technologies. Up to day 17-25, the iPSCs are induced with dual SMAD inhibition, the resulting neuro-epithelial sheet is broken up with dispase, and rosette formation is stimulated with FGF, as for neural inductions following Shi et al. (2012b). Around day 25, NMM is switched to astrocyte differentiation media (AstroDiff), and cells are subsequently dissociated to single cells with accutase once per week for ~20 days. Stocks of proliferative astrocyte progenitors can be frozen and cryostored in liquid nitrogen before switching to astrocyte maturation media (AstroMature) around day 45. Weekly dissociations and seeding at lower density yield a population of less proliferative astrocyte precursors, which can also be frozen and cryostored. Further maturation is achieved by switching the media to AMM around day 60, in which astrocytes can be finally plated and maintained for experimentation. NMM: Neural Maintenance Media, AMM: Astrocyte Maintenance Media. **(B)** The increasing expression of the astrocytic markers S100β and GFAP could be tracked throughout the protocol, and was matched by a gradual disappearance of Tuj1$^+$ neurons. At the astrocyte progenitor stage around day 40, Tuj1$^+$ neurons were prevalent and S100β levels were higher than GFAP (left). Astrocyte precursors at day 60 also displayed more S100β staining than GFAP, and Tuj1$^+$ neurons were still prominent (middle). By the mature astrocyte stage at day ~70, GFAP expression levels were equivalent to S100β, whilst Tuj1$^+$ neurons were at very low levels (right). **(C)** The proportion of S100β$^+$, GFAP$^+$ and Tuj1$^+$ cells were quantified from 3 different cell lines and a total of 10 FOV at the mature stage of the protocol.

At this stage, the astrocyte progenitors were found to be highly proliferative and could be frozen down as progenitor stocks. This enabled the maturation of one vial at a time when required for experiments. Switching to AstroMature media around 45 days and performing further dissociations to distribute cells at lower densities over the next ~15 days served to enhance the proportions of cells committing to an astrocytic fate by ~60 days (**Figure 3.5B**). S100β appeared to be more abundant than GFAP at this astrocyte precursor stage, consistent with previous reports on astrocyte differentiation in dissociated mouse and human iPSC cultures (Barnabé-Heider *et al.*, 2005; Zhao *et al.*, 2017). All iPSC lines were treated similarly during the modified Stemcell Technologies protocol, but differences were observed at the final maturation stage in terms of proliferation propensity and the time required for purifying the astrocyte population. All cell lines displayed an enrichment for putative astrocytes after a further 10-20 days in astrocyte maintenance media (AMM) (**Figure 3.5B**) (see section 2.1.4), where the proportions of cells staining positive for S100β, GFAP and Tuj1 were quantified as percentages of the total number of $DAPI^+$ nuclei from triple and quadruple labelled cultures (S100β: 76%, n=6 FOV, GFAP: 74%, n=7 FOV, Tuj1: 6%, n=10 FOV; from 2 inductions, 2 cell lines) (**Figure 3.5C**) (see section 2.3.2). At 70-80 days after dual SMAD inhibition was initiated, cell proliferation was minimal, as expected of post-mitotic mature astrocytes (Zhang *et al.*, 2016).

Having demonstrated with immunolabelling that the adapted protocol generated cells expressing markers of an astrocytic fate, I next investigated the functional properties of the cells. There is consensus that astrocytes can be distinguished from neurons on properties such as the inability to generate APs and having smaller $VGNa^+$ current densities (Barres *et*

al., 1989). However, displaying small $VGNa^+$ currents and being unable to generate APs would also be true of an immature neuron (Zhou and Hablitz, 1996; Picken Bahrey and Moody, 2003), so it was important to examine further variables that distinguish astrocytes from neurons, such as a more hyperpolarised Vm_{rest}, larger membrane area and higher permeability (Wang and Bordey, 2008). To compare the intrinsic properties of human astrocytes to those already obtained in human neurons; the same measures were recorded from enriched human astrocyte cultures (**Figure 3.6A**) (see details of patching strategy in section 2.4).

Firstly, at a population level, the voltage step profiles of human astrocytes differed strikingly from those of neurons in terms of the effective absence of rapid, inward $VGNa^+$ currents (neurons: -1.7 ± 0.2 nA, n=21 cells; from 3 cell lines, 4 inductions; astrocytes: -0.18 ± 0.03 nA, n=47 cells; from 4 cell lines, 5 inductions; $p<0.0001$, unpaired Mann-Whitney test) (**Figure 3.6B** and **C**). Secondly, the astrocytes were unable to generate APs, which was confirmed by depolarising the membrane potential to 0 mV (**Figure 3.6B**). Thirdly, the human astrocytes had larger membrane surface areas, as reflected by the proxy of membrane capacitance (neurons: 25.7 ± 1.6 pF, n=52 cells; from 3 cell lines, 5 inductions; astrocytes: 145.4 ± 32.5 pF, n=59 cells; from 4 cell lines, 5 inductions; $p<0.0001$, unpaired Mann-Whitney test) (**Figure 3.6C**), and the membranes of astrocytes were significantly more permeable, as reflected by lower membrane resistances (neurons: 1.3 ± 0.1 GΩ, n=52 cells; from 3 cell lines, 5 inductions; astrocytes: 0.39 ± 0.04 GΩ, n=59 cells; from 4 cell lines, 5 inductions; $p<0.0001$, unpaired Mann-Whitney test) (**Figure 3.6C**).

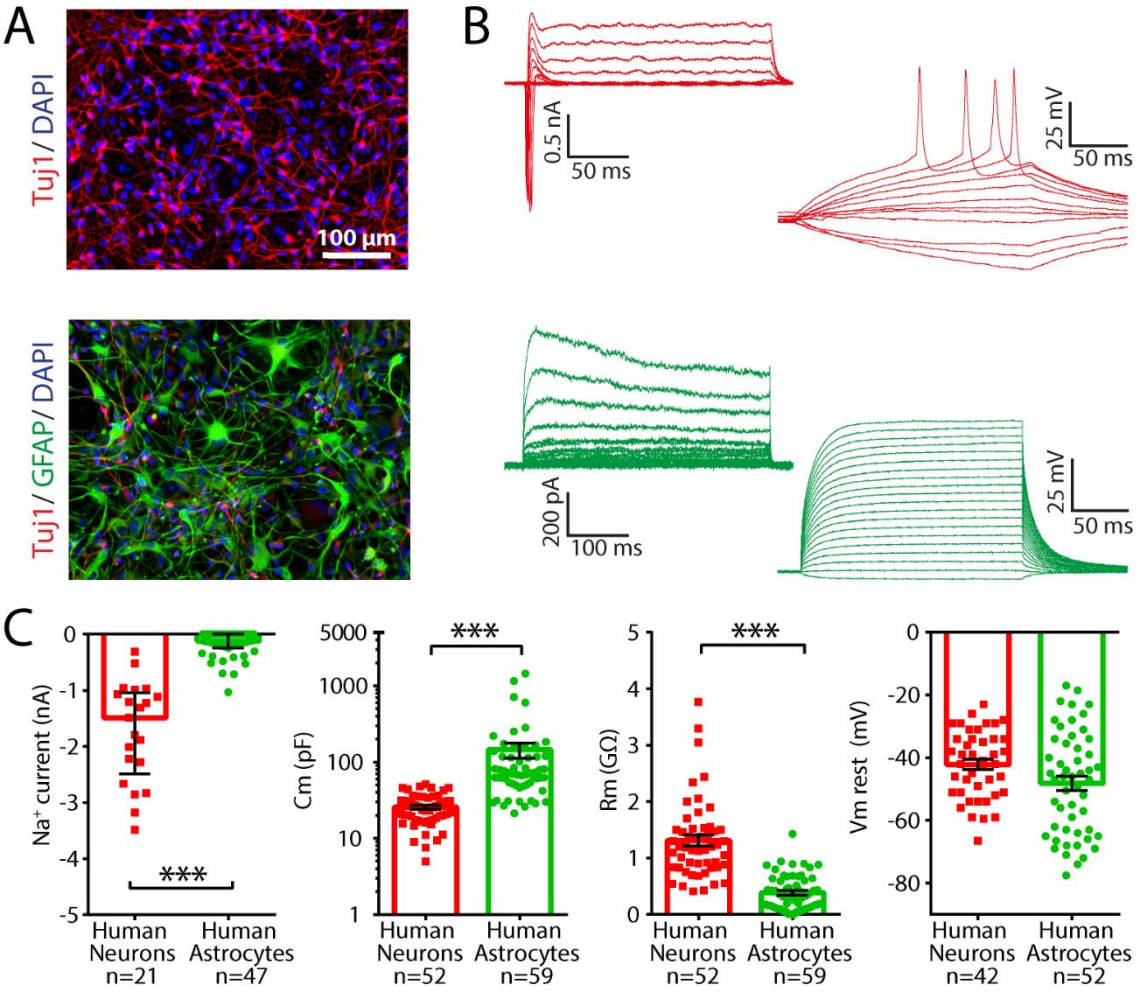

Figure 3.6 iPSC-derived human astrocytes are electrophysologically distinct from iPSC-derived neurons

Whole-cell patch clamp recordings from monocultures of human neurons (data from **Figure 3.4**) or human astrocytes revealed that their intrinsic properties were significantly different. **(A)** Immunofluorescence images show a neuronal monoculture (top) stained for Tuj1 and an astrocyte monoculture (bottom) stained for Tuj1 and GFAP. **(B)** Example traces of voltage steps (left) and current steps (right), which elicited VGNa$^+$ currents and action potentials in neurons (top), but only outward currents and passive membrane potentials in astrocytes (bottom). **(C)** All neurons displayed inward, VGNa$^+$ currents, meanwhile the majority of astrocytes either lacked these currents or they were below 1 nA in amplitude. Human astrocytes had significantly higher membrane capacitances (Cm) and lower membrane resistance (Rm). The astrocytes rested at similar membrane potentials to the neurons (Vm rest). * $p < 0.05$, ** $p < 0.01$, *** $p < 0.001$

Lastly, the distributions of Vm_{rest} measured from the two cell-types turned out not to be significantly different and the groups shared a large overlap (neurons: -42.1 ± 1.7 mV, n=42 cells; from 3 cell lines, 5 inductions; astrocytes: -48.2 ± 2.3 mV, n=52 cells; from 4 cell lines, 5 inductions; p=0.063, unpaired Mann-Whitney test) (**Figure 3.6C**).

Besides having different intrinsic membrane properties, another feature of astrocytes is the degree to which they exhibit gap-junction coupling. While gap-junctions between neurons tend to be a feature of early development (Sutor and Hagerty, 2005), astrocytes remain gap-junction connected and form a physically connected syncytium, specialised for inter-cell communication via diffusion (Theis *et al.*, 2005). To examine whether the human astrocytes generated were connected via gap-junctions, I revealed coupled cells by filling a patched astrocyte with the small gap-junction permeable molecule biocytin (biocytin ≈ 0.37 kDa) (**Figure 3.7A**) (see section 2.4.4). Over a period of 10-20 minutes, while other electrophysiological recordings were conducted, biocytin spread to an average of 61 ± 18 cells (**Figure 3.7B;** n=5 clusters; 1 cell line, 1 induction), many of which were subsequently revealed to be $GFAP^+$ (**Figure 3.7A**), thus confirming the presence of gap-junctions between the human astrocytes.

The syncytium of astrocytes is vital to ion homeostasis and one of its main functions is to efficiently clear excess K^+ and neurotransmitters, such as glutamate (Wang and Bordey, 2008; Kimelberg and Nedergaard, 2010). Astrocytic glutamate transport is primarily conducted via EAAT1 and particularly EAAT2. These transporters rely on the electrochemical gradient of Na^+ and co-transport three Na^+ ions and one H^+ ion into the cell, with each glutamate molecule, plus one K^+ ion out of the cell (Grewer and Rauen, 2005).

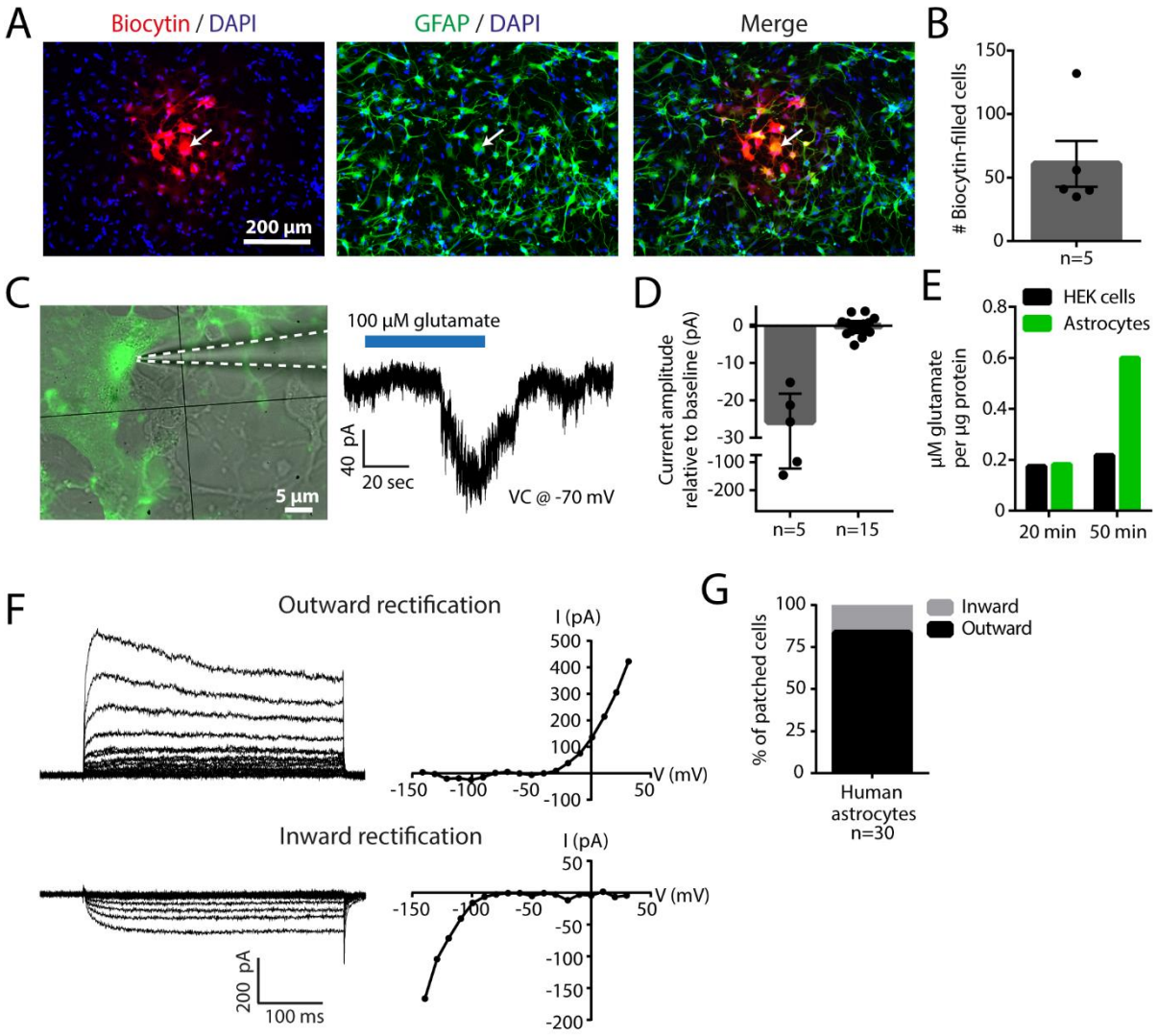

Figure 3.7 Human astrocytes exhibit appropriate functional properties
(A) Clusters of gap-junction connected human astrocytes were revealed by filling a patched astrocyte with biocytin (arrow). **(B)** The cluster size for gap-junctional connected cells was quantified from immunolabelling with streptavidin (n=5 clusters). **(C)** The capacity of individual astrocytes to take up glutamate from the extracellular space was assessed by whole-cell patch clamp recording (left). Inward current generated by bath-application of 100 µM L-glutamate for 1 minute (right), signifying the uptake of glutamate by the astrocyte. **(D)** A clear inward current was detected in 5 out of 20 putative astrocytes. The amplitude was defined as the maximal shift in holding current upon glutamate application. **(E)** At the population level, human astrocytes were capable of higher rates of glutamate uptake than HEK293 cells, as measured with an enzymatic absorbance assay. Concentrations of glutamate in the media were measured at Δt=20 min and 50 min, and samples were normalised to the amount of protein. **(F)** Example voltage-gated outward rectifying K^+ currents (top trace and IV plot), or inward rectifying K^+ currents (bottom trace and IV plot), elicited by subjecting an astrocyte to a series of voltage steps. **(G)** The direction of K^+ currents measured in patched human astrocytes was mainly outward, yet 5 out of 30 putative astrocytes (17%) displayed inward rectification.

Since the net flux of this transport is inward and positive, the activity of glutamate transporters can be detected as a positive (inward) current in astrocytes (see for example (Dallas *et al.*, 2007)). To investigate if this behaviour could be detected in individual human astrocytes, I bath applied 100 µM L-glutamate to whole-cell patched astrocytes for 1-2 minutes, before returning to normal ACSF (**Figure 3.7C**) (see section 2.4.5). Inward currents with maximal amplitudes of -61.5 ± 26.1 pA relative to baseline were recorded in 5 out of 20 astrocytes (from 4 cell lines, 4 inductions) (**Figure 3.7D**).

This sensitive, but low throughput, assay indicated that a subset of individual astrocytes was capable of glutamate uptake. To assess the capacity of human astrocytes to clear glutamate from their environment at a population level, I performed an enzymatic glutamate uptake assay (see section 2.3.9 and 2.1.11), in which human astrocyte and human embryonic kidney (HEK293) cell cultures were incubated in a solution of 50 µM L-glutamate. Media samples taken from the two cell types at defined time points revealed that the glutamate uptake capability of the iPSC-derived human astrocytes was ~3-fold greater than that of HEK293-cells, consistent with the conclusion that the astrocytes are able to transport glutamate (**Figure 3.7E**). Glutamate uptake is classically regarded as an indication of functional maturity in astrocytes, but another key astrocytic homeostatic function is K^+ uptake and spatial buffering. Following neuronal AP transmission, the presynaptic neuron re-polarises by K^+ efflux into the extracellular space, which needs to be cleared away in order to maintain neuronal excitability. For this purpose, astrocytes express both energy-driven transporters like the Na^+/K^+ ATPase that responds to changes in ion-concentrations, as well as voltage-gated K^+ channels that respond to membrane depolarisation (Cheung *et al.*, 2015).

In particular, the inward-rectifying K^+ channel $K_{ir}4.1$ has been found to play a crucial role in K^+ uptake in a proportion of mature astrocytes, which is in accordance with its higher propensity to allow K^+ influx at more hyperpolarised resting membrane potentials (Higashi *et al.*, 2001; Schröder *et al.*, 2002; Higashimori and Sontheimer, 2007; Kucheryavykh *et al.*, 2007).

To investigate the extent to which the iPSC-derived human astrocytes displayed such inward rectifying K^+ currents, patched astrocytes were subjected to a voltage step protocol ranging from -140 mV to +30 mV and the resulting leak-subtracted current-voltage (I-V) relationships were plotted (**Figure 3.7F**). Most commonly, voltage-gated outward rectifying K^+ currents, resembling those ordinarily observed in neurons, were detected as positive deflections on the I-V plot, starting from when the threshold of the responsible channels was reached. In a subset of cases however, inward rectifying K^+ currents were detected as a negative deflection towards the hyperpolarised membrane potentials on the I-V plot (5 astrocytes = 17%, n=30; from 4 cell lines, 4 inductions) (**Figure 3.7F and G**). Out of the five astrocytes displaying inward rectification, two were also tested for glutamate uptake currents, and both cells displayed this property. Taken together, these results demonstrate that a proportion of the human astrocytes exhibited the K^+ and glutamate buffering capabilities associated with mature astrocytes.

3.3 Discussion

In this chapter I have capitalised on published protocols for deriving cortical neurons from human iPSCs (Chambers *et al.*, 2009; Shi, Kirwan and Livesey, 2012) via dual SMAD inhibition and without patterning, consistent with the idea that forebrain development is a default pathway (Wilson and Houart, 2004; Li *et al.*, 2009; Lupo *et al.*, 2014). The protocol

was then adapted to produce a common cortical progenitor pool, from which it was possible to generate both human cortical neurons and astrocytes from the same neural induction. The resulting protocols mimicked aspects of *in vivo* corticogenesis, in that the same radial glia progenitor pool is believed to firstly give rise to neurons, and then switch to astrogliogenesis (Kessaris, Pringle and Richardson, 2013; Paridaen and Huttner, 2014; Takouda, Katada and Nakashima, 2017). It is, however, unknown if all astrocytes have a radial glia origin or to what extent intermediate astrocyte-restricted progenitors are involved (Y. Liu *et al.*, 2004; Kessaris, Pringle and Richardson, 2013). Nevertheless, deriving astrocytes from the same non-patterned cortical progenitor pool is in line with the regional patterning principle, whereby regional specification of the neuronal progenitor pool determines the regional patterning of the subsequently derived astrocytes (Liu and Zhang, 2011).

By performing quality control immunostaining of cortical rosettes, it was verified that neural inductions of several cell lines consistently produced a highly proliferative $Ki67^+$ and $Otx2^+$ cortical progenitor pool, which contains both $Pax6^+$ radial glia and $Tbr2^+$ intermediate progenitor subtypes. The product of neurogenic divisions of these progenitors was observed as $Tuj1^+$ neurons, migrating away from the lumen of rosettes. Furthermore, the overwhelmingly luminal location of $pHH3^+$ mitotic cells reflected the interkinetic nuclear migration behaviour of radial glia, which has been observed in similar stem cell derived systems (Kadoshima *et al.*, 2013; Ziv *et al.*, 2015). The $Tbr2^+$ labelling was also consistent with the SVZ location of intermediate progenitors (Florio and Huttner, 2014; Paridaen and Huttner, 2014). The nature of laminar formation during corticogenesis (Rakic, 1975; Kadoshima *et al.*, 2013; Livesey *et al.*, 2015) was recapitulated in part, as demonstrated with

cortical layers markers. Neurons were positive for deeper layer markers Tbr1 and CTIP2 at around 45 days from the initiation of neural induction, but almost completely negative for the upper layer marker SatB2 at this time point. Positive labelling for SatB2 was detected ~30 days later, signifying that the layer-specific neurons were born in a sequential, time-dependent manner. These results resemble those reported by Shi et al (2012b), who also observed little evidence for the spatial arrangement of cells according to layer identity. This is most likely a feature of the 2D culture system, which lacks the juxtacrine environmental cues, which are reported to be better captured by 3D organoid culture models (Srikanth and Young-Pearse, 2014; Mertens *et al.*, 2016; Kelava and Lancaster, 2017).

After maturing the enriched neuronal cultures to ~90 days from the time of neural induction, electrophysiological recordings revealed that the cells acquired features of functional neurons. However, although all neurons displayed $VGNa^{+}$ currents, many were smaller than 1 nA, which indicates a more immature phenotype (Zhou and Hablitz, 1996; Picken Bahrey and Moody, 2003). Consistent with this, only 33% were able to generate APs, with a maximum rate of only 2 consecutive APs per 200 ms. Taken together, the active properties of enriched human cortical neuronal cultures appear relatively underdeveloped. Few cells fire APs and a relatively low proportion (43%) of neurons receive spontaneous excitatory synaptic inputs. I therefore conclude that the iPSC-derived cortical neurons are functional, but immature. To provide greater context for these findings, I compared my recordings with the functional states described by Bardy and colleagues, who assessed iPSC-derived neurons according to a host of different electrophysiological measures across age ranges of 0-30 weeks (Bardy *et al.*, 2016). They provide a scale of 1-5, with higher numbers indicating greater maturation and overall,

my neurons would appear to fall within their "transitional state 3". In more detail, comparing the three active measures used in this thesis, three passive measures, as well as the proportion of neurons receiving sEPSCs and sEPSC frequency, my data compare to Bardy et al. (2016) in the following way:

Measure	**Mean value recorded in this thesis**	**Closest Bardy et al. (2016) category**	**Mean value for appropriate category**
Max $VGNa^+$ current	-1.7 nA	4	-1.66 nA
# consecutive APs	0.5 APs	1-3	0-1 AP
AP minimum threshold	-26.7 mV	1	-31 mV
Membrane capacitance	25.7 pF	3	25 PF
Membrane resistance	1.3 GΩ	5	1.44 GΩ
Resting membrane potential	-42.1 mV	3	-40 mV
Proportion of neurons with sEPSCs	43%	3	~35 %
sEPSC frequency	0.15 Hz	2	~0.1 Hz

With regards to synaptic activity, it was interesting to note that whilst less than half of the neurons (43%) received sEPSCs, 63% received inhibitory post-synaptic currents. Indeed, when I recorded both sEPSCs and sIPSCs within the same cell, no cells received only sEPSCs while 25% received only sIPSCs. Firstly, this suggests that the $Nkx2.1^+$ progenitors observed in some inductions are capable of giving rise to functional, GABA-releasing interneurons. Secondly, this data indicate that the human cortical neurons generated here display a tendency towards receiving proportionally more inhibitory activity at this maturational stage, which could be viewed as consistent with the early role of interneurons that has been described in rodent cortex (Ben-Ari *et al.*, 2004), where inhibitory synapses form before glutamatergic synapses (Hennou *et al.*, 2002).

This protocol has generated a similar proportion of interneurons when used by other members of my lab (unpublished results, Emma Whiteley, Louise Kay and Sarah Newey), as have similar published glutamatergic forebrain differentiation protocols that are also devoid of ventralising morphogens (Johnson *et al.*, 2007; Tang *et al.*, 2013; Weick *et al.*, 2013; Floruta *et al.*, 2017). The presence of interneurons may suggest that the dual SMAD inhibition protocol fails to achieve a 100% conversion rate in terms of producing progenitors associated with the dorsal telencephalon. A limited amount of endogenously arising SHH signalling could have induced the $Nkx2.1^{+}/Pax6^{-}$ progenitors detected (Liu and Zhang, 2011). Alternatively, these results may lend support to the hypothesis that the interneuron progenitor population in human cortex is more complex than in rodents, with origins outside the ganglionic eminences as well (Jakovcevski, Mayer and Zecevic, 2011; Zecevic, Hu and Jakovcevski, 2011) - a feature that could now be studied further using stem cell models.

An important achievement in this chapter is that I have demonstrated the feasibility of producing human astrocytes and neurons from the same cortical pool of radial glia progenitors. I achieved this by modifying proprietary astrocyte differentiation and maturation protocols in a manner that enabled me to: 1) start from rosettes rather than embryoid bodies, 2) successfully freeze cells mid-way through the protocol, and 3) devise a maintenance medium for further maturing the cells. Published protocols for deriving human astrocytes from iPSCs vary widely in timeframe, with 120+ days (Krencik and Zhang, 2011) or 500+ days (Sloan *et al.*, 2017) at one extreme, and 6-8 weeks (Serio *et al.*, 2013) or 5-6 weeks (Shaltouki *et al.*, 2013) reported at the other extreme. Tracking the appearance of astrocytic markers S100β and GFAP revealed that my cultures reached a stage of ~75% expression of both markers by

70-80 days, which puts the protocol used here among the shorter astrocytic differentiation methods. The gradual upregulation of S100β, followed by GFAP, occurred alongside the gradual disappearance of the neuronal marker Tuj1, in line with previous literature reporting S100β as an early astrocyte precursor marker (Barnabé-Heider *et al.*, 2005; Zhao *et al.*, 2017). It is worth noting that in addition to its historical status as the "gold standard" astrocyte marker, GFAP is also viewed as a marker of astrocyte reactivity (Eng, Ghirnikar and Lee, 2000; Zamanian *et al.*, 2012; Burda and Sofroniew, 2014). As such, the high levels of GFAP immunolabelling could indicate that the human astrocytes are leaning towards a reactive state rather than quiescence. This could be caused by the presence of FBS in the astrocyte maintenance medium, but has also been reported as an unavoidable feature of culturing cells *in vitro* (Zamanian *et al.*, 2012; Magistri *et al.*, 2016), in which case it is fair to compare these human astrocytes to rodent *in vitro* cultures of astrocytes, which commonly also include FBS in their media. See section 7.2.1 where this is further discussed.

When I tested the biophysical properties of the human astrocytes with whole-cell patch clamp recordings, I found them to differ greatly from the human neurons. The astrocytes were non-excitable in response to current injections and generated no APs. The astrocytes also exhibited larger membrane areas and lower membrane resistances, compared to the neurons. The 10-fold difference in maximum $VGNa^+$ current amplitude detected between the human neurons and astrocytes represented a striking difference between the two cell types. At the same time, approximately half of the astrocytes displayed some sign of a $VGNa^+$ current, consistent with reports that neuronal $VGNa^+$ channel subtypes (Nav1.2, Nav1.3, Nav1.5 and Nav1.6) can be expressed by astrocytes (Pappalardo, Black and Waxman, 2016).

The formation of gap-junction coupled astrocytic syncytia was confirmed by revealing the spread of biocytin from a patched astrocyte to its neighbours. The average cluster size (~60 cells) corresponded well to the value of up to 100 coupled cells reported *in vivo* (Sutor and Hagerty, 2005). This feature is critical for astrocytic responses to neuronal signalling, as it allows for the spatial buffering of glutamate and K^+ (Ozog, Siushansian and Naus, 2002; Wallraff *et al.*, 2006), ensuring repeated synaptic signalling and the prevention of excitotoxicity (Rothstein *et al.*, 1996; Marcaggi and Attwell, 2004). The uptake of these molecules depends on several mechanisms, of which I tested the EAAT1/2 mediated glutamate uptake and K^+ rectification. In line with a previous assessment of iPSC-derived human astrocytes (Krencik *et al.*, 2011), I found that at the population level, the astrocytes had a larger capacity for glutamate uptake compared to HEK293 cells. I extended these observations by also performing a single-cell electrophysiological assessment, which revealed that 25% of the astrocytes exhibited a glutamate-uptake associated current. This relatively low detection rate might not be surprising for three reasons: 1) although patch clamping a single astrocyte is a sensitive assay with which to detect individual glutamate-transport associated currents, it has been reported that about 10^5 EAAT molecules are required to generate a current comparable to a single typical ion-channel with a steady-state current of 1 pA (Grewer and Rauen, 2005). This would mean that the patch clamp technique may only reveal uptake in astrocytes with the highest levels of transporter expression. 2) If astrocytes are indeed in a reactive state as a result of the culture-conditions, glutamate uptake ability would be affected (Takahashi, Vargas and Wilcox, 2010; Robel *et al.*, 2015). 3) Evidence from mouse hippocampus suggests that there are two distinct categories of astrocytes, one of which displays functional glutamate transporters ('GluT cells') and another which, in contrast,

express glutamate receptors ('GluR cells') (Matthias *et al.*, 2003; Djukic *et al.*, 2007). If these categories apply to human cortical astrocytes, it would mean that not all putative astrocytes would be expected to show glutamate uptake.

The majority of the astrocytes displayed voltage-gated outward rectifying current behaviour, indicating that most possess delayed rectifier K^+ channels that are similar to those that serve to repolarise neurons after AP transmission. Interestingly, this K^+ current profile has been associated with the GluR category of astrocytes, which are thought to be incapable of glutamate uptake (Matthias *et al.*, 2003). In contrast, inward rectifying K^+ channels were identified in ~20% of the astrocytes, signifying that a subset possess the main mechanism for K^+ uptake from the synaptic cleft (Kucheryavykh *et al.*, 2007). Of the astrocytes that fell into this category, a subset were also tested for glutamate uptake and each of these cells also displayed a glutamate-uptake associated current, which is consistent with the GluT category of astrocytes (Matthias *et al.*, 2003). In summary, this data suggests that the human astrocytes I have generated include a subpopulation with a more mature phenotype that is reminiscent of the GluT-like category of astrocytes. This subpopulation is capable of buffering K^+ and glutamate, and can thus contribute to the homeostatic regulation of the neuronal environment.

Collectively, these data demonstrate that human cortical neurons and astrocytes can be reliably derived from iPSCs and that their identity and functionality in culture enriched for each cell type can be assessed molecularly and electrophysiologically. The overarching aim of this thesis is to investigate functional interactions between human cortical neurons and astrocytes, for which the establishment of human-based cellular models is crucial. Given the

importance of astrocytes for normal brain function and their involvement in various diseases, human iPSC-derived astrocytes are still relatively underused in the field. For this to become more common practise, the degree to which iPSC-derived astrocytes are physiologically credible needs to be established. To this end, the following chapter will investigate two hallmark astrocyte functions: Ca^{2+} activity and maintenance of ion homeostasis. Firstly, spontaneous and evoked Ca^{2+} elevations will be used as a functional readout of appropriate iPSC-derived human astrocyte activity, as astrocytes are expected to communicate with each other and neurons using Ca^{2+}. Secondly, the ability of iPSC-derived human astrocytes to respond to extracellular changes in ion concentrations, particularly during network activity, will be used to evaluate their potential for performing vital ion homeostasis when the extracellular environment is experiencing an imbalance.

Chapter 4

4 Ion homeostasis and dynamics in iPSC-derived human astrocytes

4.1 Introduction

Research using animal models has established that astrocytes possess a variety of mechanisms that enable them to detect, and then respond to, changes in their environment. These mechanisms often enable astrocytes to detect changes associated with neuronal activity, including increases in the levels of neurotransmitters in the extracellular space, or fluctuations in membrane potential that reflect the overall activity within a neuronal network. Many of the astrocytic responses to neuronal activity form part of homeostatic processes that prevent cellular damage and ensure normal function (see **Chapter 1**, section 1.3). Ion dynamics play a crucial role in the astrocytic response mechanisms, as they form part of the intracellular signal cascades that coordinate astrocytic response mechanisms, but they also represent a major route by which the astrocytes then exert their response upon the local environment. Indeed, astrocyte ion dynamics can oppose those observed in neurons, which is thought to reflect the close homeostatic interplay between the two cell types.

One of the most studied types of ion dynamics in astrocytes are intracellular Ca^{2+} signals. Since the earliest evidence that astrocytes are capable of "listening" to neuronal signalling, intracellular Ca^{2+} dynamics have been implicated (Pasti *et al.*, 1997; Lalo *et al.*, 2011). The direct application of neurotransmitters, or the release of neurotransmitters following neuronal stimulation, has been shown to generate membrane depolarisation in

astrocytes and induce intracellular Ca^{2+} elevations (Bowman and Kimelberg, 1984; Kettenmann, Backus and Schachner, 1984; Cornell-Bell *et al.*, 1990; Porter and McCarthy, 1996; Agulhon *et al.*, 2008; Lalo *et al.*, 2011). Intracellular Ca^{2+} dynamics are often viewed as a way for astrocytes to integrate synaptic transmission (Fellin and Carmignoto, 2004; Tian *et al.*, 2006; Oberheim *et al.*, 2009). Furthermore, many believe astrocytic Ca^{2+} signals to be required for reciprocal communication between astrocytes and neurons, with Ca^{2+} initiating exocytosis from astrocytes as part of gliotransmission (Halassa *et al.*, 2007; Perea and Araque, 2010; Panatier *et al.*, 2011; Navarrete *et al.*, 2013; Araque *et al.*, 2014; Gundersen, Storm-Mathisen and Bergersen, 2015). To achieve this, astrocytes express many of the same neurotransmitter receptor types as are found in neurons (Lalo *et al.*, 2011), and several mechanisms have been proposed for mediating astrocytic Ca^{2+} elevations (details in **Chapter 1**, section 1.4).

Dysregulation of Ca^{2+} signals is believed to be involved in several disorders including epilepsy, ischemia and AD, both in terms of basic astrocyte function and their interactions with neurons (Volterra and Meldolesi, 2005; Xiao, Tian and López-Schier, 2015; Verkhratsky *et al.*, 2017). Since specific species differences between human and rodent astrocytes have been uncovered (Oberheim *et al.*, 2009; Zhang *et al.*, 2016), studying disorders in which astrocytes are key players could benefit from the use of human astrocytes (Grainger *et al.*, 2018). When Ca^{2+} signalling has been studied in human stem cell derived astrocytes, a focus has been on showing Ca^{2+} propagation in response to mechanical injury (Krencik *et al.*, 2011; Roybon *et al.*, 2013; Serio *et al.*, 2013), but there is now also some evidence for responses to physiological stimuli, such as neurotransmitters (Hill *et al.*, 2012; Serio *et al.*, 2013), as well as evidence for

spontaneous astrocytic Ca^{2+} events (Hill *et al.*, 2012). One of the objectives of this chapter is to examine spontaneous and evoked intracellular Ca^{2+} dynamics in the human astrocytes generated in **Chapter 3**.

As alluded to above, intracellular ion dynamics can differ significantly between astrocytes and neurons, which is thought to reflect the close interplay between the two cell types. This is exemplified by the contribution that astrocytes make to H^+ concentrations ($[H^+]$), which determines the pH in the extracellular and intracellular compartments throughout the brain. Dynamic pH regulation is known to be critical for normal brain function as pH influences network excitability, multiple aspects of synaptic transmission and the availability of energy substrates (Traynelis and Cull-Candy, 1990; Taira *et al.*, 1993; Erecińska, Deas and Silver, 2002). In the case of neurons, membrane depolarization and network activity result in intracellular acidification (Ahmed and John, 1980; Trapp *et al.*, 1996; Zhan *et al.*, 1998; Raimondo *et al.*, 2013, 2016) through the action of Ca^{2+}/H^+ ATPases (Schwiening, Kennedy and Thomes, 1993; Makani and Chesler, 2010), the production of metabolic acids (Wang, Randall and Thayer, 1994) and bicarbonate (HCO_3^-) efflux via $GABA_A$Rs (Pasternack, Voipio and Kaila, 1993; Trapp *et al.*, 1996). Meanwhile, pH regulation mechanisms are believed to be quite different in astrocytes. When submitted to sustained membrane depolarization, astrocytes experience intracellular alkalinisation as opposed to acidification (Ahmed and John, 1980; Boyarsky *et al.*, 1988; Chesler and Kraig, 1989; Deitmer and Szatkowskit, 1990). This observation is in accordance with evidence that astrocytes possess unique mechanisms compared to neurons for regulating pH. Such mechanisms include the electrogenic sodium-bicarbonate cotransporter NBCe1, the action of which provides a link

between membrane depolarisation and HCO_3^-/H^+ fluxes (Boyarsky *et al.*, 1993; Brookes and Turner, 1994; Pappas and Ransom, 1994; Bevensee, Weed and Boron, 1997). Indeed, it has recently been shown that these mechanisms enable astrocytic pH dynamics to be more closely related to network activity than neuronal pH dynamics. This tight coupling has been suggested to enable astrocytes to rapidly respond to the ionic and metabolic demands of the network (Raimondo *et al.*, 2016).

Advances in genetically-encoded fluorescent reporter molecules are generating new opportunities for monitoring ion dynamics in defined cell populations. In the case of H^+ for example, genetically-encoded reporters have been used to investigate pH regulatory processes in rodent neurons and astrocytes (Raimondo *et al.*, 2013, 2016). Most recently, a genetically-encoded fluorescent reporter called ClopHensorN has been optimised for use in the nervous system and has generated simultaneous and independent measurement of both intracellular $[H^+]$ and $[Cl^-]$. This represents an important advance, as earlier genetically-encoded reporters were sensitive to both H^+ and Cl^-, but unable to distinguish the two ion species (Kuner and Augustine, 2000; Awaji *et al.*, 2001; Esposito *et al.*, 2008; Markova *et al.*, 2008). This problem is confounded by the fact that cell types differ in their intracellular levels of each ion, and changes in pH often co-occur with changes in $[Cl^-]_i$ (Russell and Boron, 1976). For example, astrocytic $[Cl^-]_i$ fluxes were shown to be very sensitive to manipulations of intra- and extracellular pH (Ferroni *et al.*, 2000; Makara *et al.*, 2001). The ability of ClopHensorN to distinguish H^+ and Cl^- relies upon a fusion of two different fluorescent proteins, which exhibit distinct ion sensitivity when excited with particular wavelengths of light (Bizzarri *et al.*, 2006; Arosio *et al.*, 2010). Whilst these genetically-encoded tools have been used to dissect ion

dynamics in defined rodent cell populations, they have not yet been applied in the context of iPSC-derived human cells. One objective of the current work therefore, was to capitalise on the use of genetically-encoded reporters to monitor ion dynamics in the iPSC-derived human astrocytes generated in **Chapter 3** and to assess how these ion dynamics compare with evidence from the rodent literature.

Overall, the aims of this chapter are to:

1) Establish whether iPSC-derived human astrocytes display physiologically relevant Ca^{2+} dynamics and responses to extracellular signals.

2) Investigate steady-state and activity-dependent pH regulation in iPSC-derived human astrocytes.

3) Examine the pH and Cl^- dynamics that iPSC-derived human astrocytes and neurons exhibit in response to synaptically-driven network activity.

4.2 Results

Given the importance of intracellular Ca^{2+} signalling in astrocyte physiology, I conducted a series of imaging experiments (see section 2.5.1 and 2.5.5) to investigate Ca^{2+} dynamics in iPSC-derived human astrocytes that were generated using the protocol established in **Chapter 3**. Enriched mature astrocyte cultures (age range 96-111 days) were loaded with 10 µM of the membrane permeable Ca^{2+} dye, Oregon Green BAPTA-1 AM-ester (OGB-1 AM). Live-cell fluorescence imaging (1-2 minutes at 2-4 Hz) was then performed from multiple fields of view in different sets of cultures (3 cell lines, 3 inductions) in the absence of any external stimuli (**Figure 4.1A**). Spontaneous Ca^{2+} events were observed in all of the astrocyte cultures, and these events could either occur simultaneously across multiple astrocytes (a "synchronous event"; see section 2.5.2), or else they could occur in an individual astrocyte (a "non-synchronous event") (**Figure 4.1A**). The frequency of spontaneous Ca^{2+} events was first assessed on an individual cell basis and found to occur at a frequency of 0.009 ±0.002 Hz (n=200 cells across 4 FOVs) (**Figure 4.1B**). This corresponds to an average cell displaying one Ca^{2+} event every two minutes, although only 41.5 ± 6.2% of the astrocytes exhibited spontaneous Ca^{2+} events during the time periods that were sampled.

In terms of the different event types, the mean frequency of non-synchronous events and synchronous events were not different (total events: 0.47 ± 0.2 Hz, n=4 FOV; non-synchronous events: 0.13 ± 0.009 Hz; n=4 FOV; synchronous events: 0.34 ± 0.2 Hz, n=4 FOV; $p>0.999$; un-paired Mann-Whitney test between non-synchronised and synchronised events) (**Figure 4.1B**).

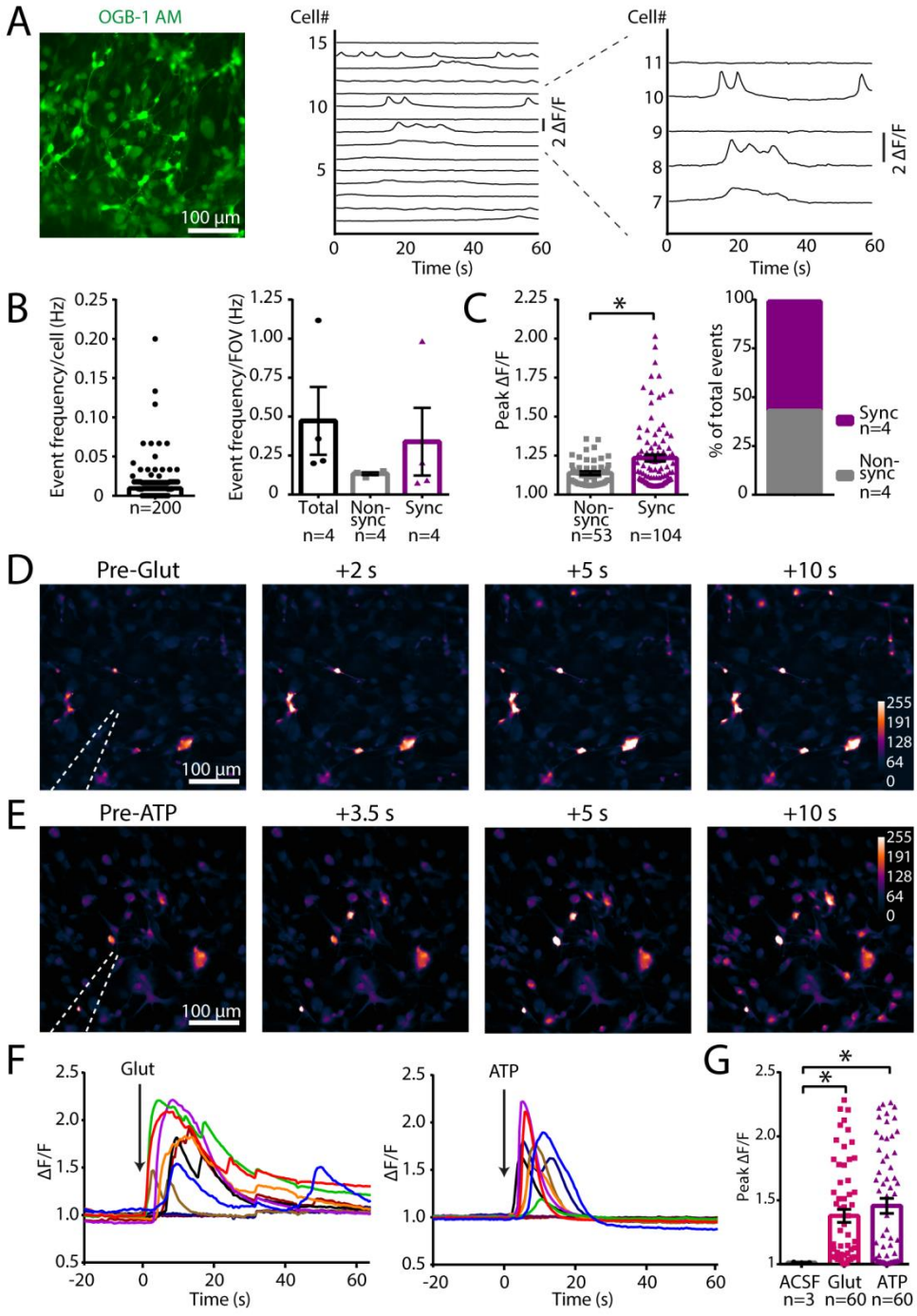

Figure 4.1 Human astrocytes display spontaneous and evoked calcium dynamics
(A) Human astrocyte monocultures were loaded with OGB-1 (AM ester form) (left). Time-lapse movies were recorded at 2 Hz and this example shows 15 regions of interest (ROIs) selected over cell somas. The staggered plot of ΔF/F traces (middle) shows that elevations in intracellular Ca^{2+} can occur in individual astrocytes ('non-synchronous' events), but also synchronously across multiple astrocytes ('synchronous events') (right). **(B)** The frequency of Ca^{2+} events per cell (left; four FOV, each with 50 ROIs) and frequency of Ca^{2+} event types per FOV (right). **(C)** The peak ΔF/F amplitude (left) and proportion of event types (right) are shown for non-synchronous and synchronous events. **(D-E)** Under the same conditions as in 'A', time-locked Ca^{2+} events were elicited by a 500 ms puff of either 100 µM L-glutamate **(D)**, or 1 mM ATP **(E)**, delivered via a patch-pipette. Nearby astrocytes respond within 2-3.5 s and the event propagation can be followed for the next 10 s (right). **(F)** ΔF/F traces from 10 ROIs demonstrate the time-locked initiation of Ca^{2+} events elicited by glutamate (left) and ATP (right). **(G)** Control experiments (2 FOV, each with 30 ROIs) confirmed that the intracellular calcium events were significantly above any response elicited by ACSF (1 higher magnification FOV, 3 ROIs).

On average, an astrocyte's synchronous Ca^{2+} events were larger in amplitude (non-synchronous: 1.14 ± 0.01 ΔF/F, n=53 detected Ca^{2+} events; synchronous: 1.23 ±0.02 ΔF/F, n=104 detected Ca^{2+} events; p=0.016, un-paired Mann-Whitney test) (**Figure 4.1C**), but represented a similar proportion of the total events (non-synchronous: 43.5 ±11.5%, n=4 FOV; synchronous: 56.5 ±11.5%, n=4 FOV; p=0.686, un-paired Mann-Whitney test) (**Figure 4.1C**). Although not shown here, the human astrocytes also responded readily with Ca^{2+} elevations to an injurious poke with a patch pipette, as has previously been observed by others (Krencik *et al.*, 2011; Roybon *et al.*, 2013; Serio *et al.*, 2013).

In rodent models, astrocytic intracellular Ca^{2+} elevations are observed in response to a variety of different neurotransmitters (Porter and McCarthy, 1995; Pasti *et al.*, 1997; Shelton and McCarthy, 2001; Araque *et al.*, 2002; Perea and Araque, 2005; Agulhon *et al.*, 2008), and glutamate and ATP have both been shown to elicit Ca^{2+} responses in the human teratocarcinoma NT2 cell line (Hill *et al.*, 2012). To investigate whether the iPSC-derived astrocytes generated in this thesis are responsive to neurotransmitters, OGB-1 AM loaded astrocytes were subjected to brief, focal applications of glutamate or ATP (500 ms duration), delivered via a patch pipette using low-pressure pulses (1-2 psi) to avoid responses associated with cell movement (Rzigalinski *et al.*, 1998) (see section 2.5.3). Glutamate (100 mM) elicited robust Ca^{2+} elevations in the astrocytes, with cells closest to the puffer pipette responding first, followed by a propagating wave of responsive cells towards the edge of the FOV over a timescale of 10 s (**Figure 4.1D**). ATP (1 mM) was also very effective at eliciting astrocytic Ca^{2+} responses, with a wave of responsive cells again propagating outward from the site of ATP delivery (**Figure 4.1E**). Peak ΔF/F increases elicited by the glutamate and ATP stimuli

were similar, and significantly different from responses to the ACSF vehicle (ACSF: 1.0 ± 0.002 ΔF/F, n=3 puff attempts on 1 cell; glutamate: 1.4 ± 0.05 ΔF/F, n=60 cells from 2 FOVs; p=0.045, Dunns multiple comparisons test; ATP: 1.5 ± 0.06 ΔF/F, n=60 cells from 2 FOVs; p=0.032, Dunns multiple comparisons test) (**Figure 4.1F** and **G**).

To complement these findings, a separate set of experiments examined the spatiotemporal properties of intracellular Ca^{2+} dynamics. Individual astrocytes (from 2 different cultures; 1 cell line, 1 induction) were subjected to patch clamp recordings and filled with the membrane impermeant Ca^{2+} dye, OGB-2 K^+ salt (see section 2.5.3). By targeting the astrocytic processes, it was observed that brief, focal glutamate pulses were able to trigger intracellular Ca^{2+} increases within an individual process, which then propagated away from the site of initiation to the rest of the cell (**Figure 4.2A**). Quantification at different intracellular locations captured the propagation and gradual attenuation of the Ca^{2+} events, with the example shown exhibiting a propagation speed of 22.7 µm/s (**Figure 4.2B**). In summary, the results from the calcium imaging experiments establish that the iPSC-derived human astrocytes display both spontaneous and evoked Ca^{2+} dynamics, supporting the idea that these cells are able to detect and respond to neuronal activity.

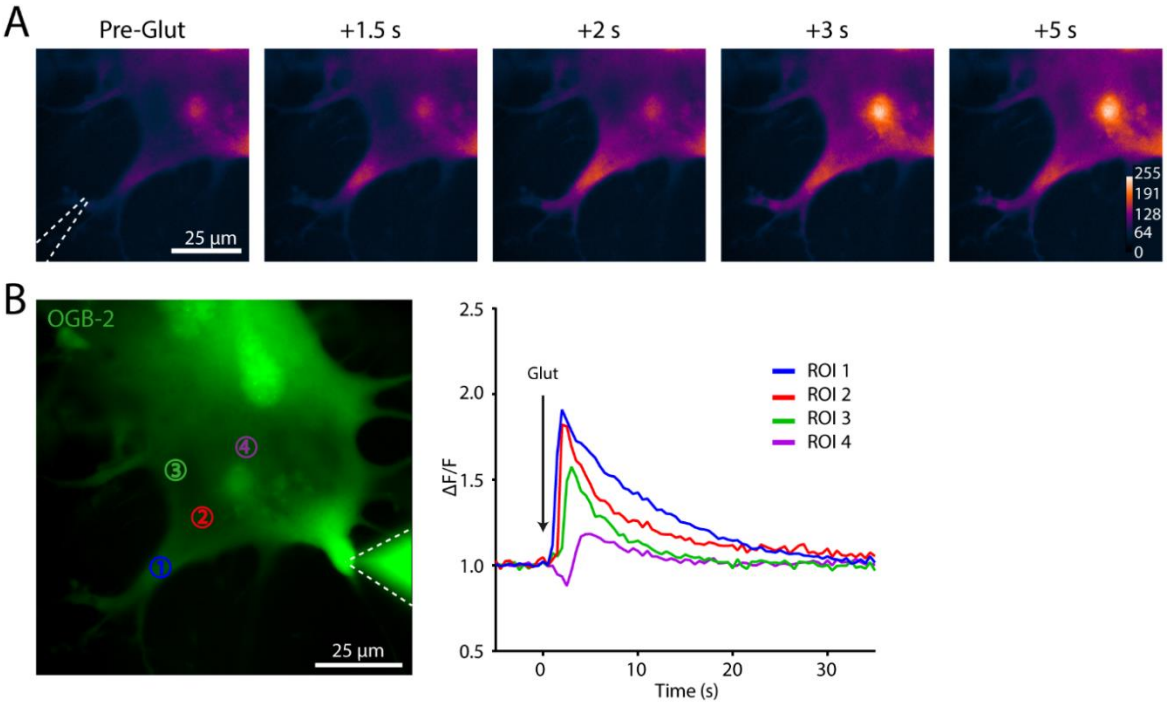

Figure 4.2 Human astrocytes display intracellular Ca^{2+} waves in response to glutamate
(A) A whole-cell patched human astrocyte filled with the Ca^{2+} dye OGB-2 (K^+ salt form) via the patch pipette. An intracellular Ca^{2+} wave was elicited by a glutamate puff (100 µM, 100 ms duration) and its propagation through the cell could be tracked over time (right). **(B)** The spread of the glutamate-induced Ca^{2+} response was measured at four different ROIs (left). The corresponding ΔF/F traces demonstrate the gradual attenuation of the Ca^{2+} event as it propagates (right).

Changes in network activity can result in different intracellular ion dynamics between astrocytes and neurons, consistent with the idea that astrocytes often serve to compensate or counteract changes in neuronal compartments (Chesler, 2003; Verkhratsky and Nedergaard, 2016). This has been demonstrated in the context of activity-dependent $[H^+]$ changes, where elevated network activity tends to generate acidification in neurons (Zhan *et al.*, 1998), but astrocytes exhibit an opposing alkalinisation (Chesler, 2003; Raimondo *et al.*, 2015). To investigate activity-dependent pH dynamics in iPSC-derived human astrocytes, I employed the genetically encoded ratiometric reporter ClopHensorN (Raimondo *et al.*, 2013) (**Figure 4.3A**) (see section 2.5.6). Due to its design, ClopHensorN has been shown to be capable of simultaneously reporting intracellular $[H^+]$ and $[Cl^-]_i$, which are ions that often

exhibit dynamic changes under the same conditions. ClopHensorN is a ratiometric reporter of pH and possesses an isosbestic point at 458 nm, where the fluorescence absorption is pH-independent (**Figure 4.3B**). Calibration curves were generated to translate fluorescence ratios into actual pH and Cl^- concentrations using standard methods (see section 2.5.7). From these it is evident that an increase in pH ratio translates into alkalinisation, whereas an increase in Cl^- ratio means a lowering of $[Cl^-]_i$ (**Figure 4.3C** and **D**). Due to the binding affinity of the E^2GFP molecule within ClopHensorN, one can observe in the calibration curves how an acidic pH promotes Cl^- binding and produces more effective quenching (**Figure 4.3D**; (Jayaraman *et al.*, 2000)). This dependency on pH is reflected by the increase in the dissociation constant for Cl^- ($K_{d,pH}$) with increasing pH.

ClopHensorN was expressed in cultures enriched for iPSC-derived human astrocytes or neurons via lentiviral transduction, and under the control of the ubiquitous CMV promoter (**Figure 4.3E**). After 1 week, ClopHensorN expression was detected in the morphologically distinct astrocytes and neurons (**Figure 4.3F**). Resting pH and $[Cl^-]_i$ were first measured from these enriched cultures, where it was possible to sample large numbers of cells across multiple cultures (from 3 cell lines, 3 inductions throughout). This revealed that the iPSC-derived astrocytes rest slightly more acidic compared to the iPSC-derived neurons (astrocytes: 7.05 ± 0.01 pH units, n=1098 cells; neurons: 7.16 ± 0.007 pH units, n=1982 cells; $p<0.0001$, Kolmogorov-Smirnov un-paired test of distributions) (**Figure 4.3G**).

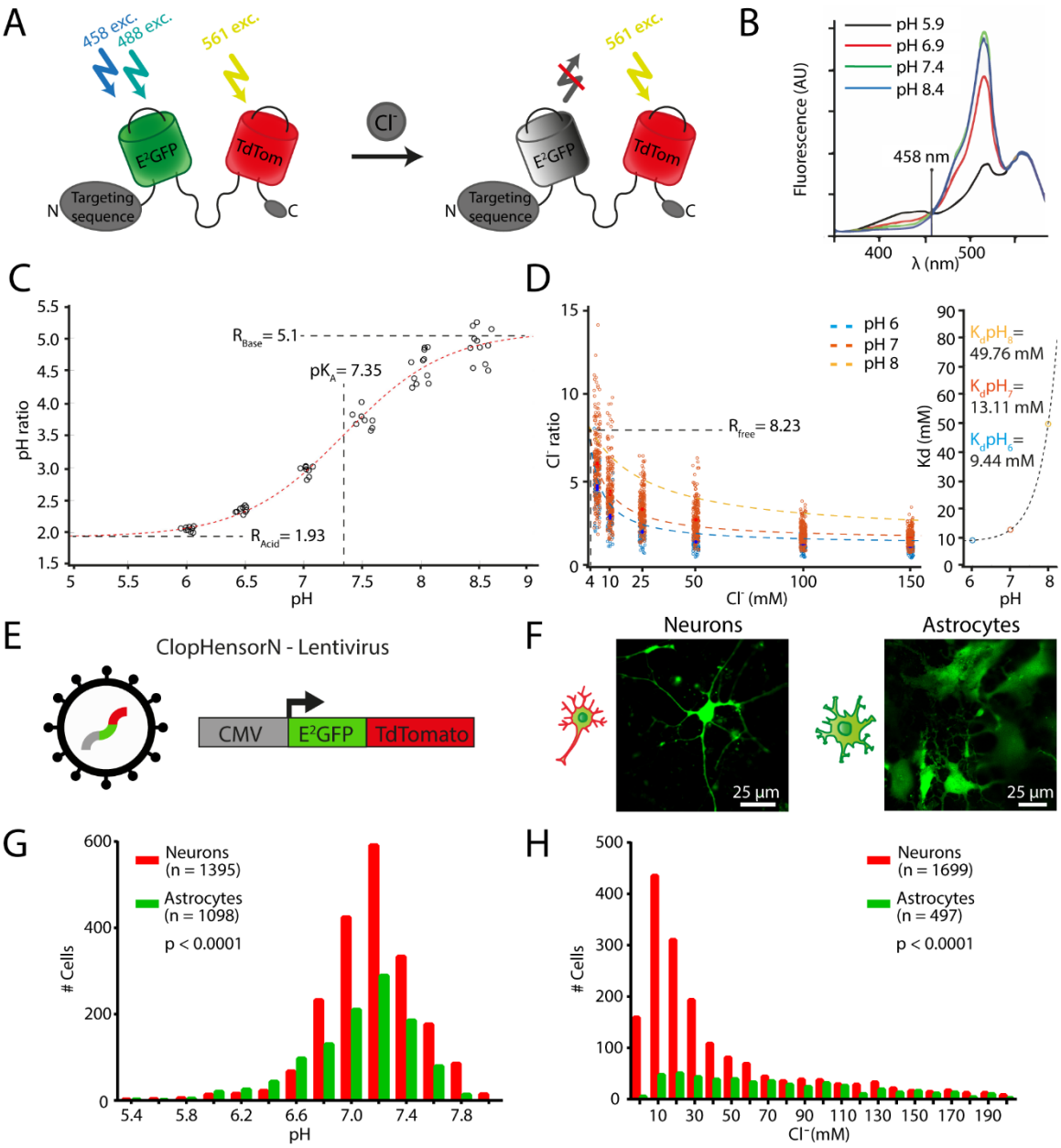

Figure 4.3 Examining intracellular pH and chloride in iPSC-derived human cells using the genetically-encoded ratiometric biosensor ClopHensorN

(A) Schematic of ClopHensorN, which consists of a fusion of two fluorescent proteins: E^{2}GFP and TdTom. E^{2}GFP is a ratiometric pH sensor, which can be excited with 458 nm and 488 nm light, and whose fluorescence is quenched by Cl^-. By reference to the TdTom fusion protein, which can be excited at 561 nm and is insensitive to pH and Cl^-, E^{2}GFP emission provides an estimate of Cl^- concentration. **(B)** ClopHensorN emission plotted as a function of excitation wavelength for four different pH values, as measured by Arosio and colleagues. The isosbestic point for E^{2}GFP is indicated at 458 nm. 'A' and 'B' are modified from Arosio et al. (2010). **(C)** pH calibration for ClopHensorN generated in HEK-293 cells with resulting R_{Acid}, R_{Base} and pK_A values indicated. **(D)** Cl^- calibration generated in HEK-293 cells at pH 6 and 7, and inferred for pH 8 (left). The R_{free} value was obtained in nominally Cl^- free conditions. The dependence of the dissociation constant (K_d) on pH (right), with the K_d at 3 different pH values indicated. **(E)** Cartoon of ClopHensorN lentiviral construct used for expression in iPSC-derived human cells, under the control of the cytomegalovirus (CMV) promoter. **(F)** Example ClopHensorN$^+$ iPSC-derived neurons (left) and astrocytes (right). **(G)** Distribution of resting pH-values measured from monocultures of human neurons and astrocytes. **(H)** Distribution of resting internal chloride concentrations in human neurons and astrocytes.

Meanwhile, the distribution of $[Cl^-]_i$ values was skewed towards lower values in neurons, but displayed a relatively flatter distribution with a higher mean intracellular $[Cl^-]_i$ in astrocytes (astrocytes: 72.4 ± 2.2 mM Cl^-, n=497 cells; neurons: 40.8 ± 1.1 mM Cl^-, n=1699 cells; $p<0.0001$, Kolmogorov-Smirnov un-paired test of distributions) (**Figure 4.3H**).

Rodent astrocytes are reported to exhibit intracellular alkalinisation during periods of elevated network activity, through a mechanism that relies upon activity-dependent depolarisation of the astrocyte membrane potential and the reversed action of an electrogenic Na^+/HCO_3^- cotransporter (NBCe1) (Boyarsky *et al.*, 1993; Brookes and Turner, 1994; Bevensee, Weed and Boron, 1997; Raimondo *et al.*, 2016). To examine if the iPSC-derived human astrocytes display similar depolarisation-dependent pH dynamics, enriched cultures of ClopHensorN-expressing astrocytes were subjected to time-lapse imaging of their intracellular pH (**Figure 4.4A** see also section 2.5.6). The membrane potential of the astrocytes was depolarised by elevating local extracellular K^+ (500 mM KCl delivered via a patch pipette using low-pressure pulses, see section 2.4.7; **Figure 4.4B**), which was confirmed by performing whole-cell current clamp recordings in a subset of astrocytes. 100% of the astrocytes (7 out of 7; from 1 cell line, 1 induction) exhibited membrane depolarisations, whose relative amplitude depended on the duration of the KCl application (**Figure 4.4B**).

Combining this manipulation with ClopHensorN time-lapse imaging revealed that the iPSC-derived human astrocytes exhibited robust intracellular alkalinisations in response to membrane depolarisation (**Figure 4.4C**) (assessed in cultures from 2 cell lines, 2 inductions). The pH shifts were quantified as the area under the curve (AUC), calculated in a window from 5 s before, to 35 s after, KCl application.

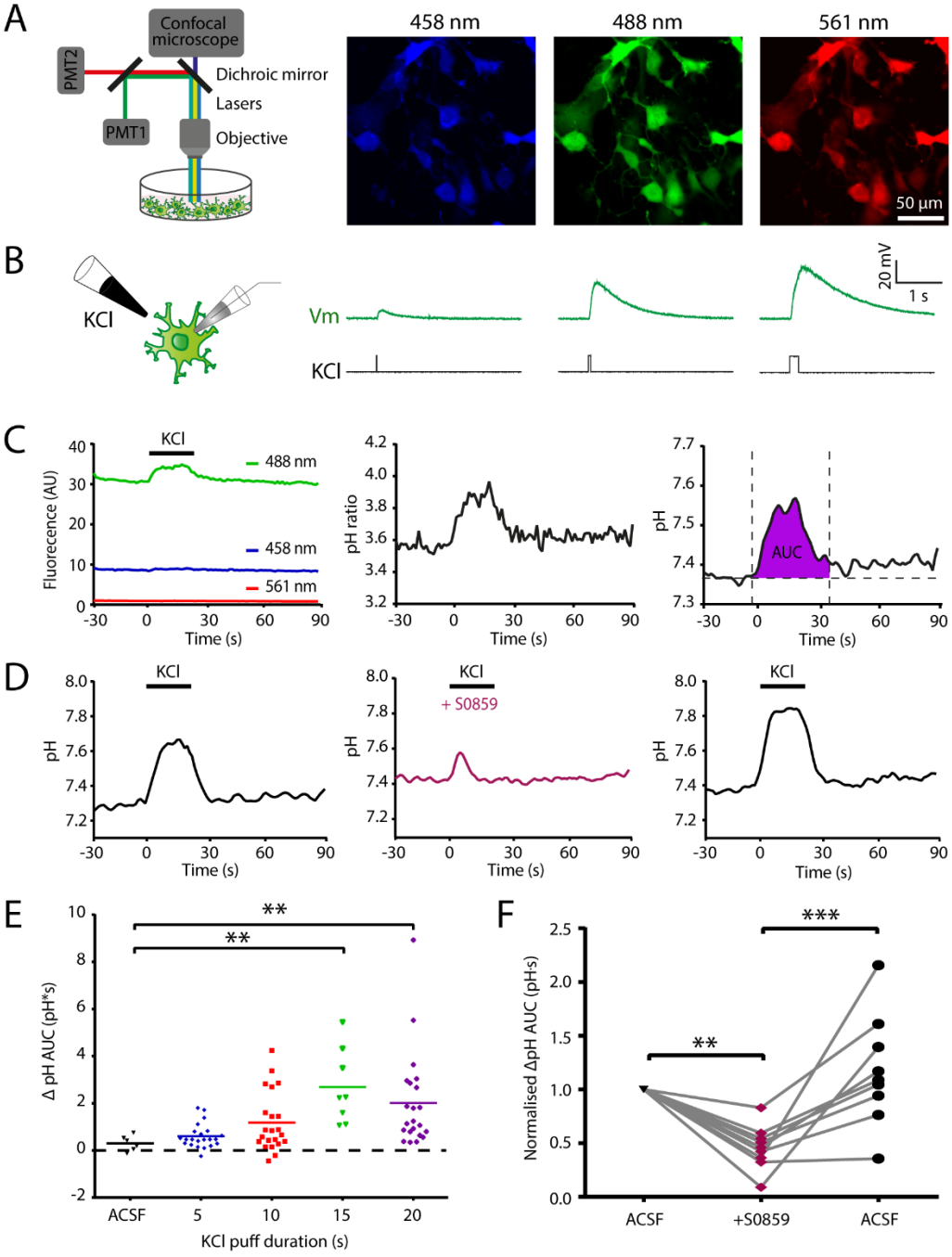

Figure 4.4 Membrane depolarisation elicits alkalinisation in human iPSC-derived astrocytes via Na^+/HCO_3^- co-transport

(A) Experimental setup (left), three laser-lines (488, 458 and 561 nm) were used to excite ClopHensorN$^+$ cells sequentially, and dichroic mirrors were used to direct the emitted light to photon multipliers tubes (PMT). Example ClopHensorN$^+$ human astrocytes acquired at three excitation wavelengths (right). **(B)** Membrane depolarisation was induced by focal delivery of KCl (left). Patch clamp recordings confirmed that astrocyte membrane depolarisation tracked with the KCl pulse (right). **(C)** Raw ClopHensorN emission signals (left) recorded from an astrocyte exposed to KCl (20 s pulse duration). The pH ratio (middle) was obtained by dividing the 488 nm signal by the 458 nm signal. Using calibration curves, the pH signal was inferred, smoothed and the area under the curve (AUC) used to estimate the depolarisation-induced effects upon pH (right). **(D)** Depolarisation-induced alkalinisation (left) was significantly reduced by bath application of the $Na^+/HCO3^-$ co-transporter inhibitor, S0859 (50 µM, middle), and could be recovered by washing (right). **(E)** Population data showing that membrane depolarisation is associated with alkaline shifts in astrocytic pH. (**F**) Population data showing that S0859 significantly reduces depolarisation-induced alkalinisation in human astrocytes. * $p < 0.05$, ** $p < 0.01$, *** $p < 0.001$

On average, the human astrocytes shifted their internal pH in the alkaline direction and longer KCl stimuli induced larger shifts ($p<0.0001$, un-paired Kruskall-Wallis test), with 15 s and 20 s eliciting an alkalinisation response that was significantly different from a vehicle-only ACSF control (ACSF: 0.30 ± 0.13 pH*s, n=6 astrocytes from 1 FOV; 15 s KCl: 2.7 ± 0.6 pH*s, n=8 astrocytes from 2 FOV; p=0.001; 20 s KCl: 2.0 ± 0.4 pH*s, n=22 astrocytes from 6 FOV; p=0.007, Dunn's multiple comparisons test) (**Figure 4.4E**).

Furthermore, these activity-dependent alkaline shifts were attenuated by bath application of the Na^+/HCO_3^- co-transporter inhibitor, S0859 (p=0.0002, paired Friedman test) (**Figure 4.4D**), consistent with the idea that the electrogenic co-transporter, NBCe1, contributes to the depolarisation-induced alkalinisation. AUC's were measured under baseline conditions, 30 minutes after S0859 application, and again 15 minutes after drug wash out (ACSF baseline AUC: 1.0 (normalised), n=9 astrocytes from 2 FOV; from 1 cell line, 1 induction; in S0859: 0.46 ± 0.07 x baseline AUC; p=0.009; ACSF washout: 1.2 ± 0.2 x baseline AUC; p=0.001, Dunn's multiple comparisons test) (**Figure 4.4F**). These data confirm that the iPSC-derived human astrocytes are able to translate changes in their membrane potential into ion dynamics.

Raising the extracellular $[K^+]$ via directly cell-targeted KCl puffs is a rather crude but robust method for proving that depolarisation is also linked to alkalinisation in human astrocytes. To examine whether this was the case under more physiologically relevant patterns of activity, iPSC-derived human cells were transplanted into mouse organotypic hippocampal brain slices (**Figure 4.5A**). These brain slices can be maintained in culture for relatively long periods of time and exhibit a variety of synaptically-driven spontaneous network events, which

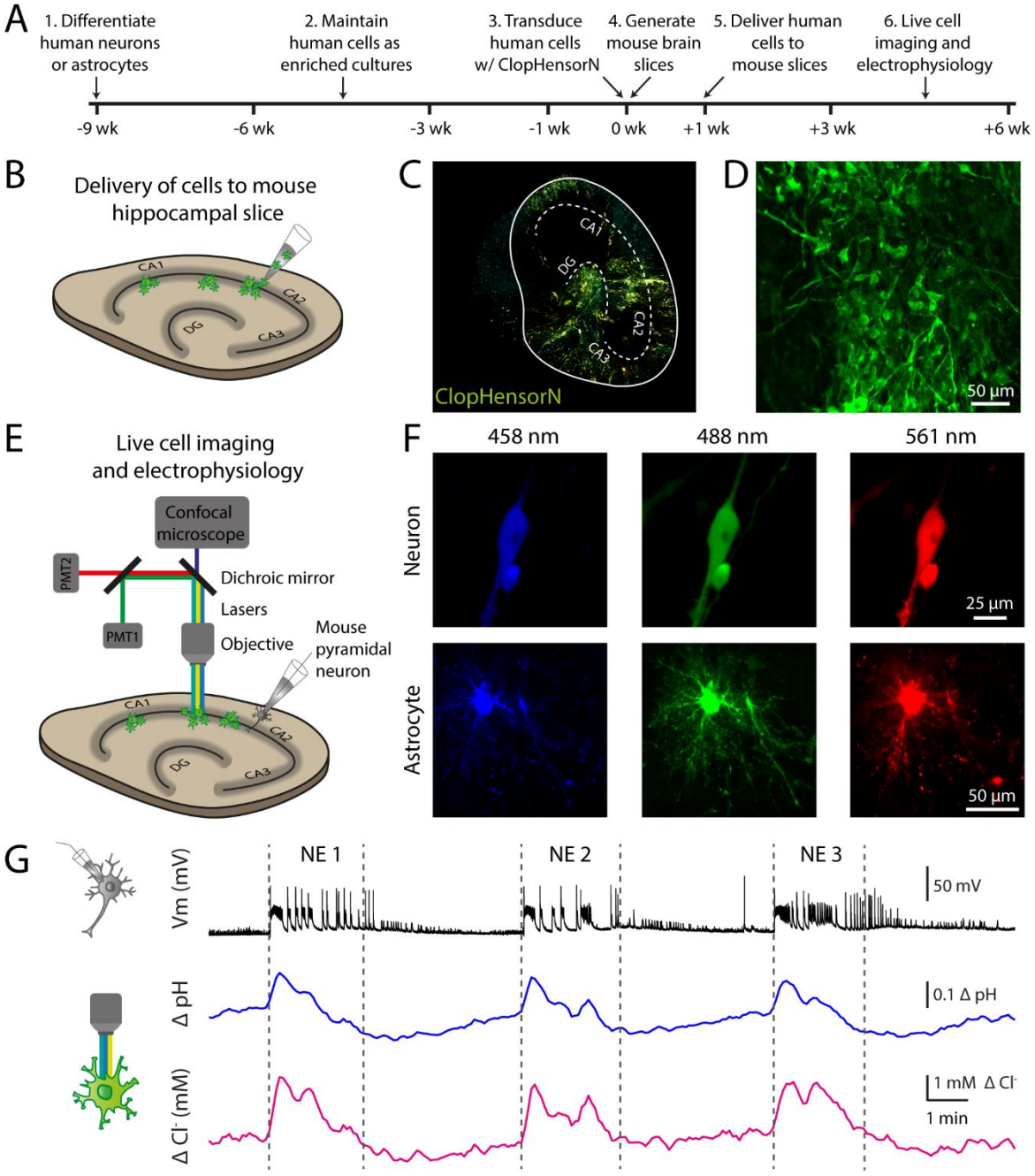

Figure 4.5 Establishing a network activity model for investigating pH and chloride dynamics in human neurons and astrocytes

(A) Timeline of experimental protocol. **(B)** Suspensions of ClopHensorN$^+$ human neurons or astrocytes were delivered by injection into the CA1 region of mouse organotypic hippocampal slices. **(C)** Example low-power image of a live mouse hippocampal slice with integrated ClopHensorN$^+$ human cells. Solid lines indicate the slice edge, dashed lines indicate the dentate gyrus (DG) and pyramidal layers. **(D)** Expanded region from 'C', having fixed the slice and enhanced the ClopHensorN signal with an anti-GFP antibody. **(E)** Schematic of the recording configuration. ClopHensorN$^+$ cells were imaged on the same confocal setup described in **Figure 4.4**. Network activity of the mouse brain slice was monitored via current clamp recordings from a pyramidal neuron in CA1-CA3. **(F)** Live images of a ClopHensorN$^+$ neuron and astrocyte. **(G)** Simultaneous recording of network activity from a mouse pyramidal neuron (top), and pH and Cl^- dynamics from a human astrocyte (bottom). Dashed lines indicate periods of synchronous network events (NEs).

involve the synchronous activity of large numbers of neurons (Dyhrfjeld-Johnsen *et al.*, 2010; Raimondo *et al.*, 2016). Cell suspensions of either human astrocytes or human neurons expressing ClopHensorN were transplanted into 1-week old organotypic brain slices and maintained for up to 6 weeks (**Figure 4.5A**). Different cell concentrations and delivery methods were attempted (see section 2.2.9 for further details) and it was found that injections of iPSC-derived cell suspensions into the pyramidal cell layers resulted in the highest rates of cell survival, with typically hundreds of cells surviving to the time of analysis (**Figure 4.5B-D**). Interestingly, surviving cells exhibited a tendency to avoid the pyramidal cell layers (as has been observed previously (Hiragi *et al.*, 2017)), and instead displayed an apparent preference to embed within the dentate gyrus area, perhaps reflecting the fact that this region can act as a neurogenic niche (Gage, 2002).

Cell imaging and electrophysiological recordings were performed using the same confocal setup and laser settings as in the previous experiment (see section 2.5.6; **Figure 4.5E**). Local network activity was monitored by performing a continuous patch clamp recording from a nearby mouse pyramidal neuron in current clamp mode (see section 2.5.8). The ClopHensorN$^+$ human astrocytes were selected for imaging according to their finely branched morphology, devoid of any particularly dominant apical or basal processes (**Figure 4.5F**). Whereas the ClopHensorN$^+$ human neurons were selected for imaging on the basis of their smooth, often oval shaped cell-body, and the presence of an extended apical and/or basal process (**Figure 4.5F**). The electrophysiology and imaging data were synchronised, fluorescence ratios were converted into estimates of pH and [Cl$^-$], and subjected to quantitative analysis (see sections 2.5.6, 2.5.7 and 2.5.8 for details). This revealed a close association

between periods of synaptically-driven network activity in the brain slices, referred to here as "network events" (NEs), and dynamic fluctuations in pH and $[Cl^-]_i$ in the iPSC-derived human cells (**Figure 4.5G**).

Recordings of NE-associated ClopHensorN responses were compared in 33 human neurons (from 1 cell line, 1 induction and 3 separate transplantation events) and 12 human astrocytes (from 1 cell line, 1 induction and 1 transplantation) according to the following measures: Pre-NE pH, Δ pH peak, time to peak pH and pH recovery time (see section 2.5.9; **Figure 4.6A**). As the duration of NEs varies, all ion dynamics were expressed relative to the duration of the NE with which they were associated (i.e. values are expressed as a percentage of NE duration, where 100% represents the end of the NE). When plotting the mean pH change associated with NEs, the differing pH dynamics in human neurons and astrocytes were clear (**Figure 4.6B**) and statistical comparisons of the various measures confirmed these differences (**Figure 4.6C**). Individual neurons and astrocytes showed similar pre-NE pH values (neurons: 7.6 ± 0.03 pH units, n=33 cells; astrocytes: 7.7 ± 0.1 pH units, n=12 cells; p=0.277, un-paired Mann-Whitney test), but subsequently shifted their pH in opposite directions. The mean peak shift in pH was acidic in neurons, but alkaline in astrocytes (neurons: -0.07 ± 0.006 pH units, n=156 NEs; astrocytes: 0.36 ± 0.11 pH units, n=35 NEs; p<0.0001, un-paired Mann-Whitney test), which was also reflected in the AUC measure (neurons: -8.1 ±0.6 pH*%NE duration, n=156 NEs; astrocytes: 23.7 ± 5.2 pH*%NE duration, n=35 NEs; p<0.0001, un-paired Mann-Whitney test).

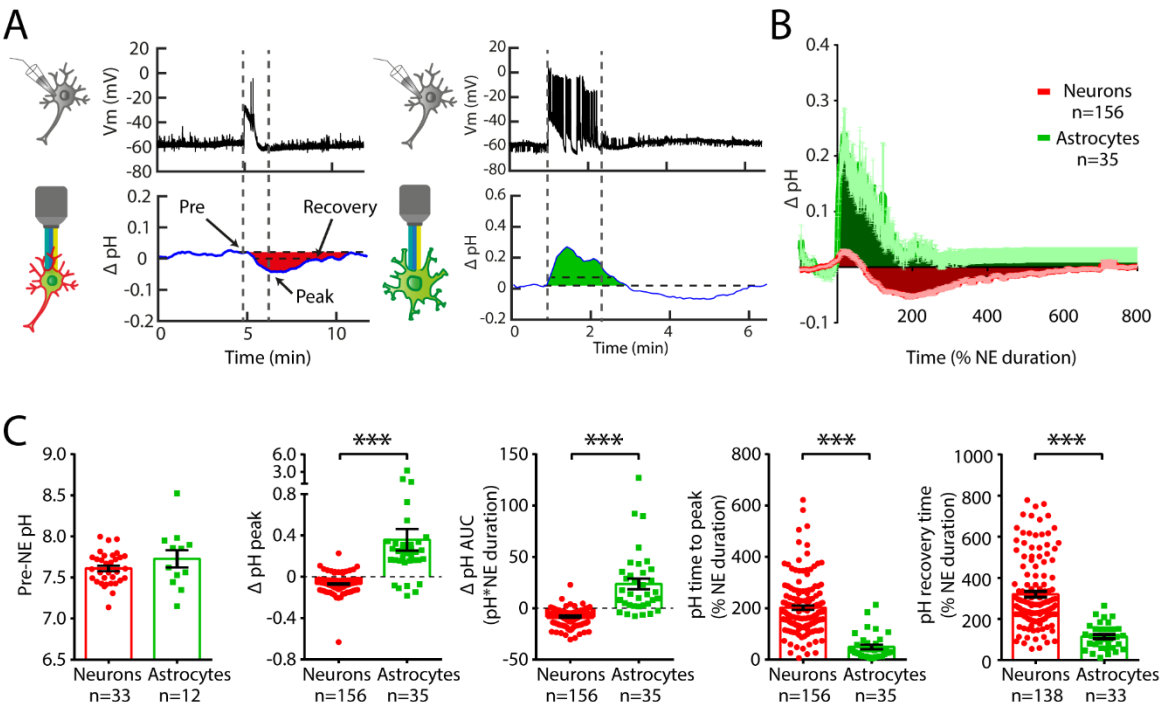

Figure 4.6 Network-evoked pH dynamics differ in human iPSC-derived neurons and astrocytes

(**A**) pH dynamics recorded in a neuron (left) or astrocyte (right), in response to a network event (NE). Arrows indicate where measures were made of pre-NE pH, peak pH change, time to peak and time to 75% recovery. The solid fills indicate where the area under the curve (AUC) was calculated. **(B)** The average pH change plotted as a function of NE duration, for both astrocytes and neurons. Astrocytes exhibit rapid alkaline shifts that closely follow the kinetics of the NE, whilst neurons exhibit acidic shifts over a slower timescale (error bars signify SEM and n's refer to numbers of NEs). The duration of each NE was normalised to 100% and the x-axis was bounded at 800%. **(C)** While human neurons and astrocytes rested at similar pH values in the period before a NE ('pre-NE'), the pH of the two cell types shifted in opposite directions in response to network activity, both in terms of peak and AUC. In addition, astrocytic pH responses were significantly faster to reach their peak and to recover when compared to neurons, which typically peaked after the end of the NE.

Furthermore, astrocytes tended to reach their peak pH change during the NE, whilst neurons would generally not reach their peak until after the NE had ended (neurons: 202.2 ± 8.4 %NE duration, n=156 NEs; astrocytes: 49.4 ± 8.5 %NE duration, n=35 NEs; $p<0.0001$, un-paired Mann-Whitney test). Similarly, the kinetics of pH recovery were significantly faster in astrocytes (neurons: 320.0 ± 14.2 %NE duration, n=138 NEs; astrocytes: 114.1 ±11.0 %NE duration, n=33 NEs; $p<0.0001$, un-paired Mann-Whitney test). Together, these findings demonstrate significant differences in pH dynamics during network activity between the

human neurons and astrocytes, and support the idea that astrocytes are significantly faster at adjusting their internal pH during periods of network activity.

To explore $[Cl^-]_i$ dynamics in human neurons and astrocytes, which often accompany pH changes, I used the ClopHensorN isosbestic pH point and the fact that the reporter's fluorescence is quenched by Cl^- (see **Figure 4.3D** and **Chapter 2**). The same measures of pre-NE $[Cl^-]_i$, Δ Cl^- peak, AUC and time to peak and recovery were calculated (**Figure 4.7A**). When plotting the average $[Cl^-]_i$ dynamics across all NEs in the two cell types, it was evident that the neurons showed little response to the NEs, whilst the astrocytes showed a tendency

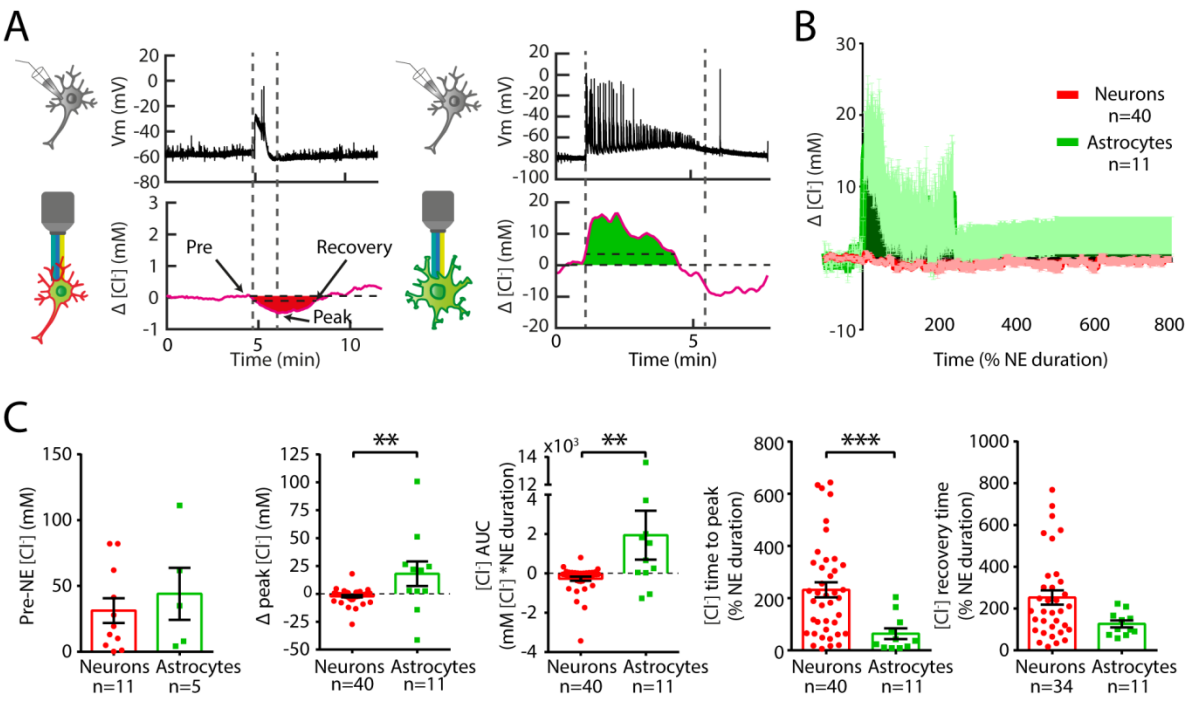

Figure 4.7 Network-evoked Cl^- dynamics differ in human iPSC-derived neurons and astrocytes

(**A**) Cl^- dynamics recorded in a neuron (left) or astrocyte (right), in response to a network event (NE). Arrows indicate where measures were made of the pre-NE Cl^-, peak Cl^- change, time to peak and time to 75% recovery. The solid fills indicate where the area under the curve (AUC) was calculated. **(B)** The average Cl^- change plotted as a function of NE duration, for both astrocytes and neurons. Astrocytes exhibit intracellular Cl^- increases that closely follow the kinetics of the NE, whilst intraneuronal Cl^- is relatively stable. **(C)** Human neurons and astrocytes rested at similar pre-NE Cl^- concentrations. Astrocytes showed significantly more intracellular Cl^- loading during network activity than neurons. Astrocytes were also faster to respond to the network activity in terms of time to peak response, but there was no significant difference in the time to recover.

to increase $[Cl^-]_i$ during the NEs (**Figure 4.7B**). $[Cl^-]_i$ levels before the NEs were similar between human neurons and astrocytes (neurons: 31.3 ± 9.4 mM Cl^-, n=11 cells; astrocytes: 44.0 ± 19.7 mM Cl^-, n=5 cells; p=0.743, un-paired Mann-Whitney test) (**Figure 4.7C**), but during NEs, astrocytes showed increases in peak $[Cl^-]_i$, whilst neuronal $[Cl^-]_i$ remained relatively stable (neurons: -2.1 ± 1.0 mM Cl^-, n=40 NEs; astrocytes: 18.0 ± 11.0 mM Cl^-, n=11 NEs; p=0.002, un-paired Mann-Whitney test). This was also evident in the AUC measurement (neurons: -273.2 ± 107.2 mM Cl^-*%NE duration, n=40 NEs; astrocytes: 1943.0 ± 1245.0 mM Cl^-*%NE duration, n=11 NEs; p=0.003, un-paired Mann-Whitney test). As with the pH dynamics, astrocytes reached the peak of the Cl^- change during the NE, whilst any change that occurred in neurons did not reach its peak until after the NE (neurons: 231.8 ± 28.8 %NE duration, n=40 NEs; astrocytes: 63.5 ± 20.5 %NE duration, n=11 NEs; p=0.0005, un-paired Mann-Whitney test) (**Figure 4.7C**). However, no significant difference was detected in the recovery time between the two cell types (neurons: 252.9 ± 34.7 %NE duration, n=34 NEs; astrocytes: 126.3 ±17.0 %NE duration, n=11 NEs; p=0.063, un-paired Mann-Whitney test). Taken together, the experiments with human cells transplanted into organotypic slices reveal that the two human cell types behave differently in terms of ion fluxes in response to network activity, and the astrocytes exhibit activity-dependent pH dynamics that are predicted from studies in rodents.

4.3 Discussion

In an attempt to further investigate the physiological relevance iPSC-derived human astrocytes, this chapter has explored different aspects of astrocytic ion dynamics. Focusing first on Ca^{2+} dynamics, which are widely associated with astrocyte signalling (Agulhon *et al.*, 2008; Lalo *et al.*, 2011), I found that human astrocytes display both synchronous and asynchronous spontaneous Ca^{2+} events. Both of these phenomena have been described in rodent astrocytes under non-pathological circumstances (Parri, Gould and Crunelli, 2001; Nett, Oloff and McCarthy, 2002) and disease states (Tashiro, Goldberg and Yuste, 2002). I found that ~42% of astrocytes exhibited spontaneous Ca^{2+} fluxes, which is somewhat lower than estimates of 64% and 67% made in mouse hippocampal and rat thalamic acute slices, respectively (Parri, Gould and Crunelli, 2001; Nett, Oloff and McCarthy, 2002), or an estimate of ~50% in iPSC-derived and foetal human astrocytes (Tcw *et al.*, 2017). The lower number measured here could represent genuine differences between the cells, or could result from the shorter imaging times (~2 minutes) compared to previous studies (6-10 minutes). Reciprocal signalling between neurons and astrocytes has been studied in rodent models over many years (for example (Porter and McCarthy, 1995; Pasti *et al.*, 1997; Araque *et al.*, 2002; Perea and Araque, 2005)), and a key element in this signalling is believed to be the responsiveness of astrocytes to neurotransmitters. Here I have demonstrated that the iPSC-derived human astrocytes are sensitive to classical neurotransmitters, by showing robust Ca^{2+} elevations in response to glutamate and ATP.

This chapter also used the genetically-encoded ratiometric reporter ClopHensorN to examine H^+ dynamics in human astrocytes and neurons, as well as Cl^- dynamics in the two

cell populations. As dynamic fluctuations in these two ion species have not previously been studied in iPSC-derived brain cells, these results provide the first insights into the mechanisms by which pH and $[Cl^-]_i$ homeostasis are established in human stem cell derived cultures. In terms of estimates of resting ion concentrations, resting pH in enriched dissociated cultures was found to be ~0.1 pH units more acidic in astrocytes, which was highly significant given the large dataset. The mean resting pH for the human astrocytes was 7.05, which is slightly more acidic than the value reported in a recent study of iPSC-derived astrocytes (mean of 7.18 pH units; (Yao *et al.*, 2018)). Although, this difference could be considered relatively minor, given potential differences associated with the imaging techniques, ACSF composition and recording conditions. Interestingly, my experiments revealed that iPSC-derived astrocytes and neurons both rested ~0.5 pH units more alkaline when they were embedded within mouse organotypic brain slices. The fact that both cell types exhibited a similar shift suggests that integration into three-dimensional brain tissue may influence resting ion homeostasis.

Compared to neurons, the distribution of resting $[Cl^-]_i$ in astrocytes was more broad and had a higher mean value. The mean $[Cl^-]_i$ for human astrocytes transplanted into mouse brain slices (~40 mM) was at the high end of values reported for mature rodent astrocytes (20-40 mM; (Simard and Nedergaard, 2004)). Meanwhile the resting $[Cl^-]_i$ levels recorded in human cortical neurons transplanted into mouse brain slices were lower than in the dissociated cultures, yet still higher than what has been reported for rodent neurons. Transplanted human neurons rested at ~30 mM $[Cl^-]_i$, which is ~3 times higher than published estimates for mature rodent hippocampal neurons (e.g. 8 mM in dissociated cultures (Kuner and Augustine, 2000), or 7 mM in acute brain slices (Staley and Proctor, 1999)), and closer to prenatal and early

postnatal measures of ~25 mM (Tyzio *et al.*, 2006). Indeed, resting neuronal $[Cl^-]_i$ has been estimated in iPSC-derived neurons on one previous occasion, where $[Cl^-]_i$ was inferred from the $GABA_A$ receptor reversal potential (Livesey *et al.*, 2014). These authors reported $[Cl^-]_i$ of ~24 mM in immature iPSC-derived neurons, which decreased with maturational time to ~8 mM (Livesey *et al.*, 2014). Together, these data are consistent with earlier observations (**Chapter 3**) that the iPSC-derived cortical neurons studied here represent a relatively immature state.

Combining ClopHensorN imaging with electrophysiology, I demonstrated that enriched cultures of dissociated human astrocytes respond to membrane depolarisation by exhibiting intracellular alkalinisation. This phenomenon is well established in astrocytes from various animal models (e.g. (Boyarsky *et al.*, 1993)). Furthermore, the pharmacological experiments conducted here supported the conclusion that this activity-dependent alkalinisation depends upon the electrogenic Na^+/HCO_3^- co-transporter, NBCe1, as has been shown in rodents. Multiple studies have implicated this co-transporter in depolarisation-mediated alkalinisation of astrocytes (Boyarsky *et al.*, 1993; Brookes and Turner, 1994; Pappas and Ransom, 1994; Bevensee, Weed and Boron, 1997; Theparambil *et al.*, 2014). The Na^+/HCO_3^- co-transporter blocker, S0859, has been shown to significantly attenuate activity-dependent astrocytic alkalinisation in rat astrocytes (Raimondo *et al.*, 2016). Remaining alkalinisations that I observed in the presence of S0859, and which have also been seen in rodent astrocytes, could occur as a result of direct acid extrusion via the action of Na^+/H^+ exchangers (Bevensee, Weed and Boron, 1997).

In an attempt to embed the human cells in a more physiological environment featuring more synaptically-active neuronal networks, it was shown that the iPSC-derived human astrocytes and neurons could readily survive in mouse organotypic hippocampal slices. This transplantation strategy may be useful for investigating various aspects of astrocyte physiology and astrocyte-neuron interactions. In my initial use of this experimental strategy, I correlated periods of network activity with intracellular ion dynamics. Simultaneous ClopHensorN imaging and electrophysiological recordings revealed opposite shifts in pH for human astrocytes and human neurons, in accordance both with established literature (Chesler and Kraig, 1989; Boyarsky *et al.*, 1993; Zhan *et al.*, 1998) and recent experiments using the same genetically-encoded fluorescent reporter in rat hippocampal astrocytes and neurons (Raimondo *et al.*, 2016).

The human astrocytes were also capable of shifting their intracellular pH more quickly than neurons in response to network activity. This is again in agreement with previous work in rodents, which demonstrated that astrocytic pH is more tightly coupled to membrane potential changes than neuronal pH (Raimondo *et al.*, 2016). Finally, in approximately 35% of the iPSC-derived human astrocytes (5 out of 14 cells), the main alkalinisation event was followed by an acidification 'overshoot' (see for example the astrocyte in **Figure 4.6A**), rather than exhibiting a monotonic return to baseline. Interestingly, such biphasic pH dynamics have been reported at a similar frequency in rat astrocytes *in vivo* (38% (Chesler and Kraig, 1989)), suggesting that this is a general feature that may be related to the timescale of activity-dependent extracellular pH changes. Together, these data reveal a remarkable similarity in the pH regulatory processes of human and rodent astrocytes.

To my knowledge, these results represent the first report of Cl^- dynamics in iPSC-derived human cells, and so potentially offer new insights into how neural activity can influence the fluxes of this ion. In reality, the direction of Cl^- fluxes was found to be variable, in the sense that I observed negative and positive activity-dependent $[Cl^-]_i$ changes in both astrocytes and neurons transplanted into mouse brain slices. For the majority of astrocytes, NEs induced a Cl^- influx whilst the neuronal population showed little net change in $[Cl^-]_i$. Similar experiments have shown that rodent neurons exhibit robust activity-dependent increases in $[Cl^-]_i$ (Isomura *et al.*, 2003; Fujiwara-Tsukamoto *et al.*, 2010; Raimondo *et al.*, 2013; Ellender *et al.*, 2014). This is thought to result from phasic GABA release at GABAergic synapses and post-synaptic membrane depolarisation, which can generate pronounced Cl^- influxes via Cl^--permeable $GABA_AR$'s (Raimondo *et al.*, 2015). The failure to observe such a response here may therefore reflect the degree to which the transplanted human neurons receive functional synaptic connections from the host neurons. Consistent with this idea, previous work has shown that host-to-graft synaptic connections with iPSC-derived neurons are rare, such that only approximately 5% of transplanted neurons receive synaptic inputs over the timescale examined here (Avaliani *et al.*, 2014).

For the majority of the human iPSC-derived astrocytes, NEs were associated with an increase in $[Cl^-]_i$. This could reflect the fact that the astrocytes are able to integrate more effectively with the host tissue. Alternatively, this could reflect the fact that astrocytes rely upon different mechanisms to respond to elevated network activity (Verkhratsky and Nedergaard, 2016). More specifically, an increase in $[Cl^-]_i$ may not require the astrocytes to receive GABAergic synaptic inputs from the host tissue, but may instead reflect the action of

one, or a combination of ion transporter proteins, which are known to be expressed by astrocytes. These include the inward transporting action of the Na^+-K^+-Cl^- co-transporter-1 (NKCC1), the reversed action of potassium chloride cotransporters (KCC's) that normally export one Cl^- for every K^+ (Annunziato, Boscia and Pignataro, 2013), or the reversed action of the Cl^-/HCO_3^- anion exchanger, which performs equimolar exchange of external HCO_3^- for internal Cl^- (Russell and Boron, 1976). The fact that the astrocytes experience activity-dependent alkalinisations, makes the Cl^-/HCO_3^- anion exchanger an attractive candidate, as increases in intracellular HCO_3^- could reverse the Cl^-/HCO_3^- anion exchanger to generate increases in $[Cl^-]_i$. However, further experimentation will be required to determine the relative contribution of these different mechanisms.

In summary, these experiments demonstrate that human iPSC-derived astrocytes exhibit many similar ion-handling capabilities as their rodent counterparts. The iPSC-derived astrocytes produce both synchronous and asynchronous spontaneous Ca^{2+} elevations, and exhibit intracellular Ca^{2+} events in response to physiologically relevant neurotransmitters. The iPSC-derived astrocytes experience activity-dependent alkalinisations during periods of network activity, which both pre-empt and oppose the activity-dependent acidic pH dynamics in neurons. These experiments support the view that iPSC-derived human astrocytes are able to perform appropriate homeostatic functions, both in the context of dissociated cultures and in more physiologically relevant contexts. This supports the relevance of using the iPSC-derived astrocytes for investigating aspects of cellular interactions in normal and diseased states. Another aspect where neurons rely on astrocytic support is for their maturation, particularly in terms of establishing functional synaptic networks. The next chapter will firstly

examine if iPSC-derived human neurons and astrocytes interact in this important way, serving to enhance neuronal maturation when co-cultured. Where this chapter has characterised some of the passive homeostatic functions of astrocytes, the following chapter will secondly explore the capabilities of the human astrocytes to engage actively in astrocyte-to-neuron signalling. As demonstrated in the beginning of this chapter, the human astrocytes possess the capacity to respond to neural transmission and translate this into internal Ca^{2+} events, but whether they can subsequently form part of a feedback loop and influence neuronal signalling is unknown.

Chapter 5

5 ASTROCYTES CAN MEDIATE PLASTICITY IN HUMAN CORTICAL NEURONS

5.1 Introduction

Throughout brain development and adulthood, astrocytes form part of a close interplay with neurons. Particularly with regards to synapses, astrocytes serve a key role from the outset, as they can contribute to synaptogenesis, synapse maturation and ultimately synaptic pruning during development; roles which all contribute to shaping neuronal networks (Clarke and Barres, 2013). In the adult brain, fine astrocytic processes enwrap individual synapses, which place them in a critical position for regulating transmission between neurons (see **Chapter 1**). Neuron-astrocyte interactions in both healthy and disease states are well-characterised in rodent models. However, the degree to which astrocyte functions and dysfunctions translate to human cells is an open question. iPSC-technologies offer an opportunity to address this question.

Pro-maturational effects on neuronal differentiation have been described in co-culture models utilising human iPSC-derived neurons and rodent astrocytes. Neuronal survival has been shown to be improved by rodent astrocyte conditioned media or physical co-culture with rodent astrocytes (Tang *et al.*, 2013). This and subsequent work (Prè *et al.*, 2014) found that physical co-culture can advance the maturation of intrinsic electrical properties of iPSC-derived neurons, as well as aspects of synaptic transmission, when compared to enriched neuronal cultures on a laminin substrate. Other studies using microelectrode arrays to assess activity in networks of human neurons have also reported that astrocyte conditioned media

can enhance spontaneous spiking activity within the cultures (Fukushima *et al.*, 2016), and even further maturational effects were seen upon co-culture with rat astrocytes (Odawara *et al.*, 2014). Likewise, studies co-culturing iPSC-derived human neurons and human astrocytes on microelectrode arrays have recently demonstrated more complex neuronal spiking patterns and circuit formation, in a manner that is dependent upon astrocytes and the ratio of inhibitory and excitatory neurons (Kayama *et al.*, 2018; Tukker *et al.*, 2018). Together, these data support the idea that rodent and human astrocytes can provide pro-maturational signals to human iPSC-derived neurons. Having generated and characterised human iPSC-derived astrocytes in the earlier work (see **Chapter 3** and **4**), an important question is whether these cells are able to convey similar maturational effects to co-cultured neurons.

Beyond supporting the maturation of neuronal networks, experimental work in rodents has implicated astrocytes in a variety of activity-dependent processes that can adjust the strength of established synaptic connections. This includes homeostatic forms of neuronal plasticity (Stellwagen and Malenka, 2006) and both short-term and long-term forms of synaptic plasticity (Pascual *et al.*, 2005; Jourdain *et al.*, 2007; Henneberger *et al.*, 2010; Panatier *et al.*, 2011). The process used to account for these synapse-modulating effects mediated by astrocytes is "gliotransmission". Gliotransmission was initially described in the 1990's as an activity-dependent feedback from astrocytes to neurons in the form of neuroactive substances (Cornell-Bell *et al.*, 1990; Parpura *et al.*, 1994; Bezzi *et al.*, 1998), and has generally been believed to involve intracellular Ca^{2+} signals in astrocytes, although this mechanistic aspect is a source of current debate (see **Chapter 1**). Consistent with the Ca^{2+}-dependent exocytosis model of gliotransmission, optogenetic strategies have been used to directly elicit

temporally-controlled Ca^{2+} events in astrocytes through light activation of the cation channel ChR2 (Boyden *et al.*, 2005). Optogenetically-induced Ca^{2+} events in astrocytes could result directly from ChR2's permeability to Ca^{2+} (Nagel *et al.*, 2003), and via more indirect mechanisms such as reversing ion transport via the Na^{+}/Ca^{2+} exchanger (Yang *et al.*, 2015).

In rodent preparations, acute optogenetic stimulation of astrocytes and the associated elevations in intracellular Ca^{2+} have been shown to evoke glutamate release that can influence nearby neurons in a short-term fashion (Sasaki *et al.*, 2012; Berlinguer-Palmini *et al.*, 2014; Perea *et al.*, 2014; Shen *et al.*, 2017a). For example, Perea and colleagues reported ChR2-evoked glutamate release from astrocytes, detected as NMDA-mediated slow inward currents in brain slice preparations. They further demonstrated enhanced synaptic transmission between nearby neurons during light-stimulation, which was mediated by the activation of presynaptic metabotropic glutamate receptors (mGluR1a) (Perea *et al.*, 2014). Other work has reported that ChR2-mediated ion fluxes and/or associated changes in intracellular osmolarity can trigger efflux of glutamate from the astrocyte through volume-regulated anion channels (VRACs) (Sasaki *et al.*, 2012), consistent with evidence that Ca^{2+} elevations evoked in astrocytes through LiGluR stimulation can result in glutamate release that is independent of vesicular mechanisms, hemichannels and glutamate-transporters (D. Li *et al.*, 2012).

iPSC technology provides a genuine opportunity to explore whether these sorts of neuron-astrocyte interactions that have been studied in rodents, also hold true for human cells. The *in vitro* iPSC system enables assessment of cellular processes at the scale of synapses, the function of which can be assessed electrophysiologically. Furthermore, the generation of

separate enriched neuronal or astrocytic cultures for subsequent co-culturing makes it relatively easy to manipulate one cell type independently from the other. In doing so, there is also the potential to investigate functional properties of astrocytes and their signalling to neurons in healthy and disease states. For these reasons, the objective of this chapter was to investigate potential human astrocyte-neuron interactions using iPSC-derived cortical neurons and astrocytes.

More specifically, the aims of this chapter are to:

1) Investigate whether human iPSC-derived astrocytes advance the functional maturation of iPSC-derived cortical neurons.

2) Establish an optogenetic paradigm in which activity-dependent astrocyte signalling can be temporally controlled with light.

3) Examine whether optogenetic stimulation of astrocytes can elicit modulation of human cortical synapses over different timescales.

5.2 Results

To investigate if iPSC-derived human astrocytes can regulate the functional maturation of iPSC-derived cortical neurons, the two cell types were placed in physical contact by co-culturing them on the same coverslip (see section 2.2.7). Given evidence for pro-maturational effects of rodent astrocytes (Tang *et al.*, 2013; Odawara *et al.*, 2014; Prè *et al.*, 2014; Fukushima *et al.*, 2016), this condition was also tested and used as a comparison for the human astrocytes. The neurons used in the co-cultures were first transduced with a CamKII-mKate construct for identification and to aid selective recording. Thus, the conditions being compared were human neurons plated on three different substrates: 1) as enriched neuronal culture on polyornithine and laminin (P+L), 2) as co-culture on rat astrocytes and 3) as co-culture on human iPSC-derived astrocytes (**Figure 5.1A**). Neuronal ages at the time of recording were: P+L: 92 ± 3.3 days (range 79-117 days), on rat astrocytes: 99 ± 2.4 days (range 87-110 days) and on human astrocytes: 79 ± 6.7 days (range 66-87 days). To compare neuronal maturity in the three conditions, whole-cell patch clamp recordings were first used to measure the intrinsic excitability of the neurons (size of $VGNa^{+}$ currents, number of APs initiated and AP threshold), as well as the passive membrane properties (membrane capacitance, membrane resistance and Vm_{rest}), (**Figure 5.1B**) (see section 2.4.2).

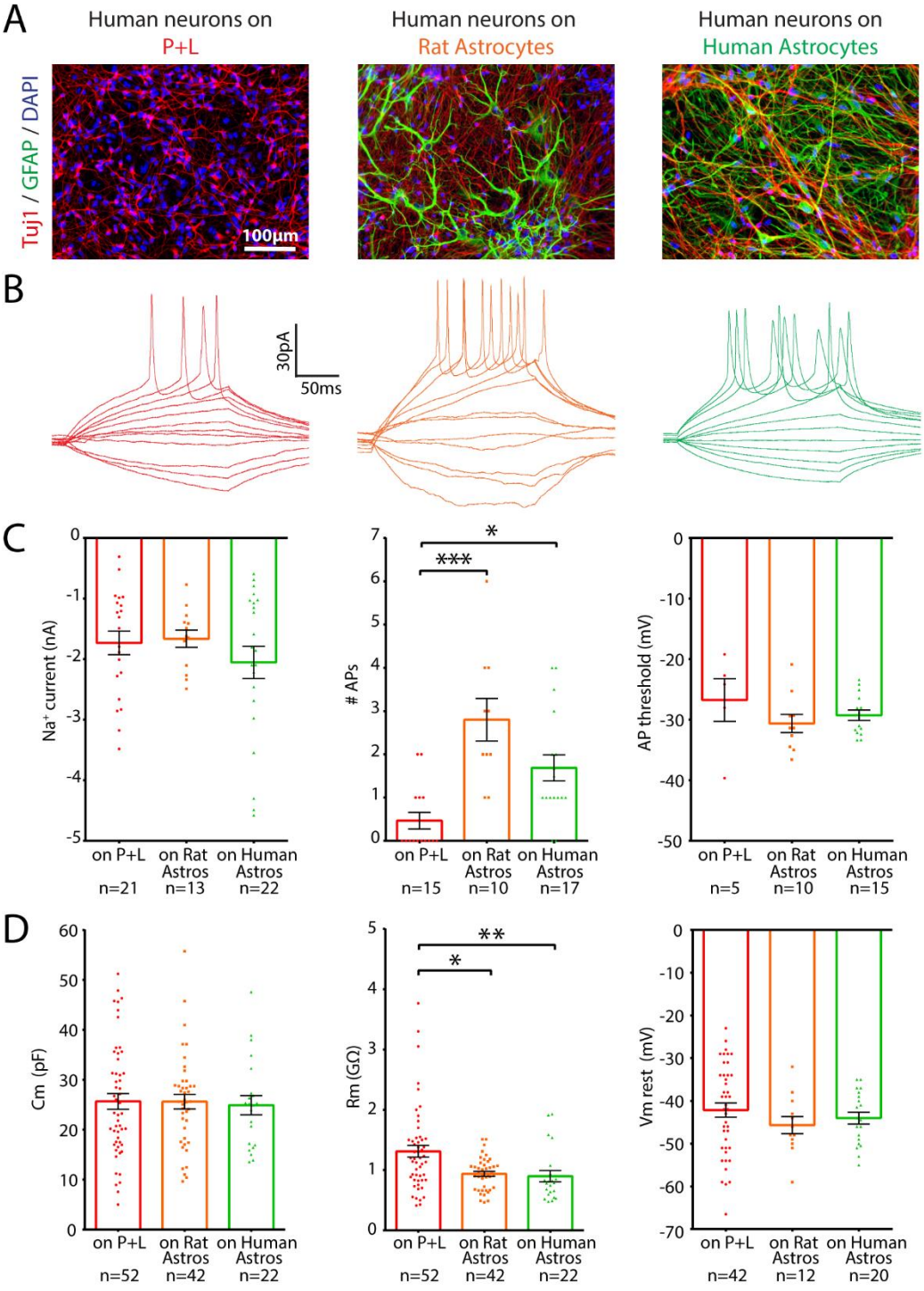

Figure 5.1 Co-culturing with astrocytes enhances aspects of human neuronal excitability

(A) Immunofluorescence images of three culture-conditions used to compare the active and passive membrane properties of human cortical neurons grown either in monoculture on polyornithine and laminin coated coverslips (P+L, left), as co-cultures with rat astrocytes (middle), or as co-cultures with human astrocytes (right). **(B)** Representative action potentials (AP's) evoked in the three conditions in response to current steps. **(C)** Co-culturing with astrocytes did not affect the size of voltage-gated Na^+ currents, but it significantly increased the number of AP's that neurons elicited. **(D)** Membrane capacitance (Cm) and resting membrane potential (Vm rest) were unaltered between culture conditions, but co-culturing with astrocytes lowered the membrane resistance (Rm).

The size of $VGNa^+$ currents did not differ between the conditions (p=0.877, un-paired Kruskall-Wallis test) and no individual differences were detected when comparing each co-culture condition with the P+L condition (on P+L: -1.7 ± 0.2 nA, n=21 neurons; from 3 cell lines, 4 inductions; on rat astrocytes: -1.7 ± 0.14 nA, n=13 neurons; from 1 cell line, 2 inductions; p<0.999; on human astrocytes: -2.1 ± 0.27 nA, n=22 neurons; from 1 cell line, 1 induction; p>0.999, Dunn's multiple comparisons test) (**Figure 5.1C**), where the 1 cell line used was the same (SBAd 03-01) in both co-culture conditions. However, the propensity of the neurons to fire APs in response to somatic current injection was greatly enhanced by co-culture with both rat and human astrocytes (p=0.0002, un-paired Kruskall-Wallis test). This effect was driven by differences between the P+L condition with respect to both co-culture conditions, as the mean number of APs for neurons grown on P+L was 0.5 ± 0.2 APs per 200 ms (n=15 neurons; from 3 cell lines, 3 inductions), whilst the equivalent number for neurons grown with rat astrocytes was 2.8 ± 0.5 APs per 200 ms (n=10 neurons; from 1 cell line, 2 inductions; p=0.0001, Dunn's multiple comparisons test) and for neurons grown with human astrocytes this value was 1.7 ± 0.3 APs per 200 ms (n=17 neurons; from 1 cell line, 1 induction p=0.011, Dunn's multiple comparisons test) (**Figure 5.1C**). The threshold for AP initiation was unaltered between conditions (p=0.219, un-paired Kruskall-Wallis test), with no individual differences detected by the multiple comparisons test (on P+L: -26.7 ± 3.5 mV, n=5 neurons; on rat astrocytes: -30.6 ± 1.5 mV, n=10 neurons; p=0.163; on human astrocytes: -29.3 ± 0.9 mV, n=15 neurons; p=0.470, Dunn's multiple comparisons test) (**Figure 5.1C**).

Furthermore, the culture condition was not associated with effects upon the membrane capacitance (p=0.858, un-paired Kruskall-Wallis test), with no differences between

individual conditions (on P+L: 25.7 ± 1.6 pF, n=52 neurons; from 3 cell lines, 5 inductions; on rat astrocytes: 25.6 ± 1.5 pF, n=42 neurons; from 1 cell line, 2 inductions; p>0.999; on human astrocytes: 24.9 ± 1.9 pF, n=22 neurons; from 1 cell line, 1 induction; p>0.999, Dunn's multiple comparisons test) (**Figure 5.1D**). Resting membrane potential was unaffected by culture condition (p=0.436, un-paired Kruskall-Wallis test), with no individual differences between conditions detected by the multiple comparisons test (on P+L: -42.1 ± 1.7 mV, n=42 neurons; on rat astrocytes: -45.7 ± 2.0 mV, n=12 neurons; p=0.458; on human astrocytes: -44.0 ± 1.4 mV, n=20 neurons; p=0.885, Dunn's multiple comparisons test) (**Figure 5.1D**). However, a significant decrease in membrane resistance was observed when neurons were co-cultured with astrocytes (p=0.002, un-paired Kruskall-Wallis test), a difference which was observable with astrocytes of either rat or human origin (on P+L: 1.3 ± 0.1 GΩ, n=52 neurons; on rat astrocytes: 0.94 ± 0.04 GΩ, n=42 neurons; p=0.018; on human astrocytes: 0.90 ± 0.09 GΩ, n=22 neurons; p=0.002, Dunn's multiple comparisons test) (**Figure 5.1D**).

Having observed that co-culturing iPSC-derived cortical neurons with astrocytes enhanced aspects of intrinsic membrane excitability, I next examined whether human astrocytes affect the functional maturation of synaptic networks. The presence of physical synapses on the neurons was first confirmed with immunolabelling of the presynaptic vesicle protein synaptophysin, whose punctate staining overlapped with neuronal processes (**Figure 5.2A**) (see section 2.3.1). To assess if astrocytic co-cultures enhanced the functional synaptic connectivity, recordings of spontaneous glutamatergic synaptic currents were conducted in a subset of the neurons presented in **Figure 5.1** (see section 2.4.3). Each neuron was held in voltage clamp at -70 mV and was classified as synaptically active if it received >1 sEPSC per

minute (**Figure 5.2B**), neurons in each condition were: P+L from 3 cell lines, 5 inductions, on rat astrocytes from 1 cell line, 2 inductions and on human astrocytes from 1 cell line, 1 induction. The proportions of synaptically active neurons were enhanced by both co-culture conditions, with the most active neurons detected on human astrocytes (on P+L: 43%, n=44 neurons; on rat astrocytes: 69%, n=42 neurons; on human astrocytes: 82%, n=22 neurons; p=0.004, chi-square contingency test) (**Figure 5.2C**). Overall the frequency of sEPSCs was significantly increased (p=0.050, un-paired Kruskall-Wallis test), which was driven by a significant difference between the P+L and human astrocyte co-culture condition, but not between the P+L and rat astrocyte condition (on P+L: 0.15 ± 0.04 Hz, n=44 neurons; on rat astrocytes: 0.26 ± 0.08 Hz, n=42 neurons; p=0.227; on human astrocytes: 0.31 ± 0.11 Hz, n=22 neurons; p=0.038, Dunn's multiple comparisons test) (**Figure 5.2C**). The amplitude of sEPSCs received by the active neurons was unchanged between conditions (p=0.532, un-paired Kruskall-Wallis test), with no differences detected between individual conditions (on P+L: 17.5 ± 1.2 pA, n=19 neurons; on rat astrocytes: 23.0 ± 3.0 pA, n=29 neurons; p=0.718; on human astrocytes: 21.2 ± 2.2 pA, n=18 neurons; p=0.595, Dunn's multiple comparisons test) (**Figure 5.2C**). These results corroborate findings from studies exploring the benefits of co-culturing iPSC-derived neurons with rat astrocytes (Tang *et al.*, 2013; Odawara *et al.*, 2014; Lischka *et al.*, 2017). But importantly, they demonstrate that human astrocytes also exhibit pro-maturational effects on synaptic networks, a feature which is considered a hallmark of astrocyte functionality (Stevens, 2008; Dodla, Mumaw and Stice, 2010; Allen, 2013; Clarke and Barres, 2013; Chung, Allen and Eroglu, 2015; Allen and Eroglu, 2017).

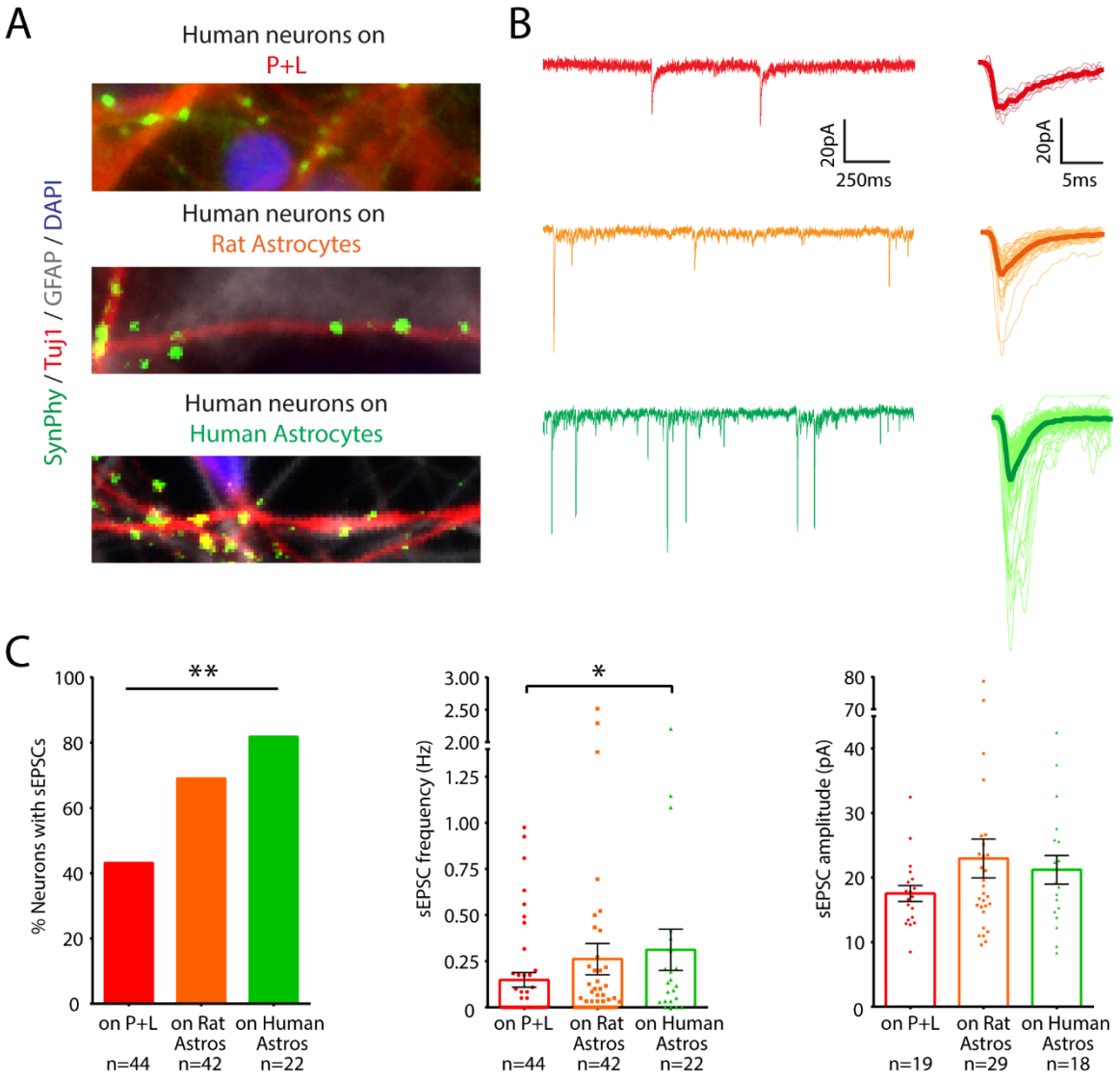

Figure 5.2 Co-culturing with astrocytes enhances synaptic networks amongst human cortical neurons

(A) The effect of astrocytes on synaptic connectivity was assessed by comparing human cortical neurons grown under one of three conditions: (i) in monoculture on polyornithine and laminin coated coverslips (P+L, top), (ii) as co-cultures with rat astrocytes (middle) or (iii) as co-cultures with human astrocytes (bottom). The presence of synapses was verified anatomically in all three culture conditions by immunolabelling with the pre-synaptic marker synaptophysin (SynPhy). Distinct SynPhy$^+$ puncta overlapped with Tuj1$^+$ neuronal processes. **(B)** Live neurons were targeted for whole-cell patch clamp electrophysiology and recordings of spontaneous excitatory post-synaptic currents (sEPSCs) are shown for representative neurons in each of the three conditions (left). Detected sEPSCs are shown with the average highlighted in bold (right). **(C)** The proportion of neurons receiving sEPSCs was significantly higher in co-cultures with either rat or human astrocytes (left). The frequency of sEPSCs was enhanced (middle), without detectable effects upon the amplitude of the sEPSCs (right). * $p < 0.05$, ** $p < 0.01$, *** $p < 0.001$

Having established that the human iPSC-derived astrocytes can influence the functional maturity of human synaptic networks, I next examined whether the astrocytes could participate in activity-dependent signalling to the human neurons. Given previous evidence from rodent literature regarding Ca^{2+}-dependent gliotransmission (Jeftinija, Jeftinija and Stefanovic, 1997; Pasti *et al.*, 1997; Parpura and Haydon, 2000; Bezzi *et al.*, 2004; Kreft *et al.*, 2004; Montana *et al.*, 2004; Zhang *et al.*, 2004; Domercq *et al.*, 2006; Liu *et al.*, 2011; Santello, Calì and Bezzi, 2012), I set out to establish an experimental paradigm in which I could selectively manipulate astrocytic Ca^{2+}-fluxes. An optogenetic strategy was adopted, on the basis that activating the light-sensitive cation channel, ChR2, can elicit Ca^{2+} events, ion fluxes and membrane depolarisation in astrocytes, which have all been implicated in activity-dependent astrocyte signalling (D. Li *et al.*, 2012; Sasaki *et al.*, 2012; Perea *et al.*, 2014; Yang *et al.*, 2015). A lentiviral construct containing ChR2 coupled to yellow fluorescent protein (YFP) and under the control of the ubiquitous CAG promoter, was generated and used to transduce astrocytes (**Figure 5.3A**) (see section 2.3.3). The ChR2(H134R) variant was used as this has been shown to generate large photocurrents at low light levels (Berndt *et al.*, 2011), which would afford the opportunity to stimulate astrocytes over a range of timescales.

ChR2(H134R) is activated by blue light, with responses peaking at an excitation wavelength of approximately 460 nm (Lin *et al.*, 2009). The ability of a 450 nm LED to stimulate intracellular Ca^{2+} events in both rat and human astrocytes was therefore tested by performing targeted whole-cell voltage clamp recordings or calcium imaging (**Figure 5.3B**).

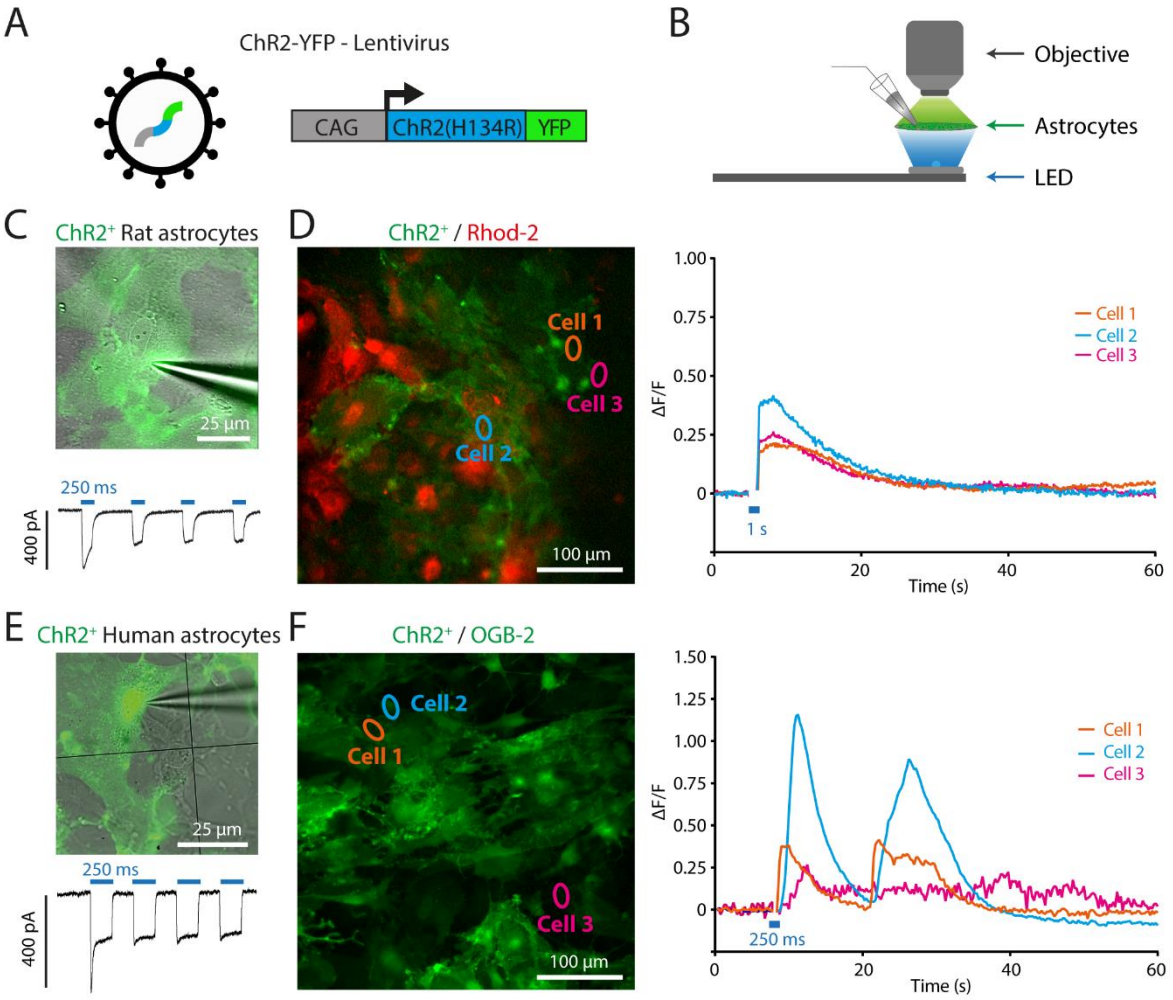

Figure 5.3 Acute ChR2-mediated optical stimulation evokes intracellular calcium events in rat and human astrocytes

(A) Illustration of the lentiviral construct used to deliver ChR2 to astrocytes. The ubiquitous CAG promoter drives expression of the ChR2 variant H134R, fused to yellow fluorescent protein (YFP). **(B)** Illustration of the recording setup, where ChR2$^+$ astrocytes could be illuminated with a 450 nm blue LED located beneath the recording chamber. **(C)** Photocurrents recorded in a ChR2$^+$ rat astrocyte. Four LED pulses of 250 ms duration elicited currents with an amplitude of 300-400 pA. **(D)** ChR2 activation generates intracellular calcium events in rat astrocytes. ChR2$^+$ rat astrocytes were loaded with the Ca^{2+} dye Rhod-2 (AM-ester form) (left). ΔF/F traces from the three highlighted astrocytes (right) reveal the intracellular calcium dynamics following ChR2 activation with a 1 s duration LED flash. **(E)** ChR2 activation generates photocurrents and intracellular calcium events in human astrocytes. Four LED pulses of 250 ms duration elicited photocurrents with an amplitude of 300-400 pA in a ChR2$^+$ human astrocyte. **(F)** ChR2$^+$ human astrocytes were loaded with the Ca^{2+} dye OGB-2 (AM-ester form) (left). ΔF/F traces from the three highlighted astrocytes (right) reveal the intracellular calcium dynamics following ChR2 activation with a 250 ms duration LED flash.

Firstly, recordings from patched rat astrocytes confirmed that LED stimulation reliably evoked depolarising photocurrents, with a typical waveform that included a fast activating current followed by a desensitizing steady-state current (Berndt *et al.*, 2011) (**Figure 5.3C**). Secondly, in line with previous findings, photocurrents in ChR2$^+$ rat astrocytes were shown to correspond with intracellular Ca^{2+} elevations (Yang *et al.*, 2015), as detected with the Ca^{2+}-dye Rhod-2 AM (see sections 2.1.9 and 2.5.1). An obvious increase in Rhod-2 fluorescence was observed in response to the LED flashes (**Figure 5.3D**). Similar to rat astrocytes, photocurrents were reliably elicited by LED flashes in whole-cell patched human astrocytes (**Figure 5.3E**). Reproducible loading with Rhod-2 proved more difficult in human astrocytes, so the more widely-used green Ca^{2+}-dye OGB-2 AM, was used (see section 2.1.9). This imaging strategy also revealed that intracellular Ca^{2+} elevations were associated with optical stimulation of ChR2$^+$ human astrocytes (**Figure 5.3F**).

Having established ChR2 as a tool to drive depolarisation and Ca^{2+} increases in astrocytes, I wanted to examine what short-term effects this might have in co-cultures with neurons. More specifically, studies in rodent systems have demonstrated enhanced synaptic transmission, as a result of astrocytic ChR2 stimulation (Sasaki *et al.*, 2012; Berlinguer-Palmini *et al.*, 2014; Perea *et al.*, 2014). I therefore set out to test whether optical stimulation of astrocytes could acutely modulate synaptic transmission in human co-cultures. By using the same optical setup, I interrogated co-cultures of ChR2-expressing human astrocytes and mKate$^+$ neurons (**Figure 5.4A**). The neurons recorded were on average 58 ± 0.9 days from induction initiation (range 56-60 days) and experiments were conducted on the same control cell line (SBAd 03-01). A stimulation paradigm using long pulses (245 ms pulses delivered at

2-4 Hz) was chosen, as this paradigm had successfully initiated photocurrents and Ca^{2+} activity in the human astrocytes (see section 2.4.6). Whole-cell patch clamp recordings from the neurons during light stimulation of the astrocytes revealed that sEPSC frequencies increased during LED stimulation compared to pre-stimulation baseline (baseline: 1.0 (normalised), acute stimulation: 2.2 ± 0.4x baseline, n=14 recordings from 10 neurons; from 1 cell line, 1 induction; p=0.004, Wilcoxon signed rank test) (**Figure 5.4B** and **C**).

Given previous findings in rodent astrocytes (Perea *et al.*, 2014), I next tested whether this acute enhancement of sEPSC frequency was mediated by mGluRs. Having first confirmed that the recorded neuron exhibited a light-dependent sEPSC enhancement, I then repeated the light stimulation in the presence of the general mGluR blocker MCPG (0.8 mM; **Figure 5.4D**). In all 3 neurons where this was performed, the frequency of sEPSCs did not increase in the presence of MCPG (baseline: 1.0 (normalised), acute stimulation + MCPG: 0.65 ± 0.19 x baseline, n=3 recordings from 3 neurons; p=0.500, Wilcoxon signed rank test) (**Figure 5.4E**). Upon washout of MCPG, light stimulation was again able to elicit sEPSC enhancement (**Figure 5.4F**). These experiments demonstrate that ChR2 stimulation of human astrocytes can acutely enhance excitatory synaptic signalling within a network of iPSC-derived cortical neurons via an mGluR-dependent mechanism (**Figure 5.4G**).

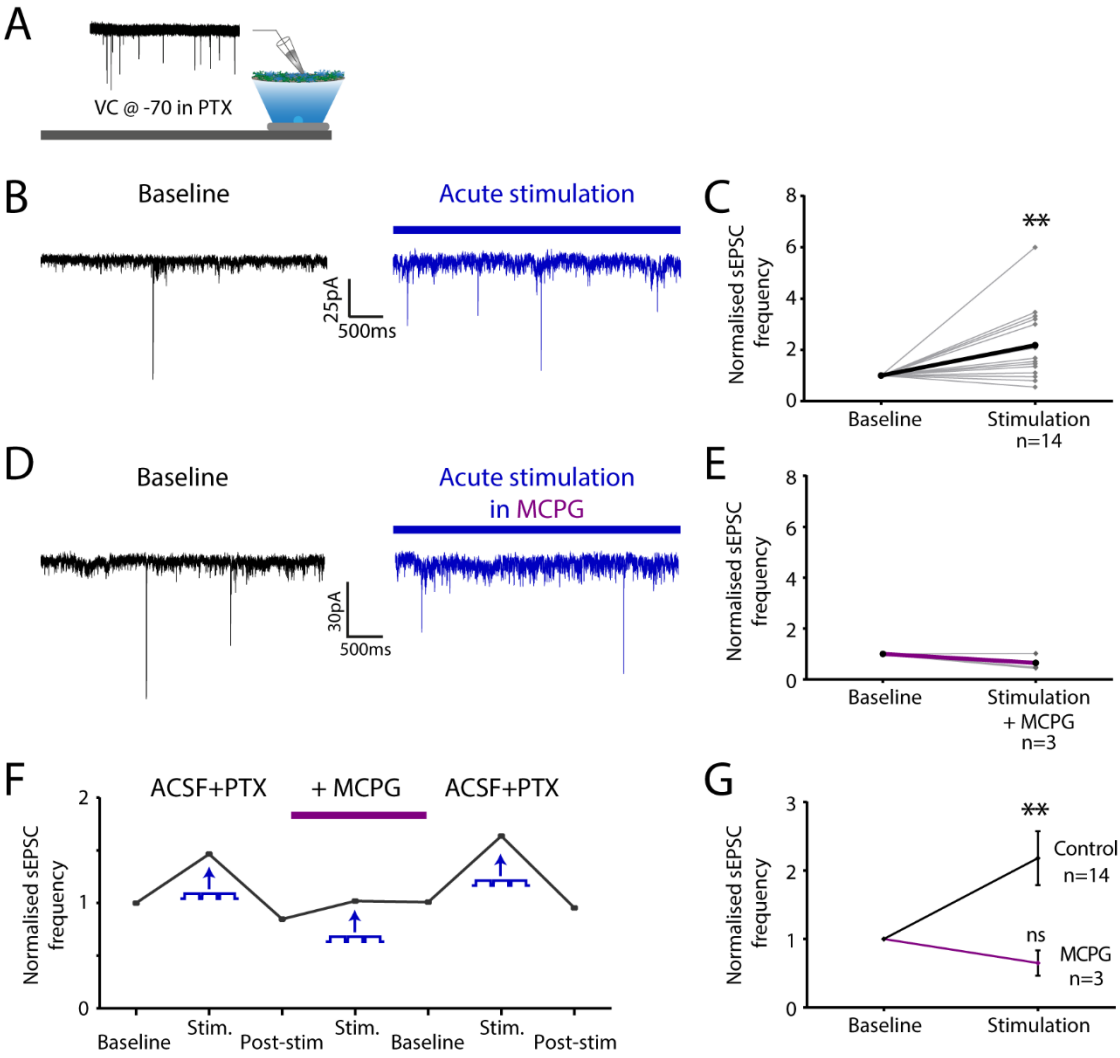

Figure 5.4 Acute ChR2-mediated optical stimulation of astrocytes enhances glutamatergic synaptic network activity via an mGluR-dependent mechanism
(A) Recording setup in which a co-culture of ChR2^{+} astrocytes and (mKate^{+}/ChR2^{-}) human neurons was illuminated via a 450 nm blue LED. Glutamatergic sEPSCs were recorded from neurons at -70 mV in voltage clamp (VC), in the presence of PTX. **(B)** After recording sEPSCs under baseline conditions, the astrocytes were stimulated with a continuous train of LED pulses (250 ms pulse duration at 2-4 Hz). **(C)** The frequency of sEPSCs increased during the period of optical stimulation of the astrocytes. All values are normalised to the baseline frequency. **(D)** Example traces from the same baseline and stimulation paradigm as in '**B**', but in the presence of the general mGluR blocker MCPG. **(E)** The increase in sEPSC frequency due to optical stimulation of astrocytes was abolished in the presence by MCPG. **(F)** Normalised sEPSC frequency changes during a single experiment. The neuron displayed a clear sEPSC frequency increase during LED stimulation, both before and after bath-application of MCPG, but not in the presence of MCPG. **(G)** Summary plot showing the averaged sEPSC frequency increase in the absence (black) and presence (purple) of MCPG.

Having established a paradigm for optically eliciting activity-dependent signalling in human astrocytes, I was keen to assess whether this could be utilised to investigate astrocyte-neuron interactions evoked over longer timescales. For this purpose, I developed an experimental setup that allowed for LED stimulation over multiple days inside a tissue culture incubator (**Figure 5.5A**) (see further details in section 2.2.8). To eliminate potential heat sources, the LEDs were mounted on a heat-sink that was suspended above the culture-plate,

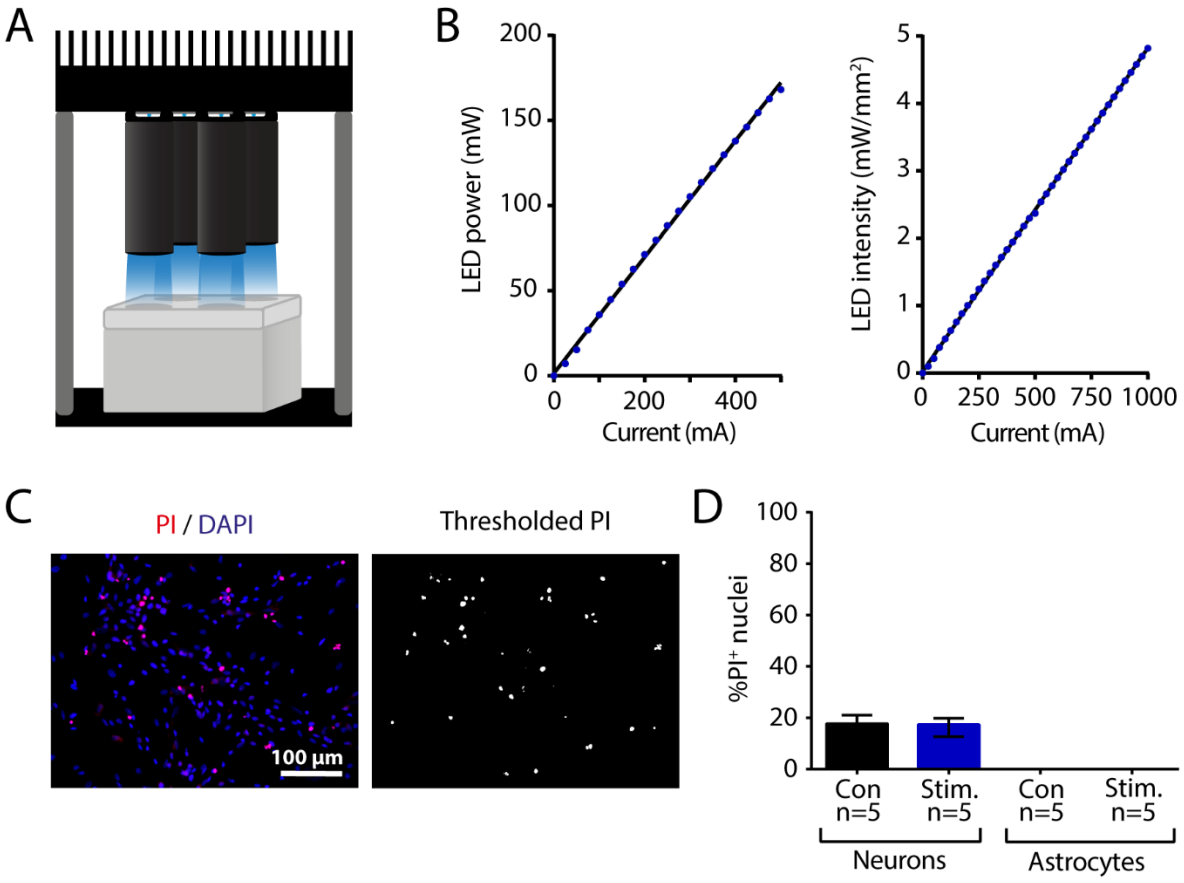

Figure 5.5 Long-term optical stimulation of astrocyte-neuron co-cultures
(A) Illustration of the LED setup used for long-term stimulation of ChR2 inside the tissue culture incubator. The inverted design and lens relay system removes any potential heat source from the cells. **(B)** LED power (left) and intensity (right) were confirmed to be linearly related to the LED current. **(C)** Assessment of cell death in co-cultures of ChR2$^+$ human astrocytes and human cortical neurons exposed to 4 days of LED stimulation. Example field of view stained with propidium iodide (PI) and DAPI (left). Quantification of PI$^+$ cells was performed by thresholding the image (right). **(D)** No difference in neuronal cell death was detected between the control (no light) and the LED stimulated condition (n=5 FOV from 1 culture in each condition). PI was never observed inside astrocytic nuclei, which are easily distinguished by their larger size and dimmer DAPI staining.

and the light was focussed onto the cells via collimating and focusing lenses. Light levels were measured at the position of the cells and the LED output was found to be linear within the range of required intensities (1-3 mW/mm^2) (**Figure 5.5B**).

A light intensity of 1 mW/mm^2 was selected for this long-duration stimulation, as this has been shown to be sufficient to elicit maximal currents from the H134R variant of ChR2 (Hochbaum *et al.*, 2014). Furthermore, I confirmed that prolonged exposure to this level of light was not associated with any cell death. Staining 1 set of co-cultures with the cell-membrane impermeant DNA marker propidium iodide (PI) (**Figure 5.5C**), revealed that pulsed light exposure over 4 days (250 ms duration pulses, at 50 s intervals) did not increase the proportion of neurons or astrocytes with damaged membranes, when compared to co-cultures maintained in the dark (PI^+ neuronal nuclei; control: 16.2 ± 2.5 %, n=5 FOV; stimulated: 16.5 ± 1.8 %, n=5 FOV, $p>0.999$, un-paired Mann-Whitney test) (**Figure 5.5D**). With this incubator setup, I investigated whether a prolonged period of astrocyte stimulation can mediate effects upon a network of synaptically-connected neurons that lasts beyond the duration of the light pulse. I first sought to optimise the experimental conditions using rat astrocyte and human iPSC-derived neuron co-cultures.

In the first series of experiments therefore, rat astrocytes were lentivirally-transduced with ChR2-YFP, prior to the addition of human iPSC-derived cortical neurons (**Figure 5.6A**). Each set of cultures was divided into a "stimulated condition", where cultures were placed on the LED incubator setup, and a "control condition", where cultures were maintained in darkness within the incubator so that the ChR2-expressing astrocytes would not be stimulated. A criteria of equivalent expression of ChR2 between control and stimulated

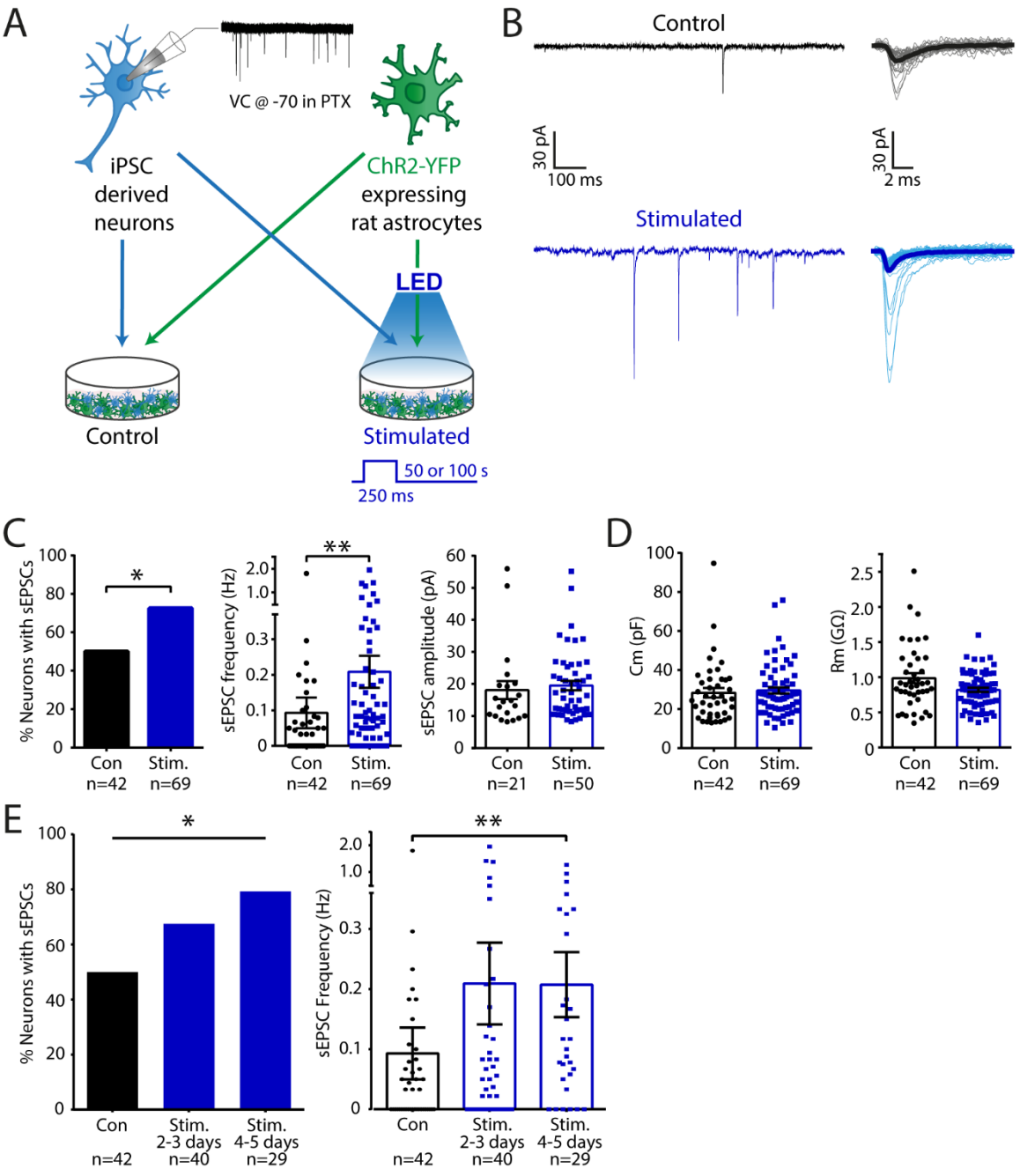

Figure 5.6 Astrocyte-mediated neuronal plasticity following long-term ChR2 stimulation of rat astrocytes

(A) Cartoon showing the experimental design. Recordings of sEPSCs were performed in co-cultures of iPSC-derived cortical neurons and ChR2$^+$ rat astrocytes. In the control condition, co-cultures were maintained in darkness in the tissue culture incubator, whereas in the stimulated astrocytes condition, 250 ms LED flashes were delivered every 50 or 100 seconds for 2-5 days. **(B)** Example traces (left) recorded from a neuron in the control (top) and stimulated condition (bottom). All detected sEPSCs are shown overlaid, with the mean sEPSC in bold (right). **(C)** Optical stimulation of astrocytes resulted in significant increases in the proportion of neurons receiving sEPSCs and the frequency of sEPSCs, without a detectable effect upon sEPSC amplitude. **(D)** Membrane capacitance (Cm) and membrane resistance (Rm) were not different between the control and stimulated conditions. **(E)** Data plotted according to how many days the culture had received LED stimulation.

conditions was imposed (see section 2.2.8) for inclusion of individual experiments in the pooled dataset. The stimulation condition involved delivering 250 ms LED light flashes, repeated every 50 seconds, for a period of 2-5 days, a protocol which was settled on after also trying delivery of trains of pulses or pulses every 100 seconds (data not shown). At the end of this period, neurons on the coverslips were targeted for electrophysiological recordings from control and stimulated cultures using an interleaved experimental design, such that the age of the neurons was matched for each experiment. Data was collected from a total of 5 separate experiments, which included iPSC-derived cortical neurons from 3 different inductions of the same control cell line (SBAd 03-01), and incorporated a neuronal age-range of 64-99 days (average age, control: 81 ± 6.6 days, stimulated: 76 ± 5.2 days).

Excitatory synaptic activity was assessed via sEPSC recordings conducted in voltage clamp at -70 mV (**Figure 5.6B**). The proportion of synaptically active neurons was found to be significantly increased by astrocytic stimulation (control: 50%, n=42 neurons; stimulated: 72.5%, n=69 neurons; p=0.017, chi-square contingency test) (**Figure 5.6C**), which was associated with an increase in the frequency of sEPSCs (control: 0.09 ± 0.04 Hz, n=42 neurons; stimulated: 0.2 ± 0.05 Hz, n=69 neurons; p=0.005, un-paired Mann-Whitney test) (**Figure 5.6C**). No effect upon the amplitude of sEPSCs was detected (control: 18.1 ± 2.8 pA, n=21 neurons; stimulated: 19.5 ± 1.5 pA, n=50 neurons; p=0.231, un-paired Mann-Whitney test) (**Figure 5.6C**).

Furthermore, the membrane capacitance and resistance were comparable for the two conditions, confirming that recordings were not biased towards different cell populations (Cm: control: 28.3 ± 2.4 pF, n=42 neurons; stimulated: 29.5 ± 1.5 pF, n=69 neurons; p=0.340, un-

paired Mann-Whitney test. Rm: control: 1.0 ± 0.07 GΩ, n=42 neurons, Stimulated: 0.8 ± 0.03 GΩ, n=69 neurons; p=0.121, un-paired Mann-Whitney test) (**Figure 5.6D**). If the data was subdivided according to the period of time that the cultures had been stimulated in the incubator, it was observed that the enhancement of sEPSCs was greater after 4-5 days than after 2-3 days, both in terms of the proportion of synaptically active neurons (control: 50%, n=42 neurons; stimulated 2-3 days: 67.5%, n=40 neurons; stimulated 4-5 days: 79.3%, n=29 neurons; p=0.035, chi-square contingency test) (**Figure 5.6E**), as well as the frequency of sEPSCs (p=0.007, un-paired Kruskall-Wallis test). The increase in sEPSC frequency was driven by a significant difference between control and 4-5 days stimulation, but not between control and 2-3 days of stimulation (in control cultures, the mean was 0.09 ± 0.04 Hz and median was 0.02 Hz, n=42 neurons; in cultures stimulated for 2-3 days, the mean was 0.2 ± 0.07 Hz and median was 0.05 Hz, n=40 neurons; p=0.152; in cultures stimulated for 4-5 days, the mean was 0.2 ± 0.05 Hz and median was 0.1 Hz, n=29 neurons; p=0.004, Dunn's multiple comparisons test) (**Figure 5.6E**). Together, these data show that a prolonged period of rodent astrocyte stimulation can mediate effects upon a network of synaptically-connected human iPSC-derived cortical neurons, i.e. elicit a form of "astrocyte-mediated neuronal plasticity".

Interestingly, these effects persisted beyond the period of light stimulation, which means structural changes might be involved in the expression of such astrocyte-mediated neuronal plasticity induced by long-duration light stimulation. Given that astrocytes have been reported to enhance structural synapse formation (Christopherson *et al.*, 2005; Kucukdereli *et al.*, 2011; Diniz *et al.*, 2012; Sultan *et al.*, 2015), I examined whether this process might underlie the observed effect. Cultures that had been set up in parallel to the

electrophysiological experiments shown in **Figure 5.6** were therefore immunolabelled: Microtubule associated protein-2 (MAP2) was used to label neurites, synaptophysin (SynPhy) to label pre-synaptic structures and Homer1 to label post-synaptic structures (see section 2.3.1). Automated image analysis software (see section 2.3.2 for details) was used to identify putative synaptic puncta associated with neurites (**Figure 5.7A** and **B**), such that pre-synaptic, post-synaptic and dual-labelled puncta could each be quantified per 100 µm of neurite (**Figure 5.7C**).

Stimulating the astrocytes through ChR2 did not significantly alter the number of structurally-defined synaptic connections within the cultures, from 1 cell line, 3 inductions (**Figure 5.7D**). No differences between the number of SynPhy$^+$ puncta (control: 7.2 ± 1.0 puncta/100 µm, n=11 FOV from 3 cultures; stimulated: 5.4 ± 0.9 puncta/100 µm, n=15 FOV from 3 cultures; p=0.087, un-paired Mann-Whitney test), Homer1$^+$ puncta (control: 7.3 ± 1.4 puncta/100 µm, n=11 FOV from 3 cultures; stimulated: 5.8 ± 1.4 puncta/100 µm, n=15 FOV from 3 cultures; p=0.237, un-paired Mann-Whitney test) or dual labelled puncta (control: 1.3 ± 0.4 puncta/100 µm, n=11 FOV from 3 cultures; stimulated: 0.6 ± 0.2 puncta/100 µm, n=15 FOV from 3 cultures; p=0.171, un-paired Mann-Whitney test) were found in the stimulated condition compared to the control condition. The average lengths of neurites were also equivalent between conditions (control: 1307 ± 318 µm, n=11 FOV from 3 cultures; stimulated: 1321 ± 328 µm, n=15 FOV from 3 cultures; p=0.959, un-paired Mann-Whitney test). These data suggest that astrocytes can mediate functional effects upon networks of synaptically-connected human cortical neurons, without apparently changing the overall numbers of structurally-defined synaptic connections.

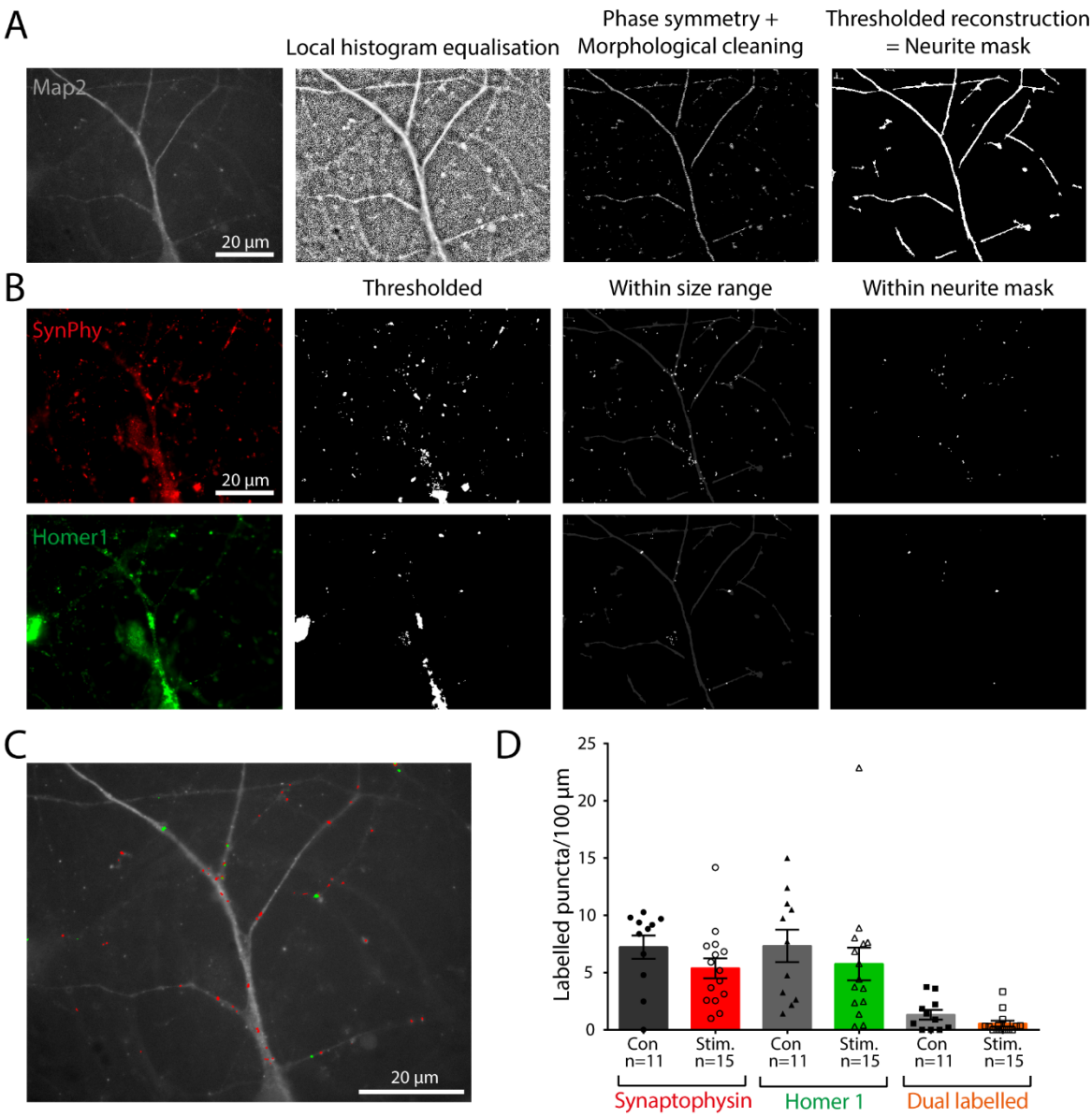

Figure 5.7 Anatomically-defined synaptic density is unaltered by astrocyte stimulation
A method was developed for the automated detection of anatomically defined synapses using the quantification of synaptic markers synaptophysin (SynPhy) and Homer1. **(A)** A mask outlining the Map2$^+$ neurites was generated following a series of image processing steps (left to right) and used to calculate the total length of neurite sampled. **(B)** Images of synaptic markers were thresholded, and then puncta were automatically identified based on size criteria and correspondence with the neurite mask. **(C)** A representative example showing the identified synaptic puncta overlaid on the original Map2 image. **(D)** The number of labelled puncta per 100 µm of neurite did not differ between the control and stimulated astrocyte conditions. This was the case when examining the synaptic markers individually or as dual labelled puncta. Sample size indicates the number of triple-labelled FOV.

To corroborate the observed functional effects upon human iPSC-derived cortical neurons, a further control experiment was conducted to confirm that the effects were mediated by ChR2 activation of the astrocytes, rather than by light exposure itself. This is important, as previous work has shown that light can directly affect NMDA receptor transmission for example (Leszkiewicz, Kandler and Aizenman, 2000). To control for potential effects associated with light stimulation, the experimental design was modified so that the "control condition" co-cultures used rat astrocytes that were not transduced with ChR2, but were exposed simultaneously to the same light protocol as the "stimulated condition" (**Figure 5.8A**).

Again, electrophysiological recordings were performed from neurons on coverslips from control and stimulated cultures (**Figure 5.8B**) using an interleaved experimental design (average age, control: 68 ± 3.4 days, stimulated: 68 ± 2.7 days, range: 64-75 days from 1 cell line (SBAD 03-01), 1 induction). Neurons in the stimulated conditions exhibited an increase in the proportion of synaptically active neurons (control: 22%, n=27 neurons; stimulated: 48%, n=25 neurons; p=0.026, one-tailed Chi-square contingency test) (**Figure 5.8C**), and these neurons also showed a significant increase in the frequency of sEPSCs (control: 0.01 ± 0.006 Hz, n=27 neurons; stimulated: 0.06 ± 0.02 Hz, n=25 neurons; p=0.025, un-paired Mann-

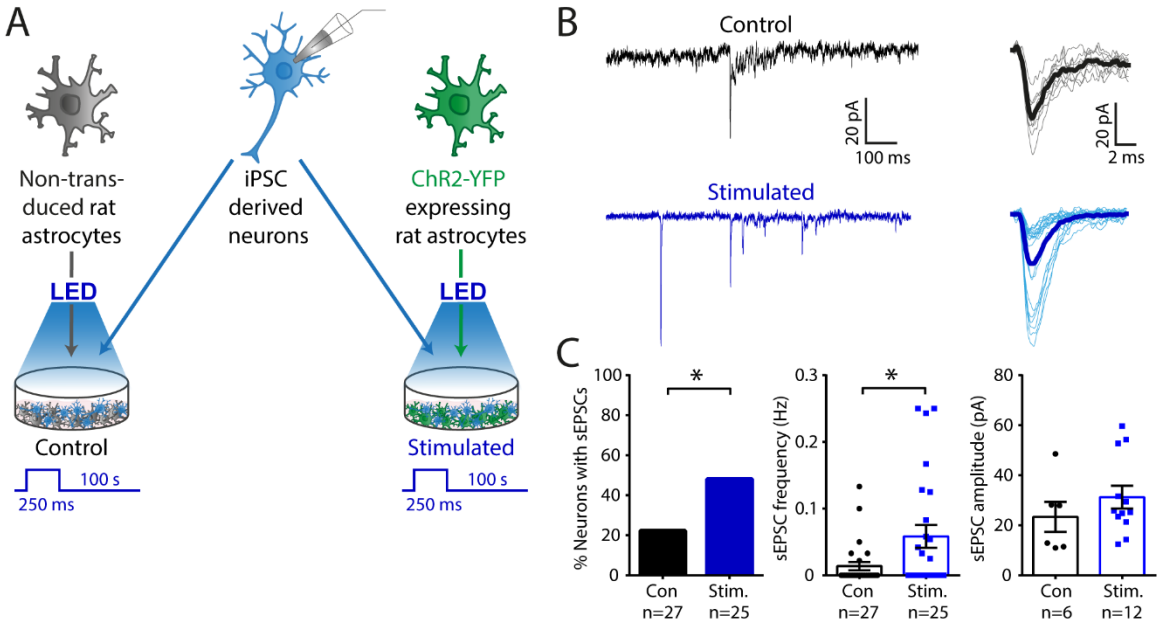

Figure 5.8 Astrocyte-mediated neuronal plasticity is robust across experimental conditions
(A) Experimental design to control for the potential effects of light exposure. iPSC-derived cortical neurons were co-cultured with rat astrocytes that were either non-transduced in the control condition, or transduced with a ChR2-expressing lentivirus in the stimulated condition. Both conditions were exposed to an LED stimulation paradigm of 250 ms pulses every 100 s for 2-7 days. **(B)** Example sEPSC recordings (left) from a neuron in the control condition (top) and a neuron in the stimulated condition (bottom). Detected sEPSCs are shown overlaid, with the mean in bold (right). **(C)** Proportions of synaptically active neurons and sEPSC frequency increased significantly without any changes occurring in the sEPSC amplitude.

Whitney test) (**Figure 5.8C**). There was no effect upon sEPSC amplitude (control: 23.3 ± 6.0 pA, n=6 neurons; stimulated: 31.3 ± 4.5 pA, n=12 neurons; p=0.291, un-paired Mann-Whitney test) (**Figure 5.8C**). These results support the conclusion that it is the long-duration ChR2-mediated stimulation of the astrocytes that mediate functional effects upon the human iPSC-derived cortical neurons, which last beyond light stimulation.

The experiments in **Figures 5.6** and **5.8** were conducted using rat astrocytes co-cultures with human iPSC-derived neurons. It was important to examine whether long-duration stimulation of human iPSC-derived astrocytes is also able to mediate comparable effects upon a network of synaptically-connected iPSC-derived human cortical neurons. During this period of experimentation, an inducible Ngn2 system (Ho *et al.*, 2015) was established in my lab and shown to reduce the time for cortical neurons to reach equivalent levels of functional maturity (Emma Whiteley, unpublished data). This strategy was implemented as studying the function of more synaptically mature neurons would be of more physiological relevance. As this protocol used Ngn2-induction at the NPC stage, it was possible to incorporate this strategy into the co-culture experiments (see details in section 2.2.3). (**Figure 5.9A** and **B**). Ngn-2 neurons were lentivirally transduced with a CamKII-mKate construct to enable their identification and aid selective patching.

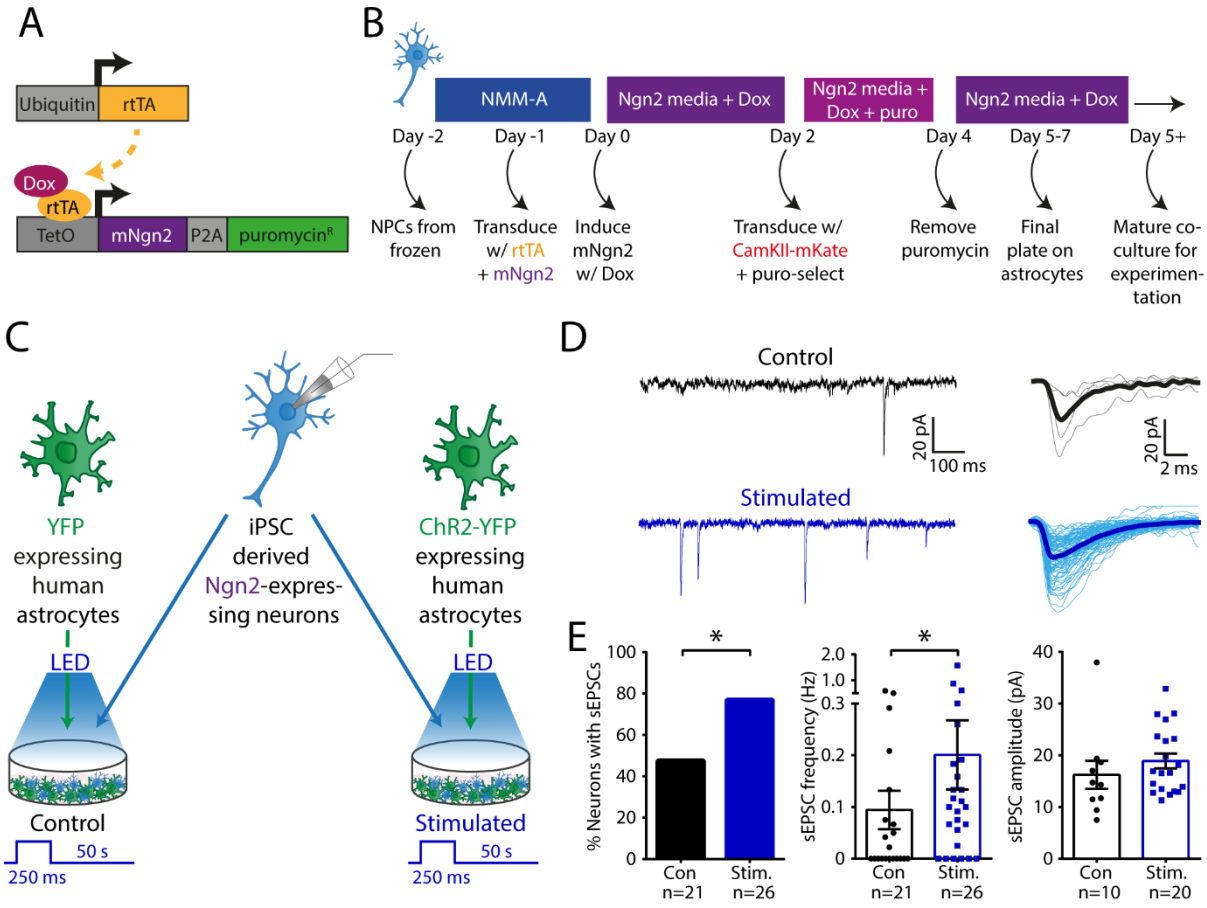

Figure 5.9 Astrocyte-mediated neuronal plasticity following long-term ChR2 stimulation of human astrocytes

(A) Lentiviral constructs used for inducible Ngn2 expression in NPCs. The constitutive ubiquitin promoter drives expression of the transcriptional activator rtTA, which is required for the binding of doxycycline (dox) to the TetO promoter. Successful transduction of both constructs is required for the expression of mNgn2 and puromycin (puro) resistance. **(B)** Protocol used for inducing Ngn2 expression, starting from NPCs. The resulting pure Ngn2-induced neurons were plated onto human astrocytes at day 5-7 and further matured in co-culture. **(C)** Experimental design for examining astrocyte-mediated neuronal plasticity in human co-cultures. Astrocytes were transduced with a CAG-driven YFP lentivirus in the control condition and with the CAG-ChR2-YFP lentivirus used in all other experiments in the stimulated condition. Co-cultures from both conditions were exposed to the same light protocol (250 ms LED pulse every 50 s for 2-4 days), after which recordings of sEPSCs were performed from mKate$^+$ neurons. **(D)** Example recordings of sEPSCs (left) in the YFP$^+$ control (top) and ChR2$^+$ stimulated conditions (bottom). All detected sEPSCs are shown overlaid, with the mean sEPSC in bold (right). **(E)** Stimulation of ChR2$^+$ human astrocytes significantly increased the proportion of neurons receiving sEPSCs, as well as the sEPSC frequency. No change was detected in sEPSC amplitudes. mNgn2: mouse Neurogenin-2, NMM-A: Neuronal Maintenance Media.

Using Ngn2-induced human neurons, a series of experiments were performed to assess the potential for human astrocytes to mediate the form of neuronal plasticity persisting after cessation of light stimulation. The "stimulated condition" co-cultures used human astrocytes that were transduced with a CAG-ChR2-YFP lentivirus, whereas the "control condition" co-cultures used human astrocytes that were transduced with CAG-YFP lentivirus (**Figure 5.9C**). This optimised experimental design allowed me to expose both conditions to the same light protocol within the incubator, and therefore concurrently control for both viral transduction and light exposure.

Cultures for each condition were set up in parallel and exposed to the standard light protocol for a period of 2-4 days, at which point electrophysiological recordings were performed on coverslips using an interleaved experimental design. sEPSCs were recorded in the presence of 100 µM PTX from confirmed mKate$^+$ neurons (**Figure 5.9D**) (average age, control: 58 ± 3.5 days; stimulated 58 ± 2.0 days, range: 54-62 days from neural induction initiation, which is approximately 30 days after Ngn2-expression was induced; 1 cell line (SBAD 03-01), 2 inductions of Ngn2). The data revealed that the proportion of synaptically active neurons was significantly increased in the ChR2 stimulated astrocyte condition (control: 48%, n=21 neurons; stimulated: 77%, n=26 neurons; p=0.038, Chi-square contingency test) (**Figure 5.9E**), which was also reflected in a significant increase in sEPSC frequency (control: 0.09 ± 0.04 Hz, n=21 neurons; stimulated: 0.2 ± 0.07 Hz, n=26 neurons; p=0.038, un-paired Mann-Whitney test) (**Figure 5.9E**). There was no detectable change in sEPSC amplitude (control: 16.2 ± 2.7 pA, n=10 neurons; stimulated: 18.9 ± 1.4 pA, n=20 neurons; p=0.231, un-paired Mann-Whitney test) (**Figure 5.9E**). Importantly, these experiments demonstrate that pure

human co-cultures of iPSC-derived astrocytes and neurons are also capable of displaying astrocyte-mediated neuronal plasticity in response to long-duration light stimulation.

In the final series of experiments, I investigated the cellular changes that underlie the neuronal plasticity following astrocyte stimulation. An increase in the frequency of sEPSCs could result from increases in intrinsic neuronal excitability and/or increases in functional synaptic connectivity. Recordings of intrinsic excitability made from the same cultures presented in **Figure 5.9** revealed no difference in the $VGNa^{+}$ currents between control and stimulated conditions (control: -1.7 ± 0.2 nA, n=21 neurons; stimulated: -2.0 ± 0.1 nA, n=26 neurons; p=0.122, un-paired Mann-Whitney test). However, spiking activity was significantly increased in the neurons from the stimulated condition, both in terms of the number of consecutive APs in response to 200 ms of somatic current injection (control: 1.4 ± 0.2 APs, n=18 neurons; stimulated: 2.5 ± ±0.4 APs, n=21 neurons; p=0.040, un-paired Mann-Whitney test) (**Figure 5.10A** and **B**), as well as a decrease in AP threshold (control: -23.6 ± 1.5 mV, n=16 neurons; stimulated: -30.2 ± 1.1 mV, n=19 neurons; p=0.002, un-paired Mann-Whitney test) (**Figure 5.10B**).

In separate experiments (average neuronal age, control: 57 ± 1.5 days; stimulated 57 ± 1.0 day, range: 55-58 days from neural induction initiation; 1 cell line (SBAD 02-01), 2 inductions of Ngn2), the effects upon functional synaptic connectivity were examined by recording spontaneous miniature EPSCs (mEPSCs) at -70mV in the presence of PTX and TTX (**Figure 5.10C**). Whilst the proportion of neurons receiving mEPSCs was not increased significantly by astrocyte stimulation (control: 55%, n=11 neurons; stimulated: 81%, n=16 neurons; p=0.135, Chi-square contingency test) (**Figure 5.10D**), the frequency of mEPSCs

was significantly increased in the stimulated condition (control: 0.3 ± 0.2 Hz, n=11 neurons; stimulated: 0.5 ± 0.1 Hz, n=16 neurons; p=0.038, un-paired Mann-Whitney test) (**Figure 5.10D**). No difference in the amplitude of mEPSCs was detected (control: 28.3 ± 5.4 pA, n=6 neurons; stimulated: 18.8 ± 2.2 pA, n=13 neurons; p=0.072, un-paired Mann-Whitney test) (**Figure 5.10D**).

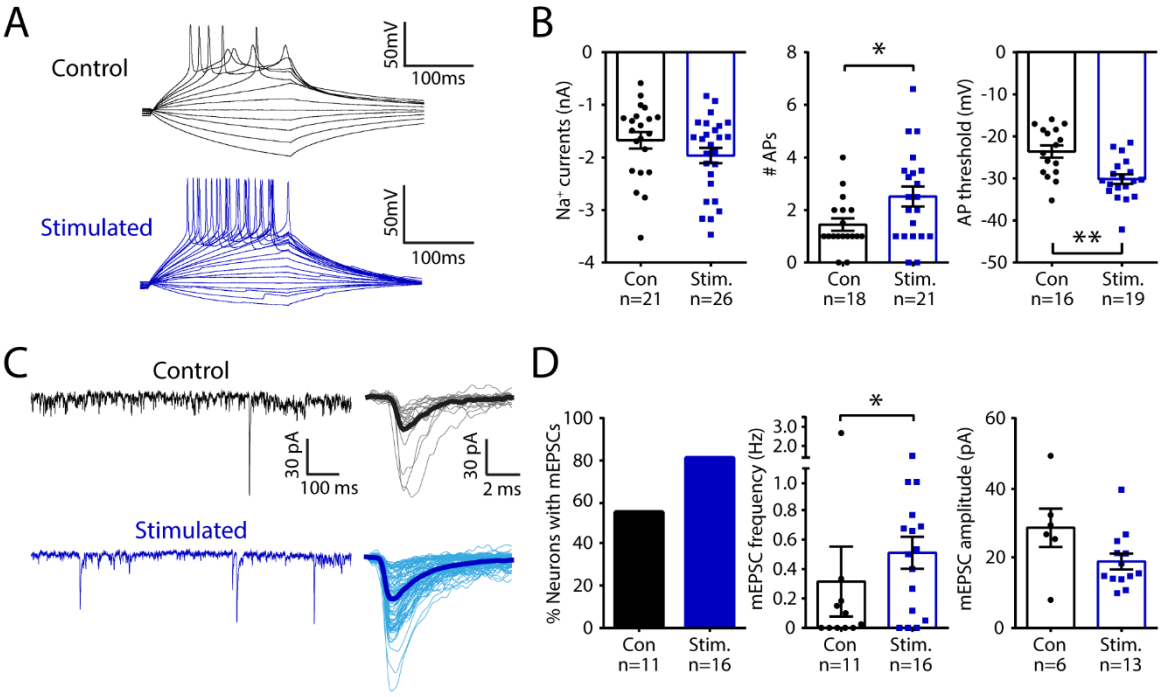

Figure 5.10 Astrocyte-mediated neuronal plasticity involves long-term effects upon both intrinsic excitability and synaptic efficacy
(A) Action potentials (APs) recorded in a control condition neuron (top) and a neuron from the stimulated astrocyte condition (bottom). **(B)** The amplitude of VGNa$^+$ currents was similar between conditions, but neurons from the stimulated astrocyte condition were capable of firing significantly more APs, with a lower AP initiation threshold. **(C)** Example traces of miniature EPSC (mEPSC) recordings performed in TTX, from a neuron in the control condition (top) and a neuron in the stimulated astrocyte condition (bottom). **(D)** No significant difference was observed in the proportion of neurons receiving mEPSCs, but astrocyte stimulation resulted in a significantly higher frequency of mEPSCs per human neuron. The amplitude of mEPSCs was not significantly different. * $p < 0.05$, ** $p < 0.01$, *** $p < 0.001$

Together, these experiments reveal that the astrocyte-mediated neuronal plasticity evoked by long-duration light stimulation involves both an increase in the intrinsic excitability and the excitatory synaptic connectivity of the iPSC-derived human neurons, but not an increase in synapse density.

5.3 Discussion

In this chapter I have utilised human iPSC-derived cortical neurons and astrocytes to establish a purely human co-culture model. Consistent with other studies that have reported pro-maturational effects of rodent astrocytes upon the intrinsic excitability and membrane properties of human iPSC-derived neurons (Tang *et al.*, 2013; Odawara *et al.*, 2014; Prè *et al.*, 2014), I detected significantly increased AP firing and a lowering of neuronal membrane resistance in rat astrocyte co-cultures. Interestingly, a comparable level of enhanced excitability was also detected in the human astrocyte co-culture condition. This is in contrast to a recent study, which reported that human astrocytes grown via a different differentiation protocol, were significantly inferior when compared to rodent astrocytes by the same measures (Lischka *et al.*, 2017).

In line with the evidence that astrocytes exert functional maturational effects on synapses, both in terms of secreted and contact mediated cues (Barker *et al.*, 2008; Clarke and Barres, 2013; Chung, Allen and Eroglu, 2015), the patch-clamp recordings conducted here revealed that both rat and human astrocytes increased the proportion of synaptically active human iPSC-derived neurons, and that human astrocytes also significantly increased the frequency of sEPSCs. In fact, the neurons in these co-cultures with human astrocytes reached levels of synaptic functionality comparable to the highest functional state reported by Bardy

et al. (2016) ("State 5": ~90% neurons with active AMPA inputs, pure human co-cultures: 82% neurons receiving >1 sEPSC per minute). This level of activity was however achieved in ACSF without Mg^{2+}, a choice made in order to aid the detection of any synaptic inputs from what is otherwise generally quite silent and synaptically immature neurons. Removing Mg^{2+} from the ACSF means that sEPSCs represent general glutamatergic signalling and can consist of a mixture of AMPA and NMDA inputs.

Similar to the effects upon intrinsic neuronal excitability, the present observations are in contrast to the recent study by Lischka et al. (2017), which failed to detect a pro-maturational effect of human astrocytes on synaptic function. On the basis of transcriptomic analysis, the authors concluded that their failure to observe pro-maturational effects was likely due to the foetal-like state of the astrocytes that were generated by their differentiation protocol. Together, these data suggest that the differentiation protocol developed in this thesis generates astrocytes with the ability to convey pro-maturational effects to co-cultured neurons, which is widely viewed as a hallmark of astrocytes.

The potential to elicit synaptic changes via ChR2 activated gliotransmission from astrocytes has been achieved in several rodent models, including *in vivo* (Perea *et al.*, 2014), acute slice (Sasaki *et al.*, 2012; Perea *et al.*, 2014) and *in vitro* culture preparations (Berlinguer-Palmini *et al.*, 2014). These studies all detected acute changes in synaptic transmission during ChR2 activation, and concluded that the synaptic enhancement was due to astrocytically released glutamate. Similarly, I tested whether a short-term effect on excitatory synaptic transmission could be elicited via ChR2 stimulation in pure human co-cultures. Indeed, blue light pulses increased the frequency of sEPSCs, and this effect persisted

during the period of light stimulation, consistent with what has been shown in the rodent literature. Furthermore, my results are in accordance with Perea et al. (2014) and Sasaki et al. (2012), who both reported that ChR2-evoked glutamate release from astrocytes acts via synaptic mGluRs. I found that the acute enhancement of excitatory synaptic transmission was blocked by a general mGluR antagonist. Extrasynaptic mGluRs are known to be a target for glutamate released from astrocytes (Fiacco and McCarthy, 2004; Q.-S. Liu *et al.*, 2004), and the activation of pre-synaptic mGluRs can modulate vesicle release through facilitation of Ca^{2+} entry, which could account for the observed increase in sEPSCs (Herrero, Miras-Portugal and Sánchez-Prieto, 1998; Schwartz and Alford, 2000; Thomas *et al.*, 2001; Fiacco and McCarthy, 2004; Q.-S. Liu *et al.*, 2004).

Having observed short-term astrocyte-mediated synaptic enhancement in pure human co-cultures, I examined whether ChR2 stimulation of astrocytes could mediate longer-lasting effects. I established an optical stimulation paradigm, which could be used to treat co-cultures over the course of several days. This enabled me to explore for the first time, whether human synaptic networks can be regulated via astrocyte-neuron signalling. First, using human neurons and rat astrocyte co-cultures to test the feasibility of the experimental setup, I revealed an astrocyte-mediated form of neuronal plasticity which persisted after cessation of light stimulation. This plasticity effect manifested as an increased proportion of synaptically active neurons, along with an increase in the frequency of sEPSCs. I then examined whether human astrocytes were able to mediate similar enhancements of synaptic transmission. As another optimisation step in addition to the forced Ngn2 expression in neurons and YFP-only expression in control condition astrocytes, it was decided to ensure that glutamatergic

signalling was isolated by adding PTX to the ACSF. This manipulation was in addition to the removal of Mg^{2+} from the ACSF as mentioned earlier, so sEPSCs can still consist of both AMPA and NMDA currents, yet the basal level of sEPSC frequency remained remarkably unaltered in the control conditions (Control with rat astrocytes: 0.09 ±0.04 Hz; control with human astrocytes: 0.09 ±0.04 Hz). Detection of astrocyte-mediated neuronal plasticity was indeed achieved in a purely human co-culture model as a result of long-duration light stimulation, thus establishing that stimulating human astrocytes via ChR2 enables them to interact with human neurons, in a manner that is consistent with gliotransmission. It is important to note however, that these studies did not examine exactly for how long the enhancing effect persisted. Cultures were always subjected to electrophysiology immediately after removal from the incubator where LED stimulation took place, which means it can solely be stated that the effects were detectable for up to 8-10 hours after the end of astrocyte stimulation. By leaving cultures in darkness for various amounts of time before recording, an assessment could be made with regards to the permanency or transiency of the effect.

Further experiments examined the underlying cellular changes and provided evidence for multiple potential mechanisms. Astrocyte stimulation lowered AP threshold and increased AP firing in co-cultured neurons, consistent with an enhancement of neuronal excitability expressed on some structural or functional basis as it persisted outside direct light stimulation. Interestingly, an observation of increased neuronal spiking was recently reported in mouse hippocampal slices during acute ChR2 stimulation of astrocytes (Shen *et al.*, 2017b). Such increases in intrinsic neuronal excitability would be expected to increase the likelihood of spontaneous APs in the network, which would result in higher frequencies of sEPSCs in

the postsynaptic neurons. In addition to changes in neuronal excitability, my recordings revealed that the frequency of mEPSCs was also greater in neurons co-cultured with stimulated astrocytes. Higher mEPSC frequency signifies an increase in the number of active synapses, either through synaptogenesis or the un-silencing of synapses. The fact that the immunolabelling experiments failed to provide evidence for the formation of new synapses, may suggest that an activity-dependent un-silencing process is a more likely mechanism for the observed increase in the frequency of mEPSCs. However, further experiments would be required to dissect the underlying processes. For instance, having established that glutamate release from human astrocytes can activate mGluRs on the human neurons, it would be interesting to test whether this receptor system is involved in a synaptic un-silencing process, as the activation of post-synaptic mGluRs can cause NMDA and AMPA receptor potentiation and insertion (Bashir *et al.*, 1993; Mukherjee and Manahan-Vaughan, 2013).

Collectively, these data provide new insights into interactions between human neurons and human astrocytes. Human iPSC-derived astrocytes have been shown for the first time to provide pro-maturational support to human synapses, as well as being capable of influencing synaptic transmission. These abilities of astrocytes to support and provide feedback signals to neuronal synapses are well documented in the rodent literature. Demonstrating that these observations hold true for human astrocytes is an important step towards validating the use of iPSC-derived cultures for disease modelling. Given that several cell types are likely to be involved in most neurodegenerative diseases, being able to establish co-culture models in which interactions between different cell types can be investigated is crucial. At a practical level, co-cultures of physiological relevance were shown here to allow

for both electrophysiological, optogenetic and immunolabelling experimentation. In the next and final results chapter, I will capitalise on these co-culture experiments and apply the optogenetic stimulation paradigm to examine astrocyte-mediated neuronal plasticity in the context of a disease-relevant question. Because this co-culture method enables neurons and astrocytes from different cell lines to be mixed following cell-type specific differentiation, it allows for the generation of interesting combinations of healthy:disease cells. Due to APOE4 being the most prominent risk factor to developing sAD and it mainly being produced by astrocytes, the impact of APOE4 genotype upon astrocyte-neuron interactions will be investigate in the next chapter.

Chapter 6

6 USING iPSC-DERIVED ASTROCYTES TO EXAMINE THE INFLUENCE OF APOLIPOPROTEIN E VARIANT UPON ASTROCYTE-NEURON SIGNALLING

6.1 Introduction

As astrocytes play vital roles in synaptic and neuronal health, it is perhaps not surprising that astrocyte dysfunction has been implicated in neurodegenerative diseases such as Alzheimer's disease (AD) (Tyzack, Lakatos and Patani, 2016; Crompton, Cordero-Llana and Caldwell, 2017; Almad and Maragakis, 2018). Several processes such as inflammation, tau protein misfolding, toxic amyloid-β (Aβ) aggregation and synapse dysfunction, have been associated with the neuronal death characteristic of AD. In early-onset familial forms of AD, the disease-causing mutations particularly affect Aβ processing, instigating an increased production of toxic oligomers (Weggen and Beher, 2012). In comparison, the link between genetic risk factors and disease pathology is less clear for late onset sporadic AD (sAD). The E4 variant of apolipoprotein E (*APOE*) has long been known to be more prevalent in individuals with sAD and to lower the age of disease onset (E. H. E. Corder *et al.*, 1993). Later genome-wide association studies revealed the same phenomenon on a larger scale, and identified *APOE4* as the major genetic risk factor (Harold *et al.*, 2009; Lambert *et al.*, 2013). Yet, much remains to be understood about how the cellular function of APOE relates to AD pathology.

APOE is a lipoprotein, whose main function is to carry lipids and cholesterol to cells across all tissues of the body (Pitas *et al.*, 1987; Lane-Donovan, Philips and Herz, 2014). In

the brain, lipid and cholesterol delivery is particularly important for neurons in terms of synapse formation and remodelling (Mauch, Na and Schumacher, 2001), and astrocytic secretion of APOE can be elicited by neuronal injury (Yin *et al.*, 2012). Despite having a high metabolic demand for cholesterol, neurons produce little APOE themselves, making the supply from astrocytes all the more crucial (Rapp, Gmeiner and Hüttinger, 2006). These observations suggest that APOE might be viewed as yet another vital factor that astrocytes provide at the tri-partite synapse, contributing to neuronal health and synaptic function.

In terms of differences between APOE isoforms that might relate to AD pathology, both Aβ -dependent and Aβ -independent mechanisms have been implicated. For example, compared to the neutral (E3) and protective (E2) isoforms, APOE4 has been found to contribute to Aβ accumulation by increasing Aβ deposition in plaques (Tiraboschi *et al.*, 2004), impairing Aβ clearance (Liu *et al.*, 2013) and surprisingly, by stimulating APP transcription (Huang *et al.*, 2017). The isoform-dependent differences in relation to APOE's interaction with Aβ is thought to stem from its folding structure, which in the case of APOE4 results in a lower affinity for binding Aβ (LaDu *et al.*, 1994) and thus weakens the ability to clear Aβ (Deane, Sagare, Hamm, Parisi, Lane, Finn, David M. Holtzman, *et al.*, 2008). The delivery of cholesterol is also affected by the altered protein structure of APOE, which lowers APOE's affinity for one of its primary receptors – the low-density lipoprotein receptors (LDLR's) (Huang, 2010). In addition, APOE4 has been found to deliver less cholesterol per molecule of APOE (Gong *et al.*, 2002). In relation to synapses, the APOE isoform appears to influence dendritic spine density (Ji *et al.*, 2003) and morphology (Dumanis *et al.*, 2009). Whether these effects reflect impaired synapse formation or increased spine elimination is

unknown, as is how these processes contribute to AD pathology. Although, mouse *in vivo* and *in vitro* studies have shown that the *ApoE4* genotype is associated with reduced excitatory transmission (Wang *et al.*, 2005), impaired working memory (Hartman *et al.*, 2001), and decreased long-term potentiation (LTP) (Trommer *et al.*, 2004).

A multitude of rodent studies have provided important insights into APOE function and its interactions with Aβ and tau processing. Yet the failure to translate this into successful therapeutic strategies has led scientists to suggest that there is a translational species gap, and some have argued that rodents might not be the most relevant animal model in which to study AD (Cavanaugh, Pippin and Barnard, 2014; Cummings, Morstorf and Zhong, 2014; Crompton, Cordero-Llana and Caldwell, 2017). For example, whereas other species, like cats, dolphins and degus are reported to develop amyloid plaques and even neurofibrillary tau tangles as they age, these phenotypes are not seen in mice and rats in the wild (Youssef *et al.*, 2016; Gunn-Moore *et al.*, 2018). Transgenic mouse models are generally unable to replicate the full repertoire of pathological and behavioural symptoms associated with human AD (Cavanaugh, Pippin and Barnard, 2014). They rely on expressing human proteins in mouse cells, with limited control over expression levels, which neglects any effects due to differences in native levels of proteins. For these reasons, iPSCs are being increasingly regarded as a means to help bridge this species gap, as they allow for the study of molecular phenotypes in human cells (Mungenast, Siegert and Tsai, 2015). In particular, the emerging differences between rodent and human astrocytes make these cells especially relevant to generate and study (Chandrasekaran *et al.*, 2016; Crompton, Cordero-Llana and Caldwell, 2017). Human iPSC-derived brain cells will naturally express the different APOE isoforms, at

presumably native levels. Being able to separately derive different cell-types also provides interesting possibilities for making co-cultures of cells with mixed *APOE* genotypes, in order to study the cellular basis of AD pathology.

To advance this area, I set out to establish such mixed co-cultures and investigate whether *APOE* variants are associated with differences in how human astrocytes signal to human cortical neurons.

Building upon the protocols established earlier in my thesis, the specific aims of the current chapter were to:

1) **Differentiate astrocytes from iPSC lines with an *APOE4/E4* genotype, derived from patients diagnosed with AD.**
2) **Compare APOE secretion in *APOE4/E4* astrocytes and healthy control astrocytes.**
3) **Examine whether *APOE4/E4* astrocytes can mediate forms of neuronal plasticity.**

6.2 Results

The *APOE* gene is located on chromosome 19 and the three different isoforms (*APOE2*, *E3* and *E4*) arise due to single nucleotide polymorphisms (SNPs) at location 112 and 158, where changing a thymine (T) to a cytosine (C), results in a switch from a cysteine (Cys) to an arginine (Arg), or vice versa. The combination of 112-Cys/158-Cys produces the relatively rare *APOE2* isoform, which is regarded as protective with respect to AD (frequency in population: 6.4% (Eisenberg, Kuzawa and Hayes, 2010)). Whereas 112-Cys/158-Arg produces the most common *APOE3* isoform, regarded as neutral in terms of AD risk (frequency in population: 78.3% (Eisenberg, Kuzawa and Hayes, 2010)). Lastly, 112-Arg/158-Arg produces the *APOE4* isoform, strongly associated with AD (frequency in population: 14.5% (Eisenberg, Kuzawa and Hayes, 2010)). *APOE4* conveys AD risk in a dose dependent manner, such that possessing just one allele increases the risk of developing sAD by a factor of 3-4, and having both *APOE4* alleles raises the risk by 8-12 fold, as well as lowering the age of onset (E. Corder *et al.*, 1993; Roses, 1996).

Given the increased risk of AD associated with the *APOE4* allele, it was important to first confirm the genotype of the cell lines used for subsequent experiments. The different isoforms can be determined using a combination of PCR and restriction digest, optimised from a protocol described previously (Zivelin *et al.*, 1997) (see section 2.3.5). A PCR fragment of 218 base pairs (bp), containing the two *APOE* SNP sites were amplified. The subsequent restriction digest takes advantage of the fact that the recognition sequences for the restriction enzymes includes Cys at location 112 (Afl II) or Arg at location 158 (Hae II) (**Figure 6.1A**).

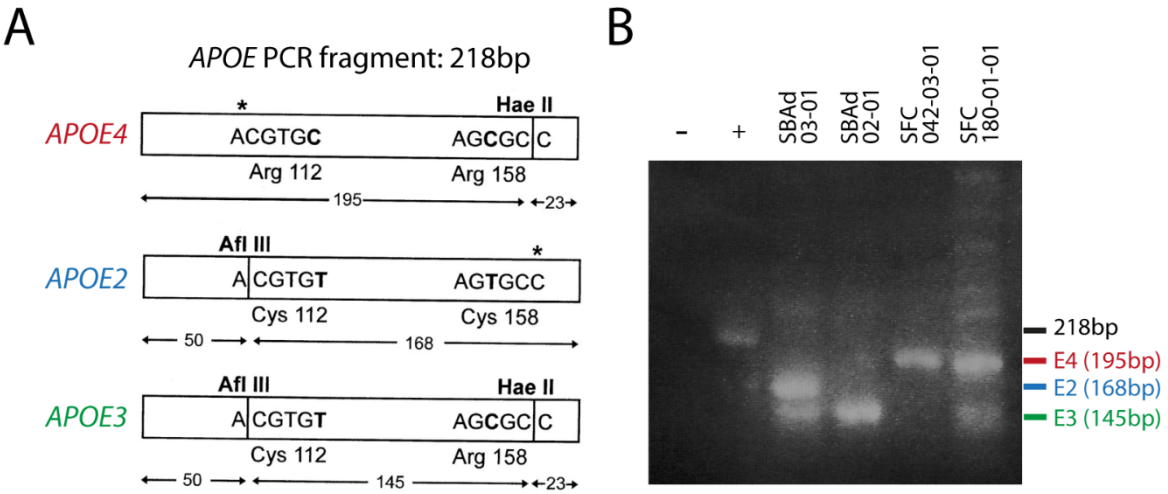

C

Cell line	Age	Gender	Diagnosis	Genotype
SBAd 03-01	31	Female	Healthy	E2/E3
SBAd 03-05	31	Female	Healthy	E2/E3
SBAd 02-01	51	Male	Healthy	E3/E3
SFC 180-01-01	60	Female	Healthy	E3/E4
SFC 042-03-01	67	Female	AD	E4/E4
SFC 140-04-01	70	Female	AD	E4/E4

Figure 6.1 Genotyping iPS cell lines for *APOE* isoforms
(A) Overview of the three human *APOE* isoforms, which arise due to single base pair variations at position 112 and 158, changing a cysteine (Cys) to an arginine (Arg), or vice versa. The restriction enzyme Afl III has a restriction site close to position 112, where it can cut if Cys is present, but not if Arg is present. Similarly, Hae II can cut at position 158 when Arg is present, but not if Cys is present (* indicates enzyme cannot cut). Arrows beneath nucleotide sequence indicate predicted fragment sizes for each scenario. Illustration modified from Zivelin et al (1997). **(B)** Example electrophoresis gel used to genotype the cell lines with unknown *APOE* identity. The undigested 218 kb PCR fragment was used as positive control (+), and dH_2O as a negative control (-). When only one band was seen, the genotype of the cell line was concluded to be homozygous, while two bands meant it was heterozygous. **(C)** Summary table showing the age, gender, clinical diagnosis and genotype information of the donors from whom the iPS cell lines used in this thesis were generated. AD: Alzheimer's disease (sporadic).

This means the *APOE* fragments are digested in such a manner that the isoforms can be distinguished by gel electrophoresis based on the resulting fragments (**Figure 6.1B**).

The PCR and restriction digest was performed on three healthy control cell lines with unknown *APOE* genotype (SBAd 03-01, SBAd 02-01 and SFC 180-01-01), as well as a cell line from an individual diagnosed with sAD (SFC 420-03-01). It was found that two of the three control cell lines lacked the *APOE4* variant and were *APOE2/E3* (SBAd 03-01) or *APOE3/E3* (SBAd 02-01). The third control cell line was found to have the genotype *APOE3/E4* (SFC 180-01-01) and, due to the presence of the single *APOE4* allele, was not included in further experiments. Another clone of the SBAd 03 line (SBAd 03-05) was therefore used as a third control cell line. Finally, the sAD cell line with unknown *APOE* genotype (SFC 042-03-01), was found to have the *APOE4/E4* genotype, which was the same as a second sAD line (SFC 140-04-01) that had been provided and genotyped by the StemBANCC consortium (**Figure 6.1C**).

To confirm that the sAD cell lines were capable of undergoing cortical differentiation, I initiated their induction according to the protocol outlined in **Chapter 3** (see section 2.2.2). As the subsequent experiments aimed to test the influence of *APOE* genotype in astrocytes, staining was performed at the rosette stage (around the time that astrocyte differentiation is initiated; **Figure 6.2**), at the astrocyte precursor stage and at the mature astrocyte stage (see section 2.3.1, **Figure 6.3**).

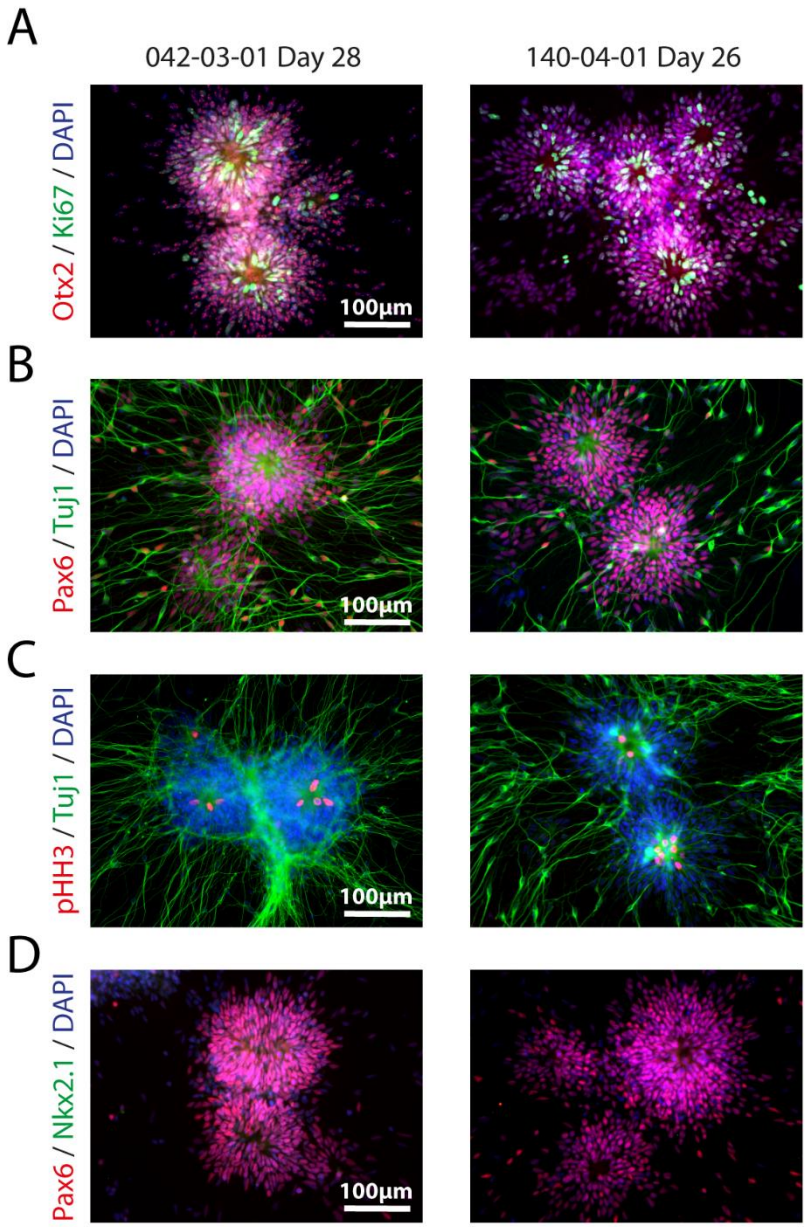

Figure 6.2 *APOE4/E4* **iPSCs are capable of generating cortical rosettes**
Rosettes from two iPSC lines derived from individuals with an *APOE4/E4* genotype and diagnosed with sporadic AD (SFC 042-03-01 and 140-04-01) were immunolabelled at day ~27 after initiating cortical neural induction with dual SMAD inhibition. **(A)** Disease cell lines form qualitatively normal, polarised rosettes of cortical neural progenitors (Otx2), many of which are undergoing proliferation (Ki67). **(B)** Rosettes from disease cell lines display prominent radial glia (Pax6) staining and these progenitors produce neurons that migrate away from the edge of rosettes (Tuj1). **(C)** As in healthy control cell lines, mitoses in disease cell lines occur predominantly close to the lumen of rosettes (pHH3). **(D)** Rosettes from these inductions stained negative for the interneuron progenitor marker, Nkx2.1.

Rosettes from both *APOE4/E4* cell lines displayed widespread staining for the cortical progenitor-marker Otx2, as well as the cycling cell-marker Ki67, demonstrating that many cells are undergoing divisions (**Figure 6.2A**). The near 100% $Pax6^+$ staining demonstrated that rosettes were mostly made up of radial glia progenitors, giving rise to $Tuj1^+$ neurons (**Figure 6.2B**). These progenitors also appeared to be performing interkinetic nuclear migration, as $pHH3^+$ mitotic cells were observed predominantly near the rosette lumen (**Figure 6.2C**). Neither of the sAD cell lines were positive for the interneuron progenitor marker Nkx2.1, but staining with the marker had previously been shown to depend more on induction than cell line (**Figure 6.2D** and **Figure 3.3**).

Astrocyte differentiation and maturation was performed as outlined in **Chapter 3** (see section 2.2.4), and staining for astrocytic markers S100β and GFAP was performed at different time points. From the staining performed on 47 day old astrocyte precursors, it was evident that $Tuj1^+$ neurons were still abundant, and that S100β staining was more prominent earlier than GFAP, as was observed in cultures from healthy controls (**Figure 3.5B**) and in previous studies (Barnabé-Heider *et al.*, 2005; Zhao *et al.*, 2017) (**Figure 6.3A**). These *APOE4/E4* cell lines also showed the disappearance of $Tuj1^+$ neurons along with increased S100β and GFAP expression as the astrocytes matured (**Figure 6.3B**). Expression levels were quantified by counting $Tuj1^+$, S100β $^+$ and $GFAP^+$ cells as percentages of the total number of $DAPI^+$ nuclei from quadruple labelled coverslips (S100β: 75%, n=9 FOV from 4 cultures, 2 cell lines, 2 inductions, GFAP: 58%, n=9, Tuj1: 9%, n=9 FOV) (see section 2.3.2, **Figure 6.3C**).

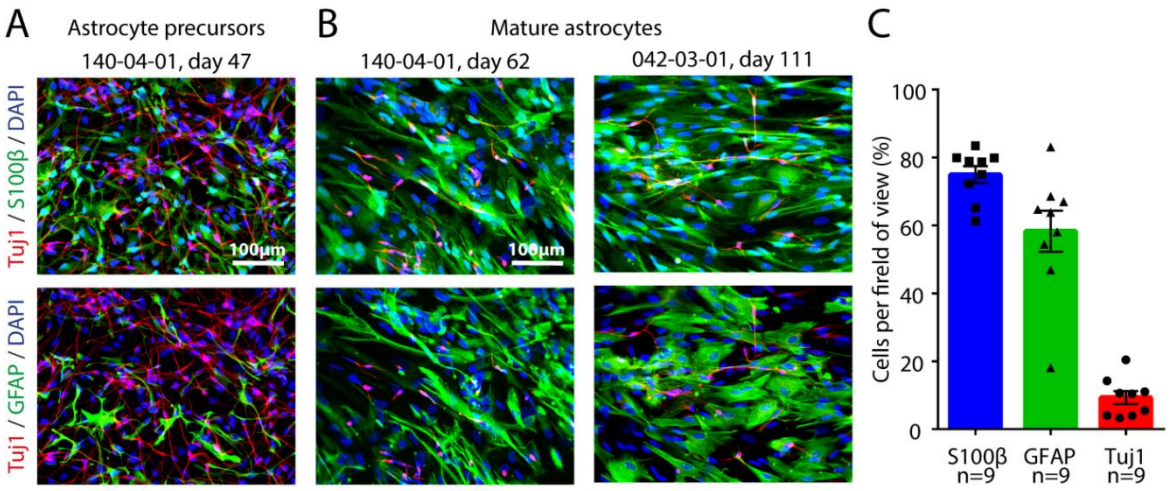

Figure 6.3 ***APOE4/E4*** **iPSCs are capable of generating immunohistochemically defined astrocytes**
The two *APOE4/E4* sporadic AD cell lines were immunolabelled for the astrocytic markers S100β and GFAP, plus the neuronal marker Tuj1, at different time points of the astrocytic differentiation protocol. **(A)** Astrocyte precursors at day ~50 displayed more S100β⁺ staining than GFAP, and were intermixed with Tuj1⁺ neurons. **(B)** In cultures corresponding to the mature astrocyte phase (day 60 onwards), GFAP expression levels had increased to match that of S100β, whilst the number of Tuj1⁺ neurons had decreased considerably. **(C)** The proportion of cells positive for S100β, GFAP and Tuj1 were quantified from the two disease cell lines at the mature astrocyte stage (n = 9 FOV from quadruple-labelled cultures).

Having confirmed the generation of human astrocytes from the *APOE4/E4* sAD cell lines, I next set out to examine the production of APOE protein from the different cell lines. APOE vesicles are produced within astrocytes and secreted into the extracellular environment, and so should be detectable in the culture media (Pitas *et al.*, 1987; Rapp, Gmeiner and Hüttinger, 2006). To establish whether this was the case, a sandwich ELISA absorbance assay was performed on samples of media collected from cultures of mature astrocytes (see section 2.3.7; 3 cell lines, 3 inductions, media present for 50-55 hrs). Absorbance measures were converted to APOE levels by using a standard curve based on serial dilutions of APOE (**Figure 6.4A**). Secreted APOE levels in the media sample could then be expressed as a fraction of the total protein within the sample, to normalise for potential differences in cell numbers. Secreted APOE levels were compared between control *APOE3/E3* astrocytes, sAD

APOE4/E4 astrocytes and a negative control that consisted of astrocytes derived from an *APOE* knockout (KO) iPSC line (generated by 'Bioneer' for StemBANCC). The amount of APOE secreted by human astrocytes was found to be associated with the *APOE* genotype of the cells (p=0.004, un-paired Kruskal-Wallis test) (**Figure 6.4B**). This overall effect was driven by a four-times higher level of APOE secretion from *APOE3/E3* astrocytes compared to *APOE4/E4* astrocytes (*APOE3/E3*: 7.2 ± 0.4 ng APOE/mg protein, n=3 technical replicates; *APOE4/E4*: 1.7 ± 0.3 ng APOE/mg protein, n=3 technical replicates; p=0.021, Dunn's multiple comparisons test). Whereas the secretion levels of *APOE4/E4* astrocytes were not different to *APOE KO* astrocytes (*APOE4/E4*: 1.7 ± 0.3 ng APOE/mg protein, n=3 technical replicates; *APOE KO*: 0.3 ± 0.3 ng APOE/mg protein, n=3 technical replicates;

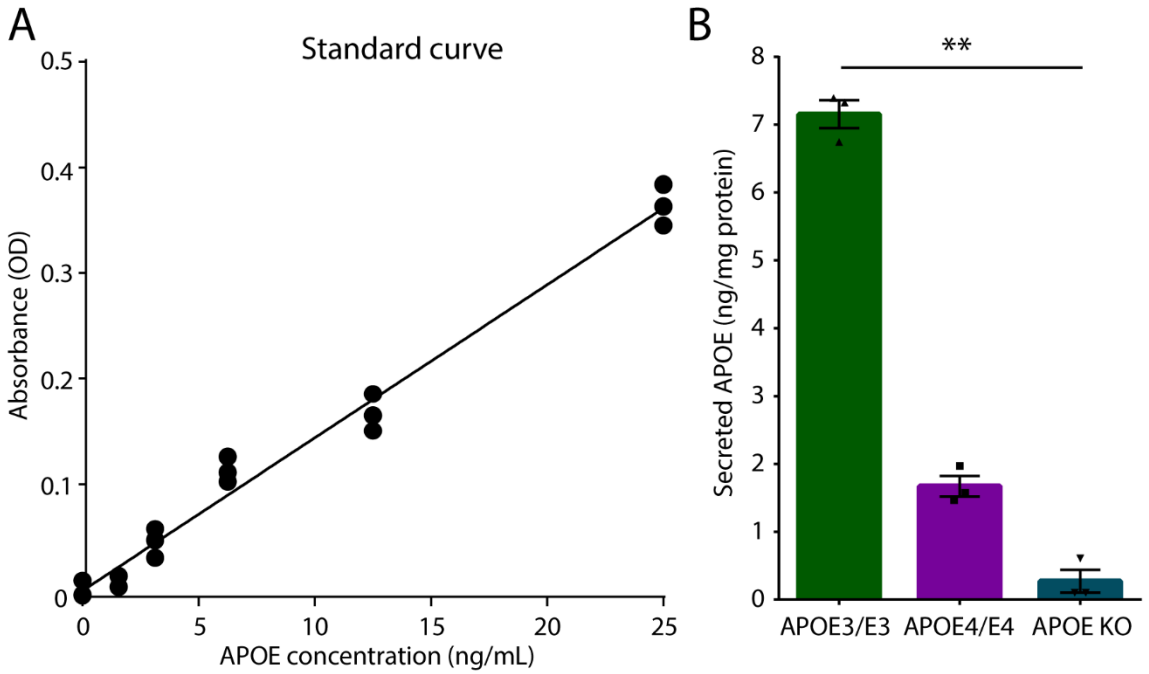

Figure 6.4 Astrocyte *APOE* genotype is associated with the secretion of different amounts of APOE

Secreted APOE was measured in the cell culture media using a sandwich ELISA, which is sensitive to all isoforms of human APOE. **(A)** Standard curve generated from a serial dilution of APOE (ng/mL). All standards were run in triplicate. **(B)** Resulting APOE concentrations measured at day 90 for healthy control *APOE3/E3* astrocytes, sporadic AD *APOE4/E4* astrocytes and astrocytes derived from an *APOE* knockout iPSC line ('APOE KO', generated by 'Bioneer' for the StemBANCC consortium). All samples were normalised to total mg protein, using a BSA assay (n=3 technical replicates from individual cultures).

p=0.534, Dunn's multiple comparisons test). These data suggest that the amount of APOE secreted by human astrocytes is associated with the particular *APOE* genotype of the cells.

The *APOE4* genotype has been proposed to inhibit mechanisms associated with neuronal plasticity, including spine formation, remodelling and elimination (Mauch, Na and Schumacher, 2001; Ji *et al.*, 2003; Dumanis *et al.*, 2009), neurite outgrowth (Kim *et al.*, 2014) and LTP (Trommer *et al.*, 2004). I therefore wanted to examine whether the *APOE4* genotype influences the astrocyte-mediated forms of plasticity described in **Chapter 5**. To achieve this, astrocytes derived from sAD *APOE4/E4* cell lines were co-cultured with healthy control *APOE2/E3* cortical neurons (see section 2.2.7), which were the same neurons used in **Chapter 5**. As in previous experiments, the astrocytes were virally transduced to express either ChR2-YFP for the stimulation condition, or YFP for the control condition (**Figure 6.5A**). Meanwhile, the cortical neural progenitors underwent forced Ngn2 expression and were virally transduced to express mKate under the control of the CamKII promoter to enable targeted patching (see section 2.2.3). Co-cultures from the two conditions were set up in parallel and exposed to the pulsed light stimulation paradigm (250 ms LED light every 50 s), over the course of 3-5 days in the tissue culture incubator (see section 2.2.8). At this point, sEPSCs were measured by performing whole-cell patch clamp recordings from confirmed $mKate^+$ neurons (average age, control: 57 ± 0.7 days; stimulated: 57 ± 0.6 days; range: 55-59 days), which corresponds to 30 days post-induction with Ngn2 (**Figure 6.5B**). I ran two independent experiments, using astrocytes from a different *APOE4/E4* line (either SFC 042-03-01 or SFC 140-04-01) in each experiment and combined the results.

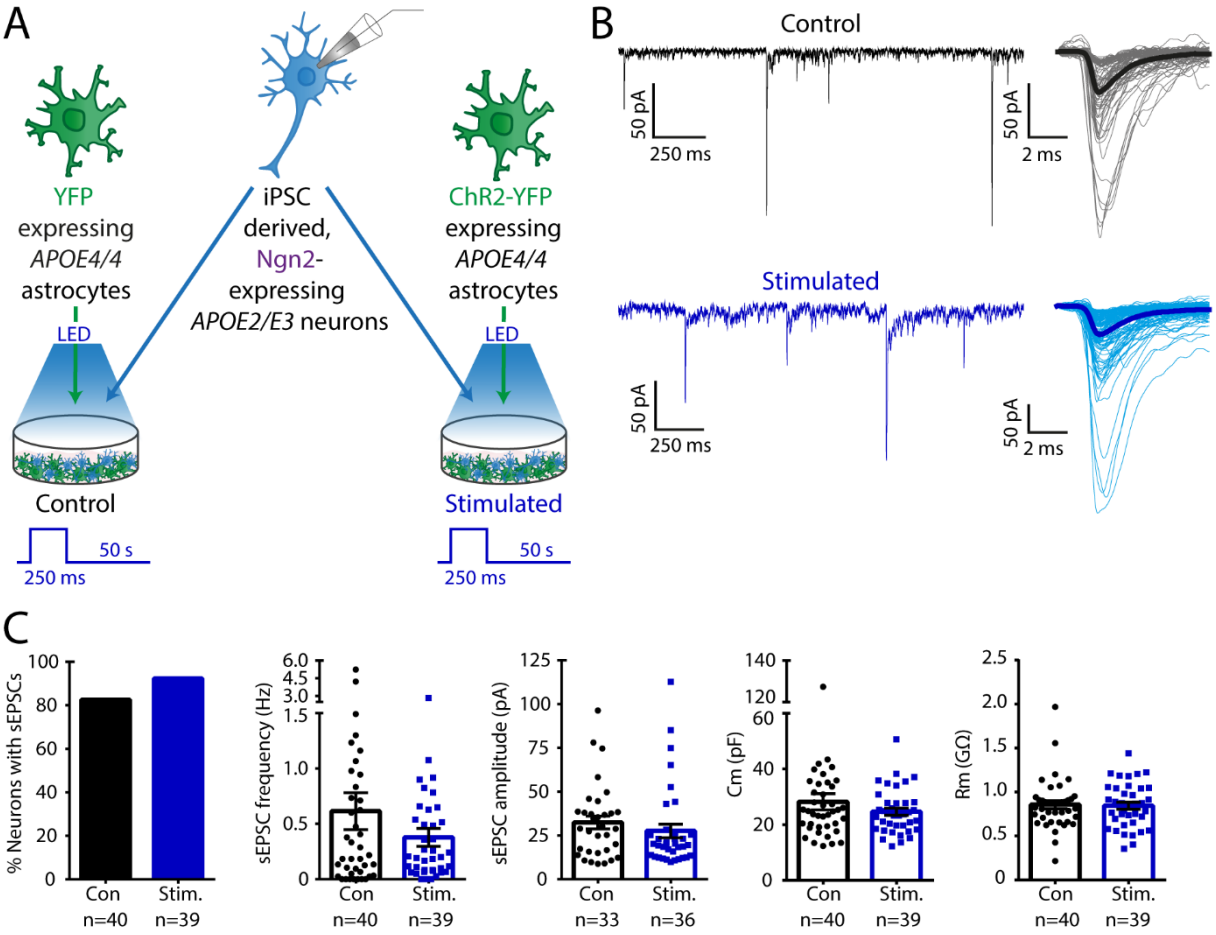

Figure 6.5 Astrocyte-mediated neuronal plasticity is absent in co-cultures with *APOE4/E4* astrocytes

(A) Illustration of the experimental design for detecting astrocyte-mediated plasticity in co-cultures of human neurons and human astrocytes. Neurogenin-2-expressing cortical neurons from a healthy control (*APOE2/E3*) cell line were co-cultured with *APOE4/E4* human astrocytes expressing either YFP in the control condition, or ChR2-YFP in the stimulated condition. Cultures were stimulated over a period of 3-5 days, using 250 ms duration LED light pulses with a pulse interval of 50 s. Recordings of sEPSCs were performed from mKate^{+} neurons. **(B)** Example recordings of sEPSCs (left) from neurons in the control (top) and stimulated conditions (bottom). Overlays show all sEPSCs detected in the full recording, with the average sEPSC highlighted in bold (right). **(C)** No differences were observed between the control and stimulated conditions in terms of the sEPSC properties or the passive membrane properties.

The proportion of synaptically active neurons was found to show no change following LED stimulation (control: 83%, n=40 neurons; stimulated: 92%, n=39 neurons; p=0.190, Chi-square contingency test) (**Figure 6.5C**). LED stimulation also did not serve to enhance the frequency of sEPSCs within individual neurons (control: 0.61 ± 0.17 Hz, n=40 neurons; stimulated: 0.38 ± 0.08 Hz, n=39 neurons; p=0.790, un-paired Mann-Whitney test) and sEPSC amplitude was unaffected (control: 32.4 ± 3.7 pA, n=33 neurons; stimulated: 27.6 ± 3.9 pA, n=36 neurons; p=0.166, un-paired Mann-Whitney test) (**Figure 6.5C**). Recordings were confirmed to have targeted neuron populations with comparable intrinsic membrane properties (Cm, control: 28.2 ± 2.9 pF, n=40 neurons; Cm, stimulated: 24.7 ± 1.3 pF, n=39 neurons; p=0.498, un-paired Mann-Whitney test), (Rm, control: 0.86 ± 0.05 GΩ, n=40 neurons; Rm, stimulated: 0.84 ± 0.04 GΩ, n=39 neurons; p=0.996, un-paired Mann-Whitney test) (**Figure 6.5C**).

Finally, immunolabelling for pre- and post-synaptic markers (see section 2.3.1) revealed no difference in the presence of anatomically defined synapses (**Figure 6.6A**). Immunolabelling for pre-synaptic (SynPhy) and post-synaptic markers (Homer1) was performed on co-cultures consisting of 03-01 healthy neurons and 042 sAD astrocytes grown under control and stimulated conditions identical to the electrophysiology experiments. Puncta overlapping with $MAP2^+$ neurites were automatically detected and quantified (see section 2.3.2, **Figure 6.6B**) and no differences between synaptic densities were detected between control and stimulated conditions (**Figure 6.6C**). This was the case whether examining the pre-synaptic marker (SynPhy, control: 2.9 ± 0.25 puncta/100 µm, n=10 FOV from 2 cultures; stimulated: 2.4 ± 0.2 puncta/100 µm, n=10 FOV from 2 cultures; p=0.143,

un-paired Mann-Whitney test), the post-synaptic marker (Homer1, control: 3.5 ± 0.6 puncta/100 µm, n=10 FOV from 2 cultures; stimulated: 2.6 ± 0.3 puncta/100 µm, n=10 FOV from 2 cultures; p=0.089, un-paired Mann-Whitney test), or dual labelled puncta (control: 0.4 ± 0.1 puncta/100 µm, n=10 FOV from 2 cultures; stimulated: 0.3 ± 0.1 puncta/100 µm, n=10 FOV from 2 cultures; p=0.971, un-paired Mann-Whitney test). Similar neurite lengths were examined from both conditions (control: 1594 ± 98.8 µm, n=10 FOV from 2 cultures; stimulated: 1585 ± 90.2 µm, n=10 FOV from 2 cultures; p=0.684, un-paired Mann-Whitney test).

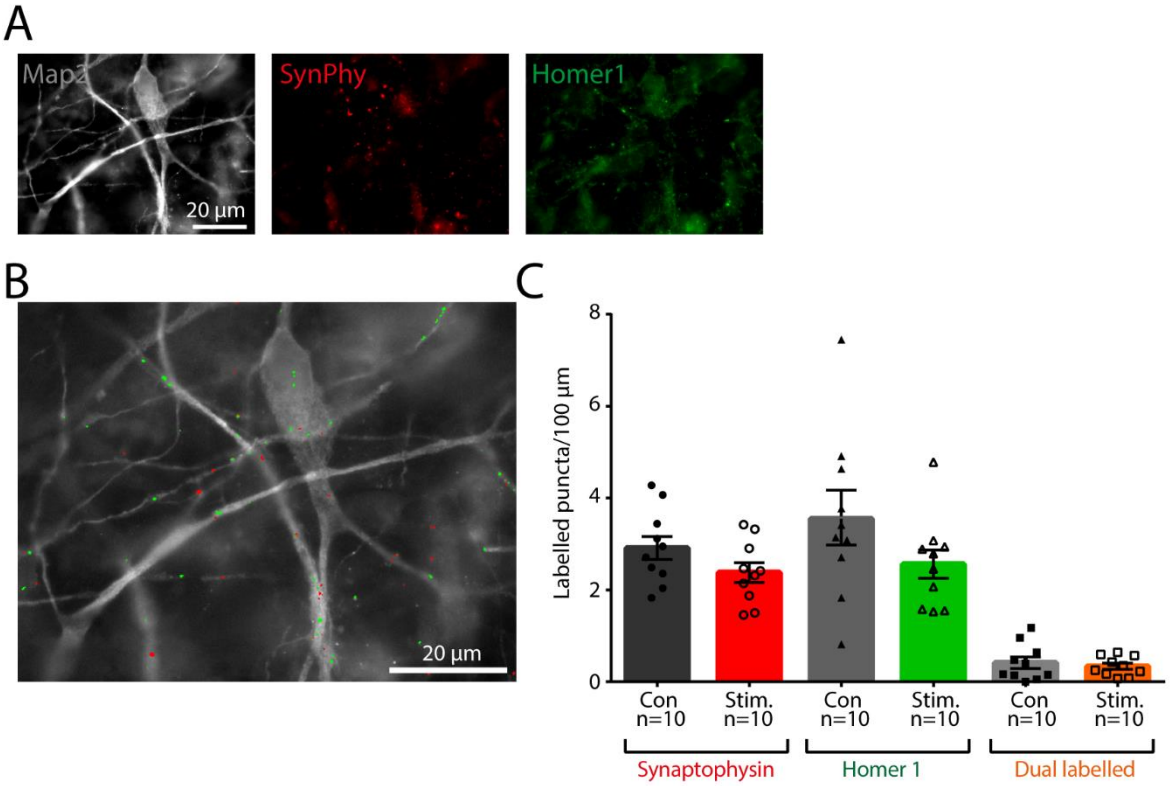

Figure 6.6 Synaptic density is unaltered by stimulation of *APOE4/E4* astrocytes
Synaptic markers synaptophysin (SynPhy) and Homer1 were quantified using customised automated detection software. Co-cultures of healthy control (*APOE2/E3*) Neurogenin-2-expressing cortical neurons and *APOE4/E4* human astrocytes were exposed to the LED protocol described in **Figure 6.5**. **(A)** Example images of a neuron and surrounding neurites (Map2, left), pre-synaptic marker (SynPhy, middle) and post-synaptic marker (Homer1, right). **(B)** The original Map2 neurite image overlaid with the synaptic puncta detected by the automated detection software. **(C)** No differences were detected in the number of labelled puncta per 100 µm of neurite between the control and stimulated astrocyte conditions (n = 10 FOV, imaged across 2 triple-labelled co-cultures for each condition).

Taken together, these data indicate that astrocytes carrying the *APOE4/E4* genotype were not able to elicit the same enhancement of functional synaptic networks as was observed for astrocytes carrying non-*APOE4* genotypes (see **Chapter 5**).

6.3 Discussion

In this chapter, I successfully generated astrocytes carrying disease-relevant *APOE* genotypes. This provides a platform for examining the impact of *APOE* genotype on astrocyte-mediated modulation of neuronal signalling. More specifically, iPSC lines from individuals diagnosed with sAD, and harbouring the *APOE4/E4* genotype, were successfully differentiated into cortical neural progenitors and then directed towards an astrocyte phenotype. These differentiations proceeded in a qualitatively normal manner and immunolabelling revealed an early S100β -rich period, followed by a period of equivalent enrichment of GFAP and S100β , reaching levels of 60-75% positively labelled cells.

Interestingly, the secretion of APOE was found to be lower from the *APOE4/E4* astrocytes than from healthy *APOE3/E3* astrocytes. This observation is in accordance with the genotype-dependent decrease in APOE protein levels reported in mouse brain and astrocytoma cultures (Riddell *et al.*, 2008), as well as recent characterisation of iPSC-derived astrocytes (Lin *et al.*, 2018). Lin and colleagues detected reduced APOE levels from *APOE4* isogenic astrocytes compared to astrocytes from the *APOE3* parent line, both by immunocytochemistry and immunoblotting (Lin *et al.*, 2018). Other studies support the idea that it is not only the amount of secreted APOE that differs between healthy controls and sAD cases, but also the capability of the astrocytes to deliver cholesterol. For example, one study that found no differences in the amount of APOE secreted from human *APOE3* and

APOE4 knock-in mouse astrocytes, still observed that the levels of secreted cholesterol were significantly different, leading to the conclusion that *APOE3* astrocytes are capable of delivering more cholesterol per APOE molecule (Gong *et al.*, 2002). It will be interesting to assess how cholesterol secretion relates to APOE secretion and *APOE* genotype in the human iPSC-derived astrocytes.

The idea that the *APOE4/E4* genotype underlies a loss-of-function phenotype in astrocytes, and more specifically in terms of astrocyte-neuronal signalling, is supported by evidence that the *APOE4/4* genotype is associated with disrupted synaptic density and plasticity in neurons (Mauch, Na and Schumacher, 2001; Ji *et al.*, 2003; Trommer *et al.*, 2004; Dumanis *et al.*, 2009). I therefore wanted to examine whether the *APOE4/4* genotype influences the astrocyte-mediated forms of plasticity that I characterised in **Chapter 5**. These previous experiments had demonstrated that iPSC-derived human astrocytes that are not of an *APOE4/E4* genotype, are able to elicit an increase in the proportion and level of synaptically active neurons. In the current chapter however, I found that these effects were absent when the same experiments were conducted using co-cultures with *APOE4/E4* astrocytes. These observations extend recent evidence in a human iPSC model, that *APOE4* astrocytes provide diminished neurotrophic support for neurons, which decreases their survival rates and synaptic integrity (Zhao *et al.*, 2017). Taken together, these data are consistent with the idea that the *APOE4/E4* genotype is associated with a limited capacity for human astrocytes to support neuronal plasticity.

One consideration is that in the experiment with *APOE4/E4* astrocytes, 83% of the control neurons were already synaptically active and this may have limited the potential to

recruit additional neurons to the functional network following astrocyte stimulation. On the other hand, this rationale could not explain the lack of increase in the frequency of synaptic inputs per neuron, which was another parameter that increased following stimulation of non-*APOE4/E4* astrocytes (compare **Figure 6.5C** to **Figures 5.6C, 5.8C, 5.9E** and **5.10D**). Interestingly, early neuronal maturation in terms of gene expression, mEPSC frequency and the number of synaptic puncta, was recently observed in both *APOE4/E4* and *PSEN1* iPSC-derived neuronal cultures (Lin *et al.*, 2018). This suggests that precocious synaptic maturation could be an intrinsic feature of AD-associated iPSC-derived neurons, or perhaps something that is associated with sAD *APOE4/E4* human astrocytes.

In summary, the data reported in this chapter demonstrate the viability of generating human astrocytes with different *APOE* genotypes, and represent the first attempt to use these cells under co-culture conditions. The optogenetic assay for inducing astrocyte-mediated neuronal plasticity is relevant to investigations concerning sAD, as this is associated with the major APOE-producing cell type: the astrocyte. By selectively controlling the astrocyte-signalling in co-culture, their contribution to neuronal plasticity was studied. My initial experiments suggest that *APOE* genotype does indeed influence the potential for astrocytes to elicit long-term enhancement of synaptic networks.

Chapter 7

7 GENERAL DISCUSSION

In this chapter, I firstly summarise the key outcomes of each results chapter in terms of experimental findings. This will be followed by sections in which I discuss major themes of the thesis, by examining the implications of the findings, how these relate to existing literature and how they might lead to future work. In particular, I will discuss the challenges associated with generating a human iPSC-derived astrocyte, what can be learned about human astrocyte-to-neuron signalling from the optogenetic experiments, and how the cellular model outlined here might be useful for studying disease mechanisms in sAD.

7.1 Summary of experimental findings

In **Chapter 3**, I demonstrated that human iPSCs can be differentiated into a common cortical progenitor pool, from which cells can be driven towards a neuronal or an astrocytic fate. Sequential appearance of cortical neuronal layer markers verified that the differentiation of neural progenitors is reminiscent of the *in vivo* inside-out pattern of cortical development. During the astrocyte differentiation protocol, progenitors generated cells that first underwent a period of predominant S100β expression, followed by upregulation of GFAP expression. Electrophysiological characterisation revealed that human neurons displayed appropriate functional properties, yet were at an immature stage in terms of AP generation and synaptic network connectivity. Importantly, when the biophysical properties of human astrocytes were assessed, they were found to lack the ability to fire APs, but to exhibit much lower voltage-gated conductances, higher membrane capacitances and lower membrane resistances than the neurons. The astrocytes showed extensive gap-junction coupling and a subpopulation were

capable of performing glutamate uptake and displayed inward rectifying K^+ currents, consistent with a more mature phenotype that could engage in homeostatic regulatory processes.

In **Chapter 4**, I provided further evidence for the functional properties of the iPSC-derived human astrocytes by exploring ion homeostasis and dynamics, particularly in relation to Ca^{2+}, H^+ and Cl^-. In accordance with the rodent literature, the iPSC-derived human astrocytes displayed a variety of Ca^{2+} signalling modes, including both spontaneous and evoked responses. I demonstrated that human astrocytes are capable of "listening" to neurons by reacting to neurotransmitters with spatiotemporally defined Ca^{2+} elevations, which propagated outwards from the place of initiation in an inter-cellular, wave-like fashion. The genetically-encoded ion sensitive reporter, ClopHensorN, revealed that astrocytes rested slightly more acidic and at higher internal [Cl^-] than neurons. Previous work has shown that rodent astrocytes tend to respond rapidly to network activity by exhibiting intracellular alkalinisation. Consistent with this, when human astrocytes were exposed to elevated extracellular K^+, the resulting astrocytic depolarisation induced intracellular alkaline pH shifts that were mediated by sodium-bicarbonate cotransporters. Providing human neurons and astrocytes with a more physiologically relevant environment was achieved through transplantation into mouse organotypic hippocampal brain slices. Under these conditions, periods of elevated network activity generated pH changes in opposite directions in transplanted human neurons and astrocytes, with astrocytic alkalinisation and recovery occurring over a faster time scale than the neuronal acidic responses. Measures of Cl^- dynamics

revealed a trend for astrocytes to load Cl^-, whereas neurons showed no significant Cl^- dynamics during network events.

In **Chapter 5**, I provided evidence that human iPSC-derived astrocytes can exert pro-maturational effects on iPSC-derived neurons when placed in physical co-culture. Baseline AP capacity, the proportion of synaptically-active neurons, and the frequency of postsynaptic currents, were all enhanced by the presence of human astrocytes. I then explored the potential for actively recruiting neuron-to-astrocyte communication. By adopting an optogenetic experimental strategy, I was able to show that direct ChR2 activation of astrocytes generated intracellular Ca^{2+} elevations and an acute enhancement of metabotropic glutamatergic receptor activation in nearby neurons. By stimulating co-cultures containing ChR2 expressing astrocytes over a period of several days, I was able to demonstrate astrocyte-mediated modulation of synaptic transmission. This long-term astrocyte-mediated neuronal plasticity was experimentally robust and increased both the synaptic inputs innervating the co-cultured neurons, as well as the intrinsic excitability of these neurons.

Chapter 6 advanced the use of iPSC co-cultures for studying astrocyte-to-neuron signalling in a disease context. First, I generated astrocytes from individuals clinically diagnosed with sAD and whom were homozygous for the *APOE4* allele. By genotyping, I confirmed the *APOE* genotypes of all the cell lines used in this thesis. Immunolabelling supported the conclusion that *APOE4/E4* iPSCs are able to generate astrocytes like healthy control lines. *APOE4/E4* iPSCs appeared to undergo normal cortical differentiation, and when driven towards an astrocytic fate, the *APOE4/E4* cells followed the same stages of early S100β expression, followed by GFAP enrichment, as was observed with healthy control cells. APOE

secretion from the *APOE4/E4* astrocytes was found to be lower than from *APOE3/E3* astrocytes, which could indicate that the lipid and cholesterol delivery from *APOE4/E4* astrocytes is impaired. Finally, when *APOE2/E3* neurons were co-cultured with ChR2^{+} *APOE4/E4* astrocytes, there was no evidence that optical stimulation of the astrocytes was able to generate neuronal plasticity.

7.2 Is this a human astrocyte that I see before me?

A principal objective of this thesis was to produce human astrocytes from iPSCs in order to be able to study their functional interactions with neurons. Given that astrocytes are a heterogeneous population of cells that can display different morphological and functional characteristics depending on the conditions, a central question remains: to what extent can I be confident that I have generated a human astrocyte? In the following sections I will address this question by discussing some of the hallmarks of astrocytes and how the cells generated in this thesis compare to these hallmarks.

7.2.1 Cellular markers of astrocytes

A standard way to infer cell identity is to distinguish different cell populations by their expression of cell-type-specific proteins, through techniques such as immunolabelling, RT-PCR or western blotting. In the case of astrocytes, the cytoskeletal protein GFAP has long been considered the "gold standard" marker across both rodent and human studies (Eng, Ghirnikar and Lee, 2000), and it was reliably and robustly detected in the human iPSC-derived astrocytes described in this thesis. However, many circumstances can influence the expression of GFAP (Tyzack, Lakatos and Patani, 2016). Firstly, GFAP is transiently expressed in human radial glial progenitors (Garcia *et al.*, 2004; Casper and McCarthy, 2006),

meaning that morphological analysis or co-labelling with other markers is often required to distinguish a radial glia cell and an astrocyte (Malatesta, Appolloni and Calzolari, 2008). Secondly, following maturation, quiescent grey matter astrocytes are associated with a downregulation of GFAP, whereas white matter astrocytes show persistent GFAP expression (Roybon *et al.*, 2013). This means that both regional identity and maturity can influence GFAP expression. Thirdly, reactive astrogliosis states have generally been associated with increased GFAP immunoreactivity, as shown for example in two mouse models of brain injury (Zamanian *et al.*, 2012). Taken together, this means that the high levels of GFAP expression detected in human astrocytes could reflect the presence of radial glia, white matter astrocytes or a transition to reactive states. However, the concomitant expression of S100β and the non-bipolar morphology of the cells, supports the conclusion that these are astrocytes rather than radial glia.

Determining whether any differentiation protocol has resulted in white matter astrocytes or cortical grey matter astrocytes is challenging, as there is presently no marker to distinguish these two populations. If it is the case that astrocyte subtypes are governed by regional patterning (Hochstim, Deneen, Lukaszewicz, Zhou and David J. Anderson, 2008; Liu and Zhang, 2011), one would predict that the astrocytes generated are those associated with cortical grey matter. According to Oberheim et al. (2009), the six layers of human cortex mainly contain interlaminar, protoplasmic and varicose projection astrocytes, which influence synapses (Wang and Bordey, 2008). In contrast, the white matter is populated by fibrous astrocytes (Oberheim *et al.*, 2009), which contact nodes of Ranvier and are thought to influence AP propagation (Wang and Bordey, 2008). These astrocyte subtypes have been

distinguished based on location and morphology in human brain tissue, but the vast heterogeneity of morphologies that were observed in the present astrocyte cultures makes such distinctions difficult. It might be possible, however, to compare the transcriptomic profile of the human astrocytes presented here with existing transcriptomics datasets which draw distinctions between astrocyte subtypes (Chai *et al.*, 2017; John Lin *et al.*, 2017). Excitingly, recent research from the Ullian lab has demonstrated how a 3D organotypic-like co-culture method can produce iPSC-derived astrocytes with morphological complexity that is close to *in vivo* human astrocytes (Krencik *et al.*, 2017). This strategy is appealing for the further study of human neuron-astrocyte interactions, if the issue of accessibility for functional techniques, such as patch clamp recordings, can be overcome.

In relation to astrocyte reactivity, the type of serum commonly used in dissociated astrocyte cultures has been reported to induce lasting gene expression changes (Foo *et al.*, 2011), some of which were found to be associated with a reactive astrocyte phenotype (Magistri *et al.*, 2016; Zhang *et al.*, 2016). The protocol used in this thesis incorporated serum in the astrocyte maintenance media, as it promoted GFAP and S100β expression, an effect which was also noted by Magistri and colleagues. When co-culturing the human astrocytes with iPSC-derived cortical neurons, serum levels were reduced to 1% but were not eliminated, as this was found to result in cell-free areas on the coverslips. To determine the reactive or quiescent state of the human astrocytes generated in this work, it would be interesting to conduct a transcriptomic analysis, reminiscent of the investigations by Magistri et al. (2016) and Zhang et al. (2016), which compared datasets from reactive and resting human astrocytes. Devising a serum-free maintenance medium might be preferable in future work. Magistri and

colleagues achieved similar or improved astrocytic marker expression by using a combination of CNTF and BMP4 compared to 2.5% FBS, when maturing NPCs isolated from foetal human brains to astrocytes. Furthermore, Foo and colleagues reported that their rodent astrocytes cultured with serum-free methods displayed functional phenotypes and astrocyte heterogeneity that matched the *in vivo* situation more closely (Foo *et al.*, 2011). Nevertheless, what can be concluded from my work is that the iPSC-derived human astrocytes were still capable of providing beneficial support for human neurons, particularly in terms of synaptic function, even if they are in a potentially serum-induced reactive state. Given that so-called "A1" reactive astrocytes were reported by Liddelow et al. (2017) to be unable to promote neuronal survival and synaptogenesis (Liddelow *et al.*, 2017), perhaps the iPSC-derived human astrocytes presented here do not represent such a detrimental state of reactiveness. It can of course be hypothesised that any neuronal benefits attained by co-culture with human astrocytes could be even greater if the astrocytes were maintained in a more quiescent state.

7.2.2 Biophysical properties of astrocytes

In addition to the expression of astrocyte-relevant proteins, the expectation is that iPSC-derived astrocytes must also display biophysical characteristics that are consistent with their cellular identity and therefore distinguish them from neurons. Firstly, astrocytes are non-excitable in terms of their ability to generate APs, which was confirmed for every astrocyte patched. Secondly, while they express many of the same voltage-gated ion channels as neurons (Bevan *et al.*, 1985; Nowak, Ascher and Berwald-Netter, 1987; Barres *et al.*, 1989), astrocytes might also possess a specific glial Na^+ channel, which has been described as having a lower current density, slower kinetics and lower activation threshold compared to their neuronal

counterparts (Barres *et al.*, 1989). The current recordings of biophysical properties demonstrate that the human astrocytes have ~10 fold smaller VGNa$^+$ current amplitudes than the neurons, and combined with the ~6-fold larger membrane capacitance of the astrocytes, this translates to a ~60-fold lower current density in the human astrocytes (astrocytes: 1 pA/pF; neurons: 66 pA/pF, calculations based on mean values). The much lower membrane resistance of human astrocytes also indicate that their membranes are much leakier, contributing to their lack of excitability.

In terms of voltage-gated K^+ channels, the human astrocytes described in this thesis mostly demonstrated outward K^+ rectification, similar to the repolarising currents seen in neurons. However, subset of the astrocytes revealed inward rectification, consistent with the capacity for buffering extracellular K^+. The kinetics of K^+ removal from the synaptic cleft after neuronal signal transmission can shape the post-synaptic response, making astrocytes an important regulator of synaptic signalling (Nedergaard and Verkhratsky, 2012; Bellot-Saez *et al.*, 2017). The dominant K^+ channel responsible for inward rectification is $K_{ir}4.1$ (Higashi *et al.*, 2001; Schröder *et al.*, 2002), whose knockdown has been shown to markedly inhibit K^+ buffering and reduce glutamate uptake (Djukic *et al.*, 2007; Kucheryavykh *et al.*, 2007). The fact that I detected an overlap between the small population of single astrocytes displaying inwardly rectifying currents *and* glutamate uptake, is indicative of the presence of $K_{ir}4.1$ channels. However, further immunolabelling and patch clamp recordings would help to confirm their expression. $K_{ir}4.1$ channels are reported to be involved in maintaining a more hyperpolarised membrane potential in astrocytes compared to neurons (Olsen and Sontheimer, 2004; Djukic *et al.*, 2007), yet the resting Vm of iPSC-derived neurons and astrocytes were

observed to be similar, which could be an indication that levels of $K_{ir}4.1$ channels are low in the human astrocytes. This observation also fits with the relatively low levels of $K_{ir}4.1$-mediated inward rectification detected in the astrocyte cultures. Nevertheless, detecting $K_{ir}4.1$ channels could potentially serve as a functional marker of astrocyte maturity, as its expression has been associated with the final stages of astrocyte differentiation (Higashimori and Sontheimer, 2007).

7.2.3 Astrocytic network properties

The functional properties expected of astrocytes are linked to their supportive role as regulators of brain homeostasis. A property that enables astrocytes to perform this role is their gap-junction connectivity (Cheung *et al.*, 2015). In **Chapter 3**, I demonstrated that iPSC-derived human astrocytes can form a syncytium that permits the diffusion of small molecules. This would be predicted to allow the astrocytes to efficiently distribute K^+ and glutamate taken up from the synaptic cleft. I demonstrated the capacity for glutamate uptake from the human astrocytes on a population basis, but the experiments with individually patched astrocytes revealed that not all astrocytes are equally capable. This observation fits with the distinction made in rodent hippocampus between glutamate transporting (GluT) astrocytes, and glutamate receptor bearing (GluR) astrocytes (Matthias *et al.*, 2003). The GluT astrocytes have previously been termed "passive" and were electrophysiologically associated with inward rectifying K_{ir} currents (Zhou and Kimelberg, 2000), and were recently identified as mature protoplasmic astrocytes (Djukic *et al.*, 2007). In contrast, the GluR astrocytes that express AMPARs have been termed "complex" (Zhou and Kimelberg, 2001), are associated with outward rectifying K^+ currents (Zhou and Kimelberg, 2000) and are

believed to represent immature astrocyte precursors (Djukic *et al.*, 2007). Filling patched cells with biocytin and conducting subsequent immunolabelling against glutamate transporters and AMPARs could elucidate whether such distinctions hold true for the human astrocytes. I would predict that the subset of GluT-like astrocytes present in my cultures are able to perform vital neuronal support through the buffering of K^+ and glutamate.

The variety of ways in which intracellular Ca^{2+} events can be initiated in astrocytes, combined with different forms of cell-to-cell propagation, adds greater complexity to the astrocytic signalling toolbox. Whether arising spontaneously, being stimulated by neurotransmitter release, or initiated by injury, the downstream functions of astrocytic Ca^{2+} signalling are also multivariate. Astrocytic Ca^{2+} elevations can, for example, modulate glutamate transporters, change the permeability of ion channels, regulate the release of trophic factors, and alter synaptic connections (Nett, Oloff and McCarthy, 2002). Live cell imaging in iPSC-derived astrocytes revealed spontaneously arising Ca^{2+} elevations, which were a mixture of asynchronous, single-cell events and synchronous events involving multiple cells. These experiments reveal a supposedly neuron-independent form of astrocytic signalling, which has also been reported in rodent model systems (Parri, Gould and Crunelli, 2001; Nett, Oloff and McCarthy, 2002; Tashiro, Goldberg and Yuste, 2002). It seems unlikely that the spontaneous Ca^{2+} events would have been initiated by the small numbers of neurons in the enriched astrocytic cultures. To confirm this however, it would be important to repeat the Ca^{2+}-imaging in the presence of TTX (Aguado *et al.*, 2002). Spontaneous Ca^{2+} oscillations in astrocytes have been shown to depend on internal Ca^{2+} induced Ca^{2+} release via IP_3 sensitive intracellular stores, which can involve an initial Ca^{2+} influx via L-type voltage-gated Ca^{2+}

channels, but is independent of mGluRs, ryanodine receptors and gap junctions (Aguado *et al.*, 2002; Nett, Oloff and McCarthy, 2002; Parri and Crunelli, 2003). Future work will be required to establish whether a similar mechanism underlies the human astrocyte spontaneous Ca^{2+} events.

Demonstrating spontaneous astrocytic Ca^{2+} signalling both *in vitro* (Aguado *et al.*, 2002; Nett, Oloff and McCarthy, 2002; Parri and Crunelli, 2003) and *in vivo* (Hirase *et al.*, 2004; Nimmerjahn *et al.*, 2004) has elevated astrocytes to a previously unappreciated role as potential signal generators, and not just signal receivers. Interestingly, such spontaneously occurring astrocyte activity has been demonstrated to be capable of inducing NMDA-mediated slow inward currents in neurons (Parri, Gould and Crunelli, 2001), which suggests that one purpose of spontaneous astrocytic Ca^{2+} elevations is to modulate neuronal signalling. Furthermore, spontaneous intracellular Ca^{2+} responses were shown to be compartmentalised in microdomains that can be located as close as 5 µm from each other (Nett, Oloff and McCarthy, 2002; Parri and Crunelli, 2003). These microdomains were reported to experience Ca^{2+} transients independently, supporting the idea that astrocytes can influence nearby structures in a local, probably synapse-specific manner. Coupled with the later observation that astrocytic microdomains are sensitive enough to detect and respond to spontaneous neurotransmitter release from individual synapses (Di Castro *et al.*, 2011), it makes a strong case for an astrocyte-neuron micro-circuit capable of fine-scale modulation of individual synapses. The fact that spontaneous Ca^{2+} signalling was observed among the iPSC-derived human astrocytes described here is an encouraging sign that they are likely to be capable of contributing to synaptic modulation in an active manner.

The robust Ca^{2+} elevations observed following glutamate and ATP application verified that the iPSC-derived human astrocytes respond to common neurotransmitters in the expected fashion. This confirms that the cells express glutamatergic and purinergic receptors, the identity of which could be explored further using pharmacological approaches. However, while the experiments proved a fundamental aspect of neuron-to-astrocyte signalling, they did not capture the full range of spatial and temporal Ca^{2+} dynamics that have been reported in the rodent literature. In this regard, it would be it interesting to further explore the mechanisms of intracellular and intercellular Ca^{2+} propagation in the astrocytes. For example, one could imagine examining whether multicellular Ca^{2+} waves occur via gap-junction connected astrocytes, or via the successive release of ATP. In addition, it would be important to investigate whether Ca^{2+}-dependent forms of neuron-astrocyte interactions take place in human co-cultures, and specifically, whether spontaneous astrocytic Ca^{2+} signalling can induce slow inward NMDA currents in neurons and whether physiological levels of synaptic transmission are sufficient to initiate Ca^{2+} events in the human astrocytes.

7.2.4 Astrocytic interactions with other cell-types

Astrocytes are often viewed as the glial cell with the most varied functions, in part because of their diverse interactions with multiple cell types, including neurons, other astrocytes, vasculature, oligodendrocytes and microglia. The generation of astrocytes during development correlates with a rapid period of synaptogenesis and previous work has argued that physical contact with astrocytes is crucial for the initiation of normal synaptogenesis (Barker *et al.*, 2008). Consistent with this idea, I detected significant pro-maturational effects on synaptic transmission when human or rodent astrocytes were introduced to the iPSC-derived neuronal

cultures. These observations demonstrate that the human iPSC-derived neurons are capable of interacting with astrocytes in a functionally meaningful way. The specific structural synaptogenic potential of human astrocytes was not examined in this thesis, but investigations by Lischka and colleagues revealed increased SV2 staining in neurons co-cultured with human astrocytes, in comparison with mouse astrocytes (Lischka *et al.*, 2017). A similar staining study could shed light on whether enhanced synaptogenesis might be the mechanism underlying the astrocyte-driven pro-maturational effects I detected on synaptic transmission. Furthermore, comparing astrocyte conditioned media to physical contact cultures could elucidate whether the pro-maturational effect operates through secreted or contact mediated cues.

At a broader network scale, astrocytes can be viewed as sophisticated environmental sensors, capable of changing their morphology, ion dynamics and release of substances, in order to influence metabolism, homeostasis and network function (Verkhratsky and Nedergaard, 2016). By acting as a bridge between multiple cell types, astrocytes are well-placed to regulate many aspects of brain function. In particular, through their intimate physical and chemical interactions with synapses, astrocytes are being increasingly regarded as integrators of synaptic information, operating in conjunction with neurons to generate network output (Oberheim *et al.*, 2009; Perea, Navarrete and Araque, 2009; Pannasch *et al.*, 2011). Astrocytes have been shown to display different Ca^{2+} dynamics according to the type and strength of nearby neuronal signalling, which has led investigators to propose that astrocytes encode information in the amplitude, frequency, periodicity and distance of their Ca^{2+} signalling (Perea and Araque, 2005; Tian *et al.*, 2006). Indeed, a model has been put

forward in which low levels of synaptic transmission lead to short-range, local feedback to the synapse or group of synapses that were recently active. Whereas strong synaptic activation is proposed to induce long-range Ca^{2+} waves within the glial network, which would have the potential to reach all synapse, previously active or not, which are enwrapped by the astrocytes participating in the wave (Fellin and Carmignoto, 2004).

In terms of network homeostasis, astrocytes are integral to regulating the extracellular ionic environment. Homeostatically regulated pH is thought to be essential for various cellular processes, including migration (Denker and Barber, 2002), cell division (Putney and Barber, 2003), synaptic vesicle loading (Tabb *et al.*, 1992) and glutamate uptake (Billups and Attwell, 1996). Neuronal activity poses a challenge for ionic homeostasis, including the regulation of intra- and extra-cellular pH (Raimondo *et al.*, 2015). In their role as homoeostasis mediators, astrocytes are crucially involved in handling challenges to the neuronal environment. The first observation that resting pH values in the human neurons and astrocytes were close to those published for rodent systems (Raimondo *et al.*, 2016), suggests that the pH regulatory mechanisms in the iPSC-derived cells are generally active. Perhaps more importantly, the human astrocytes responded to extracellular K^+ increases by exhibiting membrane depolarisation and intracellular alkalinisation, which is strong evidence that they behave similarly to rodent astrocytes during periods of neuronal activity. Furthermore, in line with established knowledge of the alkalinisation mechanism of rodent astrocytes (Brookes and Turner, 1994; Pappas and Ransom, 1994; Raimondo *et al.*, 2016), Na^+/HCO_3^- co-transporters accounted for the majority of the alkaline shift in the iPSC-derived astrocytes. Astrocytic internalisation of HCO_3^- results in a depletion of this ion in the extracellular environment,

effectively acidifying the external pH. The functional consequence is a modulation of pH-sensitive voltage- and ligand-gated channels, which serves to reduce the net excitability of neurons (Annunziato, Boscia and Pignataro, 2013). It is therefore likely that the purpose of the alkalinisation response of astrocytes is to assist in dampening the ongoing neural activity; a notion which is supported by the fact that peak astrocytic alkalinisation is reached before peak neuronal acidification and astrocytic pH dynamics were found to be more tightly coupled to the neuronal network activity (Raimondo *et al.*, 2016).

As a comparison, I also confirmed that iPSC-derived human neurons experience a prolonged acidic shift in pH as a result of network activity, as reported by (Ahmed and John, 1980; Trapp *et al.*, 1996; Zhan *et al.*, 1998; Raimondo *et al.*, 2013, 2016). Future work could investigate the mechanisms underlying these acidic shifts. Some potential candidates are 1) Ca^{2+} entry during synaptic activity causing the Ca^{2+}/H^{+} ATPase to extrude Ca^{2+} and take in H^{+} (Schwiening, Kennedy and Thomes, 1993; Makani and Chesler, 2010), 2) Production of metabolic acids: CO_2 and lactate (Wang, Randall and Thayer, 1994), 3) Intense activation of $GABA_A$ receptors, attempting to shut down network activity, which in turn has been associated with efflux of HCO_3^-, making the internal environment more acidic (Pasternack, Voipio and Kaila, 1993; Trapp *et al.*, 1996). Understanding the acidification mechanism could prove important, as it is believed that internal neuronal acidification plays a role in terminating uncontrolled network activity that occurs in conditions of hyperexcitability (Raimondo *et al.*, 2015). Ultimately, these experiments use pH homeostasis to highlight a key homeostatic role of astrocytes in regulating the ionic environment.

In summary, I have demonstrated that cells generated through the differentiation protocol presented in this thesis produce a variety of phenotypes commonly associated with astrocytes. From classical marker expression, to gap-junction connectivity, Ca^{2+} signalling, glutamate uptake and ion handling, and synapse-maturing effects in co-culture. There is of course room for more experiments designed to test the physiology of the cells against known literature, especially in terms of further functional hallmarks, including metabolic homeostasis and stress responses. Further explorations into homoeostatic functions could be an important direction for disease modelling, as problems with homeostatic control often arise in neurodegenerative diseases (Peters, Connor and Meadowcroft, 2015; Gan *et al.*, 2018).

7.3 What do the optogenetic experiments teach us about astrocyte-to-neuron communication?

On the basis that neuron-to-astrocyte communication is a well-established phenomenon, a significant portion of the thesis was concerned with signalling in the reverse direction, and the potential for astrocyte-to-neuron communication. By expressing ChR2 in the human astrocytes, I aimed to mimic the astrocytic response to neural activity and indeed demonstrated that optically-evoked depolarising photocurrents were associated with intracellular Ca^{2+} signals in astrocytes. ChR2 activation thus gave me the opportunity to selectively control the intracellular Ca^{2+} state of the astrocytes within a co-culture setting. By subsequently recording from the neurons, I observed that stimulating astrocytes mediated both increased neuronal excitability and enhancement of synaptic connectivity. In this section, I will discuss the physiological relevance of these experiments and the possible mechanisms through which these effects might be mediated.

7.3.1 The direct effects of optogenetically activating astrocytes

ChR2 is a precise and powerful tool, most commonly used in neurons as it imitates the fast inward flux of Na^+ that is associated with AP generation. In astrocytes, the ChR2-driven influx of positive ions also depolarise the membrane, which is still a normal response for astrocytes, as they depolarise due to K^+ buffering or synaptic glutamate release, particularly during strong network activity. However, ChR2 is capable of driving much larger currents than those induced by physiological buffering or glutamate release. Using a computational model of a tripartite synapse, which was based on electron microscope morphological data, physiology data and an adaptation of a "cable conductor" model, it has been estimated that synaptic glutamate release can depolarise the enwrapping astrocyte process by ~40 mV. In comparison, the average human astrocyte in this study with a Rm of ~0.4 GΩ would be depolarised ~80 mV by a 200 pA photocurrent, for example.

Yet, it appears to be secondary effects of the ChR2-mediated Na^+ influxes which matter for the astrocyte's Ca^{2+} signalling. It has been argued that due to the sensitivity of the NCX to changes in Na^+ and Ca^{2+} gradients, the ChR2-mediated Na^+ influx can reverse the action of the NCX, thereby bringing Ca^{2+} into the astrocytes (Yang *et al.*, 2015). Interestingly, this study showed that IP_3 and ryanodine receptors were not involved in ChR2-activated Ca^{2+} activity, which is somewhat surprising, as intracellular stores are thought to be the major Ca^{2+} release pathway in astrocytes (Pasti *et al.*, 1997; Nash *et al.*, 2002). This does not necessarily mean that the ChR2-evoked Ca^{2+} events are non-physiological. Indeed, it is common for the NCX to operate both in forward and reverse mode under normal circumstances, in order to maintain Na^+ and Ca^{2+} homeostasis, which is reflected by its finely

tuned sensitivity to ion concentrations (Kirischuk, Kettenmann and Verkhratsky, 1997; Lytton, 2007).

Optogenetic stimulation of both rat and human astrocytes was shown in **Chapter 5** to involve membrane depolarisation, rapid ionic fluxes and intracellular Ca^{2+} increases. I therefore hypothesise that the mechanism mediating the induction of neuronal plasticity, i.e. leading to presumed gliotransmitter release, is likely to involve one or more of these changes to the astrocytes. A likely mechanism related to depolarisation would be hemichannel opening (Bennett *et al.*, 2003), leading to non-specific outflow of cytosolic contents. Given the neurotransmitter uptake and buffering capacity of astrocytes, this could result in glutamate, ATP and K^+ being released in a depolarisation-dependent manner at the synapse. Rapid influxes of ions can cause changes in intracellular osmolarity, which can be regulated by volume-sensitive ion channels (Simard and Nedergaard, 2004). Interestingly, VRACs have already been related to optogenetically-driven astrocyte-mediated effects upon synaptic transmission (D. Li *et al.*, 2012; Sasaki *et al.*, 2012). In both studies, it was found that the activation of light-gated cation channels (either ChR2 or LiGluR) caused astrocytic release of glutamate through VRACs. They also ruled out that the glutamate release originated from hemichannels and reversal of glutamate uptake. In addition, Li and colleagues argue that the LiGluR and Ca^{2+}-translocating ChR2 (CatCh) channels were both superior at evoking Ca^{2+} events in astrocytes compared to ChR2, due to their higher relative Ca^{2+} to Na^+ permeability at lower light intensities. Switching ChR2 for LiGluR in the LED-driven astrocyte stimulation assay would be a way to potentially boost the strength of the assay, while decreasing the potential for damaging effects of light. It might also help test the relative importance of Ca^{2+}

as the mediating substance, given LiGluR's ~10 fold greater Ca^{2+} permeability (D. Li *et al.*, 2012).

7.3.2 Gliotransmission and the release of astrocytic factors

Astrocytes are highly secretory cells and can release multiple factors that impact neuronal health, metabolism and transmission (Verkhratsky *et al.*, 2016). The secretory pathways involving transport and diffusion through transmembrane pores are generally uncontroversial, but the capacity of astrocytes to display Ca^{2+}-driven exocytosis is more contentious (Bazargani and Attwell, 2016; Fiacco and McCarthy, 2018; Savtchouk and Volterra, 2018). Proponents argue that astrocytes possess the necessary machinery for Ca^{2+}-dependent exocytosis in terms of SNARE-proteins (Parpura *et al.*, 1995), VGLUTs (Crippa *et al.*, 2006), plus synaptic-like vesicles that contain gliotransmitters and are located in the vicinity of synapses (Bezzi *et al.*, 2004; Bergersen *et al.*, 2012). Furthermore, where proponents maintain that astrocytes exhibit the appropriate Ca^{2+} events to mediate release of gliotransmitters (Santello, Calì and Bezzi, 2012; Navarrete *et al.*, 2013; Volterra, Liaudet and Savtchouk, 2014; Savtchouk and Volterra, 2018), opponents raise concerns about the experimental manipulations used to evoke Ca^{2+}-dependent gliotransmission, suggesting that they are often non-physiological (Agulhon *et al.*, 2008; Fiacco and McCarthy, 2018). Another area of controversy relates to the expression of Ca^{2+}-sensing exocytotic machinery, which more recent studies have failed to observe (Li, Herault, *et al.*, 2013; Chai *et al.*, 2017), as well as whether cytosolic/vesicular glutamate levels in astrocytes are sufficient to activate neuronal receptors (Hamilton and Attwell, 2010). The debate over gliotransmission is therefore ongoing, with many hedging their bets on that more precise, physiologically relevant experimental paradigms will resolve the conflict in the future

(Hamilton and Attwell, 2010; Sloan and Barres, 2014; Volterra, Liaudet and Savtchouk, 2014; Bazargani and Attwell, 2016).

If assuming that astrocytes are capable of Ca^{2+}-dependent exocytosis, I would expect that the optogenetic manipulations employed would recruit these processes downstream of the ChR2-driven Ca^{2+} elevations. However, as components relating to exocytosis were not examined in this thesis, we are forced to consider the factors that astrocytes might be releasing, without definitive knowledge of the release mechanism. By far the factor implicated most frequently in studies on astrocyte-to-neuron communication is glutamate. Astrocytic glutamate release and subsequent modulation of neuronal transmission has been demonstrated in a variety of preparations ranging from dissociated cultures (Parpura *et al.*, 1994), to rodent brain slices (Jourdain *et al.*, 2007; Perea and Araque, 2007), and excised human brain tissue (Navarrete *et al.*, 2013). In these preparations, astrocytic Ca^{2+} responses and glutamate release were elicited by a range of stimuli, including: 1) simultaneous uncaging of Ca^{2+} in astrocytes and minimal Schaffer collateral stimulation, leading to potentiation of transmitter release, operated through mGluRs and not NMDARs (Perea and Araque, 2007); 2) electrophysiological depolarisation of astrocytes, which mediated an enhancement of synaptic strength via extrasynaptic glutamatergic NMDARs (Jourdain *et al.*, 2007); or 3) application of ATP, which resulted in glutamate release and neuronal NMDAR-mediated signalling (Navarrete *et al.*, 2013).

More recently, optogenetic methods for evoking glutamate release from astrocytes have gained popularity (Li, Agulhon, *et al.*, 2013). When stimulating $ChR2^{+}$ astrocytes acutely, glutamate was concluded to be released and to influence neuronal signalling acutely

(D. Li *et al.*, 2012; Sasaki *et al.*, 2012; Perea *et al.*, 2014). Perea and colleagues' careful pharmacological dissection demonstrated that astrocytically released glutamate acts on the mGluR1a subtype of mGluRs, normally located perisynaptically (Lujan and Somogyi, 1996). I also confirmed that ChR2 activation in astrocytes could cause acute short-term increases in synaptic transmission in pure human co-cultures, which was inhibited by the general mGluR blocker MCPG. An obvious next step would be to test if the long-term optically driven astrocyte-mediated neuronal plasticity effects might also be mediated by a similar mechanism. This could be achieved by incubating the co-cultures with an mGluR blocker during the optical stimulation paradigm.

Other factors which could potentially be released by astrocytes and influence neuronal transmission are ATP and L-serine. Purinergic signalling has been related to heterosynaptic depression, in that neuronal GABA release stimulates astrocytic ATP release, which in turn suppresses glutamate release from nearby synapses (Hamilton and Attwell, 2010). Given that inhibiting astrocytic ATP release has been shown to increase basal synaptic transmission (Pascual *et al.*, 2005), it seems that astrocytic release of ATP would be an unlikely candidate for mediating the increase in synaptic activity detected in **Chapter 5**. Although, synergistic actions of ATP and glutamate was recently shown in mouse hippocampal slices to increase neuronal excitability, both in terms of AP firing and mEPSC frequency, much like what I have observed (Shen *et al.*, 2017a).

Recently, the D-serine gliotransmission hypothesis has been replaced by an alternative theory involving L-serine. Several studies had reported the importance of D-serine as an astrocyte-released factor that controls LTP at glutamatergic synapses (Mothet *et al.*,

2006; Panatier *et al.*, 2006; Henneberger *et al.*, 2010). However, cell-specific knockout mouse models have revealed that astrocytes do not possess the enzyme for D-serine production – whereas it is abundant in neurons (Miya *et al.*, 2008; Benneyworth *et al.*, 2012). Now, astrocytes are rather hypothesised to be involved in supporting the neuronal D-serine production by supplying L-serine as part of their metabolic support of neurons (Wolosker, Balu and Coyle, 2016). This does not invalidate the involvement of astrocytes in LTP, but specifies that the factor the astrocytes supply is actually L-serine, and that the NMDAR-activating D-serine is produced and released by neurons themselves.

7.3.3 Alternatives to gliotransmission

Alternative mechanisms through which the astrocytic stimulation might exert effects upon neuronal transmission are related to the immediate homeostatic control over the synaptic micro-environment imposed by astrocytes. The so-called "astrocytic cradle" theory has been proposed as an alternative, gliotransmitter-independent model for astrocyte-to-neuron signalling (Nedergaard and Verkhratsky, 2012). The astrocytic cradle represents an extension of the tripartite synapse concept, as it focuses on the synapse-isolating properties of astrocytes. By virtue of enwrapping individual synapses, astrocytes create an isolated micro-environment, which is shielded from the "spill-in" of extrasynaptic signals and the "spill-out" of its own synaptic transmitters. Due to their capacity for K^+ regulation, enwrapping astrocytes are perfectly placed to regulate neuronal excitability through controlling synaptic K^+ levels (Bellot-Saez *et al.*, 2017).

Neuronal excitability is sensitive even to small changes in synaptic K^+ concentrations, and a prominent mechanism by which astrocytes remove K^+ is the Na^+/K^+

ATPase. However, ChR2-activation mediates a large astrocytic Na^+ influx, which would be predicted to increase the Na^+/K^+ ATPase activity, essentially making K^+ clearance more efficient and reducing excitability (Nedergaard and Verkhratsky, 2012), and thus opposing the increased excitability that was detected. Yet, the increase in intracellular Na^+ would also serve to reduce the electrochemical gradient of Na^+ within the astrocyte. This in turn could reduce glutamate uptake, as EAAT transport is dependent on the inward gradient of Na^+, which would result in prolonged sEPSCs as the synaptically-released glutamate is cleared less efficiently (Grewer and Rauen, 2005). Glutamate uptake efficiency could also be affected by changes in EAAT expression levels. It would be possible to assess the hypothesis that ChR2 stimulation influences EAAT expression via several experimental strategies, where a transcriptomic comparison might be the most sensitive to pick up any such differences between a control and a stimulated culture. Ultimately, longer sEPSCs due to altered EAAT expression or decreased activity can be assumed to increase the likelihood of correlated pre- and post-synaptic activity, which has been reported as required for processes such as synapse-unsilencing (Hanse, Seth and Riebe, 2013), and could contribute to the effects seen following long-term astrocyte stimulation.

Outside the classical gliotransmitter literature, some suggestions for factors that affect synaptic maturation include TNF-α or Gpc4 and 6 which appear to act in a coordinated fashion to un-silence post-synaptic structures (see section 1.3). The co-action of these factors have been reported as essential for obtaining fully functional synapses, via unsilencing of silent synapses through post-synaptic AMPAR insertion (Stellwagen *et al.*, 2005; Allen *et al.*, 2012). Although still operating through released factors, this mechanism suggests structural changes

to neuronal synapses, distinguishing it from the effects mentioned in the previous section. Since both the sEPSC and mEPSC frequency was observed to increase without any changes in the amplitude or numbers of synaptic puncta, this would be consistent with an unsilencing of pre-synaptically active synapses (Sinnen *et al.*, 2017). As unsilencing appears to be exactly the role of TNF-α and Gpc's during development, one could test if adding these factors to co-cultures might replicate the effect of astrocytic stimulation. How the secretion of factors like TNF-α and Gpc's is regulated, particularly outside the developmental time window is however poorly understood. For example, it is an open question whether astrocytic depolarisation, ion fluxes or Ca^{2+} activity could influence the release of these factors, which would be relevant for evaluating these as potential factors involved in the astrocyte-mediated neuronal plasticity observed here.

In summary, utilising enriched cultures of differentiated cells as the basis for co-cultures has enabled me to establish an experimental paradigm in which it is possible to selectively stimulate different cell types. It is possible to vary both the genotype of the cell types involved, as well as the temporal signalling of the different cell types by utilising optogenetic techniques. Such selective manipulation of one cell type in a co-culture is very useful for isolating the action and contribution of that particular cell type to the network readout. Definitively isolating the actions of astrocytes has previously been challenging in animal models, partly because many relevant drug targets, like channels and transporters are present on both astrocytes and neurons, but also because early developmental manipulations of astrocytes can lead to indirect detrimental effects. Cell-type targeted opsins are a useful,

non-invasive way of manipulating cell biology, and there is an ever-increasing range of opsins that are being made available to neuroscientists.

7.4 Could human neuron-astrocyte co-cultures elucidate disease mechanisms in sporadic AD?

Alzheimer's disease is a complex disease in which multiple affected processes contribute through different cell types, different pathways and at different time points during disease progression. The disease mechanisms in sAD are particularly complex, as no single mutation is associated with the development of the pathological state, as is the case in fAD. The hallmarks of amyloid-beta (Aβ) plaque formation, hyperphosphorylated tau tangle pathology, and neuron loss are shared between fAD and sAD, but the underlying processes leading to these may differ. Increasingly, the role of astrocytes in AD is being investigated and the discussion here will be focused on how astrocytes might affect neuronal degeneration through synapse loss. Astrocytes are the primary source of APOE4, which represents the highest genetic risk factor associated with sAD, and the role of APOE4 in AD-related pathology can be linked to both amyloid and synapse degeneration; yet there are also non-amyloidogenic and non-APOE pathways to consider.

7.4.1 Astrocyte dysfunction in AD

There are various lines of evidence that link non-amyloidogenic and non-APOE related dysfunction of astrocytes to AD. These relate to fundamental functions of astrocytes and include effects upon key proteins: AQP4, K_{ir} channels and Cx43, as detected in mouse models of cerebral amyloid angiopathy (an increase in vascular amyloid deposition, common among people with AD), as well as in human post mortem tissue (Wilcock, Vitek and Colton, 2009).

Loss of any of these proteins would be predicted to negatively affect the capacity for astrocytes to support synaptic function, as they converge on K^+ buffering, which if impaired, can cause excitotoxicity and synapse death (Rothstein *et al.*, 1996; Cheung *et al.*, 2015). Furthermore, glutamate uptake capacity has also been found to be diminished in human AD brains, as assessed via D-[^{3}H]aspartate binding (Masliah *et al.*, 1996) and lower glutamate transporter expression (Jacob *et al.*, 2007). Such evidence has led to hypotheses of impaired astrocytic glutamate handling in AD, predisposing the neurons to excitotoxicity (Avila-Muñoz and Arias, 2014). Further to this hypothesis, it has been shown that soluble $A\beta_{42}$ oligomers can increase basic transmission, enhance LTP and act as an agonist of NMDARs at picomolar concentrations (Puzzo *et al.*, 2008). Whereas at the nanomolar concentrations that are found in AD brains, $A\beta_{42}$ causes pervasive synaptic dysfunction which manifests as an inhibition of LTP, promotion of LTD and excitotoxicity (Marsh and Alifragis, 2018).

Functionally speaking, aberrant Ca^{2+} signalling was detected in an AD mouse model during *in vivo* imaging (Kuchibhotla *et al.*, 2009). Increased basal levels of Ca^{2+}, higher event frequency and synchronicity as detected by Kuchibhotla and colleagues could lead to increased cell death (Abramov, Canevari and Duchen, 2003). The human iPSC-derived astrocytes would provide an accessible platform on which to investigate potential differences in astrocyte excitability in terms of Ca^{2+} signalling. Lastly, and perhaps most fundamental to astrocytic support of synapses in AD, is that the astrocytes are maintained at the appropriate numbers. Data from both transgenic mouse models (Olabarria *et al.*, 2010) and post-mortem analysis of patient brains (Senitz, Reichenbach and Smith, 1995) has revealed decreased complexity of astrocytic processes and an overall loss of cerebral astrocytes. Such atrophy of astrocytic

processes would indicate a breakdown of the essential astrocytic "cradle" that surrounds synapses (Verkhratsky and Nedergaard, 2014), which would presumably prevent astrocytes from maintaining healthy and functional synapses. For these reasons, it would be interesting to examine the expression levels and associated functions of key astrocytic proteins in healthy and sAD *APOE4* iPSC-derived astrocytes. Such experiments could also use electrophysiological recordings and glutamate uptake assays to assess whether K^+ and glutamate buffering mechanisms are affected.

7.4.2 The relationship between astrocytic APOE and amyloid

The amyloid cascade is arguably the most studied aspect of AD pathogenesis. It is increasingly recognised that Aβ accumulation is not merely related to neurons, but involves other brain cell types, including astrocytes. To elucidate the link between Aβ and the *APOE* genotype, studies have unveiled how different *APOE* genotypes influence Aβ -related pathways. The build-up of Aβ can be hypothesised to result from mechanisms affecting its production, its aggregation and its clearance, and it appears that APOE is involved at each stage.

Addition of APOE4 was shown to increase neuronal Aβ production and secretion in cultured rat neuroblastoma cells (Ye *et al.*, 2005), and excitingly, this finding was recently replicated in both mice *in vivo* and human ES-derived neurons (Huang *et al.*, 2017), as well as in human iPSC-derived isogenic neuronal cell lines (Lin *et al.*, 2018; Wang *et al.*, 2018). All studies found that the mechanism through which the *APOE4* genotype influenced Aβ secretion was by enhancing the production of amyloid precursor protein (APP). However, it might be important to distinguish between the quantitative measure of overall secretion of Aβ , and the qualitative ratio between normal ($A\beta_{40}$) and pathogenic ($A\beta_{42}$) peptides, as it

was shown that alterations in Aβ $_{42}$:Aβ $_{40}$ ratios convey more neurotoxicity than absolute levels of the Aβ -peptide (Kuperstein *et al.*, 2010). With this in mind, it is worth noting that Ye et al. (2005) do not make a distinction between the two Aβ species, but report absolute Aβ . Moreover, Huang et al. (2017) and Wang et al. (2018) do not find an increase in Aβ $_{42}$:Aβ $_{40}$ ratio, but rather a proportional increase in both Aβ species in *APOE4* neurons. In collaboration with Emma Whiteley, I have measured the secreted Aβ $_{42}$:Aβ $_{40}$ ratio from several of our iPSC-derived neurons with different genetic backgrounds (**Figure 7.1A**). These results showed that neurons from fAD cell lines (both PSEN and APP mutations) have increased ratios, whilst a sAD *APOE4/E4* line displays ratios that are indistinguishable from healthy control cell lines, consistent with recent published observations (Huang *et al.*, 2017; Wang *et al.*, 2018).

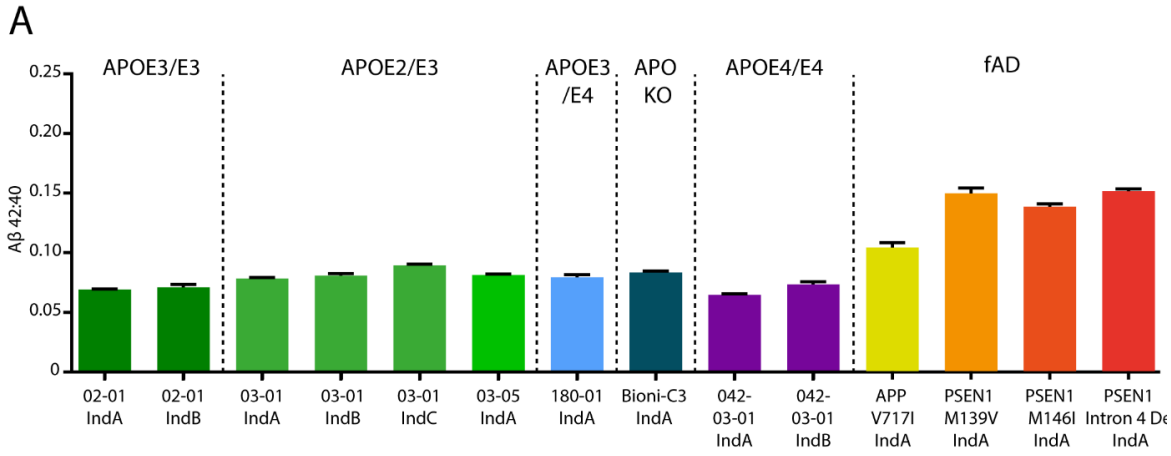

Figure 7.1 ***APOE4/4*** **neurons do not show an amyloid-β phenotype**
(A) The ratio of secreted amyloid-β oligomers $A\beta_{42}$:$A\beta_{40}$ was detected using a Meso Scale Discovery (MSD) assay. Aβ was measured in culture media collected from day 80 neurons derived from cell lines with different *APOE* genotypes, *APOE* KO and familal AD mutations in APP and PSEN1 genes. For the control iPSC lines SBAd 02-01 and SBAd 03-01 several inductions (Ind) were tested to assess variance between inductions.

Several lines of evidence indicate that APOE also governs aspects of Aβ deposition and aggregation in a genotype specific manner (E4 > E3 > E2). From cell culture experiments, it has been shown that HEK cells expressing human APOE4 produce higher amounts of toxic oligomeric species of Aβ (Hashimoto *et al.*, 2012), as well as acting to stabilise fibrils (Garai *et al.*, 2014), as compared to APOE3 and APOE2. Similar results on Aβ aggregation have also been obtained in acute brain slice preparations and an *in vivo* mouse model (Bales *et al.*, 2009). Likewise, PET-scan studies found that Aβ deposition was higher among human *APOE4* carriers, whether they were clinically categorised as healthy controls, patients with mild cognitive impairment, or suffered from AD (Fleisher *et al.*, 2013; Murphy *et al.*, 2013). At a synaptic level, secreted APOE4 was found to exacerbate synapse loss around Aβ plaques, probably by directing toxic Aβ oligomers to aggregate at synapses (Koffie *et al.*, 2012). It could be useful to validate if similar synaptic accumulation of Aβ occurs in my iPSC-based co-culture system and assess its toxicity. I have the opportunity to combine such experiments with electrophysiological recordings, which could tie in with the experiments mentioned above, regarding the potential for $A\beta_{42}$ to exert synapse-enhancing effects at low concentrations, but detrimental effects at higher doses.

Finally, APOE4 also appears to affect Aβ clearance, a mechanism that involves binding of secreted APOE to Aβ peptides and either the subsequent transport to the blood-brain-barrier (BBB), or the internalisation and degradation of Aβ by astrocytes. Conflicting reports have been made regarding the propensity of APOE to bind Aβ , with earlier studies reporting very high levels of APOE4:Aβ binding complexes (Kim, Basak and Holtzman,

2009), but multiple later studies agreeing that APOE3 binds Aβ up to ~20 times more readily than APOE4 (LaDu *et al.*, 1994; Tokuda *et al.*, 2000). APOE4:Aβ complexes from mouse brain capillaries were also found to be cleared more slowly, than when the complexes contained APOE3 or APOE2 (Deane, Sagare, Hamm, Parisi, Lane, Finn, David M Holtzman, *et al.*, 2008). In terms of astrocytic internalisation, a lower uptake of the toxic $A\beta_{42}$ peptide was recently reported from human iPSC-derived *APOE4* astrocytes (Lin *et al.*, 2018).

The human astrocytes I have generated with different *APOE* genotypes could be exposed to a similar uptake assay and, because they are not isogenic cell lines, would reveal whether the relationship between *APOE* genotype and Aβ uptake is robust across different genetic backgrounds. I would be particularly keen to perform an $A\beta_{42}$:$A\beta_{40}$ detection assay from mixed co-cultures. Even though an increased $A\beta_{42}$:$A\beta_{40}$ ratio from *APOE4/E4* neurons alone was not detected (**Figure 7.1A**), the ratio might be increased if these neurons were co-cultured with *APOE4/E4* astrocytes; given APOE4's proven reduced clearance ability. Furthermore, such an assay could be utilised to explore potential phenotype rescue scenarios, which could assess whether Aβ ratios become normalised if *APOE4/E4* or fAD neurons are co-cultured with healthy *APOE3/E3* astrocytes.

7.4.3 The effects of astrocytic APOE on synapses

The regular function of APOE particles is to distribute lipids and cholesterol to tissues or cells that need these vital membrane components for growth and repair (Mahley, 1988). This lipid and cholesterol supply is vital to neurons undergoing synapse formation and strengthening, which makes APOE an important modulator of synapses (Mauch, Na and Schumacher, 2001). The *APOE4* isoform appears to make synapses more vulnerable with age, which can be

appreciated from the age-dependent loss of physical spines detected in transgenic *APOE4* mice, compared to *APOE3* mice (Ji *et al.*, 2003). The same study also found that spine density in human post-mortem brains correlated with the number of *APOE4* alleles harboured by the individual. In line with these results, exposing cultured wild type rat neurons to APOE4 fragments was shown to decrease spines, an effect which could be rescued by a mitochondrial activating drug (Brodbeck *et al.*, 2008), which implies an interaction between APOE4 and mitochondria.

Synaptic deficits due to *APOE4* genotype also manifest at the scale of synaptic networks and behaviour. Experiments with transgenic mice expressing human APOE isoforms have demonstrated decreased LTP in the *APOE4* mice, but surprisingly, this was also the case for *APOE2* and *APOE KO* mice. (Trommer *et al.*, 2004). Such mice have furthermore been found to be profoundly impaired in working memory and on behavioural tasks (Hartman *et al.*, 2001). Synaptic, mitochondrial and plasticity effects have, among others, collectively been argued to be the result of the conformational change in the protein that the *APOE4* genotype infers. The arginine at position 112 induces a domain interaction between the lipid- and receptor-binding domains of APOE4, which impairs its binding of cholesterol and interaction with lipid receptors (Huang, 2010).

Levels of APOE measured in the brain, CSF and plasma of *ApoE* targeted replacement mice were found to be genotype-dependent, with E2>E3>E4 (Riddell *et al.*, 2008). The same study found that the cause of lower APOE4 levels was preferential astrocytic degradation of APOE4, resulting in less protein being secreted. Furthermore, deficiencies in cholesterol packaging have also been associated with the *APOE4* isoform, both in terms of

less cholesterol being delivered per APOE molecule (Gong *et al.*, 2002), as well as neurons displaying decreased uptake of APOE4 compared to APOE3 (Rapp, Gmeiner and Hüttinger, 2006). These lines of evidence have motivated a hypothesis describing how the disease-mechanisms of *APOE4* could be caused by a lack of APOE protein and therefore reduced availability of cholesterol for neurons. This would resemble a loss of function mechanism.

Less secreted APOE could also explain the reduced neurotrophic support reported in iPSC neuron-astrocyte co-cultures by Zhao et al. (2017), which manifested as a decrease in MAP2 staining and impaired neuronal survival (Zhao *et al.*, 2017). As a previous study had showed, neurite outgrowth was limited in the absence of APOE (achieved by using an APOE KO mouse), and addition of APOE3 stimulated outgrowth, whereas addition of APOE4 reduced neurites to KO levels, or even below if the dose was increased (Nathan *et al.*, 2002). Similarly, the spine density was shown to be the same in an *APOE4* animal as in the absence of APOE in a KO animal (Ji *et al.*, 2003). Also, impaired cholesterol delivery would leave synapses vulnerable and more likely to be degraded than repaired (Chung *et al.*, 2016). Lastly, lower levels of APOE in *APOE4* carriers can also impact Aβ -related pathways, ultimately affecting synapses. Less APOE available for performing Aβ clearance would be expected to manifest as an aggregation and clearance deficit, as reported in both mice and iPSCs-derived cells (Deane, Sagare, Hamm, Parisi, Lane, Finn, David M Holtzman, *et al.*, 2008; Lin *et al.*, 2018); with impaired clearance leading to the recognised synaptotoxic effects (Koffie *et al.*, 2012).

In light of the hypothesis that sAD pathogenesis might arise from reduced levels of APOE4, future disease modelling would benefit from accounting for potential effects

associated with differences in the level of APOE protein. I detected less APOE secretion from human iPSC-derived *APOE4/E4* astrocytes than from *APOE3/E3* astrocytes, which is in accordance with findings by Riddell et al. (2008) and Lin et al. (2018), but future work could extend this analysis to include neurons and co-cultures. Furthermore, because little is known about what non-pathological conditions stimulate APOE secretion from astrocytes, it would be interesting to test whether stimulating astrocytic ion fluxes and depolarisation (e.g. via ChR2 activation) influences APOE secretion from healthy control astrocytes. There is currently disagreement in terms of cholesterol contents measured from iPSC-derived astrocytes. Less cholesterol carried by *APOE4* human astrocytes has been reported (Zhao *et al.*, 2017), while on the other hand increases in cholesterol metabolism of *APOE4* astrocytes was detected (Lin *et al.*, 2018). Cholesterol would be a useful component to measure from the types of co-cultures generated for this thesis, given its relation to plasticity and synapse re-modelling, and again the optogenetic assay provides the opportunity to examine if stimulation of astrocytes alters cholesterol metabolism.

7.4.4 Modelling sAD with iPSC-derived cells

A significant concern in trying to model AD is that ageing is probably the most relevant factor, and it is unclear how this aspect might be captured by iPSC technology. Addressing this fact remains very much at the forefront of the field, but several iPSC studies on AD have provided encouragement to the field by recapitulating various cellular phenotypes associated with AD. Among the phenotypes detected are: Aβ oligomer production and induction of oxidative stress of the ER from both a sAD and fAD cell line (Kondo *et al.*, 2013), likewise in a PSEN1 line compared to its isogenic control (Oksanen *et al.*, 2017); increased secretion of

Aβ and phosphorylated tau elevation in two fAD and one sAD case (Israel *et al.*, 2012); increased total Aβ production, tau phosphorylation, and GABAergic neuron degeneration (Wang *et al.*, 2018); decreased cholesterol carrying capacity and reduced neurotrophic support from *APOE4* astrocytes (Zhao *et al.*, 2017); and altered Aβ degradation and lipid metabolism in sAD astrocytes and microglia (Lin *et al.*, 2018). The recent study by Wang et al. (2018) attests to toxic neuronal effects being gained by the *APOE4* genotype, as they can evoke AD-like phenotypes by reintroducing *APOE4* into *APOE* null neurons and ameliorate the *APOE4*-induced phenotype by using an APOE structure correction molecule. In contrast, the study by Lin et al. (2018), where AD-like phenotypes are detected across multiple cell types, all generated from the same isogenic iPSC-lines, argues that the *APOE4* genotype mediates a loss of function.

The picture of how APOE4 specifically affects synapse numbers has been less clear in recent iPSC studies. Zhao and colleagues detected a slight decrease in PSD95 and VGLUT1 protein expression when neurons were co-cultured on *APOE4/E4* astrocytes, although their latest time point was at just 20 days (Zhao *et al.*, 2017). In comparison, whilst they did not use co-cultures, Lin et al. (2018) detected an increase in synaptophysin and PSD95 staining, plus elevated mEPSC frequency in their *APOE4/E4* neurons (Lin *et al.*, 2018). Although I did not perform comparative synaptic staining of control *APOE3* and sAD *APOE4* neurons, I performed electrophysiological measurements from neurons in co-cultures where *APOE2/E3* neurons were grown on either *APOE2/E3* or *APOE4/E4* human astrocytes. The basal levels of synaptically active neurons and their sEPSC frequency in the control condition (YFP-expressing astrocytes exposed to light) were 48% and 0.1 Hz on *APOE2/E3* astrocytes, versus

83% and 0.6 Hz on *APOE4/E4* astrocytes. This suggests my cultures might be behaving similarly to the Lin et al. (2018) report of accelerated maturation in *APOE4/E4* neurons (Lin *et al.*, 2018). They found that *APOE4* in the neurons alone matured their synaptic inputs, whereas I have observed that *APOE4* in astrocytes might be inducing a seemingly similar effect on control *APOE2/E3* neurons. Lin and colleagues have also made the same observation of early maturation with fAD PSEN1 mutant neurons, and demonstrated that neuronal differentiation genes were upregulated in *APOE4* neurons, which all speaks to early maturation potentially being a common phenotype in iPSC-derived models of AD. It would be interesting to investigate the synaptic behaviour of a purely *APOE4/E4* co-culture, and compare it to a neuron *APOE4/E4* and astrocyte *APOE3* culture, to try and tease out the contribution of *APOE4* neurons and astrocytes to synaptic phenotypes.

In summary, there is compelling evidence that APOE4 could be causing both a toxic gain of function, particularly in neurons, as well as a loss of protective function, particularly in astrocytes. This means that there are reasons to believe that lowering toxic APOE4 levels would be a potential therapeutic option, but that likewise, increasing APOE4 levels to normal E3 levels may also be of benefit (Liu *et al.*, 2013). Some argue that the loss of function hypothesis fits better with the gradual progression of sAD throughout an individual's lifetime, as ageing cells lose their competence in handling stresses and AD can be viewed as an accumulation of cellular stressors (Bu, 2009). The studies by Wang et al. (2018) and Lin et al. (2018) can both be said to support the amyloid cascade hypothesis, in that they examine how *APOE* genotype affects phenotypes and pathways associated with Aβ . However, these studies fall short of providing links to changes at synapses that could account for the cognitive

deficits in AD. This means that there remains an important role for new experimental systems that can offer mechanistic insight into how *APOE* genotype might cause changes in synaptic function and synaptic stability. The ability to produce enriched cultures of human neurons and astrocytes, both from healthy people and *APOE4* patients diagnosed with sAD, affords new opportunities for closer examination of the interplay between neurons and astrocytes in sAD pathogenesis.

7.5 Concluding remarks

In this thesis I have examined different aspects of neuron-astrocyte interactions in human iPSC-derived cells. I found that the human astrocytes exhibited several hallmarks of astrocytic function and that they interact functionally with neurons in co-culture scenarios. In particular, I have demonstrated that iPSC-derived human astrocytes can exert pro-maturational enhancement of neuronal excitability and synaptic function, as well as homeostatically regulating key ions in response to synaptic network activity. I also showed that a form of astrocyte-mediated neuronal plasticity that is consistent with gliotransmission can be elicited when astrocyte signalling is controlled with ChR2. As the hope for human iPSC-based platforms is to be able to improve disease modelling, the experiments presented here represent an important stepping stone towards establishing more relevant co-culture models in a human context. The co-culture methods and the optogenetic assay developed here have particular relevance for studying neuron-astrocyte interactions that affect synapses, and the final experiments indicate that *APOE* genotype might influence the ability of human astrocytes to modulate neuronal transmission.

References

Abramov, A. Y., Canevari, L. and Duchen, M. R. (2003) 'Changes in intracellular calcium and glutathione in astrocytes as the primary mechanism of amyloid neurotoxicity.', *The Journal of neuroscience : the official journal of the Society for Neuroscience*. Society for Neuroscience, 23(12), pp. 5088–95. doi: 10.1523/JNEUROSCI.23-12-05088.2003.

Abud, E. M. *et al.* (2017) 'iPSC-Derived Human Microglia-like Cells to Study Neurological Diseases.', *Neuron*. NIH Public Access, 94(2), pp. 278-293.e9. doi: 10.1016/j.neuron.2017.03.042.

Adamsky, A. *et al.* (2018) 'Astrocytic Activation Generates De Novo Neuronal Potentiation and Memory Enhancement', *Cell*. Elsevier Inc., 174(1), pp. 59-71.e14. doi: 10.1016/j.cell.2018.05.002.

Adelman, W. J. and Fitzhugh, R. (1975) 'Solutions of the Hodgkin-Huxley equations modified for potassium accumulation in a periaxonal space.', *Federation proceedings*, 34(5), pp. 1322–9. Available at: http://www.ncbi.nlm.nih.gov/pubmed/1123087 (Accessed: 16 November 2018).

Aguado, F. *et al.* (2002) 'Neuronal activity regulates correlated network properties of spontaneous calcium transients in astrocytes in situ', *Journal of Neuroscience*. Society for Neuroscience, 22(1529–2401), pp. 9430–9444. doi: 22/21/9430 [pii].

Agulhon, C. *et al.* (2008) 'What is the role of astrocyte calcium in neurophysiology?', *Neuron*, 59(6), pp. 932–46. doi: 10.1016/j.neuron.2008.09.004.

Agulhon, C. *et al.* (2012) 'Calcium signaling and gliotransmission in normal vs. Reactive astrocytes', *Frontiers in Pharmacology*. Frontiers Media SA, 3 JUL, p. 139. doi: 10.3389/fphar.2012.00139.

Agulhon, C., Fiacco, T. A. and McCarthy, K. D. (2010) 'Hippocampal short- and long-term plasticity are not modulated by astrocyte Ca2+ signaling', *Science*. American Association for the Advancement of Science, 327(5970), pp. 1250–1254. doi: 10.1126/science.1184821.

Ahmed, Z. and John, A. C. (1980) 'Intracellular pH Changes Induced by Calcium Influx during Electrical Activity in Molluscan Neurons', *J. Gen. Physiol.*, 75(April), pp. 403–426. doi: 10.1085/jgp.75.4.403.

Allen, N. J. *et al.* (2012) 'Astrocyte glypicans 4 and 6 promote formation of excitatory synapses via GluA1 AMPA receptors.', *Nature SUPPLEMENTARY*. NIH Public Access, 486(7403), pp. 410–4. doi: 10.1038/nature11059.

Allen, N. J. (2013) 'Role of glia in developmental synapse formation.', *Current opinion in neurobiology*, 23(6), pp. 1027–33. doi: 10.1016/j.conb.2013.06.004.

Allen, N. J. (2014) 'Astrocyte regulation of synaptic behavior.', *Annual review of cell and developmental biology*, 30, pp. 439–63. doi: 10.1146/annurev-cellbio-100913-013053.

Allen, N. J. and Barres, B. A. (2009) 'Glia — more than just brain glue', *Nature*, 457(February), pp. 675–677. doi: 10.1038/457675a.

Allen, N. J. and Eroglu, C. (2017) 'Cell Biology of Astrocyte-Synapse Interactions', *Neuron*. Elsevier Inc., 96(3), pp. 697–708. doi: 10.1016/j.neuron.2017.09.056.

Almad, A. and Maragakis, N. J. (2018) 'A stocked toolbox for understanding the role of astrocytes in disease', *Nature Reviews Neurology*. Nature Publishing Group, pp. 351–362. doi: 10.1038/s41582-018-0010-2.

Alzheimer's Research UK (2018) *ARUK Dementia Statistics Hub |Public perception. https://www.dementiastatistics.org/statistics/different-types-of-dementia/, Dementia Statistics*. Available at: https://www.dementiastatistics.org/statistics/different-types-of-dementia/ (Accessed: 4 January 2019).

Alzheimer, A. (1911) 'Über eigenartige Krankheitsfälle des späteren Alters', *Zbl. ges. Neurol. Psych*, 4, pp. 356–385.

Van den Ameele, J. *et al.* (2014) 'Thinking out of the dish: What to learn about cortical development using pluripotent stem cells', *Trends in Neurosciences*. Elsevier Ltd, 37(6), pp. 334–342. doi: 10.1016/j.tins.2014.03.005.

Anderson, S. and Vanderhaeghen, P. (2014) 'Cortical neurogenesis from pluripotent stem cells: Complexity emerging from simplicity', *Current Opinion in Neurobiology*. NIH Public Access, pp. 151–157. doi: 10.1016/j.conb.2014.03.012.

Annunziato, L., Boscia, F. and Pignataro, G. (2013) 'Ionic transporter activity in astrocytes, microglia, and oligodendrocytes during brain ischemia', *Journal of Cerebral Blood Flow and Metabolism*. SAGE Publications, pp. 969–982. doi: 10.1038/jcbfm.2013.44.

Araque, A *et al.* (1998) 'Calcium elevation in astrocytes causes an NMDA receptor-dependent increase in the frequency of miniature synaptic currents in cultured hippocampal neurons.', *The Journal of neuroscience : the official journal of the Society for Neuroscience*, 18(17), pp. 6822–6829. doi: 10.1523/jneurosci.5572-07.2008.

Araque, Alfonso *et al.* (1998) 'Glutamate-dependent astrocyte modulation of synaptic transmission between cultured hippocampal neurons', *European Journal of Neuroscience*. Wiley/Blackwell (10.1111), 10(0953–816X), pp. 2129–2142. doi: 10.1046/j.1460-9568.1998.00221.x.

Araque, A. *et al.* (1999) 'Tripartite synapses: glia, the unacknowledged partner', *Trends in Neurosciences*. Elsevier Current Trends, 22(5), pp. 208–215. doi: 10.1016/S0166-2236(98)01349-6.

Araque, A. *et al.* (2000) 'SNARE protein-dependent glutamate release from astrocytes.', *The Journal of neuroscience : the official journal of the Society for Neuroscience*. Society for

Neuroscience, 20(2), pp. 666–73. doi: 10.1523/JNEUROSCI.20-02-00666.2000.

Araque, A. *et al.* (2002) 'Synaptically released acetylcholine evokes Ca2+ elevations in astrocytes in hippocampal slices.', *The Journal of neuroscience : the official journal of the Society for Neuroscience*. Society for Neuroscience, 22(7), pp. 2443–50. doi: 20026212.

Araque, A. *et al.* (2014) 'Gliotransmitters travel in time and space', *Neuron*, 81(4), pp. 728–739. doi: 10.1016/j.neuron.2014.02.007.

Arendt, T. *et al.* (2015) 'Early neurone loss in Alzheimer's disease: cortical or subcortical?', *Acta neuropathologica communications*. BioMed Central, 3, p. 10. doi: 10.1186/s40478-015-0187-1.

Arosio, D. *et al.* (2010) 'Simultaneous intracellular chloride and pH measurements using a GFP-based sensor', *Nature Methods*. Nature Publishing Group, 7(7), pp. 516–518. doi: 10.1038/nmeth.1471.

Avaliani, N. *et al.* (2014) 'Optogenetics reveal delayed afferent synaptogenesis on grafted human-induced pluripotent stem cell-derived neural progenitors', *Stem Cells*, 32(12), pp. 3088–3098. doi: 10.1002/stem.1823.

Avila-Muñoz, E. and Arias, C. (2014) 'When astrocytes become harmful: Functional and inflammatory responses that contribute to Alzheimer's disease', *Ageing Research Reviews*. Elsevier, 18, pp. 29–40. doi: 10.1016/J.ARR.2014.07.004.

Awaji, T. *et al.* (2001) 'Novel green fluorescent protein-based ratiometric indicators for monitoring pH in defined intracellular microdomains', *Biochemical and Biophysical Research Communications*, 289(2), pp. 457–462. doi: 10.1006/bbrc.2001.6004.

Bales, K. R. *et al.* (2009) 'Human APOE isoform-dependent effects on brain beta-amyloid levels in PDAPP transgenic mice.', *The Journal of neuroscience : the official journal of the Society for Neuroscience*. Society for Neuroscience, 29(21), pp. 6771–9. doi: 10.1523/JNEUROSCI.0887-09.2009.

Bardy, C. *et al.* (2016) 'Predicting the functional states of human iPSC-derived neurons with single-cell RNA-seq and electrophysiology', *Molecular Psychiatry*. Nature Publishing Group, 21(10), pp. 1573–1588. doi: 10.1038/mp.2016.158.

Barker, A. J. *et al.* (2008) 'Developmental control of synaptic receptivity', *J Neurosci*. Society for Neuroscience, 28(33), pp. 8150–8160. doi: 10.1523/JNEUROSCI.1744-08.2008.

Barnabé-Heider, F. *et al.* (2005) 'Evidence that Embryonic Neurons Regulate the Onset of Cortical Gliogenesis via Cardiotrophin-1', *Neuron*. Cell Press, 48(2), pp. 253–265. doi: 10.1016/J.NEURON.2005.08.037.

Barnabé-Heider, F. and Miller, F. D. (2003) 'Endogenously produced neurotrophins regulate survival and differentiation of cortical progenitors via distinct signaling pathways.', *The Journal of neuroscience : the official journal of the Society for Neuroscience*. Society for Neuroscience, 23(12), pp. 5149–60. doi: 10.1523/JNEUROSCI.23-12-05149.2003.

Barres, B. A. *et al.* (1989) 'Glial and neuronal forms of the voltage-dependent sodium channel: characteristics and cell type distribution', *Neuron*, 2, pp. 1375-l388.

Barres, B. A. (2008) 'The Mystery and Magic of Glia: A Perspective on Their Roles in Health and Disease', *Neuron*. Elsevier, pp. 430–440. doi: 10.1016/j.neuron.2008.10.013.

Bashir, Z. I. *et al.* (1993) 'Induction of LTP in the hippocampus needs synaptic activation of glutamate metabotropic receptors', *Nature*, 363(6427), pp. 347–350. doi: 10.1038/363347a0.

Bazargani, N. and Attwell, D. (2016) 'Astrocyte calcium signaling: the third wave', *Nature Neuroscience*, 19(2), pp. 182–189. doi: 10.1038/nn.4201.

Bellot-Saez, A. *et al.* (2017) 'Astrocytic modulation of neuronal excitability through K+spatial buffering', *Neuroscience and Biobehavioral Reviews*. Pergamon, pp. 87–97. doi: 10.1016/j.neubiorev.2017.03.002.

Ben-Ari, Y. *et al.* (2004) 'Interneurons set the tune of developing networks.', *Trends in neurosciences*, 27(7), pp. 422–7. doi: 10.1016/j.tins.2004.05.002.

Bennett, M. V. L. *et al.* (2003) 'New roles for astrocytes: gap junction hemichannels have something to communicate.', *Trends in neurosciences*. NIH Public Access, 26(11), pp. 610–7. doi: 10.1016/j.tins.2003.09.008.

Benneyworth, M. A. *et al.* (2012) 'Cell selective conditional null mutations of serine racemase demonstrate a predominate localization in cortical glutamatergic neurons.', *Cellular and molecular neurobiology*. NIH Public Access, 32(4), pp. 613–24. doi: 10.1007/s10571-012-9808-4.

Beppu, K. *et al.* (2013) 'Report Optogenetic Countering of Glial Acidosis Suppresses Glial Glutamate Release and Ischemic Brain Damage', *Neuron*. Elsevier Inc., 81(2), pp. 314–320. doi: 10.1016/j.neuron.2013.11.011.

Bergersen, L. H. *et al.* (2012) 'Immunogold detection of L-glutamate and D-serine in small synaptic-like microvesicles in adult hippocampal astrocytes', *Cerebral Cortex*. Oxford University Press, 22(7), pp. 1690–1697. doi: 10.1093/cercor/bhr254.

Berlinguer-Palmini, R. *et al.* (2014) 'Arrays of microLEDs and astrocytes: biological amplifiers to optogenetically modulate neuronal networks reducing light requirement.', *PloS one*, 9(9), p. e108689. doi: 10.1371/journal.pone.0108689.

Berndt, A. *et al.* (2011) 'High-efficiency channelrhodopsins for fast neuronal stimulation at low light levels.', *Proceedings of the National Academy of Sciences of the United States of America*, 108(18), pp. 7595–600. doi: 10.1073/pnas.1017210108.

Bevan, Y. S. *et al.* (1985) 'The presence of voltage-gated sodium, potassium and chloride channels in rat cultured astrocytes', *Proceedings of the royal society of London*, 225, pp. 299–313.

Bevensee, M. O., Weed, R. A. and Boron, W. F. (1997) 'Intracellular pH Regulation in

Cultured Astrocytes from Rat Hippocampus . I. Role of HCO3-', *The Journal of General Physiology*. The Rockefeller University Press, 110(4), pp. 453–465. doi: 10.1085/jgp.110.4.453.

Bezzi, P. *et al.* (1998) 'Prostaglandins stimulate calcium-dependent glutamate release in astrocytes', *Nature*. Nature Publishing Group, 391(6664), pp. 281–285. doi: 10.1038/34651.

Bezzi, P. *et al.* (2004) 'Astrocytes contain a vesicular compartment that is competent for regulated exocytosis of glutamate', *Nature Neuroscience*. Nature Publishing Group, 7(6), pp. 613–620. doi: 10.1038/nn1246.

Bialas, A. R. and Stevens, B. (2013) 'TGF-β signaling regulates neuronal C1q expression and developmental synaptic refinement.', *Nature neuroscience*. NIH Public Access, 16(12), pp. 1773–82. doi: 10.1038/nn.3560.

Bianchi, F. *et al.* (2018) 'Rapid and efficient differentiation of functional motor neurons from human iPSC for neural injury modelling', *Stem Cell Research*. Elsevier, 32, pp. 126–134. doi: 10.1016/J.SCR.2018.09.006.

Billups, B. and Attwell, D. (1996) 'Modulation of non-vesicular glutamate release by pH', *Nature*. Nature Publishing Group, 379(6561), pp. 171–174. doi: 10.1038/379171a0.

Bizzarri, R. *et al.* (2006) 'Development of a novel GFP-based ratiometric excitation and emission pH indicator for intracellular studies.', *Biophysical journal*. The Biophysical Society, 90(9), pp. 3300–14. doi: 10.1529/biophysj.105.074708.

Bowman, C. L. and Kimelberg, H. K. (1984) 'Excitatory amino acids directly depolarize rat brain astrocytes in primary culture', *Nature*. Nature Publishing Group, 311(5987), pp. 656–659. doi: 10.1038/311656a0.

Boyarsky, G. *et al.* (1988) 'pH regulation in single glomerular mesangial cells. I. Acid extrusion in absence and presence of HCO3-.', *The American journal of physiology*, 255(6 Pt 1), pp. C844–C856. doi: 10.1152/ajpcell.1988.255.6.C844.

Boyarsky, G. *et al.* (1993) 'Intracellular pH regulation in single cultured astrocytes from rat forebrain.', *Glia*. Wiley-Blackwell, 8(4), pp. 241–8. doi: 10.1002/glia.440080404.

Boyden, E. S. *et al.* (2005) 'Millisecond-timescale, genetically targeted optical control of neural activity', *Nature Neuroscience*. Nature Publishing Group, 8(9), pp. 1263–1268. doi: 10.1038/nn1525.

Braak, H. and Braak, E. (1991) 'Neuropathological stageing of Alzheimer-related changes', *Acta Neuropathologica*, 82, pp. 239–259.

Bramham, C. R. *et al.* (1990) 'Distribution of glutamate-like immunoreactivity in excitatory hippocampal pathways: A semiquantitative electron microscopic study in rats', *Neuroscience*. Pergamon, 39(2), pp. 405–417. doi: 10.1016/0306-4522(90)90277-B.

Brennand, K. *et al.* (2015) 'Phenotypic differences in hiPSC NPCs derived from patients

with schizophrenia', *Molecular Psychiatry*. Nature Publishing Group, 20(3), pp. 361–368. doi: 10.1038/mp.2014.22.

Brodbeck, J. *et al.* (2008) 'Rosiglitazone increases dendritic spine density and rescues spine loss caused by apolipoprotein E4 in primary cortical neurons.', *Proceedings of the National Academy of Sciences of the United States of America*. National Academy of Sciences, 105(4), pp. 1343–6. doi: 10.1073/pnas.0709906104.

Brookes, N. and Turner, R. J. (1994) 'K(+)-induced alkalinization in mouse cerebral astrocytes mediated by reversal of electrogenic Na(+)-HCO3- cotransport.', *The American journal of physiology*, 267(6 Pt 1), pp. C1633-40. doi: 10.1152/ajpcell.1994.267.6.C1633.

Bu, G. (2009) 'Apolipoprotein E and its receptors in Alzheimer's disease: pathways, pathogenesis and therapy.', *Nature reviews. Neuroscience*. Nature Publishing Group, 10(5), pp. 333–44. doi: 10.1038/nrn2620.

Burda, J. E. and Sofroniew, M. V. (2014) 'Reactive gliosis and the multicellular response to CNS damage and disease', *Neuron*. Elsevier Inc., 81(2), pp. 229–248. doi: 10.1016/j.neuron.2013.12.034.

Bushong, E. A. *et al.* (2002) 'Protoplasmic astrocytes in CA1 stratum radiatum occupy separate anatomical domains.', *The Journal of neuroscience : the official journal of the Society for Neuroscience*. Society for Neuroscience, 22(1), pp. 183–192. doi: 22/1/183 [pii].

Bystron, I., Blakemore, C. and Rakic, P. (2008) 'Development of the human cerebral cortex: Boulder Committee revisited', *Nature Reviews Neuroscience*. Nature Publishing Group, 9(2), pp. 110–122. doi: 10.1038/nrn2252.

Cahoy, J. *et al.* (2008) 'A Transcriptome Database for Astrocytes, Neurons, and Oligodendrocytes: A New Resource for Understanding Brain Development and Function', *Journal of Neuroscience*. Society for Neuroscience, 28(1), pp. 264–278. doi: 10.1523/JNEUROSCI.4178-07.2008.

Călin, A. *et al.* (2018) 'Chemogenetic Recruitment of Specific Interneurons Suppresses Seizure Activity', *Frontiers in Cellular Neuroscience*, 12(September), pp. 1–18. doi: 10.3389/fncel.2018.00293.

Casper, K. B. and McCarthy, K. D. (2006) 'GFAP-positive progenitor cells produce neurons and oligodendrocytes throughout the CNS', *Molecular and Cellular Neuroscience*. Academic Press, 31(4), pp. 676–684. doi: 10.1016/J.MCN.2005.12.006.

Castellano, J. M. *et al.* (2011) 'Human apoE isoforms differentially regulate brain amyloid-β peptide clearance.', *Science translational medicine*. NIH Public Access, 3(89), p. 89ra57. doi: 10.1126/scitranslmed.3002156.

Di Castro, M. A. *et al.* (2011) 'Local Ca2+ detection and modulation of synaptic release by astrocytes', *Nature Neuroscience*, 14(10), pp. 1276–1284. doi: 10.1038/nn.2929.

Cavanaugh, S. E., Pippin, J. J. and Barnard, N. D. (2014) 'Animal models of Alzheimer

disease: Historical pitfalls and a path forward', *Altex*, 31(3), pp. 279–302. doi: 10.14573/altex.1310071.

Chai, H. *et al.* (2017) 'Neural Circuit-Specialized Astrocytes: Transcriptomic, Proteomic, Morphological, and Functional Evidence.', *Neuron*. Elsevier, 95(3), pp. 531-549.e9. doi: 10.1016/j.neuron.2017.06.029.

Chambers, S. M. *et al.* (2009) 'Highly efficient neural conversion of human ES and iPS cells by dual inhibition of SMAD signaling.', *Nature biotechnology*, 27(3), pp. 275–280. doi: 10.1038/nbt0509-485a.

Chandrasekaran, A. *et al.* (2016) 'Astrocyte Differentiation of Human Pluripotent Stem Cells: New Tools for Neurological Disorder Research', *Frontiers in Cellular Neuroscience*. Frontiers Media SA, 10, p. 215. doi: 10.3389/fncel.2016.00215.

Charles, A. C. *et al.* (1991) 'Intercellular signaling in glial cells: Calcium waves and oscillations in response to mechanical stimulation and glutamate', *Neuron*, 6(6), pp. 983–992. doi: 10.1016/0896-6273(91)90238-U.

Chesler, M. (2003) 'Regulation and Modulation of pH in the Brain', *Brain*. American Physiological Society, 83(4), pp. 1183–1221. doi: 10.1152/physrev.00010.2003.

Chesler, M. and Kraig, R. (1989) 'Intracellular pH transients of mammalian astrocytes', *The Journal of Neuroscience*, 9(6), pp. 2011–2019. doi: 10.1523/JNEUROSCI.09-06-02011.1989.

Cheung, G. *et al.* (2015) 'Activity-Dependent Plasticity of Astroglial Potassium and Glutamate Clearance.', *Neural plasticity*, 2015, p. 109106. doi: 10.1155/2015/109106.

Chih, C.-P., Lipton, P. and Roberts, E. L. (2001) 'Do active cerebral neurons really use lactate rather than glucose?', *Trends in Neurosciences*. Elsevier Current Trends, 24(10), pp. 573–578. doi: 10.1016/S0166-2236(00)01920-2.

Chinchalongporn, V. *et al.* (2015) 'Connectivity and circuitry in a dish versus in a brain.', *Alzheimer's research & therapy*, 7(1), p. 44. doi: 10.1186/s13195-015-0129-y.

Christopherson, K. S. *et al.* (2005) 'Thrombospondins are astrocyte-secreted proteins that promote CNS synaptogenesis.', *Cell*, 120(3), pp. 421–33. doi: 10.1016/j.cell.2004.12.020.

Chung, W.-S. *et al.* (2016) 'Novel allele-dependent role for APOE in controlling the rate of synapse pruning by astrocytes', *Proceedings of the National Academy of Sciences*, 113(36), pp. 10186–10191. doi: 10.1073/pnas.1609896113.

Chung, W. S. *et al.* (2013) 'Astrocytes mediate synapse elimination through MEGF10 and MERTK pathways', *Nature*. Nature Publishing Group, 504(7480), pp. 394–400. doi: 10.1038/nature12776.

Chung, W. S., Allen, N. J. and Eroglu, C. (2015) 'Astrocytes control synapse formation, function, and elimination', *Cold Spring Harbor Perspectives in Biology*. Cold Spring Harbor Laboratory Press, 7(9), p. a020370. doi: 10.1101/cshperspect.a020370.

Clarke, L. E. and Barres, B. A. (2013) 'Emerging roles of astrocytes in neural circuit development', *Nature Reviews Neuroscience*. NIH Public Access, pp. 311–321. doi: 10.1038/nrn3484.

Connors, B. W., Benardo, L. S. and Prince, D. A. (1983) 'Coupling between neurons of the developing rat neocortex.', *The Journal of neuroscience : the official journal of the Society for Neuroscience*. Society for Neuroscience, 3(4), pp. 773–82. doi: 10.1523/JNEUROSCI.03-04-00773.1983.

Corder, E. *et al.* (1993) 'Gene Dose of Apolipoprotein E Type 4 Allele and the Risk of Alzheimer's Disease in Late Onset Families', *Science*, 261(5123), pp. 921–923.

Corder, E. H. E. *et al.* (1993) 'Gene Dose of Apolipoprotein E Type 4 Allele and the Risk of Alzheimer's Disease in Late Onset Families', *Science*. American Association for the Advancement of Science, 261(5123), pp. 921–923. doi: 10.1126/science.2880399.

Cornell-Bell, A. H. *et al.* (1990) 'Glutamate induces calcium waves in cultured astrocytes: long-range glial signaling', *Science*, 247(24), pp. 2–5.

Corrada, M. M. *et al.* (2010) 'Dementia incidence continues to increase with age in the oldest old: the 90+ study.', *Annals of neurology*. NIH Public Access, 67(1), pp. 114–21. doi: 10.1002/ana.21915.

Crippa, D. *et al.* (2006) 'Synaptobrevin2-expressing vesicles in rat astrocytes: insights into molecular characterization, dynamics and exocytosis.', *The Journal of physiology*. Wiley-Blackwell, 570(Pt 3), pp. 567–82. doi: 10.1113/jphysiol.2005.094052.

Crompton, L. A., Cordero-Llana, O. and Caldwell, M. A. (2017) 'Astrocytes in a dish: Using pluripotent stem cells to model neurodegenerative and neurodevelopmental disorders', *Brain Pathology*, 27(4), pp. 530–544. doi: 10.1111/bpa.12522.

Cummings, J. L., Morstorf, T. and Zhong, K. (2014) 'Alzheimer's disease drug-development pipeline: few candidates, frequent failures.', *Alzheimer's research & therapy*. BioMed Central, 6(4), p. 37. doi: 10.1186/alzrt269.

Dallas, M. *et al.* (2007) 'Hypoxia suppresses glutamate transport in astrocytes.', *The Journal of neuroscience : the official journal of the Society for Neuroscience*, 27(15), pp. 3946–55. doi: 10.1523/JNEUROSCI.5030-06.2007.

Dawson, T. M., Golde, T. E. and Lagier-Tourenne, C. (2018) 'Animal models of neurodegenerative diseases', *Nature Neuroscience*. Nature Publishing Group, 21(10), pp. 1370–1379. doi: 10.1038/s41593-018-0236-8.

Deane, R., Sagare, A., Hamm, K., Parisi, M., Lane, S., Finn, M. B., Holtzman, David M., *et al.* (2008) 'apoE isoform-specific disruption of amyloid β peptide clearance from mouse brain', *J Clinical Investigation - SUPPLEMENTARY*. American Society for Clinical Investigation, 118(12), pp. 4002–4013. doi: 10.1172/JCI36663.

Deane, R., Sagare, A., Hamm, K., Parisi, M., Lane, S., Finn, M. B., Holtzman, David M, *et*

al. (2008) 'apoE isoform – specific disruption of amyloid β peptide clearance from mouse brain', *The Journal of Clinical Investigation*, 118(12), pp. 4002–4013. doi: 10.1172/JCI36663DS1.

Deitmer, B. Y. J. W. and Szatkowskit, M. (1990) 'Membrane potential dependence of intracellular pH regulation by identified glial cells in the leech central ner- vous system', *Journal of Physiology*, 421, pp. 617–631.

Denker, S. P. and Barber, D. L. (2002) 'Cell migration requires both ion translocation and cytoskeletal anchoring by the Na-H exchanger NHE1.', *The Journal of cell biology*. The Rockefeller University Press, 159(6), pp. 1087–96. doi: 10.1083/jcb.200208050.

Dimou, L. and Götz, M. (2014) 'Glial Cells as Progenitors and Stem Cells: New Roles in the Healthy and Diseased Brain', *Physiological Reviews*. American Physiological Society Bethesda, MD, 94(3), pp. 709–737. doi: 10.1152/physrev.00036.2013.

Ding, Q. *et al.* (2013) 'A TALEN genome-editing system for generating human stem cell-based disease models.', *Cell stem cell*. NIH Public Access, 12(2), pp. 238–51. doi: 10.1016/j.stem.2012.11.011.

Diniz, L. P. *et al.* (2012) 'Astrocyte-induced synaptogenesis is mediated by transforming growth factor β signaling through modulation of d-serine levels in cerebral cortex neurons', *Journal of Biological Chemistry*. American Society for Biochemistry and Molecular Biology, 287(49), pp. 41432–41445. doi: 10.1074/jbc.M112.380824.

Djukic, B. *et al.* (2007) 'Conditional Knock-Out of Kir4.1 Leads to Glial Membrane Depolarization, Inhibition of Potassium and Glutamate Uptake, and Enhanced Short-Term Synaptic Potentiation', *Journal of Neuroscience*, 27(42), pp. 11354–11365. doi: 10.1523/JNEUROSCI.0723-07.2007.

Dodla, M. C., Mumaw, J. and Stice, S. L. (2010) 'Role of astrocytes, soluble factors, cells adhesion molecules and neurotrophins in functional synapse formation: implications for human embryonic stem cell derived neurons.', *Current stem cell research & therapy*, 5(3), pp. 251–60. Available at: http://www.ncbi.nlm.nih.gov/pubmed/20214556 (Accessed: 26 November 2015).

Domercq, M. *et al.* (2006) 'P2Y1 receptor-evoked glutamate exocytosis from astrocytes: control by tumor necrosis factor-alpha and prostaglandins.', *The Journal of biological chemistry*. American Society for Biochemistry and Molecular Biology, 281(41), pp. 30684–96. doi: 10.1074/jbc.M606429200.

Dossi, E., Vasile, F. and Rouach, N. (2018) 'Human astrocytes in the diseased brain', *Brain Research Bulletin*. Elsevier, 136, pp. 139–156. doi: 10.1016/j.brainresbull.2017.02.001.

Drapeau, P. and Nachshen, D. a. (1988) 'Effects of lowering extracellular and cytosolic pH on calcium fluxes, cytosolic calcium levels, and transmitter release in presynaptic nerve terminals isolated from rat', *J. Gen. Physiol.*, 91(February), pp. 305–315. doi: 10.1085/jgp.91.2.305.

Du, Y. *et al.* (2015) 'Freshly dissociated mature hippocampal astrocytes exhibit passive membrane conductance and low membrane resistance similarly to syncytial coupled astrocytes', *Journal of Neurophysiology*. American Physiological Society, 113(10), pp. 3744–3750. doi: 10.1152/jn.00206.2015.

Dumanis, S. B. *et al.* (2009) 'ApoE4 decreases spine density and dendritic complexity in cortical neurons in vivo.', *The Journal of neuroscience : the official journal of the Society for Neuroscience*. NIH Public Access, 29(48), pp. 15317–22. doi: 10.1523/JNEUROSCI.4026-09.2009.

Dyhrfjeld-Johnsen, J. *et al.* (2010) 'Interictal spikes precede ictal discharges in an organotypic hippocampal slice culture model of epileptogenesis.', *Journal of clinical neurophysiology : official publication of the American Electroencephalographic Society*. NIH Public Access, 27(6), pp. 418–24. doi: 10.1097/WNP.0b013e3181fe0709.

Dzubay, J. A. and Jahr, C. E. (1999) 'The concentration of synaptically released glutamate outside of the climbing fiber-Purkinje cell synaptic cleft.', *The Journal of neuroscience : the official journal of the Society for Neuroscience*. Society for Neuroscience, 19(13), pp. 5265–74. doi: 10.1523/JNEUROSCI.19-13-05265.1999.

Edri, R. *et al.* (2015) 'Analysing human neural stem cell ontogeny by consecutive isolation of Notch active neural progenitors', *Nature Communications*. Nature Publishing Group, 6(1), p. 6500. doi: 10.1038/ncomms7500.

Ehrlich, M. *et al.* (2017) 'Rapid and efficient generation of oligodendrocytes from human induced pluripotent stem cells using transcription factors.', *Proceedings of the National Academy of Sciences of the United States of America*. National Academy of Sciences, 114(11), pp. E2243–E2252. doi: 10.1073/pnas.1614412114.

Eiraku, M. *et al.* (2008) 'Self-Organized Formation of Polarized Cortical Tissues from ESCs and Its Active Manipulation by Extrinsic Signals', *Cell Stem Cell*. Cell Press, 3(5), pp. 519–532. doi: 10.1016/J.STEM.2008.09.002.

Eisenberg, D. T. A., Kuzawa, C. W. and Hayes, M. G. (2010) 'Worldwide allele frequencies of the human apolipoprotein E gene: climate, local adaptations, and evolutionary history.', *American journal of physical anthropology*, 143(1), pp. 100–11. doi: 10.1002/ajpa.21298.

Ellender, T. J. *et al.* (2014) 'Excitatory effects of parvalbumin-expressing interneurons maintain hippocampal epileptiform activity via synchronous afterdischarges.', *The Journal of Neuroscience*. Society for Neuroscience, 34(46), pp. 15208–22. doi: 10.1523/JNEUROSCI.1747-14.2014.

Emdad, L. *et al.* (2012) 'Efficient Differentiation of Human Embryonic and Induced Pluripotent Stem Cells into Functional Astrocytes', *Stem Cells and Development*, 21(3), pp. 404–410. doi: 10.1089/scd.2010.0560.

Eng, L. F., Ghirnikar, R. S. and Lee, Y. L. (2000) 'Glial Fibrillary Acidic Protein: GFAP-Thirty-One Years (1969–2000)', *Neurochemical Research*, 25(9/10), pp. 1439–1451.

Available at: https://link.springer.com/content/pdf/10.1023%2FA%3A1007677003387.pdf.

Erecińska, M., Deas, J. and Silver, I. A. (2002) 'The Effect of pH on Glycolysis and Phosphofructokinase Activity in Cultured Cells and Synaptosomes', *Journal of Neurochemistry*. John Wiley & Sons, Ltd (10.1111), 65(6), pp. 2765–2772. doi: 10.1046/j.1471-4159.1995.65062765.x.

Esposito, A. *et al.* (2008) 'pHlameleons: A family of FRET-based protein sensors for quantitative pH imaging', *Biochemistry*, 47(49), pp. 13115–13126. doi: 10.1021/bi8009482.

Espuny-Camacho, I. *et al.* (2013) 'Pyramidal neurons derived from human pluripotent stem cells integrate efficiently into mouse brain circuits in vivo.', *Neuron*. Elsevier, 77(3), pp. 440–56. doi: 10.1016/j.neuron.2012.12.011.

Fanelli, A. *et al.* (2009) 'Temporal and spatial analysis of astrocyte calcium waves.', *Conference proceedings : ... Annual International Conference of the IEEE Engineering in Medicine and Biology Society. IEEE Engineering in Medicine and Biology Society. Conference*, 2009, pp. 6038–6041. doi: 10.1109/IEMBS.2009.5334534.

Fellin, T. and Carmignoto, G. (2004) 'Neurone-to-astrocyte signalling in the brain represents a distinct multifunctional unit', *Journal of Physiology*. Wiley-Blackwell, pp. 3–15. doi: 10.1113/jphysiol.2004.063214.

Ferroni, S. *et al.* (2000) 'pH modulation of an inward rectifier chloride current in cultured rat cortical astrocytes', *Neuroscience*, 100(2), pp. 431–438. doi: 10.1016/S0306-4522(00)00272-4.

Fiacco, T. A. *et al.* (2007) 'Selective Stimulation of Astrocyte Calcium In Situ Does Not Affect Neuronal Excitatory Synaptic Activity', *Neuron*. Cell Press, 54(4), pp. 611–626. doi: 10.1016/J.NEURON.2007.04.032.

Fiacco, T. A. and McCarthy, K. D. (2004) 'Intracellular Astrocyte Calcium Waves In Situ Increase the Frequency of Spontaneous AMPA Receptor Currents in CA1 Pyramidal Neurons', *Journal of Neuroscience*. Society for Neuroscience, 24(3), pp. 722–732. doi: 10.1523/JNEUROSCI.2859-03.2004.

Fiacco, T. A. and McCarthy, K. D. (2018) 'Multiple Lines of Evidence Indicate That Gliotransmission Does Not Occur under Physiological Conditions', *The Journal of Neuroscience*. Society for Neuroscience, 38(1), pp. 3–13. doi: 10.1523/JNEUROSCI.0016-17.2017.

Figueiredo, M. *et al.* (2014) 'Cell Calcium Comparative analysis of optogenetic actuators in cultured astrocytes', *Cell Calcium*. Elsevier Ltd, 56(3), pp. 208–214. doi: 10.1016/j.ceca.2014.07.007.

Fleisher, A. S. *et al.* (2013) 'Apolipoprotein E ε4 and age effects on florbetapir positron emission tomography in healthy aging and Alzheimer disease', *Neurobiology of Aging*. Elsevier, 34(1), pp. 1–12. doi: 10.1016/J.NEUROBIOLAGING.2012.04.017.

Florio, M. and Huttner, W. B. (2014) 'Neural progenitors, neurogenesis and the evolution of the neocortex', *Development*, 141(11), pp. 2182–2194. doi: 10.1242/dev.090571.

Floruta, C. M. *et al.* (2017) 'Default Patterning Produces Pan-cortical Glutamatergic and CGE/LGE-like GABAergic Neurons from Human Pluripotent Stem Cells', *Stem Cell Reports*. ElsevierCompany., 9(5), pp. 1463–1476. doi: 10.1016/j.stemcr.2017.09.023.

Foo, L. C. *et al.* (2011) 'Development of a method for the purification and culture of rodent astrocytes.', *Neuron*. NIH Public Access, 71(5), pp. 799–811. doi: 10.1016/j.neuron.2011.07.022.

Freeman, M. R. (2010) 'Specification and morphogenesis of astrocytes.', *Science (New York, N.Y.)*. NIH Public Access, 330(6005), pp. 774–8. doi: 10.1126/science.1190928.

Fremeau, R. T. *et al.* (2004) 'VGLUTs define subsets of excitatory neurons and suggest novel roles for glutamate', *Trends in Neurosciences*. Elsevier Current Trends, 27(2), pp. 98–103. doi: 10.1016/J.TINS.2003.11.005.

Fujiwara-Tsukamoto, Y. *et al.* (2010) 'Prototypic Seizure Activity Driven by Mature Hippocampal Fast-Spiking Interneurons', *Journal of Neuroscience*. Society for Neuroscience, 30(41), pp. 13679–13689. doi: 10.1523/JNEUROSCI.1523-10.2010.

Fukushima, K. *et al.* (2016) 'Establishment of a Human Neuronal Network Assessment System by Using a Human Neuron/Astrocyte Co-Culture Derived from Fetal Neural Stem/Progenitor Cells.', *Journal of biomolecular screening*, 21(1), pp. 54–64. doi: 10.1177/1087057115610055.

Gage, F. H. (2002) 'Neurogenesis in the Adult Brain', *Molecular and Cellular Neuroscience*, 22(3), pp. 612–613. doi: 10.1016/B978-0-12-394447-4.40021-0.

Gan, L. *et al.* (2018) 'Converging pathways in neurodegeneration, from genetics to mechanisms', *Nature Neuroscience*. Nature Publishing Group, 21(10), pp. 1300–1309. doi: 10.1038/s41593-018-0237-7.

Garai, K. *et al.* (2014) 'The binding of apolipoprotein E to oligomers and fibrils of amyloid-β alters the kinetics of amyloid aggregation.', *Biochemistry*. American Chemical Society, 53(40), pp. 6323–31. doi: 10.1021/bi5008172.

Garcia, A. D. R. *et al.* (2004) 'GFAP-expressing progenitors are the principal source of constitutive neurogenesis in adult mouse forebrain', *Nature Neuroscience*. Nature Publishing Group, 7(11), pp. 1233–1241. doi: 10.1038/nn1340.

Gaspard, N. *et al.* (2008) 'An intrinsic mechanism of corticogenesis from embryonic stem cells', *Nature*. Nature Publishing Group, 455(7211), pp. 351–357. doi: 10.1038/nature07287.

Gaude, P. *et al.* (2005) 'Germ layer induction from embryonic stem cells', *Experimental Hematology*, 33(9), pp. 955–964. doi: 10.1016/j.exphem.2005.06.009.

Ge, W.-P. *et al.* (2012) 'Local generation of glia is a major astrocyte source in postnatal

cortex.', *Nature*. NIH Public Access, 484(7394), pp. 376–80. doi: 10.1038/nature10959.

Glenner, G. G. and Wong, C. W. (1984) 'Alzheimer's disease: Initial report of the purification and characterization of a novel cerebrovascular amyloid protein', *Biochemical and Biophysical Research Communications*, 120(3), pp. 885–890.

Gong, J. S. *et al.* (2002) 'Apolipoprotein E (ApoE) isoform-dependent lipid release from astrocytes prepared from human ApoE3 and ApoE4 knock-in mice.', *The Journal of biological chemistry*. American Society for Biochemistry and Molecular Biology, 277(33), pp. 29919–29926. doi: 10.1074/jbc.M203934200.

Götz, M., Stoykova, A. and Gruss, P. (1998) 'Pax6 Controls Radial Glia Differentiation in the Cerebral Cortex', *Neuron*. Cell Press, 21(5), pp. 1031–1044. doi: 10.1016/S0896-6273(00)80621-2.

Gourine, A. V *et al.* (2010) 'Astrocytes control breathing through pH-dependent release of ATP', *Science*, 329(5991), pp. 571–575. doi: 10.1126/science.1190721.

Grainger, A. I. *et al.* (2018) 'In vitro Models for Seizure-Liability Testing Using Induced Pluripotent Stem Cells', *Frontiers in Neuroscience*. Frontiers, 12, p. 590. doi: 10.3389/fnins.2018.00590.

Grewer, C. and Rauen, T. (2005) 'Electrogenic glutamate transporters in the CNS: Molecular mechanism, pre-steady-state kinetics, and their impact on synaptic signaling', *Journal of Membrane Biology*. NIH Public Access, pp. 1–20. doi: 10.1007/s00232-004-0731-6.

Grundke-Iqbal, I. *et al.* (1986) 'Microtubule- associated protein tau. A component of Alzheimer paired helical filaments', *Journal of Biological Chemistry*, 261(13), pp. 6084–6089. doi: 10.1109/JSTQE.2016.2553442.

Grynkiewicz, G., Poenie, M. and Tsien, R. Y. (1985) '<1985-grynkiewicz-A New Generation of Ca2+ Indicatorsw ith Greatly Improved fluorescence properties.pdf>', *The Journal of Biologica Chemistry*, 260(6), pp. 3440–3450.

Gundersen, V., Storm-Mathisen, J. and Bergersen, L. H. (2015) 'Neuroglial Transmission.', *Physiological reviews*, 95(3), pp. 695–726. doi: 10.1152/physrev.00024.2014.

Gunn-Moore, D. *et al.* (2018) 'Alzheimer's disease in humans and other animals: A consequence of postreproductive life span and longevity rather than aging', *Alzheimer's & Dementia*. Elsevier, 14(2), pp. 195–204. doi: 10.1016/J.JALZ.2017.08.014.

Guthrie, P. B. *et al.* (1999) 'ATP released from astrocytes mediates glial calcium waves.', *The Journal of neuroscience : the official journal of the Society for Neuroscience*. Society for Neuroscience, 19(2), pp. 520–8. doi: 10.1523/JNEUROSCI.19-02-00520.1999.

Haenseler, W. *et al.* (2017) 'A Highly Efficient Human Pluripotent Stem Cell Microglia Model Displays a Neuronal-Co-culture-Specific Expression Profile and Inflammatory Response.', *Stem cell reports*. Elsevier, 8(6), pp. 1727–1742. doi: 10.1016/j.stemcr.2017.05.017.

Halassa, M. M. *et al.* (2007) 'Synaptic islands defined by the territory of a single astrocyte.', *The Journal of neuroscience : the official journal of the Society for Neuroscience*. Society for Neuroscience, 27(24), pp. 6473–7. doi: 10.1523/JNEUROSCI.1419-07.2007.

Hama, H. *et al.* (2004) 'PKC signaling mediates global enhancement of excitatory synaptogenesis in neurons triggered by local contact with astrocytes.', *Neuron*. Elsevier, 41(3), pp. 405–15. doi: 10.1016/S0896-6273(04)00007-8.

Hamilton, N. B. and Attwell, D. (2010) 'Do astrocytes really exocytose neurotransmitters?', *Nature Reviews Neuroscience*. Nature Publishing Group, 11(4), pp. 227–238. doi: 10.1038/nrn2803.

Hanse, E., Seth, H. and Riebe, I. (2013) 'AMPA-silent synapses in brain development and pathology', *Nature Reviews Neuroscience*. Nature Publishing Group, 14(12), pp. 839–850. doi: 10.1038/nrn3642.

Hansen, D. V *et al.* (2013) 'Non-epithelial stem cells and cortical interneuron production in the human ganglionic eminences.', *Nature neuroscience*. NIH Public Access, 16(11), pp. 1576–87. doi: 10.1038/nn.3541.

Hardy, J. and Selkoe, D. J. (2002) 'The amyloid hypothesis of Alzheimer's disease: Progress and problems on the road to therapeutics', *Science*. American Association for the Advancement of Science, pp. 353–356. doi: 10.1126/science.1072994.

Harold, D. *et al.* (2009) 'Genome-wide association study identifies variants at CLU and PICALM associated with Alzheimer's disease.', *Nature genetics*. Europe PMC Funders, 41(10), pp. 1088–93. doi: 10.1038/ng.440.

Harris, J. J., Jolivet, R. and Attwell, D. (2012) 'Synaptic Energy Use and Supply', *Neuron*. Cell Press, 75(5), pp. 762–777. doi: 10.1016/J.NEURON.2012.08.019.

Hartman, R. E. *et al.* (2001) 'Behavioral phenotyping of GFAP-ApoE3 and -ApoE4 transgenic mice: ApoE4 mice show profound working memory impairments in the absence of Alzheimer's-like neuropathology', *Experimental Neurology*, 170(2), pp. 326–344. doi: 10.1006/exnr.2001.7715.

Hashimoto, T. *et al.* (2012) 'Apolipoprotein E, especially apolipoprotein E4, increases the oligomerization of amyloid β peptide.', *The Journal of neuroscience : the official journal of the Society for Neuroscience*. NIH Public Access, 32(43), pp. 15181–92. doi: 10.1523/JNEUROSCI.1542-12.2012.

Hassinger, T. D. *et al.* (1995) 'Evidence for glutamate-mediated activation of hippocampal neurons by glial calcium waves', *Journal of Neurobiology*, 28(2), pp. 159–170. doi: 10.1002/neu.480280204.

Hassinger, T. D. *et al.* (1996) 'An extracellular signaling component in propagation of astrocytic calcium waves.', *Proceedings of the National Academy of Sciences of the United States of America*. National Academy of Sciences, 93(23), pp. 13268–73. Available at:

http://www.ncbi.nlm.nih.gov/pubmed/8917580 (Accessed: 26 August 2018).

Heinemann, U. and Lux, H. D. (1977) 'Ceiling of stimulus induced rises in extracellular potassium concentration in the cerebral cortex of cat', *Brain Research*, 120, pp. 231–249. doi: 10.4039/Ent4874-3.

Hendry, S. H. *et al.* (1987) 'Numbers and proportions of GABA-immunoreactive neurons in different areas of monkey cerebral cortex.', *The Journal of neuroscience : the official journal of the Society for Neuroscience*. Society for Neuroscience, 7(5), pp. 1503–19. doi: 10.1523/JNEUROSCI.07-05-01503.1987.

Hendzel, M. J. *et al.* (1997) 'Mitosis-specific phosphorylation of histone H3 initiates primarily within pericentromeric heterochromatin during G2 and spreads in an ordered fashion coincident with mitotic chromosome condensation.', *Chromosoma*, 106(6), pp. 348–60. Available at: http://www.ncbi.nlm.nih.gov/pubmed/9362543 (Accessed: 9 June 2018).

Henneberger, C. *et al.* (2010) 'Long-term potentiation depends on release of D-serine from astrocytes.', *Nature*. Nature Publishing Group, 463(7278), pp. 232–236. doi: 10.1038/nature08673.

Hennou, S. *et al.* (2002) 'Early sequential formation of functional GABA $_{A}$ and glutamatergic synapses on CA1 interneurons of the rat foetal hippocampus', *European Journal of Neuroscience*. Wiley/Blackwell (10.1111), 16(2), pp. 197–208. doi: 10.1046/j.1460-9568.2002.02073.x.

Herrero, I., Miras-Portugal, M. T. and Sánchez-Prieto, J. (1998) 'Functional switch from facilitation to inhibition in the control of glutamate release by metabotropic glutamate receptors.', *The Journal of biological chemistry*. American Society for Biochemistry and Molecular Biology, 273(4), pp. 1951–8. doi: 10.1074/JBC.273.4.1951.

Higashi, K. *et al.* (2001) 'An inwardly rectifying K^+ channel, Kir4.1, expressed in astrocytes surrounds synapses and blood vessels in brain', *American Journal of Physiology-Cell Physiology*. American Physiological SocietyBethesda, MD , 281(3), pp. C922–C931. doi: 10.1152/ajpcell.2001.281.3.C922.

Higashimori, H. and Sontheimer, H. (2007) 'Role of Kir4.1 channels in growth control of glia', *GLIA*, 55(16), pp. 1668–1679. doi: 10.1002/glia.20574.

Hill, E. J. *et al.* (2012) 'NT2 Derived Neuronal and Astrocytic Network Signalling', *PLoS ONE*. Edited by H. Okazawa. Public Library of Science, 7(5), p. e36098. doi: 10.1371/journal.pone.0036098.

Hiragi, T. *et al.* (2017) 'Differentiation of Human Induced Pluripotent Stem Cell (hiPSC)-Derived Neurons in Mouse Hippocampal Slice Cultures.', *Frontiers in cellular neuroscience*. Frontiers Media SA, 11, p. 143. doi: 10.3389/fncel.2017.00143.

Hirase, H. *et al.* (2004) 'Calcium dynamics of cortical astrocytic networks in vivo', *PLoS Biology*. Edited by Winfred Denk. Public Library of Science, 2(4), p. e96. doi:

10.1371/journal.pbio.0020096.

Ho, S.-M. *et al.* (2015) 'Rapid Ngn2-induction of Excitatory Neurons from hiPSC-Derived Neural Progenitor Cells', *Methods*, 101, pp. 1–12. doi: 10.1016/j.ymeth.2015.11.019.

Hochbaum, D. R. *et al.* (2014) 'All-optical electrophysiology in mammalian neurons using engineered microbial rhodopsins.', *Nature methods*, 11(8), pp. 825–33. doi: 10.1038/nmeth.3000.

Hochstim, C., Deneen, B., Lukaszewicz, A., Zhou, Q. and Anderson, David J. (2008) 'Identification of Positionally Distinct Astrocyte Subtypes whose Identities Are Specified by a Homeodomain Code', *Cell*, 133(3), pp. 510–522. doi: 10.1016/j.cell.2008.02.046.

Hochstim, C., Deneen, B., Lukaszewicz, A., Zhou, Q. and Anderson, David J (2008) 'Identification of Positionally Distinct Astrocyte Subtypes whose Identities Are Specified by a Homeodomain Code', *Cell - supplementary figures*. NIH Public Access, 133(3), pp. 510–522. doi: 10.1016/j.cell.2008.02.046.

Huang, Y.-W. A. *et al.* (2017) 'ApoE2, ApoE3, and ApoE4 Differentially Stimulate APP Transcription and Aβ Secretion', *Cell*, 168(3), pp. 427–441. doi: 10.1016/j.cell.2016.12.044.

Huang, Y. (2010) 'Aβ-independent roles of apolipoprotein E4 in the pathogenesis of Alzheimer's disease', *Trends in Molecular Medicine*. Elsevier Ltd, 16(6), pp. 287–294. doi: 10.1016/j.molmed.2010.04.004.

Isomura, Y. *et al.* (2003) 'Synaptically Activated Cl- Accumulation Responsible for Depolarizing GABAergic Responses in Mature Hippocampal Neurons', *Journal of Neurophysiology*. American Physiological Society, 90(4), pp. 2752–2756. doi: 10.1152/jn.00142.2003.

Israel, M. A. *et al.* (2012) 'Probing sporadic and familial Alzheimer's disease using induced pluripotent stem cells.', *Nature*. Nature Publishing Group, a division of Macmillan Publishers Limited. All Rights Reserved., 482(7384), pp. 216–20. doi: 10.1038/nature10821.

Iwabuchi, S. *et al.* (2002) 'Photolytic flash-induced intercellular calcium waves using caged calcium ionophore in cultured astrocytes from newborn rats', *Experimental Brain Research*, 146(1), pp. 103–116. doi: 10.1007/s00221-002-1149-y.

Jacob, C. P. *et al.* (2007) 'Alterations in Expression of Glutamatergic Transporters and Receptors in Sporadic Alzheimer's Disease', *Journal of Alzheimer's Disease*. IOS Press, 11(1), pp. 97–116. doi: 10.3233/JAD-2007-11113.

Jacobsen, C. T. and Miller, R. H. (2003) 'Control of astrocyte migration in the developing cerebral cortex', *Developmental Neuroscience*, 25(2–4), pp. 207–216. doi: 10.1159/000072269.

Jakovcevski, I., Mayer, N. and Zecevic, N. (2011) 'Multiple origins of human neocortical interneurons are supported by distinct expression of transcription factors.', *Cerebral cortex (New York, N.Y. : 1991)*. Oxford University Press, 21(8), pp. 1771–82. doi: 10.1093/cercor/bhq245.

Jarrett, J. T., Berger, E. P. and Lansbury, P. T. (1993) 'The carboxy terminus of the beta amyloid protein is critical for the seeding of amyloid formation: implications for the pathogenesis of Alzheimer's disease.', *Biochemistry*, 32(18), pp. 4693–7. Available at: http://www.ncbi.nlm.nih.gov/pubmed/8490014 (Accessed: 18 December 2018).

Jayaraman, S. *et al.* (2000) 'Mechanism and cellular applications of a green fluorescent protein-based halide sensor.', *The Journal of biological chemistry*. American Society for Biochemistry and Molecular Biology, 275(9), pp. 6047–50. doi: 10.1074/JBC.275.9.6047.

Jeftinija, S. D., Jeftinija, K. V and Stefanovic, G. (1997) 'Cultured astrocytes express proteins involved in vesicular glutamate release', *Brain Research*. Elsevier, 750(1–2), pp. 41–47. doi: 10.1016/S0006-8993(96)00610-5.

Ji, Y. *et al.* (2003) 'Apolipoprotein E isoform-specific regulation of dendritic spine morphology in apolipoprotein E transgenic mice and Alzheimer's disease patients', *Neuroscience*, 122(2), pp. 305–315. doi: 10.1016/j.neuroscience.2003.08.007.

Jiang, X. and Nardelli, J. (2016) 'Cellular and molecular introduction to brain development.', *Neurobiology of disease*. NIH Public Access, 92(Pt A), pp. 3–17. doi: 10.1016/j.nbd.2015.07.007.

John Lin, C.-C. *et al.* (2017) 'Identification of diverse astrocyte populations and their malignant analogs', *Nature Neuroscience*, 20(3). doi: 10.1038/nn.4493.

Johnson, M. A. *et al.* (2007) 'Functional Neural Development from Human Embryonic Stem Cells: Accelerated Synaptic Activity via Astrocyte Coculture', *Journal of Neuroscience*. NIH Public Access, 27(12), pp. 3069–3077. doi: 10.1523/JNEUROSCI.4562-06.2007.

Jolivet, R. *et al.* (2010) 'Comment on recent modeling studies of astrocyte-neuron metabolic interactions', *Journal of Cerebral Blood Flow and Metabolism*. Nature Publishing Group, 30(12), pp. 1982–1986. doi: 10.1038/jcbfm.2010.132.

Jorm, A. F. and Jolley, D. (1998) 'The incidence of dementia: A meta-analysis', *Neurology*. Wolters Kluwer Health, Inc. on behalf of the American Academy of Neurology, 51(3), pp. 728–733. doi: 10.1212/WNL.51.3.728.

Jourdain, P. *et al.* (2007) 'Glutamate exocytosis from astrocytes controls synaptic strength.', *Nature neuroscience*, 10(3), pp. 331–9. doi: 10.1038/nn1849.

Kadoshima, T. *et al.* (2013) 'Self-organization of axial polarity, inside-out layer pattern, and species-specific progenitor dynamics in human ES cell-derived neocortex.', *Proceedings of the National Academy of Sciences of the United States of America*. National Academy of Sciences, 110(50), pp. 20284–9. doi: 10.1073/pnas.1315710110.

Kang, J. *et al.* (1998) 'Astrocyte-mediated potentiation of inhibitory synaptic transmission', *Nature Neuroscience*. Nature Publishing Group, 1(8), pp. 683–692. doi: 10.1038/3684.

Kayama, T. *et al.* (2018) 'Temporally coordinated spiking activity of human induced pluripotent stem cell-derived neurons co-cultured with astrocytes', *Biochemical and*

Biophysical Research Communications. Academic Press, 495(1), pp. 1028–1033. doi: 10.1016/j.bbrc.2017.11.115.

Kelava, I. and Lancaster, M. A. (2017) 'Stem Cell Models of Human Brain Development', *Cell Stem Cell*, 18(6), pp. 736–748. doi: 10.1016/j.stem.2016.05.022.

Kessaris, N., Pringle, N. and Richardson, W. D. (2013) 'Specification of CNS glia from neural stem cells in the embryonic neuroepithelium', *Philosophical transactions of the Royal Society*, 363(February 2007), pp. 71–85. doi: 10.1098/rstb.2006.2013.

Kettenmann, H., Backus, K. H. and Schachner, M. (1984) 'Aspartate, glutamate and γ-aminobutyric acid depolarize cultured astrocytes', *Neuroscience Letters*. Elsevier, 52(1–2), pp. 25–29. doi: 10.1016/0304-3940(84)90345-8.

Khakh, B. S. and Sofroniew, M. V (2015) 'Diversity of astrocyte functions and phenotypes in neural circuits.', *Nature neuroscience*. NIH Public Access, 18(7), pp. 942–52. doi: 10.1038/nn.4043.

Kikuchi, T. *et al.* (2017) 'Human iPS cell-derived dopaminergic neurons function in a primate Parkinson's disease model', *Nature*. Nature Publishing Group, 548(7669), pp. 592–596. doi: 10.1038/nature23664.

Kim, J., Basak, J. M. and Holtzman, D. M. (2009) 'The role of apolipoprotein E in Alzheimer's disease.', *Neuron*, 63(3), pp. 287–303. doi: 10.1016/j.neuron.2009.06.026.

Kim, Jaekwang *et al.* (2014) 'Apolipoprotein E in Synaptic Plasticity and Alzheimer's Disease: Potential Cellular and Molecular Mechanisms', *Molecules and Cells*. Korean Society for Molecular and Cellular Biology, 37(11), pp. 767–776. doi: 10.14348/molcells.2014.0248.

Kim, K. *et al.* (2011) 'Role of Excitatory Amino Acid Transporter-2 (EAAT2) and glutamate in neurodegeneration: Opportunities for developing novel therapeutics', *Journal of Cellular Physiology*. NIH Public Access, pp. 2484–2493. doi: 10.1002/jcp.22609.

Kimelberg, H. K. and Nedergaard, M. (2010) 'Functions of Astrocytes and their Potential As Therapeutic Targets', *Neurotherapeutics*, 7(4), pp. 338–353. doi: 10.1016/j.nurt.2010.07.006.

Kindberg, A. A. *et al.* (2014) 'An in vitro model of human neocortical development using pluripotent stem cells: cocaine-induced cytoarchitectural alterations.', *Disease models & mechanisms*, 7(12), pp. 1397–405. doi: 10.1242/dmm.017251.

Kirischuk, S., Kettenmann, H. and Verkhratsky, A. (1997) 'Na+/Ca2+ exchanger modulates kainate-triggered Ca2+ signaling in Bergmann glial cells in situ', *FASEB journal : official publication of the Federation of American Societies for Experimental Biology*, 11(6), pp. 566–572.

Koffie, R. M. *et al.* (2012) 'Apolipoprotein E4 effects in Alzheimer's disease are mediated by synaptotoxic oligomeric amyloid-β.', *Brain : a journal of neurology*, 135(Pt 7), pp. 2155–68. doi: 10.1093/brain/aws127.

Kondo, T. *et al.* (2013) 'Modeling Alzheimer's Disease with iPSCs Reveals Stress Phenotypes Associated with Intracellular Aβ and Differential Drug Responsiveness', *Cell Stem Cell*. Cell Press, 12(4), pp. 487–496. doi: 10.1016/J.STEM.2013.01.009.

Kosik, K., Joachim, C. and Selkoe, D. (1987) 'Microtubule-associated protein tau (T) is a major antigenic component of paired helical filaments in Alzheimer disease', *Alzheimer Disease & Associated Disorders*, 1(3), p. 203. doi: 10.1097/00002093-198701030-00022.

Kreft, M. *et al.* (2004) 'Properties of Ca2+-dependent exocytosis in cultured astrocytes', *Glia*, 46(4), pp. 437–445. doi: 10.1002/glia.20018.

Krencik, R. *et al.* (2011) 'Specification of transplantable astroglial subtypes from human pluripotent stem cells.', *Nature biotechnology*. NIH Public Access, 29(6), pp. 528–34. doi: 10.1038/nbt.1877.

Krencik, R. *et al.* (2017) 'Systematic Three-Dimensional Coculture Rapidly Recapitulates Interactions between Human Neurons and Astrocytes', *Stem Cell Reports*, 9(6), pp. 1745–1753. doi: 10.1016/j.stemcr.2017.10.026.

Krencik, R., van Asperen, J. V. and Ullian, E. M. (2016) 'Human astrocytes are distinct contributors to the complexity of synaptic function', *Brain Research Bulletin*. doi: 10.1016/j.brainresbull.2016.08.012.

Krencik, R. and Zhang, S.-C. (2011) 'Directed differentiation of functional astroglial subtypes from human pluripotent stem cells.', *Nature protocols*. Nature Publishing Group, a division of Macmillan Publishers Limited. All Rights Reserved., 6(11), pp. 1710–7. doi: 10.1038/nprot.2011.405.

Kucheryavykh, Y. V. *et al.* (2007) 'Downregulation of Kir4.1 inward rectifying potassium channel subunits by RNAi impairs potassium transfer and glutamate uptake by cultured cortical astrocytes', *Glia*. Wiley-Blackwell, 55(3), pp. 274–281. doi: 10.1002/glia.20455.

Kuchibhotla, K. V. *et al.* (2009) 'Synchronous Hyperactivity and Intercellular Calcium Waves in Astrocytes in Alzheimer Mice', *Science - SUPPLEMENTARY*. NIH Public Access, 323(5918), pp. 1211–1215. doi: 10.1126/science.1169096.

Kucukdereli, H. *et al.* (2011) 'Control of excitatory CNS synaptogenesis by astrocyte-secreted proteins Hevin and SPARC.', *Proceedings of the National Academy of Sciences of the United States of America*. National Academy of Sciences, 108(32), pp. E440-9. doi: 10.1073/pnas.1104977108.

Kuffler, S. W., Nicholls, J. G. and Orkand, R. K. (1966) 'Physiological properties of glial cells in the central nervous system of amphibia', *Journal of neurophysiology*, Volume 29(Issue 4).

Kuga, N. *et al.* (2011) 'Large-Scale Calcium Waves Traveling through Astrocytic Networks In Vivo', *Journal of Neuroscience*. Society for Neuroscience, 31(7), pp. 2607–2614. doi: 10.1523/JNEUROSCI.5319-10.2011.

Kuner, T. and Augustine, G. J. (2000) 'A genetically encoded ratiometric indicator for chloride: Capturing chloride transients in cultured hippocampal neurons', *Neuron*, 27(3), pp. 447–459. doi: 10.1016/S0896-6273(00)00056-8.

Kuperstein, I. *et al.* (2010) 'Neurotoxicity of Alzheimer's disease Aβ peptides is induced by small changes in the Aβ42 to Aβ40 ratio.', *The EMBO journal*. European Molecular Biology Organization, 29(19), pp. 3408–20. doi: 10.1038/emboj.2010.211.

Laake, J. H. *et al.* (1999) 'Postembedding immunogold labelling reveals subcellular localization and pathway-specific enrichment of phosphate activated glutaminase in rat cerebellum', *Neuroscience*. Pergamon, 88(4), pp. 1137–1151. doi: 10.1016/S0306-4522(98)00298-X.

LaDu, M. J. *et al.* (1994) 'Isoform-specific binding of apolipoprotein E to β-amyloid', *Journal of Biological Chemistry*, 269(38), pp. 23403–23406.

Lalo, U. *et al.* (2006) 'NMDA receptors mediate neuron-to-glia signaling in mouse cortical astrocytes.', *The Journal of neuroscience : the official journal of the Society for Neuroscience*, 26(10), pp. 2673–83. doi: 10.1523/JNEUROSCI.4689-05.2006.

Lalo, U. *et al.* (2011) 'Ionotropic receptors in neuronal-astroglial signalling: What is the role of "excitable" molecules in non-excitable cells', *Biochimica et Biophysica Acta - Molecular Cell Research*. Elsevier, pp. 992–1002. doi: 10.1016/j.bbamcr.2010.09.007.

Lalo, U., Verkhratsky, A. and Pankratov, Y. (2011) 'Ionotropic ATP receptors in neuronal-glial communication', *Seminars in Cell and Developmental Biology*. Academic Press, pp. 220–228. doi: 10.1016/j.semcdb.2011.02.012.

Lambert, J. C. *et al.* (2013) 'Meta-analysis of 74,046 individuals identifies 11 new susceptibility loci for Alzheimer's disease.', *Nature genetics*, 45(12), pp. 1452–8. doi: 10.1038/ng.2802.

Lane-Donovan, C., Philips, G. T. and Herz, J. (2014) 'More than Cholesterol Transporters: Lipoprotein Receptors in CNS Function and Neurodegeneration', *Neuron*. NIH Public Access, pp. 771–787. doi: 10.1016/j.neuron.2014.08.005.

Leszkiewicz, D. N., Kandler, K. and Aizenman, E. (2000) 'Enhancement of NMDA receptor-mediated currents by light in rat neurones in vitro', *Journal of Physiology*. Wiley-Blackwell, 524(2), pp. 365–374. doi: 10.1111/j.1469-7793.2000.t01-1-00365.x.

Letinic, K., Zoncu, R. and Rakic, P. (2002) 'Origin of GABAergic neurons in the human neocortex', *Nature*. Nature Publishing Group, 417(6889), pp. 645–649. doi: 10.1038/nature00779.

Levine, A. J. and Brivanlou, A. H. (2007) 'Proposal of a model of mammalian neural induction.', *Developmental biology*. NIH Public Access, 308(2), pp. 247–56. doi: 10.1016/j.ydbio.2007.05.036.

Li, D. *et al.* (2012) 'Optogenetic activation of LiGluR-expressing astrocytes evokes anion

channel-mediated glutamate release', *Journal of Physiology*. Wiley-Blackwell, 590(4), pp. 855–873. doi: 10.1113/jphysiol.2011.219345.

Li, D., Herault, K., *et al.* (2013) 'Lack of Evidence for Vesicular Glutamate Transporter Expression in Mouse Astrocytes', *Journal of Neuroscience*. Society for Neuroscience, 33(10), pp. 4434–4455. doi: 10.1523/JNEUROSCI.3667-12.2013.

Li, D., Agulhon, C., *et al.* (2013) 'New tools for investigating astrocyte-to-neuron communication', *Frontiers in Cellular Neuroscience*. Frontiers Media SA, 7, p. 193. doi: 10.3389/fncel.2013.00193.

Li, X.-J. *et al.* (2009) 'Coordination of sonic hedgehog and Wnt signaling determines ventral and dorsal telencephalic neuron types from human embryonic stem cells', *Development*. Company of Biologists, 136(23), pp. 4055–4063. doi: 10.1242/dev.036624.

Li, X. *et al.* (2012) 'MEK Is a Key Regulator of Gliogenesis in the Developing Brain', *Neuron*. Elsevier, 75(6), pp. 1035–1050. doi: 10.1016/j.neuron.2012.08.031.

Li, X. *et al.* (2018) 'Fast Generation of Functional Subtype Astrocytes from Human Pluripotent Stem Cells.', *Stem cell reports*. Elsevier, 11(4), pp. 998–1008. doi: 10.1016/j.stemcr.2018.08.019.

Liddelow, S. A. *et al.* (2017) 'Neurotoxic reactive astrocytes are induced by activated microglia', *Nature*. Nature Publishing Group, 541(7638), pp. 481–487. doi: 10.1038/nature21029.

Lin, J. Y. *et al.* (2009) 'Characterization of engineered channelrhodopsin variants with improved properties and kinetics.', *Biophysical journal*, 96(5), pp. 1803–14. doi: 10.1016/j.bpj.2008.11.034.

Lin, Y. T. *et al.* (2018) 'APOE4 Causes Widespread Molecular and Cellular Alterations Associated with Alzheimer's Disease Phenotypes in Human iPSC-Derived Brain Cell Types', *Neuron*. Elsevier, 98(6), pp. 1141-1154.e7. doi: 10.1016/j.neuron.2018.05.008.

Lischka, F. W. *et al.* (2017) 'Neonatal mouse cortical but not isogenic human astrocyte feeder layers enhance the functional maturation of induced pluripotent stem cell-derived neurons in culture', *Glia*, (November 2017), pp. 725–748. doi: 10.1002/glia.23278.

Liu, Chia-Chen *et al.* (2013) 'Apolipoprotein E and Alzheimer disease: risk, mechanisms and therapy.', *Nature reviews. Neurology*, 9(2), pp. 106–18. doi: 10.1038/nrneurol.2012.263.

Liu, H. and Zhang, S.-C. (2011) 'Specification of neuronal and glial subtypes from human pluripotent stem cells.', *Cellular and molecular life sciences : CMLS*. NIH Public Access, 68(24), pp. 3995–4008. doi: 10.1007/s00018-011-0770-y.

Liu, Q.-S. *et al.* (2004) 'Astrocyte activation of presynaptic metabotropic glutamate receptors modulates hippocampal inhibitory synaptic transmission.', *Neuron glia biology*. NIH Public Access, 1(4), pp. 307–16. doi: 10.1017/S1740925X05000190.

Liu, T. *et al.* (2011) 'Calcium Triggers Exocytosis from Two Types of Organelles in a Single Astrocyte', *Journal of Neuroscience*, 31(29), pp. 10593–10601. doi: 10.1523/JNEUROSCI.6401-10.2011.

Liu, Y. *et al.* (2004) 'CD44 expression identifies astrocyte-restricted precursor cells', *Developmental Biology*, 276(1), pp. 31–46. doi: 10.1016/j.ydbio.2004.08.018.

Livesey, M. R. *et al.* (2014) 'Maturation of AMPAR composition and the GABAAR reversal potential in hPSC-derived cortical neurons.', *The Journal of neuroscience : the official journal of the Society for Neuroscience*, 34(11), pp. 4070–5. doi: 10.1523/JNEUROSCI.5410-13.2014.

Livesey, M. R. *et al.* (2015) 'Functional properties of in vitro excitatory cortical neurons derived from human pluripotent stem cells.', *The Journal of physiology*. doi: 10.1113/JP270660.

Lodato, S., Shetty, A. S. and Arlotta, P. (2014) 'Cerebral cortex assembly: generating and reprogramming projection neuron diversity', *Trends in Neurosciences*, 38(2), pp. 117–125. doi: 10.1016/j.tins.2014.11.003.

Ludwin, S. K., Kosek, J. C. and Eng, L. F. (1976) 'The topographical distribution of S-100 and GFA proteins in the adult rat brain: An immunohistochemical study using horseradish peroxidase-labelled antibodies', *The Journal of Comparative Neurology*. Wiley-Blackwell, 165(2), pp. 197–207. doi: 10.1002/cne.901650206.

Lujan, R. and Somogyi, P. (1996) 'Perisynaptic Location of Metabotropic Glutamate Receptors mGluR1 and mGluR5 on Dendrites and Dendritic Spines in the Rat Hippocampus', *European Journal of Neuroscience*, 8, pp. 1–13. Available at: file:///Users/charrier/Documents/Library.papers3/2006/Unknown/2006-64.pdf%0Apapers3://publication/uuid/9A0BDDB2-E94E-4ADC-8DE4-17507ABAC78F.

Lupo, G. *et al.* (2014) 'From pluripotency to forebrain patterning: an in vitro journey astride embryonic stem cells.', *Cellular and molecular life sciences : CMLS*. Springer, 71(15), pp. 2917–30. doi: 10.1007/s00018-014-1596-1.

Lytton, J. (2007) 'Na $^{+}$ /Ca $^{2+}$ exchangers: three mammalian gene families control Ca $^{2+}$ transport', *Biochemical Journal*, 406(3), pp. 365–382. doi: 10.1042/BJ20070619.

Magistri, M. *et al.* (2016) 'A comparative transcriptomic analysis of astrocytes differentiation from human neural progenitor cells', *European Journal of Neuroscience*. Edited by K. Mitchell, 44(10), pp. 2858–2870. doi: 10.1111/ejn.13382.

Maher, B. J., McGinley, M. J. and Westbrook, G. L. (2009) 'Experience-dependent maturation of the glomerular microcircuit.', *Proceedings of the National Academy of Sciences of the United States of America*. National Academy of Sciences, 106(39), pp. 16865–70. doi: 10.1073/pnas.0808946106.

Maherali, N. *et al.* (2008) 'A high efficiency system for the generation and study of human

induced pluripotent stem cells', *Cell stem cell*, 3(3), pp. 340–345. doi: 10.1016/j.stem.2008.08.003.

Mahley, R. W. (1988) 'Apolipoprotein E : Cholesterol Transport Protein with Expanding Role in Cell Biology', *Science*, 240, pp. 622–630. doi: 10.1126/science.3283935.

Mahley, R. W., Nathan, B. P. and Pitas, R. E. (1996) 'Apolipoprotein E: Structure, function, and possible roles in Alzheimer's disease', *Annals of the New York Academy of Sciences*. Wiley/Blackwell (10.1111), 777(1), pp. 139–145. doi: 10.1111/j.1749-6632.1996.tb34412.x.

Makani, S. and Chesler, M. (2010) 'Rapid rise of extracellular pH evoked by neural activity is generated by the plasma membrane calcium ATPase.', *Journal of neurophysiology*. American Physiological Society, 103(2), pp. 667–76. doi: 10.1152/jn.00948.2009.

Makara, J. K. *et al.* (2001) 'pH-sensitive inwardly rectifying chloride current in cultured rat cortical astrocytes', *GLIA*. John Wiley & Sons, Inc., 34(1), pp. 52–58. doi: 10.1002/glia.1039.

Malatesta, P., Appolloni, I. and Calzolari, F. (2008) 'Radial glia and neural stem cells', *Cell and Tissue Research*. Springer-Verlag, 331(1), pp. 165–178. doi: 10.1007/s00441-007-0481-8.

Mangia, S. *et al.* (2011) 'Response to comment on recent modeling studies of astrocyte-neuron metabolic interactions: Much ado about nothing', *Journal of Cerebral Blood Flow and Metabolism*, 31(6), pp. 1346–1353. doi: 10.1038/jcbfm.2011.29.

Manuel, M. N. *et al.* (2015) 'Regulation of cerebral cortical neurogenesis by the Pax6 transcription factor', *Frontiers in Cellular Neuroscience*. Frontiers Media SA, 9, p. 70. doi: 10.3389/fncel.2015.00070.

Marcaggi, P. and Attwell, D. (2004) 'Role of glial amino acid transporters in synaptic transmission and brain energetics', *Glia*. Wiley-Blackwell, 47(3), pp. 217–225. doi: 10.1002/glia.20027.

Marchetto, M. C. N., Winner, B. and Gage, F. H. (2010) 'Pluripotent stem cells in neurodegenerative and neurodevelopmental diseases.', *Human molecular genetics*. Oxford University Press, 19(R1), pp. R71-6. doi: 10.1093/hmg/ddq159.

Mariani, J. *et al.* (2012) 'Modeling human cortical development in vitro using induced pluripotent stem cells', *Proceedings of the National Academy of Sciences*. National Academy of Sciences, 109(31), pp. 12770–12775. doi: 10.1073/pnas.1202944109.

Markova, O. *et al.* (2008) 'Genetically encoded chloride indicator with improved sensitivity', *Journal of Neuroscience Methods*, 170(1), pp. 67–76. doi: 10.1016/j.jneumeth.2007.12.016.

Markram, H. *et al.* (2004) 'Interneurons of the neocortical inhibitory system', *Nature Reviews Neuroscience*. Nature Publishing Group, 5(10), pp. 793–807. doi: 10.1038/nrn1519.

Marsh, J. and Alifragis, P. (2018) 'Synaptic dysfunction in Alzheimer's disease: the effects of

amyloid beta on synaptic vesicle dynamics as a novel target for therapeutic intervention.', *Neural regeneration research*. Wolters Kluwer -- Medknow Publications, 13(4), pp. 616–623. doi: 10.4103/1673-5374.230276.

Martinez-Hernandez, A., Bell, K. P. and Norenberg, M. D. (1977) 'Glutamine Synthetase: Glial Localization in Brain', *Science*. American Association for the Advancement of Science, 195(4284), pp. 1356–1358. doi: 10.1126/science.167.3922.1252.

Masamoto, K. *et al.* (no date) 'Unveiling astrocytic control of cerebral blood flow with optogenetics', *Nature Publishing Group*. Nature Publishing Group, pp. 1–11. doi: 10.1038/srep11455.

Masliah, E. *et al.* (1996) 'Deficient glutamate tranport is associated with neurodegeneration in Alzheimer's disease', *Annals of Neurology*. John Wiley & Sons, Ltd, 40(5), pp. 759–766. doi: 10.1002/ana.410400512.

Mateizel, I. *et al.* (2006) 'Derivation of human embryonic stem cell lines from embryos obtained after IVF and after PGD for monogenic disorders', *Human Reproduction*. Oxford University Press, 21(2), pp. 503–511. doi: 10.1093/humrep/dei345.

Matthias, K. *et al.* (2003) 'Segregated expression of AMPA-type glutamate receptors and glutamate transporters defines distinct astrocyte populations in the mouse hippocampus.', *The Journal of neuroscience : the official journal of the Society for Neuroscience*, 23(5), pp. 1750–1758. doi: 23/5/1750 [pii].

Mattis, J. *et al.* (2012) 'Principles for applying optogenetic tools derived from direct comparative analysis of microbial opsins.', *Nature methods*. Nature Publishing Group, 9(2), pp. 159–72. doi: 10.1038/nmeth.1808.

Mauch, D. H., Na, K. and Schumacher, S. (2001) 'CNS Synaptogenesis Promoted by Glia-Derived Cholesterol', *Science*, 294(November), pp. 1354–1358. doi: 10.1126/science.294.5545.1354.

Mederos, S. *et al.* (2019) 'Melanopsin for precise optogenetic activation of astrocyte- neuron networks', (September 2018), pp. 915–934. doi: 10.1002/glia.23580.

Merkle, F. T. and Eggan, K. (2013) 'Modeling Human Disease with Pluripotent Stem Cells: from Genome Association to Function', *Cell Stem Cell*. Elsevier, 12(6), pp. 656–668. doi: 10.1016/j.stem.2013.05.016.

Mertens, J. *et al.* (2016) 'Evaluating cell reprogramming, differentiation and conversion technologies in neuroscience', *Nature Reviews Neuroscience*. Nature Publishing Group, pp. 424–437. doi: 10.1038/nrn.2016.46.

Miya, K. *et al.* (2008) 'Serine racemase is predominantly localized in neurons in mouse brain', *The Journal of Comparative Neurology*. Wiley-Blackwell, 510(6), pp. 641–654. doi: 10.1002/cne.21822.

Mohn, T. C. and Koob, A. O. (2015) 'Adult Astrogenesis and the Etiology of Cortical

Neurodegeneration.', *Journal of experimental neuroscience*. SAGE Publications, 9(Suppl 2), pp. 25–34. doi: 10.4137/JEN.S25520.

Molofsky, A. V. and Deneen, B. (2015) 'Astrocyte development: A Guide for the Perplexed', *GLIA*. Wiley-Blackwell, pp. 1320–1329. doi: 10.1002/glia.22836.

Molyneaux, B. J. *et al.* (2007) 'Neuronal subtype specification in the cerebral cortex', *Nature Reviews Neuroscience*. Nature Publishing Group, pp. 427–437. doi: 10.1038/nrn2151.

Montana, V. *et al.* (2004) 'Vesicular Glutamate Transporter-Dependent Glutamate Release from Astrocytes', *Journal of Neuroscience*, 24(11), pp. 2633–2642. doi: 10.1523/JNEUROSCI.3770-03.2004.

Moore, S. *et al.* (2015) 'APP Metabolism Regulates Tau Proteostasis in Human Cerebral Cortex Neurons', *Cell Reports*. Cell Press, 11(5), pp. 689–696. doi: 10.1016/J.CELREP.2015.03.068.

Mothet, J. P. *et al.* (2006) 'A critical role for the glial-derived neuromodulator d-serine in the age-related deficits of cellular mechanisms of learning and memory', *Aging Cell*. Wiley/Blackwell (10.1111), 5(3), pp. 267–274. doi: 10.1111/j.1474-9726.2006.00216.x.

Mucke, L. *et al.* (2000) 'High-level neuronal expression of abeta 1-42 in wild-type human amyloid protein precursor transgenic mice: synaptotoxicity without plaque formation.', *The Journal of neuroscience : the official journal of the Society for Neuroscience*. Society for Neuroscience, 20(11), pp. 4050–8. doi: 10.1523/JNEUROSCI.20-11-04050.2000.

Mukherjee, S. and Manahan-Vaughan, D. (2013) 'Role of metabotropic glutamate receptors in persistent forms of hippocampal plasticity and learning', *Neuropharmacology*. Elsevier Ltd, 66, pp. 65–81. doi: 10.1016/j.neuropharm.2012.06.005.

Mungenast, A. E., Siegert, S. and Tsai, L.-H. (2015) 'Modeling Alzheimer's disease with human induced pluripotent stem (iPS) cells', *Molecular and Cellular Neuroscience*. doi: 10.1016/j.mcn.2015.11.010.

Muratore, C. R. *et al.* (2014) 'The familial Alzheimer's disease APPV717I mutation alters APP processing and Tau expression in iPSC-derived neurons.', *Human molecular genetics*. Oxford University Press, 23(13), pp. 3523–36. doi: 10.1093/hmg/ddu064.

Murphy-Royal, C. *et al.* (2017) 'Astroglial glutamate transporters in the brain: Regulating neurotransmitter homeostasis and synaptic transmission', *Journal of Neuroscience Research*, 95(11), pp. 2140–2151. doi: 10.1002/jnr.24029.

Murphy, K. R. *et al.* (2013) 'Mapping the effects of ApoE4, age and cognitive status on 18F-florbetapir PET measured regional cortical patterns of beta-amyloid density and growth', *NeuroImage*. Academic Press, 78, pp. 474–480. doi: 10.1016/J.NEUROIMAGE.2013.04.048.

Nagel, G. *et al.* (2003) 'Channelrhodopsin-2, a directly light-gated cation-selective membrane channel.', *Proceedings of the National Academy of Sciences of the United States*

of America, 100(24), pp. 13940–5. doi: 10.1073/pnas.1936192100.

Nagy, J. I., Dudek, F. E. and Rash, J. E. (2004) 'Update on connexins and gap junctions in neurons and glia in the mammalian nervous system', *Brain Research Reviews*. Elsevier, 47(1–3), pp. 191–215. doi: 10.1016/J.BRAINRESREV.2004.05.005.

Namihira, M. *et al.* (2009) 'Committed neuronal precursors confer astrocytic potential on residual neural precursor cells.', *Developmental cell*. Elsevier, 16(2), pp. 245–55. doi: 10.1016/j.devcel.2008.12.014.

Nash, M. S. *et al.* (2002) 'Determinants of metabotropic glutamate receptor-5-mediated Ca2+and inositol 1,4,5-trisphosphate oscillation frequency: Receptor density versus agonist concentration', *Journal of Biological Chemistry*. American Society for Biochemistry and Molecular Biology, 277(39), pp. 35947–35960. doi: 10.1074/jbc.M205622200.

Nathan, B. P. *et al.* (2002) 'Apolipoprotein E4 inhibits, and apolipoprotein E3 promotes neurite outgrowth in cultured adult mouse cortical neurons through the low-density lipoprotein receptor-related protein', *Brain Research*. Elsevier, 928(1–2), pp. 96–105. doi: 10.1016/S0006-8993(01)03367-4.

Navarrete, M. *et al.* (2013) 'Astrocyte calcium signal and gliotransmission in human brain tissue.', *Cerebral Cortex*, 23(5), pp. 1240–6. doi: 10.1093/cercor/bhs122.

Nedergaard, M. (1994) 'Direct Signaling from Astrocytes to Neurons in Cultures of Mammalian Brain Cells', *Science*, 263(March), pp. 1768–1770.

Nedergaard, M. and Verkhratsky, A. (2012) 'Artifact versus reality - How astrocytes contribute to synaptic events?', *Glia*, 60(7), pp. 1013–1023. doi: doi:10.1002/glia.22288.

Nett, W. J., Oloff, S. H. and McCarthy, K. D. (2002) 'Hippocampal Astrocytes In Situ Exhibit Calcium Oscillations That Occur Independent of Neuronal Activity', *Journal of Neurophysiology*. American Physiological SocietyBethesda, MD, 87(1), pp. 528–537. doi: 10.1152/jn.00268.2001.

Newman, E. A. (2005) 'Calcium Increases in Retinal Glial Cells Evoked by Light- Induced Neuronal Activity', *J. Neurosci.* Society for Neuroscience, 25(23), pp. 5502–5510. doi: 20026212.

NIH (2010) *Importance of Mouse Genome. http://www.genome.gov/10001345*, *National Human Genome Research Institute*. Available at: https://www.genome.gov/10001345/importance-of-mouse-genome/ (Accessed: 4 January 2019).

Nimmerjahn, A. *et al.* (2004) 'Sulforhodamine 101 as a specific marker of astroglia in the neocortex in vivo', *Nature Methods*. Nature Publishing Group, 1(1), pp. 31–37. doi: 10.1038/nmeth706.

Nowak, L., Ascher, P. and Berwald-Netter, Y. (1987) 'Ionic channels in mouse astrocytes in culture.', *The Journal of neuroscience : the official journal of the Society for Neuroscience*,

7(1), pp. 101–9. Available at: http://www.ncbi.nlm.nih.gov/pubmed/2433415.

Oberheim, N. A. *et al.* (2009) 'Uniquely Hominid Features of Adult Human Astrocytes', *Journal of Neuroscience*, 29(10), pp. 3276–3287. doi: 10.1523/JNEUROSCI.4707-08.2009.

Odawara, A. *et al.* (2014) 'Long-term electrophysiological activity and pharmacological response of a human induced pluripotent stem cell-derived neuron and astrocyte co-culture.', *Biochemical and biophysical research communications*, 443(4), pp. 1176–81. doi: 10.1016/j.bbrc.2013.12.142.

Oikonomou, G. and Shaham, S. (2011) 'The glia of Caenorhabditis elegans.', *Glia*. NIH Public Access, 59(9), pp. 1253–63. doi: 10.1002/glia.21084.

Oksanen, M. *et al.* (2017) 'PSEN1 Mutant iPSC-Derived Model Reveals Severe Astrocyte Pathology in Alzheimer's Disease', *Stem Cell Reports*. Elsevier, 9(6), pp. 1885–1897. doi: 10.1016/j.stemcr.2017.10.016.

Olabarria, M. *et al.* (2010) 'Concomitant astroglial atrophy and astrogliosis in a triple transgenic animal model of Alzheimer's disease', *Glia*. Wiley-Blackwell, 58(7), p. NA-NA. doi: 10.1002/glia.20967.

Olsen, M. L. and Sontheimer, H. (2004) 'Mislocalization of Kir channels in malignant glia.', *Glia*. NIH Public Access, 46(1), pp. 63–73. doi: 10.1002/glia.10346.

Ono, K. *et al.* (2014) 'Glutamate release from astrocyte cell-line GL261 via alterations in the intracellular ion environment', *Journal of Neural Transmission*. Springer Vienna, 121(3), pp. 245–257. doi: 10.1007/s00702-013-1096-8.

Opie, L. (1965) 'Effect of extracellular pH on function and metabolism of isolated perfused rat heart', *Am. J. Physiol.*, pp. 1075–1080. doi: 10.1152/ajplegacy.1965.209.6.1075.

Ozog, M. A., Siushansian, R. and Naus, C. C. G. (2002) 'Blocked gap junctional coupling increases glutamate-induced neurotoxicity in neuron-astrocyte co-cultures.', *Journal of neuropathology and experimental neurology*, 61(2), pp. 132–41. Available at: http://www.ncbi.nlm.nih.gov/pubmed/11855382 (Accessed: 21 June 2018).

Paluzzi, S. *et al.* (2007) 'Adult astroglia is competent for Na+/Ca2+ exchanger-operated exocytotic glutamate release triggered by mild depolarization', *Journal of Neurochemistry*. Wiley/Blackwell (10.1111), 103(3), pp. 1196–1207. doi: 10.1111/j.1471-4159.2007.04826.x.

Palygin, O. *et al.* (2010) 'Ionotropic NMDA and P2X1/5 receptors mediate synaptically induced Ca2+ signalling in cortical astrocytes', *Cell Calcium*. Churchill Livingstone, 48(4), pp. 225–231. doi: 10.1016/J.CECA.2010.09.004.

Panatier, A. *et al.* (2006) 'Glia-Derived d-Serine Controls NMDA Receptor Activity and Synaptic Memory', *Cell*. Cell Press, 125(4), pp. 775–784. doi: 10.1016/J.CELL.2006.02.051.

Panatier, A. *et al.* (2011) 'Astrocytes Are Endogenous Regulators of Basal Transmission at Central Synapses', *Cell*, 146(5), pp. 785–798. doi: 10.1016/j.cell.2011.07.022.

Pannasch, U. *et al.* (2011) 'Astroglial networks scale synaptic activity and plasticity.', *Proceedings of the National Academy of Sciences of the United States of America*, 108(20), pp. 8467–72. doi: 10.1073/pnas.1016650108.

Pappalardo, L. W., Black, J. A. and Waxman, S. G. (2016) 'Sodium channels in astroglia and microglia.', *Glia*. NIH Public Access, 64(10), pp. 1628–45. doi: 10.1002/glia.22967.

Pappas, C. A. and Ransom, B. R. (1994) 'Depolarization-induced alkalinization (DIA) in rat hippocampal astrocytes.', *J. Neurophysiol.*, 72(6), pp. 2816–26. doi: 10.1152/jn.1994.72.6.2816.

Paridaen, J. T. and Huttner, W. B. (2014) 'Neurogenesis during development of the vertebrate central nervous system', *EMBO Reports*. EMBO Press, pp. 351–364. doi: 10.1002/embr.201438447.

Parpura, V. *et al.* (1994) 'Glutamate-mediated astrocyte-neuron signalling', *Nature*. Nature Publishing Group, 369(6483), pp. 744–747. doi: 10.1038/369744a0.

Parpura, V. *et al.* (1995) 'Expression of synaptobrevin II, cellubrevin and syntaxin but not SNAP-25 in cultured astrocytes', *FEBS Letters*, 377(3), pp. 489–492. doi: 10.1016/0014-5793(95)01401-2.

Parpura, V. and Haydon, P. G. (2000) 'Physiological astrocytic calcium levels stimulate glutamate release to modulate adjacent neurons.', *Proceedings of the National Academy of Sciences of the United States of America*. National Academy of Sciences, 97(15), pp. 8629–34. Available at: http://www.ncbi.nlm.nih.gov/pubmed/10900020 (Accessed: 22 July 2018).

Parri, H. R. and Crunelli, V. (2003) 'The role of Ca2+ in the generation of spontaneous astrocytic Ca2+ oscillations', *Neuroscience*. Pergamon, 120(4), pp. 979–992. doi: 10.1016/S0306-4522(03)00379-8.

Parri, H. R., Gould, T. M. and Crunelli, V. (2001) 'Spontaneous astrocytic Ca2+ oscillations in situ drive NMDAR-mediated neuronal excitation', *Nature Neuroscience*. Nature Publishing Group, 4(8), pp. 803–812. doi: 10.1038/90507.

Pascual, O. *et al.* (2005) 'Astrocytic purinergic signaling coordinates synaptic networks.', *Science (New York, N.Y.)*. American Association for the Advancement of Science, 310(5745), pp. 113–6. doi: 10.1126/science.1116916.

Pasternack, M., Voipio, J. and Kaila, K. (1993) 'lntracellular carbonic anhydrase activity and its role in GABA-induced acidosis in isolated rat hippocampal pyramidal neurones', *Acta Physiologica Scandinavica*, 148, pp. 229–231.

Pasti, L. *et al.* (1997) 'Intracellular calcium oscillations in astrocytes: a highly plastic, bidirectional form of communication between neurons and astrocytes in situ.', *The Journal of neuroscience : the official journal of the Society for Neuroscience*, 17(20), pp. 7817–30. doi: 10.1038/nrn1722.

Peinado, A., Yuste, R. and Katz, L. C. (1993) 'Extensive dye coupling between rat

neocortical neurons during the period of circuit formation', *Neuron*. Cell Press, 10(1), pp. 103–114. doi: 10.1016/0896-6273(93)90246-N.

Pellerin, L. and Magistretti, P. J. (1994) 'Glutamate uptake into astrocytes stimulates aerobic glycolysis: a mechanism coupling neuronal activity to glucose utilization.', *Proceedings of the National Academy of Sciences*, 91(22), pp. 10625–10629. doi: 10.1073/pnas.91.22.10625.

Pelluru, D. *et al.* (2016) 'Optogenetic stimulation of astrocytes in the posterior hypothalamus increases sleep at night in C57BL/6J mice', *European Journal of Neuroscience*. Edited by R. Silver, 43(10), pp. 1298–1306. doi: 10.1111/ejn.13074.

Perea, G. *et al.* (2014) 'Optogenetic astrocyte activation modulates response selectivity of visual cortex neurons in vivo.', *Nature communications*, 5, p. 3262. doi: 10.1038/ncomms4262.

Perea, G. and Araque, A. (2005) 'Properties of Synaptically Evoked Astrocyte Calcium Signal Reveal Synaptic Information Processing by Astrocytes', *Journal of Neuroscience*, 25(9), pp. 2192–2203. doi: 10.1523/JNEUROSCI.3965-04.2005.

Perea, G. and Araque, A. (2007) 'Astrocytes potentiate transmitter release at single hippocampal synapses.', *Science (New York, N.Y.)*, 317(5841), pp. 1083–6. doi: 10.1126/science.1144640.

Perea, G. and Araque, A. (2010) 'GLIA modulates synaptic transmission.', *Brain research reviews*, 63(1–2), pp. 93–102. doi: 10.1016/j.brainresrev.2009.10.005.

Perea, G., Navarrete, M. and Araque, A. (2009) 'Tripartite synapses: astrocytes process and control synaptic information', *Trends in Neurosciences*, pp. 421–431. doi: 10.1016/j.tins.2009.05.001.

Peters, D. G., Connor, J. R. and Meadowcroft, M. D. (2015) 'The relationship between iron dyshomeostasis and amyloidogenesis in Alzheimer's disease: Two sides of the same coin.', *Neurobiology of disease*. doi: 10.1016/j.nbd.2015.08.007.

Petravicz, J., Fiacco, T. A. and McCarthy, K. D. (2008) 'Loss of IP3 receptor-dependent Ca2+ increases in hippocampal astrocytes does not affect baseline CA1 pyramidal neuron synaptic activity.', *The Journal of neuroscience : the official journal of the Society for Neuroscience*. NIH Public Access, 28(19), pp. 4967–73. doi: 10.1523/JNEUROSCI.5572-07.2008.

Phatnani, H. and Maniatis, T. (2015) 'Astrocytes in neurodegenerative disease.', *Cold Spring Harbor perspectives in biology*. Cold Spring Harbor Laboratory Press, 7(6). doi: 10.1101/cshperspect.a020628.

Picken Bahrey, H. L. and Moody, W. J. (2003) 'Early development of voltage-gated ion currents and firing properties in neurons of the mouse cerebral cortex.', *Journal of neurophysiology*. American Physiological SocietyBethesda, MD, 89(4), pp. 1761–73. doi:

10.1152/jn.00972.2002.

Pitas, R. E. *et al.* (1987) 'Astrocytes synthesize apolipoprotein E and metabolize apolipoprotein E-containing lipoproteins', *Biochimica et Biophysica Acta (BBA)/Lipids and Lipid Metabolism*. Elsevier, 917(1), pp. 148–161. doi: 10.1016/0005-2760(87)90295-5.

Porter, J. T. and McCarthy, K. D. (1995) 'GFAP-positive hippocampal astrocytes in situ respond to glutamatergic neuroligands with increases in [Ca2+]i', *Glia*, 13(2), pp. 101–112. doi: 10.1002/glia.440130204.

Porter, J. T. and McCarthy, K. D. (1996) 'Hippocampal astrocytes in situ respond to glutamate released from synaptic terminals.', *The Journal of Neuroscience*, 16(16), pp. 5073–5081. doi: 10.1523/JNEUROSCI.16-16-05073.1996.

Prè, D. *et al.* (2014) 'A time course analysis of the electrophysiological properties of neurons differentiated from human induced pluripotent stem cells (iPSCs).', *PloS one*. Public Library of Science, 9(7), p. e103418. doi: 10.1371/journal.pone.0103418.

Prichard, J. *et al.* (1991) 'Lactate rise detected by 1H NMR in human visual cortex during physiologic stimulation', *Pnas*, 88(July), pp. 5829–5831.

Prince, M. *et al.* (2015) 'World Alzheimer Report 2015: The Global Impact of Dementia | Alzheimer's Disease International', pp. 10–35. Available at: https://www.alz.co.uk/research/world-report-2015.

Putney, L. K. and Barber, D. L. (2003) 'Na-H exchange-dependent increase in intracellular pH times G2/M entry and transition.', *The Journal of biological chemistry*. American Society for Biochemistry and Molecular Biology, 278(45), pp. 44645–9. doi: 10.1074/jbc.M308099200.

Puzzo, D. *et al.* (2008) 'Picomolar amyloid-beta positively modulates synaptic plasticity and memory in hippocampus.', *The Journal of neuroscience : the official journal of the Society for Neuroscience*. NIH Public Access, 28(53), pp. 14537–45. doi: 10.1523/JNEUROSCI.2692-08.2008.

Raimondo, J. *et al.* (2013) 'A genetically-encoded chloride and pH sensor for dissociating ion dynamics in the nervous system', *Frontiers in Cellular Neuroscience*. Frontiers Media SA, 7, p. 202. doi: 10.3389/fncel.2013.00202.

Raimondo, J. V *et al.* (2015) 'Ion dynamics during seizures', *Frontiers in Cellular Neuroscience*. Frontiers Media SA, 9, p. 419. doi: 10.3389/fncel.2015.00419.

Raimondo, J. V *et al.* (2016) 'Tight Coupling of Astrocyte pH Dynamics to Epileptiform Activity Revealed by Genetically Encoded pH Sensors.', *The Journal of neuroscience : the official journal of the Society for Neuroscience*, 36(26), pp. 7002–13. doi: 10.1523/JNEUROSCI.0664-16.2016.

Rakic, P. (1975) 'Timing of major ontogenetic events in the visual cortex of the rhesus monkey.', *UCLA forum in medical sciences*, (18), pp. 3–40. Available at:

http://www.ncbi.nlm.nih.gov/pubmed/812226 (Accessed: 10 June 2018).

Rapp, A., Gmeiner, B. and Hüttinger, M. (2006) 'Implication of apoE isoforms in cholesterol metabolism by primary rat hippocampal neurons and astrocytes', *Biochimie*. Elsevier, 88(5), pp. 473–483. doi: 10.1016/j.biochi.2005.10.007.

Reichert, S., Randall, R. A. and Hill, C. S. (2013) 'A BMP regulatory network controls ectodermal cell fate decisions at the neural plate border.', *Development (Cambridge, England)*, 140(21), pp. 4435–44. doi: 10.1242/dev.098707.

Riddell, D. R. *et al.* (2008) 'Impact of Apolipoprotein E (ApoE) Polymorphism on Brain ApoE Levels', *Journal of Neuroscience*. Society for Neuroscience, 28(45), pp. 11445–11453. doi: 10.1523/JNEUROSCI.1972-08.2008.

Robel, S. *et al.* (2015) 'Reactive astrogliosis causes the development of spontaneous seizures.', *The Journal of neuroscience : the official journal of the Society for Neuroscience*. Society for Neuroscience, 35(8), pp. 3330–45. doi: 10.1523/JNEUROSCI.1574-14.2015.

Robinton, D. A. and Daley, G. Q. (2012) 'The promise of induced pluripotent stem cells in research and therapy', *Nature*, 481, pp. 295–305. doi: 10.1038/nature10761.

Roessmann, U. and Gambetti, P. (1986) 'Astrocytes in the developing human brain', *Acta Neuropathologica*, 70(3–4), pp. 308–313. doi: 10.1007/BF00686089.

Rose, C. R. and Deitmer, J. W. (1994) 'Evidence that glial cells modulate extracellular pH transients induced by neuronal activity in the leech central nervous system.', *The Journal of physiology*. Wiley-Blackwell, 481 (Pt 1)(Pt 1), pp. 1–5. Available at: http://www.ncbi.nlm.nih.gov/pubmed/7853232 (Accessed: 20 August 2018).

Roses, A. D. (1996) 'Apolipoprotein E Alleles As Risk Factors in Alzheimer ' S Disease', (4), pp. 387–400.

Rothstein, J. D. *et al.* (1996) 'Knockout of glutamate transporters reveals a major role for astroglial transport in excitotoxicity and clearance of glutamate', *Neuron*. Cell Press, 16(3), pp. 675–686. doi: 10.1016/S0896-6273(00)80086-0.

Roybon, L. *et al.* (2013) 'Human stem cell-derived spinal cord astrocytes with defined mature or reactive phenotypes.', *Cell reports*, 4(5), pp. 1035–48. doi: 10.1016/j.celrep.2013.06.021.

Russell, J. and Boron, W. (1976) 'Role of chloride transport in regulation of intracellular pH', *Nature*. Nature Publishing Group, 264(5581), pp. 73–74. doi: 10.1038/264073a0.

Rzigalinski, B. A. *et al.* (1998) 'Intracellular Free Calcium Dynamics in Stretch-Injured Astrocytes', *Journal of Neurochemistry*. Wiley/Blackwell (10.1111), 70(6), pp. 2377–2385. doi: 10.1046/j.1471-4159.1998.70062377.x.

Sances, S. *et al.* (2016) 'Modeling ALS with motor neurons derived from human induced pluripotent stem cells.', *Nature neuroscience*. NIH Public Access, 19(4), pp. 542–53. doi:

10.1038/nn.4273.

Sandor, C. *et al.* (2017) 'Transcriptomic profiling of purified patient-derived dopamine neurons identifies convergent perturbations and therapeutics for Parkinson's disease.', *Human molecular genetics*. Oxford University Press, 26(3), pp. 552–566. doi: 10.1093/hmg/ddw412.

Santello, M., Calì, C. and Bezzi, P. (2012) 'Gliotransmission and the tripartite synapse', *Advances in Experimental Medicine and Biology*. Springer, Vienna, 970, pp. 307–331. doi: 10.1007/978-3-7091-0932-8_14.

Sanzgiri, R. P., Araque, A. and Haydon, P. G. (1999) 'Prostaglandin E2 stimulates glutamate receptor-dependent astrocyte neuromodulation in cultured hippocampal cells', *Journal of Neurobiology*, 41(2), pp. 221–229. doi: 10.1002/(SICI)1097-4695(19991105)41:2<221::AID-NEU5>3.0.CO;2-A.

Sasaki, T. *et al.* (2012) 'Application of an optogenetic byway for perturbing neuronal activity via glial photostimulation.', *Proceedings of the National Academy of Sciences of the United States of America*. National Academy of Sciences, 109(50), pp. 20720–5. doi: 10.1073/pnas.1213458109.

Savtchouk, I. and Volterra, A. (2018) 'Gliotransmission: Beyond Black-and-White', *The Journal of Neuroscience*. Society for Neuroscience, 38(1), pp. 14–25. doi: 10.1523/JNEUROSCI.0017-17.2017.

Sayed, N., Liu, C. and Wu, J. C. (2016) 'Translation of Human-Induced Pluripotent Stem Cells: From Clinical Trial in a Dish to Precision Medicine.', *Journal of the American College of Cardiology*. NIH Public Access, 67(18), pp. 2161–2176. doi: 10.1016/j.jacc.2016.01.083.

Schitine, C. *et al.* (2015) 'Astrocyte heterogeneity in the brain: from development to disease', *Frontiers in Cellular Neuroscience*. Frontiers, 9, p. 76. doi: 10.3389/fncel.2015.00076.

Scholzen, T. and Gerdes, J. (2000) 'The Ki-67 protein: from the known and the unknown', *Journal of Cellular Physiology*, 182(August 1999), pp. 311–322. doi: 10.1002/(SICI)1097-4652(200003)182:3<311::AID-JCP1>3.0.CO;2-9.

Schröder, W. *et al.* (2002) 'AMPA receptor-mediated modulation of inward rectifier K+channels in astrocytes of mouse hippocampus', *Molecular and Cellular Neuroscience*, 19(3), pp. 447–458. doi: 10.1006/mcne.2001.1080.

Schummers, J., Yu, H. and Sur, M. (2008) 'Tuned Responses of Astrocytes and Their Influence on Hemodynamic Signals in the Visual Cortex', *Science*. American Association for the Advancement of Science, 320(5883), pp. 1638–1643. doi: 10.1126/science.1156120.

Schwartz, N. E. and Alford, S. (2000) 'Physiological activation of presynaptic metabotropic glutamate receptors increases intracellular calcium and glutamate release.', *Journal of neurophysiology*, 84(1), pp. 415–427. doi: 10.1152/jn.2000.84.1.415.

Schwiening, C. J., Kennedy, H. J. and Thomes, R. C. (1993) 'Calcium-hydrogen exchange by the plasma membrane Ca-ATPase of voltage-clamped snail neurons', *Proceedings of the royal society of London*, 253, pp. 285–289.

Selkoe, D. J. (2002) 'Alzheimer's disease is a synaptic failure', *Science*. American Association for the Advancement of Science, pp. 789–791. doi: 10.1126/science.1074069.

Senitz, D., Reichenbach, A. and Smith, T. G. (1995) 'Surface complexity of human neocortical astrocytic cells: changes with development, aging, and dementia.', *Journal fur Hirnforschung*, 36(4), pp. 531–7. Available at: http://www.ncbi.nlm.nih.gov/pubmed/8568224 (Accessed: 5 November 2018).

Serio, A. *et al.* (2013) 'Astrocyte pathology and the absence of non-cell autonomy in an induced pluripotent stem cell model of TDP-43 proteinopathy.', *Proceedings of the National Academy of Sciences of the United States of America*, 110(12), pp. 4697–702. doi: 10.1073/pnas.1300398110.

Shaltouki, A. *et al.* (2013) 'Efficient generation of astrocytes from human pluripotent stem cells in defined conditions', *Stem Cells*, 31(5), pp. 941–952. doi: 10.1002/stem.1334.

Shcheglovitov, A. *et al.* (2013) 'SHANK3 and IGF1 restore synaptic deficits in neurons from 22q13 deletion syndrome patients', *Nature*, 503(7475), pp. 267–71. doi: 10.1038/nature12618.

Shelton, M. K. and McCarthy, K. D. (2001) 'Hippocampal Astrocytes Exhibit Ca2+ - Elevating Muscarinic Cholinergic and Histaminergic Receptors In Situ', *Journal of Neurochemistry*. John Wiley & Sons, Ltd (10.1111), 74(2), pp. 555–563. doi: 10.1046/j.1471-4159.2000.740555.x.

Shen, W. *et al.* (2017a) 'An autocrine purinergic signaling controls astrocyte-induced neuronal excitation', *Scientific Reports*. Springer US, 7(1), pp. 1–13. doi: 10.1038/s41598-017-11793-x.

Shen, W. *et al.* (2017b) 'An autocrine purinergic signaling controls astrocyte-induced neuronal excitation', *Scientific Reports - SUPPLEMENTARY*. Nature Publishing Group, 7(1), p. 11280. doi: 10.1038/s41598-017-11793-x.

Shi, Y. *et al.* (2012a) 'Human cerebral cortex development from pluripotent stem cells to functional excitatory synapses.', *Nature neuroscience*, 15(3), pp. 477–86, S1. doi: 10.1038/nn.3041.

Shi, Y. *et al.* (2012b) 'Human cerebral cortex development from pluripotent stem cells to functional excitatory synapses', *Nature Neuroscience- SUPPLEMENTARY*, 15(3), pp. 477–486. doi: 10.1038/nn.3041.

Shi, Y., Kirwan, P. and Livesey, F. J. (2012) 'Directed differentiation of human pluripotent stem cells to cerebral cortex neurons and neural networks.', *Nature protocols*, 7(10), pp. 1836–46. doi: 10.1038/nprot.2012.116.

Sidoryk-Wegrzynowicz, M. *et al.* (2011) 'Role of astrocytes in brain function and disease.',

Toxicologic pathology. NIH Public Access, 39(1), pp. 115–23. doi: 10.1177/0192623310385254.

Simard, M. and Nedergaard, M. (2004) 'The neurobiology of glia in the context of water and ion homeostasis', *Neuroscience*, pp. 877–896. doi: 10.1016/j.neuroscience.2004.09.053.

Simeone, A. (1998) 'Otx1 and Otx2 in the development and evolution of the mammalian brain', *Embo J.* European Molecular Biology Organization, 17(23), pp. 6790–6798. doi: 10.1093/emboj/17.23.6790.

Sinnen, B. L. *et al.* (2017) 'Optogenetic control of synaptic composition and function', *Neuron*, 93(3), pp. 646–660. doi: 10.1097/COC.0b013e3182a79009.Pain.

Sloan, S. A. *et al.* (2017) 'Human Astrocyte Maturation Captured in 3D Cerebral Cortical Spheroids Derived from Pluripotent Stem Cells', *Neuron*, 95(4), pp. 779-790.e6. doi: 10.1016/j.neuron.2017.07.035.

Sloan, S. A. and Barres, B. A. (2014) 'Looks can be deceiving: reconsidering the evidence for gliotransmission.', *Neuron*. Elsevier, 84(6), pp. 1112–5. doi: 10.1016/j.neuron.2014.12.003.

Small, D. H., Mok, S. S. and Bornstein, J. C. (2001) 'Alzheimer's disease and Abeta toxicity: from top to bottom.', *Nature reviews. Neuroscience*. Nature Publishing Group, 2(8), pp. 595–8. doi: 10.1038/35086072.

Söhl, G., Maxeiner, S. and Willecke, K. (2005) 'Expression and functions of neuronal gap junctions', *Nature Reviews Neuroscience*. Nature Publishing Group, 6(3), pp. 191–200. doi: 10.1038/nrn1627.

Sontheimer, H., Black, J. A. and Waxman, S. G. (1996) 'Voltage-gated Na+ channels in gila: Properties and possible functions', *Trends in Neurosciences*, 19(8), pp. 325–331. doi: 10.1016/0166-2236(96)10039-4.

Sproul, A. A. *et al.* (2014) 'Characterization and Molecular Profiling of PSEN1 Familial Alzheimer's Disease iPSC-Derived Neural Progenitors', *PLoS ONE*. Edited by D. R. Borchelt. Public Library of Science, 9(1), p. e84547. doi: 10.1371/journal.pone.0084547.

Srikanth, P. and Young-Pearse, T. L. (2014) 'Stem cells on the brain: modeling neurodevelopmental and neurodegenerative diseases using human induced pluripotent stem cells.', *Journal of neurogenetics*. Informa Healthcare New York, 28(1–2), pp. 5–29. doi: 10.3109/01677063.2014.881358.

Staley, K. J. and Proctor, W. R. (1999) 'Modulation of mammalian dendritic GABA $_{A}$ receptor function by the kinetics of Cl^- and HCO_3^- transport', *The Journal of Physiology*. Wiley/Blackwell (10.1111), 519(3), pp. 693–712. doi: 10.1111/j.1469-7793.1999.0693n.x.

Stellwagen, D. *et al.* (2005) 'Differential regulation of AMPA receptor and GABA receptor trafficking by tumor necrosis factor-alpha.', *The Journal of neuroscience : the official journal of the Society for Neuroscience*, 25(12), pp. 3219–28. doi: 10.1523/JNEUROSCI.4486-04.2005.

Stellwagen, D. and Malenka, R. C. (2006) 'Synaptic scaling mediated by glial TNF-α', *Nature*. Nature Publishing Group, 440(7087), pp. 1054–1059. doi: 10.1038/nature04671.

Stevens, B. (2008) 'Neuron-astrocyte signaling in the development and plasticity of neural circuits.', *Neuro-Signals*, 16(4), pp. 278–88. doi: 10.1159/000123038.

Stiles, J. and Jernigan, T. L. (2010) 'The basics of brain development.', *Neuropsychology review*. Springer, 20(4), pp. 327–48. doi: 10.1007/s11065-010-9148-4.

Stout, C. E. *et al.* (2002) 'Intercellular calcium signaling in astrocytes via ATP release through connexin hemichannels.', *The Journal of biological chemistry*. American Society for Biochemistry and Molecular Biology, 277(12), pp. 10482–8. doi: 10.1074/jbc.M109902200.

Strittmatter, W. J. *et al.* (1993) 'Apolipoprotein E: high-avidity binding to beta-amyloid and increased frequency of type 4 allele in late-onset familial Alzheimer disease.', *Proceedings of the National Academy of Sciences*. National Academy of Sciences, 90(5), pp. 1977–1981. doi: 10.1073/pnas.90.5.1977.

De Strooper, B. and Karran, E. (2016) 'The Cellular Phase of Alzheimer's Disease.', *Cell*. Elsevier, 164(4), pp. 603–15. doi: 10.1016/j.cell.2015.12.056.

Sultan, S. *et al.* (2015) 'Synaptic Integration of Adult-Born Hippocampal Neurons Is Locally Controlled by Astrocytes', *Neuron*, 88(5), pp. 957–972. doi: 10.1016/j.neuron.2015.10.037.

Sutor, B. and Hagerty, T. (2005) 'Involvement of gap junctions in the development of the neocortex', *Biochimica et Biophysica Acta - Biomembranes*. Elsevier, pp. 59–68. doi: 10.1016/j.bbamem.2005.09.005.

Suzuki, I. K. and Vanderhaeghen, P. (2015) 'Is this a brain which I see before me? Modeling human neural development with pluripotent stem cells', *Development*, 142(18), pp. 3138–3150. doi: 10.1242/dev.120568.

Tabb, J. S. *et al.* (1992) 'Glutamate transport into synaptic vesicles: Roles of membrane potential, pH gradient, and intravesicular pH', *Journal of Biological Chemistry*, 267(22), pp. 15412–15418.

Taira, T. *et al.* (1993) 'Intrinsic proton modulation of excitatory transmission in rat hippocampal slices', *NeuroReport*, 4, pp. 93–96. Available at: file:///N:/Documents/Research papers/neonics/taira et al 2011.pdf.

Takahashi, D. K., Vargas, J. R. and Wilcox, K. S. (2010) 'Increased coupling and altered glutamate transport currents in astrocytes following kainic-acid-induced status epilepticus.', *Neurobiology of disease*, 40(3), pp. 573–85. doi: 10.1016/j.nbd.2010.07.018.

Takahashi, K. *et al.* (2007) 'Induction of pluripotent stem cells from adult human fibroblasts by defined factors.', *Cell*, 131(5), pp. 861–72. doi: 10.1016/j.cell.2007.11.019.

Takahashi, K. and Yamanaka, S. (2006) 'Induction of pluripotent stem cells from mouse embryonic and adult fibroblast cultures by defined factors.', *Cell*, 126(4), pp. 663–76. doi:

10.1016/j.cell.2006.07.024.

Takano, T. *et al.* (2006) 'Astrocyte-mediated control of cerebral blood flow', *Nature Neuroscience*. Nature Publishing Group, 9(2), pp. 260–267. doi: 10.1038/nn1623.

Takata, N. *et al.* (2018) 'Optogenetic astrocyte activation evokes BOLD fMRI response with oxygen consumption without neuronal activity modulation', *Glia*, 66(9), pp. 2013–2023. doi: 10.1002/glia.23454.

Takouda, J., Katada, S. and Nakashima, K. (2017) 'Emerging mechanisms underlying astrogenesis in the developing mammalian brain.', *Proceedings of the Japan Academy. Series B, Physical and biological sciences*. The Japan Academy, 93(6), pp. 386–398. doi: 10.2183/pjab.93.024.

Tanaka, K. *et al.* (2009) 'Epilepsy and Exacerbation of Brain Injury in Mice Lacking the Glutamate Transporter GLT-1 Epilepsy and Exacerbation of Brain Injury in Mice Lacking the Glutamate Transporter GLT-1', *In Situ*, 1699(1997), pp. 1699–1703. doi: 10.1126/science.276.5319.1699.

Tang, F. *et al.* (2014) 'Lactate-mediated glia-neuronal signalling in the mammalian brain', *Nature Communications*. Nature Publishing Group, 5, pp. 1–13. doi: 10.1038/ncomms4284.

Tang, X. *et al.* (2013) 'Astroglial cells regulate the developmental timeline of human neurons differentiated from induced pluripotent stem cells.', *Stem cell research*. NIH Public Access, 11(2), pp. 743–57. doi: 10.1016/j.scr.2013.05.002.

Tashiro, A. *et al.* (2015) 'Purification and Injection of Retroviral Vectors.', *Cold Spring Harbor protocols*, 2015(10), pp. 925–31. doi: 10.1101/pdb.prot086371.

Tashiro, A., Goldberg, J. and Yuste, R. (2002) 'Calcium oscillations in neocortical astrocytes under epileptiform conditions', *Journal of Neurobiology*, 50(1), pp. 45–55. doi: 10.1002/neu.10019.

Tcw, J. *et al.* (2017) 'An efficient platform for astrocyte differentiation from human induced pluripotent stem cells', *Stem Cell Reports*. ElsevierCompany., 9. doi: 10.1101/133496.

Terry, R. D. *et al.* (1991) 'Physical basis of cognitive alterations in Alzheimer's disease: synapse loss is the major correlate of cognitive impairment.', *Annals of neurology*, 30(4), pp. 572–80. doi: 10.1002/ana.410300410.

Theis, M. *et al.* (2005) 'Emerging complexities in identity and function of glial connexins', *Trends in Neurosciences*. Elsevier Current Trends, pp. 188–195. doi: 10.1016/j.tins.2005.02.006.

Theparambil, S. M. *et al.* (2014) 'The Electrogenic Sodium Bicarbonate Cotransporter NBCe1 Is a High-Affinity Bicarbonate Carrier in Cortical Astrocytes', *Journal of Neuroscience*. Society for Neuroscience, 34(4), pp. 1148–1157. doi: 10.1523/JNEUROSCI.2377-13.2014.

Thomas, L. S. *et al.* (2001) 'Glutamate release inhibiting properties of the novel mGlu5 receptor antagonist 2-methyl-6-(phenylethynyl)-pyridine (MPEP): Complementary in vitro and in vivo evidence', *Neuropharmacology*. Pergamon, 41(4), pp. 523–527. doi: 10.1016/S0028-3908(01)00091-0.

Thompson, P. M. *et al.* (2010) 'Detecting Sisease-Specific Patterns of Brain Structure Using Cortical Pattern Matching and a Population-Based Probabilistic Brain Atlas', in *Information processing in medical imaging : proceedings of the ... conference*. NIH Public Access, pp. 488–501. doi: 10.1007/3-540-45729-1_52.

Tian, G. F. *et al.* (2006) 'Imaging of cortical astrocytes using 2-photon laser scanning microscopy in the intact mouse brain', *Advanced Drug Delivery Reviews*. Elsevier, pp. 773–787. doi: 10.1016/j.addr.2006.07.001.

Tiraboschi, P. *et al.* (2004) 'Impact of APOE genotype on neuropathologic and neurochemical markers of Alzheimer disease', *Neurology*, 62(11), pp. 1977–1983. doi: 10.1212/01.WNL.0000128091.92139.0F.

Tokuda, T. *et al.* (2000) 'Lipidation of apolipoprotein E influences its isoform-specific interaction with Alzheimer's amyloid beta peptides.', *The Biochemical journal*. Portland Press Ltd, 348 Pt 2(Pt 2), pp. 359–65. Available at: http://www.ncbi.nlm.nih.gov/pubmed/10816430 (Accessed: 7 November 2018).

Trapp, S. *et al.* (1996) 'Acidosis of rat dorsal vagal neurons in situ during spontaneous and evoked activity', *Journal of Physiology*, 496(3), pp. 695–710. doi: 10.1113/jphysiol.1996.sp021720.

Traynelis, S. F. and Cull-Candy, S. G. (1990) 'Proton inhibition of N-methyl-D-aspartate receptors in cerebellar neurons', *Nature*. Nature Publishing Group, 345(6273), pp. 347–350. doi: 10.1038/345347a0.

Trommer, B. L. *et al.* (2004) 'ApoE isoform affects LTP in human targeted replacement mice', *NeuroReport*, 15(17), pp. 2655–2658. doi: 10.1097/00001756-200412030-00020.

Tukker, A. M. *et al.* (2018) 'Human iPSC-derived neuronal models for in vitro neurotoxicity assessment', *NeuroToxicology*. Elsevier, 67, pp. 215–225. doi: 10.1016/J.NEURO.2018.06.007.

Tyzack, G., Lakatos, A. and Patani, R. (2016) 'Human Stem Cell-Derived Astrocytes: Specification and Relevance for Neurological Disorders', *Current Stem Cell Reports*. Springer International Publishing, 2(3), pp. 236–247. doi: 10.1007/s40778-016-0049-1.

Tyzio, R. *et al.* (2006) 'Maternal oxytocin triggers a transient inhibitory switch in GABA signaling in the fetal brain during delivery.', *Science (New York, N.Y.)*. American Association for the Advancement of Science, 314(5806), pp. 1788–92. doi: 10.1126/science.1133212.

VanderWall, K. B. *et al.* (2019) 'Astrocytes Regulate the Development and Maturation of

Retinal Ganglion Cells Derived from Human Pluripotent Stem Cells', *Stem Cell Reports*. Elsevier, 12(2), pp. 201–212. doi: 10.1016/j.stemcr.2018.12.010.

Verkhratsky, a and Steinhäuser, C. (2000) 'Ion channels in glial cells.', *Brain research. Brain research reviews*, 32(2–3), pp. 380–412. doi: 10.1016/S0165-0173(99)00093-4.

Verkhratsky, A. (2010) 'Physiology of neuronal–glial networking', *Neurochemistry International*. Pergamon, 57(4), pp. 332–343. doi: 10.1016/J.NEUINT.2010.02.002.

Verkhratsky, A. *et al.* (2016) 'Astrocytes as secretory cells of the central nervous system: idiosyncrasies of vesicular secretion.', *The EMBO journal*. EMBO Press, 35(3), pp. 239–57. doi: 10.15252/embj.201592705.

Verkhratsky, A. *et al.* (2017) 'Astroglial calcium signalling in Alzheimer's disease', *Biochemical and Biophysical Research Communications*. Academic Press, pp. 1005–1012. doi: 10.1016/j.bbrc.2016.08.088.

Verkhratsky, A. and Nedergaard, M. (2014) 'Astroglial cradle in the life of the synapse.', *Philosophical transactions of the Royal Society of London. Series B, Biological sciences*. The Royal Society, 369(1654), p. 20130595. doi: 10.1098/rstb.2013.0595.

Verkhratsky, A. and Nedergaard, M. (2016) 'The homeostatic astroglia emerges from evolutionary specialization of neural cells', *Philosophical Transactions of the Royal Society B: Biological Sciences*. The Royal Society, p. 20150428. doi: 10.1098/rstb.2015.0428.

Verkhratsky, A., Rodríguez, J. J. and Parpura, V. (2012) 'Calcium signalling in astroglia', *Molecular and Cellular Endocrinology*. Elsevier, pp. 45–56. doi: 10.1016/j.mce.2011.08.039.

Volterra, A., Liaudet, N. and Savtchouk, I. (2014) 'Astrocyte Ca2+ signalling: An unexpected complexity', *Nature Reviews Neuroscience*. Nature Publishing Group, pp. 327–335. doi: 10.1038/nrn3725.

Volterra, A. and Meldolesi, J. (2005) 'Astrocytes, from brain glue to communication elements: the revolution continues', *Nature Reviews Neuroscience*. Nature Publishing Group, 6. doi: 10.1038/nrn1722.

Wallraff, A. *et al.* (2006) 'The Impact of Astrocytic Gap Junctional Coupling on Potassium Buffering in the Hippocampus', *Journal of Neuroscience*, 26(20), pp. 5438–5447. doi: 10.1523/JNEUROSCI.0037-06.2006.

Wang, C. *et al.* (2005) 'Human apoE4-targeted replacement mice display synaptic deficits in the absence of neuropathology', *Neurobiology of Disease*, 18(2), pp. 390–398. doi: 10.1016/j.nbd.2004.10.013.

Wang, C. *et al.* (2018) 'Gain of toxic apolipoprotein E4 effects in human iPSC-derived neurons is ameliorated by a small-molecule structure corrector', *Nature Medicine*. Nature Publishing Group, 24(5), pp. 647–657. doi: 10.1038/s41591-018-0004-z.

Wang, D. D. and Bordey, A. (2008) 'The astrocyte odyssey', *Progress in Neurobiology*. NIH

Public Access, pp. 342–367. doi: 10.1016/j.pneurobio.2008.09.015.

Wang, G. W., Randall, R. D. and Thayer, S. A. (1994) 'Glutamate-induced intracellular acidification of cultured hippocampal neurons demonstrates altered energy metabolism resulting from Ca2+ loads', *Journal of Neurophysiology*, 72(6), pp. 2563–2569. doi: 10.1016/S0161-6420(91)32313-3.

Wang, S. *et al.* (2013) 'Human iPSC-derived oligodendrocyte progenitor cells can myelinate and rescue a mouse model of congenital hypomyelination', *Cell Stem Cell*. NIH Public Access, 12(2), pp. 252–264. doi: 10.1016/j.stem.2012.12.002.

Wang, X. *et al.* (2006) 'Astrocytic Ca2+ signaling evoked by sensory stimulation in vivo', *Nature Neuroscience*. Nature Publishing Group, 9(6), pp. 816–823. doi: 10.1038/nn1703.

Watanabe, K. *et al.* (2005) 'Directed differentiation of telencephalic precursors from embryonic stem cells', *Nature Neuroscience*, 8(3), pp. 288–296. doi: 10.1038/nn1402.

Weggen, S. and Beher, D. (2012) 'Molecular consequences of amyloid precursor protein and presenilin mutations causing autosomal-dominant Alzheimer's disease', *Alzheimer's Research and Therapy*. BioMed Central, p. 9. doi: 10.1186/alzrt107.

Weick, J. P. *et al.* (2013) 'Deficits in human trisomy 21 iPSCs and neurons.', *Proceedings of the National Academy of Sciences of the United States of America*. National Academy of Sciences, 110(24), pp. 9962–7. doi: 10.1073/pnas.1216575110.

Westerlund, U. *et al.* (2003) 'Stem cells from the adult human brain develop into functional neurons in culture', *Experimental Cell Research*. Academic Press, 289(2), pp. 378–383. doi: 10.1016/S0014-4827(03)00291-X.

Wilcock, D. M., Vitek, M. P. and Colton, C. A. (2009) 'Vascular amyloid alters astrocytic water and potassium channels in mouse models and humans with Alzheimer's disease', *Neuroscience*. NIH Public Access, 159(3), pp. 1055–1069. doi: 10.1016/j.neuroscience.2009.01.023.

Wilmut, I. *et al.* (1997) 'Viable offspring derived from fetal and adult mammalian cells', *Nature*. Nature Publishing Group, 385(6619), pp. 810–813. doi: 10.1038/385810a0.

Wilson, P. G. and Stice, S. S. (2006) 'Development and differentiation of neural rosettes derived from human embryonic stem cells', *Stem Cell Reviews*. Humana Press, pp. 67–77. doi: 10.1385/SCR:2:1:67.

Wilson, S. W. and Houart, C. (2004) 'Early Steps in the Development of the Forebrain', *Developmental Cell*. Cell Press, 6(2), pp. 167–181. doi: 10.1016/S1534-5807(04)00027-9.

Wolosker, H., Balu, D. T. and Coyle, J. T. (2016) 'The Rise and Fall of the D-Serine-Mediated Gliotransmission Hypothesis', *Trends in Neurosciences*, pp. 712–721. doi: 10.1016/j.tins.2016.09.007.

Wonders, C. P. and Anderson, S. A. (2006) 'The origin and specification of cortical

interneurons.', *Nature reviews. Neuroscience*, 7(9), pp. 687–96. doi: 10.1038/nrn1954.

Xiao, Y., Tian, W. and López-Schier, H. (2015) 'Optogenetic stimulation of neuronal repair', *Current Biology*. Elsevier, 25(22), pp. R1068–R1069. doi: 10.1016/j.cub.2015.09.038.

Xue-Shan, Z. *et al.* (2016) 'Imbalanced cholesterol metabolism in Alzheimer's disease', *Clinica Chimica Acta*. Elsevier, pp. 107–114. doi: 10.1016/j.cca.2016.02.024.

Yagi, T. *et al.* (2011) 'Modeling familial Alzheimer's disease with induced pluripotent stem cells', *Human Molecular Genetics*. Oxford University Press, 20(23), pp. 4530–4539. doi: 10.1093/hmg/ddr394.

Yamashita, A. *et al.* (2014) 'Astrocytic Activation in the Anterior Cingulate Cortex is Critical for Sleep Disorder Under Neuropathic Pain', 247(February), pp. 235–247. doi: 10.1002/syn.21733.

Yang, J. *et al.* (2015) 'Na(+)-Ca(2+) exchanger mediates ChR2-induced [Ca(2+)]i elevation in astrocytes.', *Cell calcium*. doi: 10.1016/j.ceca.2015.06.008.

Yang, Y., Higashimori, H. and Morel, L. (2013) 'Developmental maturation of astrocytes and pathogenesis of neurodevelopmental disorders', *Journal of Neurodevelopmental Disorders*. BioMed Central, 5(1), p. 22. doi: 10.1186/1866-1955-5-22.

Yao, H. *et al.* (2018) 'Intracellular pH Regulation in iPSCs-derived Astrocytes from Subjects with Chronic Mountain Sickness', *Neuroscience*. Pergamon, 375, pp. 25–33. doi: 10.1016/j.neuroscience.2018.02.008.

Ye, S. *et al.* (2005) 'Apolipoprotein (apo) E4 enhances amyloid beta peptide production in cultured neuronal cells: apoE structure as a potential therapeutic target.', *Proceedings of the National Academy of Sciences of the United States of America*. National Academy of Sciences, 102(51), pp. 18700–5. doi: 10.1073/pnas.0508693102.

Yin, C. *et al.* (2012) 'Mechanical injured neurons stimulate astrocytes to express apolipoprotein E through ERK pathway.', *Neuroscience letters*, 515(1), pp. 77–81. doi: 10.1016/j.neulet.2012.03.023.

Young, L. *et al.* (2010) 'Detection of Mycoplasma in cell cultures', *Nature Protocols*. Nature Publishing Group, 5(5), pp. 929–934. doi: 10.1038/nprot.2010.43.

Youssef, S. A. *et al.* (2016) 'Pathology of the Aging Brain in Domestic and Laboratory Animals, and Animal Models of Human Neurodegenerative Diseases', *Veterinary Pathology*, 53(2), pp. 327–348. doi: 10.1177/0300985815623997.

Yu, Y.-C. *et al.* (2012) 'Preferential electrical coupling regulates neocortical lineage-dependent microcircuit assembly', *Nature*. Nature Publishing Group, 486(7401), pp. 113–117. doi: 10.1038/nature10958.

Zamanian, J. L. *et al.* (2012) 'Genomic Analysis of Reactive Astrogliosis', *Journal of Neuroscience*. NIH Public Access, 32(18), pp. 6391–6410. doi: 10.1523/JNEUROSCI.6221-

11.2012.

Zecevic, N., Hu, F. and Jakovcevski, I. (2011) 'Interneurons in the developing human neocortex.', *Developmental neurobiology*. NIH Public Access, 71(1), pp. 18–33. doi: 10.1002/dneu.20812.

Zhan, R. Z. *et al.* (1998) 'Intracellular acidification induced by membrane depolarization in rat hippocampal slices: Roles of intracellular Ca2+ and glycolysis', *Brain Research*. Elsevier, 780(1), pp. 86–94. doi: 10.1016/S0006-8993(97)01149-9.

Zhang, F. *et al.* (2007) 'Multimodal fast optical interrogation of neural circuitry', *Nature*, 446(7136), pp. 633–639. doi: 10.1038/nature05744.

Zhang, Q. *et al.* (2004) 'Fusion-related release of glutamate from astrocytes.', *The Journal of biological chemistry*. American Society for Biochemistry and Molecular Biology, 279(13), pp. 12724–33. doi: 10.1074/jbc.M312845200.

Zhang, X.-B. (2013) 'Cellular reprogramming of human peripheral blood cells.', *Genomics, proteomics & bioinformatics*. Elsevier, 11(5), pp. 264–74. doi: 10.1016/j.gpb.2013.09.001.

Zhang, Y. *et al.* (2013) 'Rapid single-step induction of functional neurons from human pluripotent stem cells.', *Neuron*, 78(5), pp. 785–98. doi: 10.1016/j.neuron.2013.05.029.

Zhang, Y. *et al.* (2016) 'Purification and Characterization of Progenitor and Mature Human Astrocytes Reveals Transcriptional and Functional Differences with Mouse', *Neuron*. Elsevier Inc., 89(1), pp. 37–53. doi: 10.1016/j.neuron.2015.11.013.

Zhao, J. *et al.* (2017) 'APOE ε4/ε4 diminishes neurotrophic function of human iPSC-derived astrocytes', *Human molecular genetics*, 26(14), pp. 2690–2700. doi: 10.1093/hmg/ddx155.

Zhou, F. M. and Hablitz, J. J. (1996) 'Postnatal development of membrane properties of layer I neurons in rat neocortex.', *The Journal of neuroscience : the official journal of the Society for Neuroscience*. Society for Neuroscience, 16(3), pp. 1131–9. doi: 10.1523/JNEUROSCI.16-03-01131.1996.

Zhou, M. and Kimelberg, H. K. (2000) 'Freshly Isolated Astrocytes From Rat Hippocampus Show Two Distinct Current Patterns and Different [K^+]$_o$ Uptake Capabilities', *Journal of Neurophysiology*, 84(6), pp. 2746–2757. doi: 10.1152/jn.2000.84.6.2746.

Zhou, M. and Kimelberg, H. K. (2001) 'Freshly isolated hippocampal CA1 astrocytes comprise two populations differing in glutamate transporter and AMPA receptor expression.', *The Journal of neuroscience : the official journal of the Society for Neuroscience*. Society for Neuroscience, 21(20), pp. 7901–8. doi: 10.1523/JNEUROSCI.21-20-07901.2001.

Ziv, O. *et al.* (2015) 'Quantitative Live Imaging of Human Embryonic Stem Cell Derived Neural Rosettes Reveals Structure-Function Dynamics Coupled to Cortical Development', *PLOS Computational Biology*. Edited by D. V. Schaffer, 11(10), p. e1004453. doi:

10.1371/journal.pcbi.1004453.

Zivelin, A. *et al.* (1997) 'Improved method for genotyping apolipoprotein E polymorphisms by a PCR-based assay simultaneously utilizing two distinct restriction enzymes.', *Clinical chemistry*, 43(9), pp. 1657–9. Available at: http://www.ncbi.nlm.nih.gov/pubmed/9299950 (Accessed: 13 August 2015).

APPENDIX A

STEMdiff™ Astrocyte Differentiation Kit and

STEMdiff™ Astrocyte Maturation Kit

Catalog #08540 1 Kit

Catalog #08550

STEMCELL™ TECHNOLOGIES
Scientists Helping Scientists™ | WWW.STEMCELL.COM
TOLL FREE PHONE 1 800 667 0322 • PHONE +1 604 877 0713
INFO@STEMCELL.COM • TECHSUPPORT@STEMCELL.COM
FOR GLOBAL CONTACT DETAILS VISIT OUR WEBSITE

Product Description

The STEMdiff™ Astrocyte Differentiation Kit (Catalog #08540) is used to rapidly and efficiently generate astrocytic precursors from neural progenitor cells (NPCs) derived from human pluripotent stem cells (hPSCs) using the STEMdiff™ Neural Induction Medium (Catalog #05835) embryoid body protocol. The astrocytic precursors generated can be matured using the STEMdiff™ Astrocyte Maturation Kit (Catalog #08550) to produce a highly pure population of astrocytes (> 85% GFAP-positive astrocytes; < 15% class III β-tubulin-positive neurons). Cells derived using these products are versatile tools for modeling human neurological development and disease, drug screening, toxicity testing, and cell therapy validation.

Product Information

The following components are sold as part of a complete kit (Catalog #08540 or Catalog #08550) and are not available for individual sale.

COMPONENT NAME	COMPONENT #	SIZE	STORAGE	SHELF LIFE
STEMdiff™ Astrocyte Differentiation Kit (Catalog #08540)				
STEMdiff™ Astrocyte Differentiation Basal Medium	08541	100 mL	Store at 2 - 8°C.	Stable until expiry date (EXP) on label.
STEMdiff™ Astrocyte Differentiation Supplement A	08542	8 mL	Store at 2 - 8°C.	Stable until expiry date (EXP) on label.
STEMdiff™ Astrocyte Differentiation Supplement B	08543	2 mL	Store at -20°C.	Stable until expiry date (EXP) on label.
STEMdiff™ Astrocyte Differentiation Supplement C	08544	100 µL	Store at -20°C.	Stable until expiry date (EXP) on label.
STEMdiff™ Astrocyte Maturation Kit (Catalog #08550)				
STEMdiff™ Astrocyte Maturation Basal Medium	08551	100 mL	Store at 2 - 8°C.	Stable until expiry date (EXP) on label.
STEMdiff™ Astrocyte Maturation Supplement A	08552	9 mL	Store at 2 - 8°C.	Stable until expiry date (EXP) on label.
STEMdiff™ Astrocyte Maturation Supplement B	08553	2 mL	Store at -20°C.	Stable until expiry date (EXP) on label.
STEMdiff™ Astrocyte Maturation Supplement C	08554	100 µL	Store at -20°C.	Stable until expiry date (EXP) on label.

Materials Required But Not Included

PRODUCT NAME	CATALOG #
Corning® Matrigel® hESC-qualified Matrix	354277
DMEM/F-12 with 15 mM HEPES	36254
ACCUTASE™	07920
STEMdiff™ Neural Rosette Selection Reagent	05832

Astrocyte Differentiation and Maturation Protocol

Generation of astrocytes from NPCs requires both the STEMdiff™ Astrocyte Differentiation Kit (Catalog #08540) and the STEMdiff™ Astrocyte Maturation Kit (Catalog #08550). The procedure integrates into the STEMdiff™ Neural Induction Medium (Catalog #05835) embryoid body protocol after rosette selection, as depicted below.

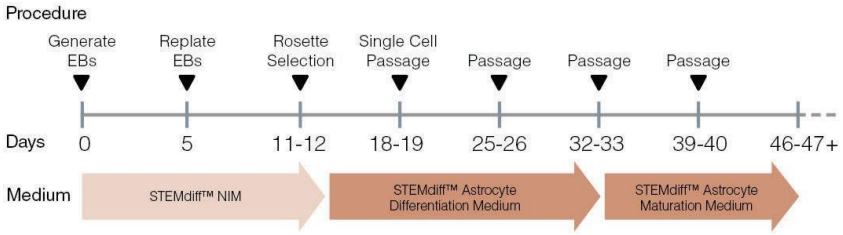

EBs: Embryoid Bodies; STEMdiff™ NIM: STEMdiff™ Neural Induction Medium

Preparation of Reagents and Materials

A. COATING CELL CULTURE VESSELS WITH CORNING® MATRIGEL®

Corning® Matrigel® hESC-qualified Matrix should be aliquoted and frozen. Consult the Certificate of Analysis supplied with the Corning® Matrigel® for the recommended aliquot size ("Dilution Factor") to make up 24 mL of diluted matrix. Make sure to always keep Corning® Matrigel® on ice when thawing and handling to prevent it from gelling.

NOTE: Use tissue culture-treated cultureware.

1. Thaw one aliquot of Corning® Matrigel® on ice.
2. Dispense 24 mL of cold DMEM/F-12 into a 50 mL conical tube and keep on ice.
3. Add thawed Corning® Matrigel® to the cold DMEM/F-12 (in the 50 mL tube) and mix well. The vial may be washed with cold medium if desired.
4. Immediately use the diluted Corning® Matrigel® solution to coat tissue culture-treated cultureware. See Table 1 for recommended coating volumes.
5. Swirl the cultureware to spread the Corning® Matrigel® solution evenly across the surface.

   NOTE: If the surface of the cultureware is not fully coated by the Corning® Matrigel® solution, it should not be used.
6. Incubate at room temperature (15 - 25°C) for at least 1 hour before use. Do not let the Corning® Matrigel® solution evaporate.

   NOTE: If not used immediately, the cultureware must be sealed to prevent evaporation of the Corning® Matrigel® solution (e.g. with Parafilm®) and can be stored at 2 - 8°C for up to 1 week after coating. Allow stored coated cultureware to come to room temperature (15 - 25°C) for 30 minutes before moving onto the next step.
7. Immediately prior to seeding cells, gently tilt the cultureware onto one side and allow the excess Corning® Matrigel® solution to collect at the edge. Remove the excess Corning® Matrigel® solution using a serological pipette or by aspiration. Ensure that the coated surface is not scratched.

Table 1: Recommended Volumes for Coating Cultureware

VESSEL	APPROXIMATE SURFACE AREA	VOLUME OF CORNING® MATRIGEL®
96-well plate	0.33 cm^2/well	50 µL/well
4- or 24-well plate	2 cm^2/well	250 µL/well
35 mm dish	10 cm^2	1.5 mL
60 mm dish	20 cm^2	2.5 mL

B. PREPARATION OF COMPLETE STEMdiff™ ASTROCYTE DIFFERENTIATION MEDIUM

Use sterile techniques to prepare complete STEMdiff™ Astrocyte Differentiation Medium (Differentiation Basal Medium + Differentiation Supplement A + Differentiation Supplement B + Differentiation Supplement C). The following example is for preparing 100 mL of complete medium. For other volumes, adjust accordingly.

1. Thaw Supplement B and Supplement C at room temperature (15 - 25°C) or at 2 - 8°C overnight. Mix thoroughly.

2. Add 8 mL of Supplement A, 2 mL of Supplement B, and 100 µL of Supplement C to 100 mL of Basal Medium. Mix thoroughly.

   NOTE: If not used immediately, store complete STEMdiff™ Astrocyte Differentiation Medium at 2 - 8°C for up to 10 days. Pre-warm complete medium to 37°C before use.

C. PREPARATION OF COMPLETE STEMdiff™ ASTROCYTE MATURATION MEDIUM

Use sterile techniques to prepare complete STEMdiff™ Astrocyte Maturation Medium (Maturation Basal Medium + Maturation Supplement A + Maturation Supplement B + Maturation Supplement C). The following example is for preparing 100 mL of complete medium. For other volumes, adjust accordingly.

1. Thaw Supplement B and Supplement C at room temperature (15 - 25°C) or at 2 - 8°C overnight. Mix thoroughly.
2. Add 9 mL of Supplement A, 2 mL of Supplement B, and 100 µL of Supplement C to 100 mL of Basal Medium. Mix thoroughly.

   NOTE: If not used immediately, store complete STEMdiff™ Astrocyte Maturation Medium at 2 - 8°C for up to 1 week. Pre-warm complete medium to 37°C before use.

Directions for Use

Please read the entire protocol before proceeding. Use sterile techniques when performing the following protocols.

A. GENERATION OF ASTROCYTE PRECURSORS

For a detailed protocol for generating central nervous system (CNS)-type NPCs using embryoid body (EB) formation with the AggreWell™800 plate (Catalog #27865), refer to the Technical Manual: Generation and Culture of Neural Progenitor Cells Using the STEMdiff™ Neural System (Document #28782), available on our website at www.stemcell.com or contact us to request a copy.

The following instructions are for a single well of a 6-well plate. For other cultureware adjust volume accordingly.

1. At day 11 - 12 after EB formation, place selected neural rosettes into an appropriate culture vessel in 2 mL of STEMdiff™ Neural Induction Medium. Incubate at 37°C and 5% CO_2.
2. One day after rosette replating (day 12 - 13 from EB formation), replace medium with 2 mL complete STEMdiff™ Astrocyte Differentiation Medium. Incubate at 37°C.
3. Perform daily full medium changes with pre-warmed (37°C) complete STEMdiff™ Astrocyte Differentiation Medium. Incubate at 37°C and 5% CO_2.
4. At day 18 - 19 from EB formation, cells will be approximately 80 - 90% confluent and will be ready to passage.

B. PASSAGING ASTROCYTE PRECURSORS

The following instructions are for a single well of a 6-well plate. For other cultureware adjust volumes accordingly.

1. Aspirate STEMdiff™ Astrocyte Differentiation Medium and add 1 mL ACCUTASE™.
2. Incubate at 37°C and 5% CO_2 for 5 - 10 minutes.
3. Add 5 mL DMEM/F-12 and wash cells off the vessel.
4. Centrifuge cell suspension at 400 x *g* for 5 minutes and remove supernatant.
5. Resuspend cells in suitable volume of complete STEMdiff™ Astrocyte Differentiation Medium (e.g. 5 mL) and perform a cell count.
6. Seed cells onto Matrigel®-coated vessels at a density of 1 x 10^5 cells/cm^2.
7. Incubate at 37°C and 5% CO_2, changing medium every other day.
8. In 5 - 7 days from replating (25 - 27 days from EB formation) cells will be approximately 80 - 90% confluent. Passage cells according to section B steps 1 - 6, seeding cells onto new Matrigel®-coated vessels at a density of 1.5 x 10^5 cells/cm^2. Incubate at 37°C and 5% CO_2.
9. Repeat passage (section B steps 1 - 6) one more time prior to switching to STEMdiff™ Astrocyte Maturation Medium (section C).

C. ASTROCYTE MATURATION

When cells have been passaged twice (approximately day 32 - 33) in STEMdiff™ Astrocyte Differentiation Medium, prepare STEMdiff™ Astrocyte Maturation Medium and passage cells as described below.

The following instructions are for a single well of a 6-well plate. For other cultureware adjust volumes accordingly.

1. Aspirate STEMdiff™ Astrocyte Differentiation Medium and add 1 mL ACCUTASE™.
2. Incubate at 37°C and 5% CO_2 for 5 - 10 minutes.
3. Add 5 mL of DMEM/F-12 and wash cells off the well.
4. Centrifuge cell suspension at 400 x *g* for 5 minutes and remove supernatant.
5. Resuspend cells in a suitable volume of complete STEMdiff™ Astrocyte Maturation Medium (e.g. 5 mL) and perform a cell count.
6. Seed cells onto Corning® Matrigel®-coated vessels at a density of 1.5 x 10^5 cells/cm^2.
7. Incubate at 37°C and 5% CO_2. Change medium every other day.
8. In 5 - 7 days (day 37 - 40) cells will be approximately 80 - 90% confluent. Passage cells according to section C steps 1 - 6 and seed cells onto new Matrigel®-coated vessels at a density of 1.5 x 10^5 cells/cm^2. After two passages in STEMdiff™ Astrocyte Maturation Medium, mature astrocytes (GFAP+) will be observed.

   NOTE: Recommended seeding densities range from 1.5 x 10^5 cells/cm^2 to 2 x 10^5 cells/cm^2. If astrocytes are to be used for immunocytochemistry, a lower seeding density at day 46 is recommended, ranging from 5 x 10^4 cells/cm^2 to 1 x 10^5 cells/cm^2.

Appendix B

Quick-Start Protocol April 2016

MinElute® PCR Purification Kit

The MinElute PCR Purification Kit (cat. nos. 28004 and 28006) can be stored at room temperature (15–25°C) for up to 12 months if not otherwise stated on label. Store spin columns at 2–8°C upon arrival.

Further information

- *MinElute Handbook*: **www.qiagen.com/HB-2069**
- Safety Data Sheets: **www.qiagen.com/safety**
- Technical assistance: **support.qiagen.com**

Notes before starting

- This protocol is for cleanup of up to 5 µg PCR product (70 bp to 4 kb).
- Add ethanol (96–100%) to Buffer PE concentrate before use (see bottle label for volume).
- All centrifugation steps are carried out at 17,900 x *g* (13,000 rpm) in a conventional tabletop microcentrifuge at room temperature (15–25°C).
- Add 1:250 volume pH indicator I to Buffer PB. Add pH indicator I to the entire buffer contents. Do not add pH indicator I to buffer aliquots. The yellow color of Buffer PB with pH indicator I indicates a pH of ≤7.5. The adsorption of DNA to the membrane is efficient only at pH ≤7.5.

  Note: If the purified PCR product is to be used in sensitive microarray applications, it may be beneficial to use Buffer PB without addition of pH indicator I.
- Symbols: centrifuge processing; vacuum processing.

Sample to Insight

QIAGEN

1. Add 5 volumes of Buffer PB to 1 volume of the PCR reaction and mix. Check that the color of the mixture is yellow (similar to Buffer PB without the PCR sample). If the color of the mixture is orange or violet, add 10 µl 3 M sodium acetate, pH 5.0, and mix. The color of the mixture will turn to yellow.
2. Place a MinElute column in a provided 2 ml collection tube or into a vacuum manifold. See the *MinElute Handbook* for details on how to set up a vacuum manifold.
3. Apply the sample to the MinElute column and centrifuge for 1 min or apply vacuum until the entire sample has passed through the column. Discard flow-through and place the MinElute column back into the same collection tube.
4. Add 750 µl Buffer PE to the MinElute column and centrifuge for 1 min or apply vacuum. Discard flow-through and place the MinElute column back in the same collection tube.
5. Centrifuge the column in a 2 ml collection tube (provided) for 1 min. Residual ethanol from Buffer PE will not be completely removed unless the flow-through is discarded before this additional centrifugation.
6. Place each MinElute column in a clean 1.5 ml microcentrifuge tube.
7. To elute DNA, add 10 µl Buffer EB (10 mM Tris·Cl, pH 8.5) or water to the center of the MinElute membrane. (Ensure that the elution buffer is dispensed directly onto the center of the membrane for complete elution of bound DNA.) Let the column stand for 1 min, and then centrifuge the column for 1 min.
8. If the purified DNA is to be analyzed on a gel, add 1 volume of Loading Dye to 5 volumes of purified DNA. Mix the solution by pipetting up and down before loading the gel.

For up-to-date licensing information and product-specific disclaimers, see the respective QIAGEN kit handbook or user manual.
Scan QR code for handbook.

APPENDIX C

Optimizing Restriction Endonuclease Reactions

Protocols.io also provides an interactive version of this protocol where you can discover and share optimizations with the research community.

https://www.neb.com/protocols/2012/12/07/optimizing-restriction-endonuclease-reactions

There are several key factors to consider when setting up a restriction endonuclease digest. Using the proper amounts of DNA, enzyme and buffer components in the correct reaction volume will allow you to achieve optimal digestion. By definition, 1 unit of restriction enzyme will completely digest 1 µg of substrate DNA in a 50 µl reaction in 60 minutes. This enzyme : DNA : reaction volume ratio can be used as a guide when designing reactions.
However, most researchers follow the "typical" reaction conditions listed, where a 5–10 fold overdigestion is recommended to overcome variability in DNA source, quantity and purity. NEB offers the following tips to help you to achieve maximal success in your restriction endonuclease reactions.

A "Typical" Restriction Digest

Restriction Enzyme	10 units is sufficient, generally 1 µl is used
DNA	1 µg
10X NEBuffer	5 µl (1X)
Total Reaction Volume 50 µl Incubation Time	
	1 hour*
Incubation Temperature Enzyme dependent	

* Can be decreased to 5-15 minutes by using a Time-Saver™ Qualified enzyme.

Enzyme

- Keep on ice when not in the freezer
- Should be the last component added to reaction
- Mix components by pipetting the reaction mixture up and down, or by "flicking" the reaction tube. Follow with a quick ("touch") spin-down in a microcentrifuge. Do not vortex the reaction.
- In general, we recommend 5–10 units of enzyme per µg DNA, and 10–20 units for genomic DNA in a 1 hour digest.
- NEB has introduced a line of High-Fidelity (HF®) enzymes that provide added flexibility to reaction setup.

DNA

- Should be free of contaminants such as phenol, chloroform, alcohol, EDTA, detergents or excessive salts. Extra wash steps during purification are recommended.
- Methylation of DNA can inhibit digestion with certain enzymes. For more information about methylation, Effect of CpG Methylation on Restriction Enzyme Cleavage and Dam and Dcm Methylases of *E.coli*

Buffer

- Use at a 1X concentration
- Supplement with SAM (S-Adenosyl methionine) to the recommended concentration if required.

Reaction Volume

- A 50 µl reaction volume is recommended for digestion of 1 µg of substrate
- Enzyme volume should not exceed 10% of the total reaction volume to prevent star activity due to excess glycerol
- Additives in the restriction enzyme storage buffer (e.g., glycerol, salt) as well as contaminants found in the substrate solution (e.g., salt, EDTA, or alcohol) can be problematic in smaller reaction volumes. The following guidelines can be used for techniques that require smaller reaction volumes.

Restriction Enzyme* DNA 10X NEBuffer

10 µl rxn**	1 unit	0.1 µg 1 µl
25 µl rxn	5 units	0.5 µg 2.5 µl
50 µl rxn	10 units	1 µg 5 µl

- * Restriction Enzymes can be diluted using the recommended diluent buffer when smaller amounts are needed.
  ** 10 µl rxns should not be incubated for longer than 1 hour to avoid evaporation.

Incubation Time

- Incubation time is typically 1 hour
- Can often be decreased by using an excess of enzyme, or by using one of our Time-Saver Qualified enzymes.
- It is possible, with many enzymes, to use fewer units and digest for up to 16 hours. For more information, visit Extended Digests with Restriction Endonucleases.

Stopping a Reaction

If no further manipulation of DNA is required:

- Terminate with a stop solution (10 µl per 50 µl rxn) [1x: 2.5% Ficoll®-400, 10mM EDTA, 3.3mM Tris-Hcl, 0.08% SDS, 0.02% Dye 1, 0.001% Dye 2, pH 8.0@25°C] (e.g., NEB #B7024)

When further manipulation of DNA is required:

- Heat inactivation can be used
- Remove enzyme by using a spin column (NEB #T1030) or phenol/chloroform extraction

Storage

- Storage at -20°C is recommended for most restriction enzymes. For a few enzymes, storage at -80°C is recommended for periods longer than 30 days. Please refer to the enzyme's technical data sheet or catalog entry for storage information.
- 10X NEBuffers should also be stored at -20°C

Stability

- All enzymes are assayed for activity every 4 months. The expiration date is found on the label.
- Exposure to temperatures above -20°C should be minimized whenever possible

Control Reactions

If you are having difficulty cleaving your DNA substrate, we recommend the following control reactions:

- Control DNA (DNA with multiple known sites for the enzyme, e.g. lambda or adenovirus-2 DNA) with restriction enzyme to test enzyme viability
- If the control DNA is cleaved and the experimental DNA resists cleavage, the two DNAs can be mixed to determine if an inhibitor is present in the experimental sample. If an inhibitor (often salt, EDTA or phenol) is present, the control DNA will not cut after mixing.

Digestion with HaeII and AflIII

					% Activity in NEBuffer			
Name	**Cat#**	**Temp°C**	**Supplied Buffer**	**Add SAM**	**1.1**	**2.1**	**3.1**	**CutSmart ®**
AflIII	R0541	37	NEBuffer 3.1	No	10	50	100	50
HaeII	R0107	37	CutSmart Buffer	No	25	100	10	100

Recommended digest in CutSmart Buffer

Name	Time-Saver ™	Heat Inactivation (°C)	Methylation Sensitivity
AflIII	No	80	None
HaeII	Yes	80	cpg (Blocked)

Notes:

1. Digest in CutSmart Buffer (or NEBuffer 4 + BSA) at 37 °C.
2. At least one enzyme has < 100% activity in this buffer, so additional units of enzyme and/or longer incubation time may be necessary.

Appendix D

INSTRUCTIONS

Thermo

Pierce™ BCA Protein Assay Kit

23225 23227

Number	Description
23225	**Pierce BCA Protein Assay Kit**, sufficient reagents for 500 test-tube or 5000 microplate assays
23227	**Pierce BCA Protein Assay Kit**, sufficient reagents for 250 test-tube or 2500 microplate

Assays

Kit Contents:

BCA Reagent A, 1000mL (in Product No. 23225) or 500mL (in Product No. 23227), containing sodium carbonate, sodium bicarbonate, bicinchoninic acid and sodium tartrate in 0.1M sodium hydroxide

BCA Reagent B, 25mL, containing 4% cupric sulfate

Albumin Standard Ampules, 2mg/mL, 10 ξ 1mL ampules, containing bovine serum albumin (BSA) at 2mg/mL in 0.9% saline and 0.05% sodium azide

Storage: Upon receipt store at room temperature. Product shipped at ambient temperature.

Note: If either Reagent A or Reagent B precipitates upon shipping in cold weather or during long-term storage, dissolve precipitates by gently warming and stirring solution. Discard any kit reagent that shows discoloration or evidence of microbial contamination.

Table of Contents

1296.9

Introduction

The Thermo Scientific™ Pierce™ BCA Protein Assay is a detergent-compatible formulation based on bicinchoninic acid (BCA) for the colorimetric detection and quantitation of total protein. This method combines the well-known reduction of Cu^{+2} to Cu^{+1} by protein in an alkaline medium (the biuret reaction) with the highly sensitive and selective colorimetric detection of the cuprous cation (Cu^{+1}) using a unique reagent containing bicinchoninic acid.[1] The purple-colored reaction product of this assay is formed by the chelation of two molecules of BCA with one cuprous ion. This water-soluble complex exhibits a strong absorbance at 562nm that is nearly linear with increasing protein concentrations over a broad working range (20-2000μg/mL). The BCA method is not a true end-point method; that is, the final color continues to develop. However, following incubation, the rate of continued color development is sufficiently slow to allow large numbers of samples to be assayed together.

The macromolecular structure of protein, the number of peptide bonds and the presence of four particular amino acids (cysteine, cystine, tryptophan and tyrosine) are reported to be responsible for color formation with BCA.[2] Studies with di-, tri- and tetrapeptides suggest that the extent of color formation caused by more than the mere sum of individual color- producing functional groups.[2] Accordingly, protein concentrations generally are determined and reported with reference to standards of a common protein such as bovine serum albumin (BSA). A

series of dilutions of known concentration are prepared from the protein and assayed alongside the unknown(s) before the concentration of each unknown is determined based on the standard curve. If precise quantitation of an unknown protein is required, it is advisable to select a protein

standard that is similar in quality to the unknown; for example, a bovine gamma globulin (BGG) standard (see Related Thermo Scientific Products) may be used when assaying immunoglobulin samples.

Two assay procedures are presented. Of these, the Test Tube Procedure requires a larger volume (0.1mL) of protein sample; however, because it uses a sample to working reagent ratio of 1:20 (v/v), the effect of interfering substances is minimized. The Microplate Procedure affords the sample handling ease of a microplate and requires a smaller volume (10-25□L) of protein sample; however, because the sample to working reagent ratio is 1:8 (v/v), it offers less flexibility in overcoming interfering substance concentrations and obtaining low levels of detection.

Preparation of Standards and Working Reagent (required for both assay procedures)

Preparation of Diluted Albumin (BSA) Standards

Use Table 1 as a guide to prepare a set of protein standards. Dilute the contents of one Albumin Standard (BSA) ampule into several clean vials, preferably using the same diluent as the sample(s). Each 1mL ampule of 2mg/mL Albumin Standard is sufficient to prepare a set of diluted standards for either working range suggested in Table 1. There will be sufficient volume for three replications of each diluted standard.

Table 1. Preparation of Diluted Albumin (BSA) Standards

Dilution Scheme for Standard Test Tube Protocol and Microplate Procedure (Working Range = 20-2,000□g/mL)

Vial	Volume of Diluent (□L)	Volume and Source of BSA (□L)	Final BSA Concentration (□g/mL)
A	0	300 of Stock	2000
B	125	375 of Stock	1500
C	325	325 of Stock	1000
D	175	175 of vial B dilution	750
E	325	325 of vial C dilution	500
F	325	325 of vial E dilution	250
G	325	325 of vial F dilution	125
H	400	100 of vial G dilution	25
I	400	0	0 = Blank

Dilution Scheme for Enhanced Test Tube Protocol (Working Range = 5–250□g/mL)

Vial	Volume of Diluent (□L)	Volume and Source of BSA (□L)	Final BSA Concentration (□g/mL)
A	700	100 of Stock	250
B	400	400 of vial A dilution	125
C	450	300 of vial B dilution	50
D	400	400 of vial C dilution	25
E	400	100 of vial D dilution	5
F	400	0	0 = Blank

Preparation of the BCA Working Reagent (WR)

1. Use the following formula to determine the total volume of WR required:

(# standards + # unknowns) □ (# replicates) □ (volume of WR per sample) = total volume WR required Example: for the standard test-tube procedure with 3 unknowns and 2 replicates of each sample:

(9 standards + 3 unknowns) □ (2 replicates) □ (2mL) = 48mL WR required

Note: 2.0mL of the WR is required for each sample in the test-tube procedure, while only 200 µl of WR reagent is required for each sample in the microplate procedure.

2. Prepare WR by mixing 50 parts of BCA Reagent A with 1 part of BCA Reagent B (50:1, Reagent A:B). For the above example, combine 50mL of Reagent A with 1mL of Reagent B.

Note: When Reagent B is first added to Reagent A, turbidity is observed that quickly disappears upon mixing to yield a clear, green WR. Prepare sufficient volume of WR based on the number of samples to be assayed. The WR is stable for several days when stored in a closed container at room temperature (RT).

Procedure Summary (Test-tube Procedure, Standard Protocol)

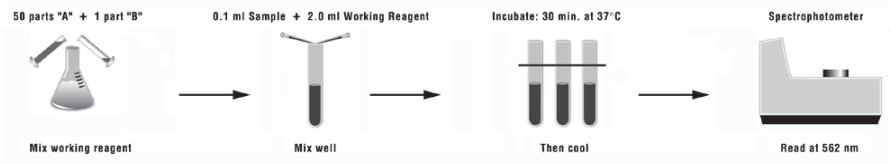

Test-tube Procedure (Sample to WR ratio = 1:20)

1. Pipette 0.1mL of each standard and unknown sample replicate into an appropriately labeled test tube.
2. Add 2.0mL of the WR to each tube and mix well.
3. Cover and incubate tubes at selected temperature and time:
   - Standard Protocol: 37°C for 30 minutes (working range = 20-2000□g/mL)
   - RT Protocol: RT for 2 hours (working range = 20-2000□g/mL)
   - Enhanced Protocol: 60°C for 30 minutes (working range = 5-250□g/mL)

Notes:

- Increasing the incubation time or temperature increases the net 562nm absorbance for each test and decreases both the minimum detection level of the reagent and the working range of the protocol.
- Use a water bath to heat tubes for either Standard (37°C incubation) or Enhanced (60°C incubation) Protocol. Using a forced-air incubator can introduce significant error in color development because of uneven heat transfer.

4. Cool all tubes to RT.
5. With the spectrophotometer set to 562nm, zero the instrument on a cuvette filled only with water. Subsequently, measure the absorbance of all the samples within 10 minutes.

Note: Because the BCA assay does not reach a true end point, color development will continue even after cooling to RT. However, because the rate of color development is low at RT, no significant error will be introduced if the 562nm absorbance measurements of all tubes are made within 10 minutes of each other.

6. Subtract the average 562nm absorbance measurement of the Blank standard replicates from the 562nm absorbance measurement of all other individual standard and unknown sample replicates.
7. Prepare a standard curve by plotting the average Blank-corrected 562nm measurement for each BSA standard vs. its concentration in µg/mL. Use the standard curve to determine the protein concentration of each unknown sample.

Microplate Procedure (Sample to WR ratio = 1:8)

1. Pipette 25□L of each standard or unknown sample replicate into a microplate well (working range = 20-2000□g/mL) (e.g., Thermo Scientific™ Pierce™ 96-Well Plates, Product No. 15041).

Note: If sample size is limited, 10□L of each unknown sample and standard can be used (sample to WR ratio = 1:20). However, the working range of the assay in this case will be limited to 125-2000□g/mL.

2. Add 200□L of the WR to each well and mix plate thoroughly on a plate shaker for 30 seconds.
3. Cover plate and incubate at 37°C for 30 minutes.
4. Cool plate to RT. Measure the absorbance at or near 562nm on a plate reader.

Notes:

- Wavelengths from 540-590nm have been used successfully with this method.
- Because plate readers use a shorter light path length than cuvette spectrophotometers, the Microplate Procedure requires a greater sample to WR ratio to obtain the same sensitivity as the standard Test Tube Procedure. If higher 562nm measurements are desired, increase the incubation time to 2 hours.
- Increasing the incubation time or ratio of sample volume to WR increases the net 562nm measurement for each well and lowers both the minimum detection level of the reagent and the working range of the assay. As long as all standards and unknowns are treated identically, such modifications may be useful

5. Subtract the average 562nm absorbance measurement of the Blank standard replicates from the 562nm measurements of all

other individual standard and unknown sample replicates.

6. Prepare a standard curve by plotting the average Blank-corrected 562nm measurement for each BSA standard vs. its concentration in µg/mL. Use the standard curve to determine the protein concentration of each unknown sample.

Note: If using curve-fitting algorithms associated with a microplate reader, a four-parameter (quadratic) or best-fit curve will provide more accurate results than a purely linear fit. If plotting results by hand, a point-to-point curve is preferable to a linear fit to the standard points.

Troubleshooting

Problem	Possible Cause	Solution
No color in any tubes	Sample contains a copper chelating agent	Dialyze, desalt or dilute sample Increase copper concentration in working reagent (e.g., use 50:2, Reagent A:B) Remove interfering substances from sample using Product No. 23215
Blank absorbance is OK, but standards and samples show less color than expected	Strong acid or alkaline buffer, alters working reagent pH	Dialyze, desalt, or dilute sample
	Color measured at the wrong wavelength	Measure the absorbance at 562nm
Color of samples appears darker than expected	Protein concentration is too high	Dilute sample
	Sample contains lipids or lipoproteins	Add 2% SDS to the sample to eliminate interference from lipids[3]
		Remove interfering substances from sample using Product No. 23215
All tubes (including blank) are dark purple	Buffer contains a reducing agent	Dialyze or dilute sample
	Buffer contains a thiol	Remove interfering substances from sample using Product No. 23215
	Buffer contains biogenic amines (catecholamines)	
Need to measure color at a different wavelength	Spectrophotometer or plate reader does not have 562nm filter	Color may be measure at any wavelength between 540nm and 590nm, although the slope of standard curve and overall assay sensitivity will be reduced

Interfering substances

Certain substances are known to interfere with the BCA assay including those with reducing potential, chelating agents, and strong acids or bases. Because they are known to interfere with protein estimation at even minute concentrations, avoid the following substances as components of the sample buffer:

Ascorbic acid	EGTA	Iron	Impure sucrose
Catecholamines	Impure glycerol	Lipids	Tryptophan
Creatinine	Hydrogen peroxide	Melibiose	Tyrosine
Cysteine	Hydrazides	Phenol Red	Uric acid

Other substances interfere to a lesser extent with protein estimation using the BCA assay, and these have only minor (tolerable) effects below a certain concentration in the original sample. Maximum compatible concentrations for many substances in the Standard Test Tube Protocol are listed in Table 2 (see last page of Instructions). Substances were compatible at the indicated concentration in the Standard Test Tube Protocol if the error in protein concentration estimation caused by the presence of the substance was less than or equal to 10%. The substances were tested using WR prepared immediately before each experiment. Blank-corrected 562nm absorbance measurements (for a 1000µg/mL BSA standard + substance) were compared to the net 562nm measurements of the same standard prepared in 0.9% saline. Maximum compatible concentrations will be lower In the Microplate Procedure where the sample to WR ratio is 1:8 (v/v).

Furthermore, it is possible to have a substance additive affect such that even though a single component is present at a concentration below its listed compatibility, a sample buffer containing a combination of substances could interfere with the assay.

Strategies for eliminating or minimizing the effects of interfering substances

The effects of interfering substances in the Pierce BCA Protein Assay may be eliminated or overcome by one of several methods.

- Remove the interfering substance by dialysis or gel filtration.
- Dilute the sample until the substance no longer interferes. This strategy is effective only if the starting protein concentration is sufficient to remain in the working range of the assay upon dilution.
- Precipitate the proteins in the sample with acetone or trichloroacetic acid (TCA). The liquid containing the substance that interfered is discarded and the protein pellet is easily solubilized in ultrapure water or directly in the alkaline BCA WR.[4] A protocol detailing this procedure is available from our website. Alternatively, Product No. 23215 may be used (see Related

Thermo Scientific Products).

- Increase the amount of copper in the WR (prepare WR as 50:2 or 50:3, Reagent A:B), which may eliminate interference by copper-chelating agents.

Note: For greatest accuracy, the protein standards must be treated identically to the sample(s).

Related Thermo Scientific Products

15041	**Pierce 96-Well Plates,** 100/pkg.
15075	**Reagent Reservoirs,** 200/pkg.
15036	**Sealing Tape for 96-Well Plates,** 100/pkg.
23209	**Albumin Standard Ampules, 2mg/mL**, 10 □ 1mL ampules, containing bovine serum albumin (BSA)
23208	**Pre-Diluted Protein Assay Standards: Bovine Serum Albumin (BSA) Set**, 7 □ 3.5mL
23212	**Bovine Gamma Globulin Standard, 2mg/mL**, 10 □ 1mL ampules
23213	**Pre-Diluted Protein Assay Standards**, (BGG) Set, 7 □ 3.5mL aliquots
23235	**Pierce Micro BCA Protein Assay Kit**, working range of 0.5-20□g/mL
23236	**Coomassie Plus™ (Bradford) Assay Kit**, working range of 1-1500□g/mL
23215	**Compat-Able™ Protein Assay Preparation Reagent Set**
23250	**Pierce BCA Protein Assay Kit□Reducing Agent Compatible**

Additional Information

Please visit our website for additional information including the following items:

- Tech Tip #8: Eliminate interfering substances from samples for BCA Protein Assay

Alternative Total Protein Assay Reagents

If interference by a reducing substance or metal-chelating substance contained in the sample cannot be overcome, try the Thermo Scientific Coomassie Plus (Bradford) Assay Kit (Product No. 23236), which is less sensitive to such substances.

Cleaning and Re-using Glassware

Exercise care when re-using glassware. All glassware must be cleaned and given a thorough final rinse with ultrapure water.

Response characteristics for different proteins

Each of the commonly used total protein assay methods exhibits some degree of varying response toward different proteins. These differences relate to amino acid sequence, pI, structure and the presence of certain side chains or prosthetic groups that can dramatically alter the protein's color response. Most protein assay methods use BSA or immunoglobulin (IgG) as the standard against which the concentration of protein in the sample is determined (Figure 1). However, if great accuracy is required, prepare the standard curve from a pure sample of the target protein. Typical protein-to-protein variation in color response is listed in Table 3. All proteins were tested at 1000□g/mL using the 30-minute/37°C Test Tube Protocol. The average net color response for BSA was normalized to 1.00 and the average net color response of the other proteins is expressed as a ratio to the response of BSA.

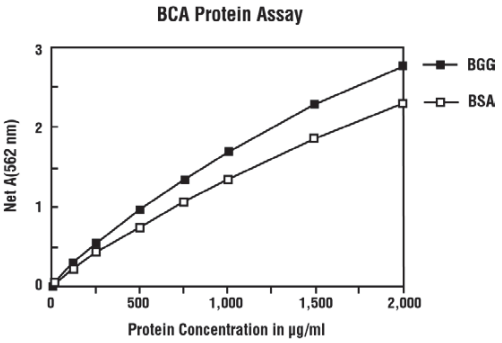

Figure 1: Typical color response curves for BSA and BGG using the Standard Test Tube Protocol (37°C/30-minute incubation).

Table 3. Protein-to-protein variation. Absorbance ratios (562nm) for proteins relative to BSA using the Standard Test Tube Protocol.

Ratio = (Avg "test" net Abs.) / (avg. BSA net Abs.)

Protein Tested	Ratio
Albumin, bovine serum	1.00
Aldolase, rabbit muscle	0.85
α-Chymotrypsinogen, bovine	1.14
Cytochrome C, horse heart	0.83
Gamma globulin, bovine	1.11
IgG, bovine	1.21
IgG, human	1.09
IgG, mouse	1.18
IgG, rabbit	1.12
IgG, sheep	1.17
Insulin, bovine pancreas	1.08
Myoglobin, horse heart	0.74
Ovalbumin	0.93
Transferrin, human	0.89
1.02	
Standard Deviation	**0.15**
Coefficient of Variation	**14.7%**

Cited References

1. Smith, P.K., *et al.* (1985). Measurement of protein using bicinchoninic acid. *Anal Biochem* **150:**76-85.
2. Wiechelman, K., *et al*. (1988). Investigation of the bicinchoninic acid protein assay: Identification of the groups responsible for color formation. *Anal Biochem* **175**:231-7.
3. Kessler, R. and Fanestil, D. (1986). Interference by lipids in the determination of protein using bicinchoninic acid. *Anal Biochem* **159:**138-42.
4. Brown, R., *et al.* (1989). Protein measurement using bicinchoninic acid: elimination of interfering substances. *Anal Biochem* **180:**136-9.

Product References

Adilakshami, T. and Laine, R.O. (2002). Ribosomal protein S25 mRNA partners with MTF-1 and La to provide a p53-mediated mechanism for survival or death. *J Biol Chem* **277:**4147-51.

Fischer, T., *et al.* (1999). Clathrin-coated vesicles bearing GAIP possess GTPase-activating protein activity in vitro. *Proc Nat Acad Sci* **96:**6722-7.

Prozialeck, W.C., *et al*. (2002). Chlamydia trachomatis disrupts N-cadherin-dependent cell-cell junctions and sequester **?**-catenin in human cervical epithelial cells. *Infection and Immunity* **70:**2605-13.

Roberts, K.P., *et al.* (2002). A comparative analysis of expression and processing of the rat epididymal fluid and sperm-bound forms of proteins D and E. *Biology of Reproduction* **67:**525-33.

Table 2. Compatible substance concentrations in the Thermo Scientific Pierce BCA Protein Assay (see text for details).[§]

Substance	Compatible Concentration
Salts/Buffers	
ACES, pH 7.8	25mM
Ammonium sulfate	1.5M
Asparagine	1mM
Bicine, pH 8.4	20mM
Bis-Tris, pH 6.5	33mM
Borate (50mM), pH 8.5 (# 28384)	undiluted
B-PER™ Reagent (#78248)	undiluted
Calcium chloride in TBS, pH 7.2	10mM
Na-Carbonate/Na-Bicarbonate (0.2M), pH 9.4 (# 28382)	undiluted
Cesium bicarbonate	100mM
CHES, pH 9.0	100mM
Na-Citrate (0.6M), Na-Carbonate (0.1M), pH 9.0 (# 28388)	1:8 dilution*
Na-Citrate (0.6M), MOPS (0.1M), pH 7.5 (#28386)	1:8 dilution*
Cobalt chloride in TBS, pH 7.2	0.8mM
EPPS, pH 8.0	100mM
Ferric chloride in TBS, pH 7.2	10mM
Glycine•HCl, pH 2.8	100mM
Guanidine•HCl	4M
HEPES, pH 7.5	100mM
Imidazole, pH 7.0	50mM
MES, pH 6.1	100mM
MES (0.1M), NaCl (0.9%), pH 4.7 (#28390)	undiluted
MOPS, pH 7.2	100mM
Modified Dulbecco's PBS, pH 7.4 (#28374)	undiluted
Nickel chloride in TBS, pH 7.2	10mM
PBS; Phosphate (0.1M), NaCl (0.15M), pH 7.2 (# 28372)	undiluted
PIPES, pH 6.8	100mM
RIPA lysis buffer; 50mM Tris, 150mM NaCl, 0.5% DOC, 1% NP-40, 0.1% SDS, pH 8.0	undiluted
Sodium acetate, pH 4.8	200mM
Sodium azide	0.2%
Sodium bicarbonate	100mM
Sodium chloride	1M
Sodium citrate, pH 4.8 or pH 6.4	200mM
Sodium phosphate	100mM
Tricine, pH 8.0	25mM
Triethanolamine, pH 7.8	25mM
Tris	250mM
TBS; Tris (25mM), NaCl (0.15M), pH 7.6 (# 28376)	undiluted
Tris (25mM), Glycine (192mM), pH 8.0 (# 28380)	1:3 dilution*

Substance	Compatible Concentration
Detergents**	
Brij™-35	5.0%
Brij-56, Brij-58	1.0%
CHAPS, CHAPSO	5.0%
Deoxycholic acid	5.0%
Octyl β-glucoside	5.0%
Nonidet P-40 (NP-40)	5.0%
Octyl β-thioglucopyranoside	5.0%
SDS	5.0%
Span™ 20	1.0%
Triton™ X-100	5.0%
Triton X-114, X-305, X-405	1.0%
Tween™-20, Tween-60, Tween-80	5.0%
Zwittergent™ 3-14	1.0%
Chelating agents	
EDTA	10mM
EGTA	--------
Sodium citrate	200mM
Reducing & Thiol-Containing Agents	
N-acetylglucosamine in PBS, pH 7.2	10mM
Ascorbic acid	--------
Cysteine	--------
Dithioerythritol (DTE)	1mM
Dithiothreitol (DTT)	1mM
Glucose	10mM
Melibiose	--------
2-Mercaptoethanol	0.01%
Potassium thiocyanate	3.0M
Thimerosal	0.01%
Misc. Reagents & Solvents	
Acetone	10%
Acetonitrile	10%
Aprotinin	10mg/L
DMF, DMSO	10%
DMSO	10%
Ethanol	10%
Glycerol (Fresh)	10%
Hydrazides	--------
Hydrides (Na_2BH_4 or $NaCNBH_3$)	--------
Hydrochloric Acid	100mM
Leupeptin	10mg/L

* Diluted with ultrapure water.
** Detergents were tested using high-purity Thermo Scientific Surfact-Amps Products, which have low peroxide content.
-- Dashed-line entry indicates that the material is incompatible with the assay.

[§] For a more extensive list of substances, download Tech Tip # 68: Protein assay compatibility table from our website. This Tech Tip includes compatible substances for all of our protein assays and enables easy comparisons.

APPENDIX E

INSTRUCTIONS

Thermo SCIENTIFIC

Human Apo E (AD2) ELISA Kit

EHAPOE

Number	Description
EHAPOE	**Human Apo E ELISA Kit**, sufficient reagents for 96 determinations

Kit Contents	Size
Anti-Human Apo E Precoated 96-well Strip Plate	1 each
Lyophilized Recombinant Human Apo E Standard	2 vials
20X Wash Buffer	25mL
Biotinylated Antibody Reagent	2 vials
Streptavidin-HRP Reagent	200uL
TMB Substrate	12mL
Stop Solution, contains 0.2M sulfuric acid	8mL
Assay Diluent (5X concentrated buffer)	15 mL
Adhesive Plate Sealer	2

For research use only. Not for use in diagnostic procedures.

Storage: May be stored for up to 6 months at 2º to 8ºC from the date of shipment. Opened microplate wells or reagents may be store for up to 1 month at 2º to 8ºC. Return unused wells to the pouch containing desiccant pack, reseal along entire edge. Reconstituted standard can be stored at -80ºC for up to 1 week.
Note: the kit can be used within one year if the whole kit is stored at -20ºC. Avoid repeated freeze- thaw cycles.

Table of Contents

Introduction

The Thermo Scientific™ Pierce™ Human Apo E (AD2) ELISA Kit is an enzyme-linked immunosorbent assay for measuring human apo E in serum, plasma, and cell culture media.

Procedure Summary

1. Prepare all reagents, samples and standards as instructed.

2. Add 100µL standard and sample to wells. Cover plate & incubate at RT for 2.5 hours.

3. Wash plate four times

Antibody to wells. Cover plate & incubate at RT for 1 hour.

4. Add 100µL Biotinylated

5. Wash plate four times

6. Add 100µL of

HRP Reagent to each well.

7. Cover & incubate plate at RT for 45 minutes.

8. Wash plate four times

9. Add 100µL TMB Substrate to each well.

10. Develop plate at room temperature in the dark for 30 minutes.

11. Add 50µL of Stop Solution to each well.

12. Measure absorbance and calculate results

Additional Materials Required

- Precision pipettors with disposable plastic tips to deliver 5-1000µL and plastic pipettes to deliver 5-15mL
- Ultrapure water for Wash Buffer and Standard reconstitution
- A glass or plastic 1L container to prepare Wash Buffer
- A squirt wash bottle or an automated 96-well plate washer
- 1.5mL polypropylene or polyethylene tubes to prepare standards - do not use polystyrene, polycarbonate or glass tubes
- Disposable reagent reservoirs
- A standard ELISA plate reader for measuring absorbance at 450nm and 550nm. If a 550nm filter is not available, the absorbance may be read at 450nm only. Refer to the instruction manual supplied with the instrument being used.

Precautions

- All specimens and reagents must be at room temperature (20-25°C) before use in the assay.
- Review all instructions carefully and verify components against the Kit Contents list (page 1) before beginning the assay. Do
- not use a 37°C water bath to thaw samples. Thaw samples at room temperature.
- If using a multichannel pipettor, always use a new disposable reagent reservoir for the addition of each reagent. Use new disposable pipette tips for each transfer to avoid cross-contamination.
- Use a new adhesive plate cover for each incubation step.
- Avoid microbial contamination of reagents.
- Avoid exposing reagents to excessive heat or light during storage and incubation.
- Do not mix reagents from different kit lots. Discard unused ELISA components after completing the assay.
- Do not use glass pipettes to measure the TMB Substrate Solution. Take care not to contaminate the solution. If the solution is blue before use, DO NOT USE IT.
- Individual components may contain antibiotics and preservatives. Wear gloves while performing the assay to avoid contact with samples and reagents. Please follow proper disposal procedures.
- Some components of this kit contain sodium azide. Please dispose of reagents according to local regulations.

Sample Preparation

- Serum, plasma, and cell culture media sample types may be tested in this assay; 100µL per well of diluted sample is required. See reagent preparation step 3 for sample dilution recommendations.
- Store samples to be assayed within 24 hours at 2-8°C. For long-term storage, aliquot and freeze samples at -70°C. Avoid repeated freeze-thaw cycles when storing samples.
- Samples and standards must be assayed in duplicate each time the assay is performed.
- Equilibrate samples gradually to room temperature before beginning the assay. Do not use a heated water bath to thaw or warm samples.
- Mix samples by gently inverting the tubes.
- If samples are clotted, grossly hemolyzed, lipemic or contaminated, make a note on the template and interpret results with caution.

Reagent Preparation

1. Bring all reagents and samples to room temperature (18 - 25ºC) before use.

2. Assay Diluent should be diluted 5-fold with deionized or distilled water before use.

3. **Sample dilution:** 1X Assay Diluent should be used for dilution of serum, plasma, and cell culture supernatant samples. The suggested dilution for normal serum/plasma is 1,000 fold.

   Note: Levels of Apo E may vary between different samples. Optimal dilution factors for each sample must be determined by the investigator.

4. **Preparation of standard:** Briefly spin a vial of lyophilized standard. Add 400 µL 1X Assay Diluent (Assay Diluent should be diluted 5-fold with deionized or distilled water before use) into the lyophilized standard vial to prepare a 400 ng/mL standard solution. Dissolve the powder thoroughly by gentle mixing. Pipette 300 µL 1X Assay Diluent into each tube. Use the 400 ng/mL standard solution to produce a dilution series (shown below). Mix each tube thoroughly before the next transfer. 1X Assay Diluent serves as the zero standard (0 pg/mL).

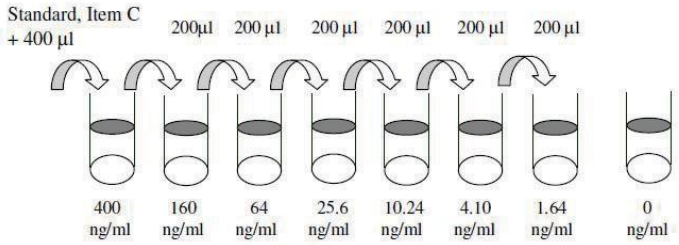

5. If the 20X Wash Buffer contains visible crystals, warm to room temperature and mix gently until dissolved. Dilute 20mL of the Wash Buffer Concentrate into deionized or distilled water to yield 400mL of 1X Wash Buffer.

6. Briefly spin the Biotinylated Antibody Reagent vial before use. Add 100µL of 1X Assay Diluent into the vial to prepare a biotinylated antibody concentrate. Pipette up and down to mix gently (the concentrate can be stored at 4ºC for 5 days). The biotinylated antibody concentrate should be diluted 80-fold with 1X Assay Diluent and used in step 4 of Assay Procedure.

7. Briefly spin the Streptavidin-HRP Reagent vial and pipette up and down to mix gently before use, as precipitates may form during storage. The Streptavidin-HRP Reagent should be diluted 1500-fold with 1X Assay Diluent.

   For example: Briefly spin the vial and pipette up and down to mix gently . Add 8µL of HRP-Streptavidin concentrate into a tube with 12mL 1X Assay Diluent to prepare a 1,500-fold diluted HRP-Streptavidin solution (Use the diluted Strept-HRP solution same day; Do not store diluted solution for future use). Mix Well.

Assay Procedure

1. Bring all reagents and samples to room temperature (18 - 25ºC) before use. It is recommended that all standards and samples be run at least in duplicate.

2. Add 100µL of each standard (see Reagent Preparation step 3) and sample into appropriate wells. Cover wells and incubate for 2.5 hours at room temperature with gentle shaking.

Note: Overnight incubations at 4°C with gentle shaking can be performed, but may increase overall signals including background.

3. Discard the solution and wash 4 times with 1X Wash Buffer. Wash by filling each well with Wash Buffer (300µL) using a multi-channel Pipette or autowasher. Complete removal of liquid at each step is essential for good performance. After the last wash, remove any remaining Wash Buffer by aspirating or decanting. Invert the plate and blot it against clean paper towels.

4. Add 100µL of 1X prepared biotinylated antibody (Reagent Preparation step 6) to each well. Incubate for 1 hour at room temperature with gentle shaking.

5. Discard the solution. Repeat the wash as in step 3.

6. Add 100µL of prepared Streptavidin-HRP solution (see Reagent Preparation step 7) to each well. Incubate for 45 minutes at room temperature with gentle shaking.

7. Discard the solution. Repeat the wash as in step 3.

8. Add 100µL of TMB Substrate to each well. Incubate for 30 minutes at room temperature in the dark with gentle shaking.

9. Add 50 µl of Stop Solution to each well.

10. The plate must be evaluated within 30 minutes of stopping the reaction. Measure absorbance on an ELISA plate reader set at 450nm and 550nm. Subtract 550nm values from 450nm values to correct for optical imperfections in the microplate. If 550nm is not available, measure absorbance at 450nm only. Omitting the 550nm measurement will result in higher absorbance values.

11. Calculation of Results:

- Generate the standard curve by plotting the average absorbance (450nm minus 550nm) obtained for each Standard concentration on the vertical (Y) axis vs. the corresponding Apo E concentration on the horizontal (X) axis.
- Calculate results manually using graph paper or with a curve-fitting statistical software package. If using curve-fitting software, plot a four-parameter logistic curve fit. Alternatively, a point-to-point curve fit may be used. Determine the amount of Apo E in each sample by interpolating from the Apo E concentration (X axis) to the absorbance value (Y axis).
- If the sample was diluted, multiply the interpolated value obtained by the dilution factor to determine amount of Apo E in the sample.
- Absorbance values obtained for duplicates should be within 10% of the mean value. Carefully consider duplicate values that differ from the mean by greater than 10%.

Performance Characteristics

Typical Data: These standard curves are for demonstration only. A standard curve must be run with each assay.

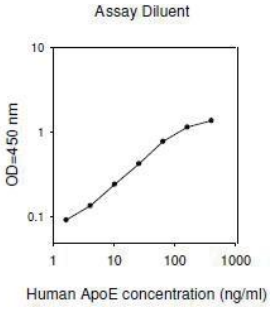

Sensitivity: 1.5 ng/mL

The sensitivity or Lower Limit of Detection (LLD) was determined by assaying replicates of zero and the standard curve. The mean signal of zero + 2 standard deviations read in dose from the standard curve is the LLD. This value is the smallest dose that is not zero with 95% confidence.

Spiking & Recovery: Pooled serum, plasma, and cell culture media samples were spiked with recombinant Human Apo E. Endogenous Human Apo E levels were determined by testing non-spiked samples alongside spiked aliquots of the same samples. Expected values were calculated by adding endogenous Apo E levels to those of the spiked control. Percent recovery was calculated by dividing observed by expected values.

Sample Type	Average % Recovery	Range (%)
Serum	136	126-142
Plasma	131	116-144
Cell Culture Media	78	69-91

Linearity: The serum, plasma, and cell culture media samples were spiked with recombinant Human Apo E, serially diluted in sample diluent and evaluated. Observed values were compared to expected values to calculate percent recovery and demonstrate the dilution linearity of the assay.

Sample Type	Average % Expected		Range (%)	
	1:2 Dilution	1:4 Dilution	1:2 Dilution	1:4 Dilution
Serum	123	97	117-129	89-105
Plasma	132	112	126-140	103-128
Cell Culture Media	143	136	135-150	128-144

Reproducibility: Assay reproducibility was evaluated in each sample matrix. To determine intra-assay precision, two standard curves and 3 samples for each standard curve are run. The standard curve concentration points as well as the samples are tested in duplicates on a single plate. Two different concentration values are obtained for each sample, using the two separate standard curves. The two concentration values for each sample is compared to each other using the CV% calculation. To evaluate inter- assay precision, the second standard curve is tested on a separate plate along with the second set of samples.

Intra-Assay CV%: <10%

Inter-Assay CV%: <12%

Specificity: This ELISA pair antibody detects human ApoE (isoforms ApoE2, ApoE3 and ApoE4).

Explanation of symbols

Symbol	Description	Symbol	Description
	Manufacturer		Catalog number
	Use by		Temperature limitation
	Consult instructions for use		Caution, consult accompanying documents
	Batch code		

Data Templates

	1	2	3	4	5	6	7	8	9	10	11	12
A												
B												
C												
D												
E												
F												
G												
H												

	1	2	3	4	5	6	7	8	9	10	11	12
A												
B												
C												
D												
E												
F												
G												
H												

Appendix F

MSD® MULTI-SPOT Assay System

Aβ Peptide Panel 1 Kits

AJ3338, AJ3340, AJ3342

V-PLEX®

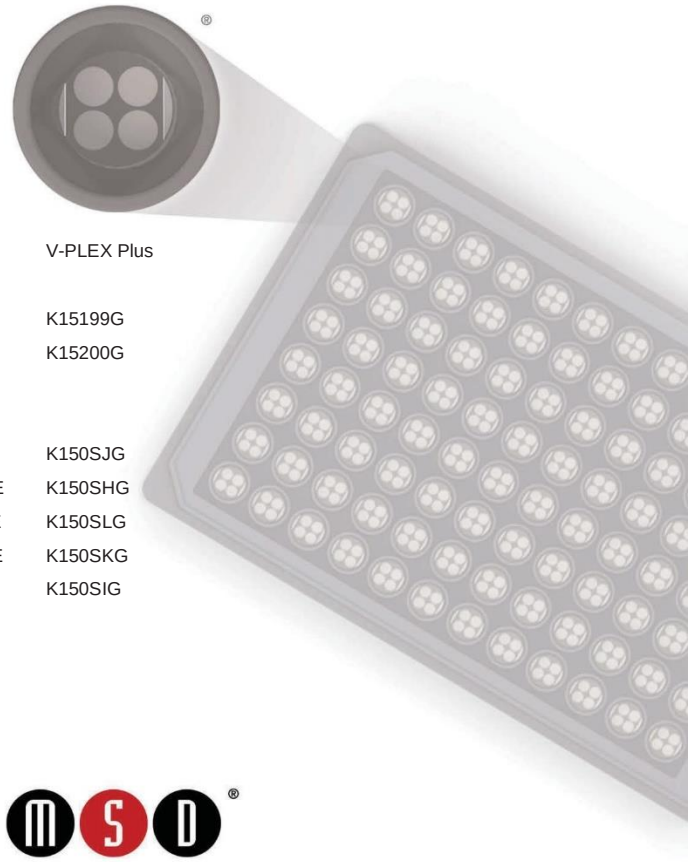

	V-PLEX®	V-PLEX Plus
Multiplex Kits		
Aβ Peptide Panel 1 (4G8)	K15199E	K15199G
Aβ Peptide Panel 1 (6E10)	K15200E	K15200G
Singleplex Kits Aβ40 Peptide (4G8)	K150SJE	K150SJG
Aβ38 Peptide (4G8)	K150SHE	K150SHG
Aβ42 Peptide (4G8)	K150SLE	K150SLG
Aβ40 Peptide (6E10)	K150SKE	K150SKG
Aβ38 Peptide (6E10)	K150SIE	K150SIG

MSD®

www.mesoscale.com®

MSD Neurodegenerative Disease Assays

Aβ Peptide Panel 1 Kits

Aβ40, Aβ38, Aβ42

For use with human cerebrospinal fluid (CSF), rodent CSF, rodent plasma/serum, cell culture supernatants, and tissue homogenates.

This package insert must be read in its entirety before using this product.

FOR RESEARCH USE ONLY.

NOT FOR USE IN DIAGNOSTIC PROCEDURES.

MESO SCALE DISCOVERY®
A division of Meso Scale Diagnostics, LLC.
1601 Research Blvd. Rockville, MD 20850
USA www.mesoscale.com

18084-v4-2018Apr | 2

Table of Contents

Contact Information

MSD Customer Service

Phone: 1-240-314-2795
Fax: 1-301-990-2776
Email: CustomerService@mesoscale.com

MSD Scientific Support

Phone: 1-240-314-2798
Fax: 1-240-632-2219 attn: Scientific Support
Email: ScientificSupport@mesoscale.com

Introduction

Beta-amyloid (Aβ peptides derived from amyloid precursor protein (APP) are found in human CSF and have proven to be informative biomarkers with respect to neurodegeneration, especially Alzheimer's disease (AD). Amyloid plaques, the hallmark feature of the brains from AD patients upon autopsy, are enriched in Aβ42. A significant body of work supports that levels of Aβ42 drop in CSF concomitantly with its accumulation in the brain, first in aggregates and proto-fibrils, and ultimately in fibrils and plaques.[1,2] Quantification of Aβ42 in human CSF, especially in combination with other biomarkers, has proven to be useful in discriminating AD from other dementias and to stage AD patients with respect to the natural progression of the disease.[3,4]

The amyloid hypothesis is the most advanced theory for the cause of AD and has been the foundation for numerous clinical trials to date.[5] This hypothesis states that oligomeric and/or aggregated forms of Aβ42 are toxic to neurons. A variety of small molecule and biological approaches have been explored in an effort to reduce the brain burden of Aβ42. The small molecule approach has largely been directed at reducing the production of Aβ42, while the biologics approach has been focused on effective clearing of Aβ42 from the brain.

Amyloid peptides are generated through successive cleavage of APP by β- and γ -secretase. Depending on the exact site of γ-secretase cleavage, benign peptides Aβ38 and Aβ40 may be produced instead of neurotoxic Aβ42. Clinical trials to date have included small molecules that inhibit β-secretase or those that modulate γ-secretase to favor production of Aβ38 and Aβ37 over Aβ42 and Aβ40.[6] The Aβ Peptide Panel 1 provides a sensitive and efficient means to measure changes in concentrations of the Aβ peptides in samples during clinical research with these small molecules. While the Aβ Peptide Panel 1 (6E10) and (4G8) kits are validated for human CSF, they are also compatible with other sample types including conditioned neuronal cell culture medium, cell lysates, and tissue homogenates including mouse brain, and thus provide a platform for use in early discovery through pre-clinical and clinical research studies. The Aβ Peptide Panel 1 (4G8) Kit has also been validated for mouse EDTA plasma.

Principle of the Assay

MSD neurodegenerative disease assays provide a rapid and convenient method for measuring the levels of peptide and protein targets within a single, small-volume sample. The assays in the Aβ Peptide Panel 1 are sandwich immunoassays. MSD provides a plate pre-coated with capture antibodies on independent and well-defined spots as shown in the layout below. Assay kits are provided with 4-spot MULTI-SPOT® plates (Figures 1 and 2). The user adds the sample and a solution containing detection antibodies conjugated with electrochemiluminescent labels (MSD SULFO-TAG™) over the course of one or more incubation periods. Analytes in the sample bind to capture antibodies immobilized on the working electrode surface; recruitment of the detection antibodies by the bound analytes completes the sandwich. The user adds an MSD buffer that creates the appropriate chemical environment for electrochemiluminescence and loads the plate into an MSD instrument where a voltage applied to the plate electrodes causes the captured labels to emit light. The instrument measures the intensity of emitted light (which is proportional to the amount of analyte present in the sample) and provides a quantitative measure of each analyte in the sample. V-PLEX assay kits have been validated according to the principles outlined in "Fit-for-Purpose Method Development and Validation for Successful Biomarker Measurement" by J. W. Lee, et al.[9]

1. Aβ40
2. Aβ38
3. *BSA blocked*
4. Aβ42

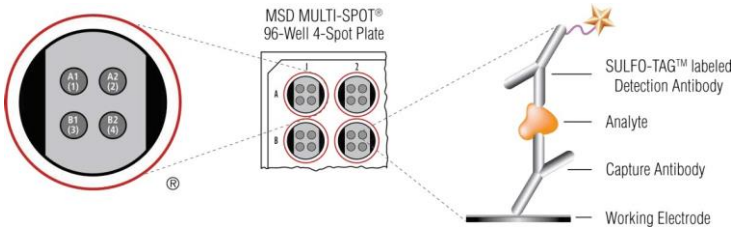

Figure 1. Spot diagram showing placement of analyte capture antibodies for the A/3 Peptide Panel 1 and A/338 singleplex kits. The numbering convention for the different spots is maintained in the software visualization tools, on the plate packaging, and in the data files.

1. Aβ
2. *BSA blocked*
3. *BSA blocked*
4. *BSA blocked*

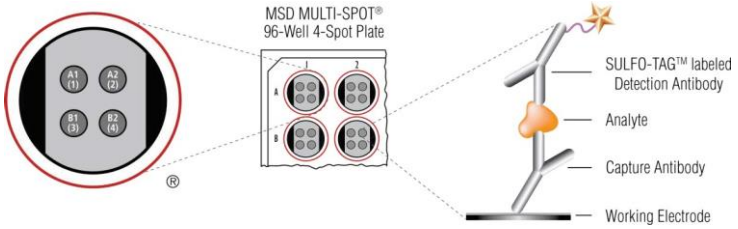

Figure 2. Spot diagram showing placement of analyte capture antibodies for A/340 and A/342 singleplex plates. A/340 and A/342 singleplex kits are provided on 4-spot plates with analyte capture antibody coated on spot A1. Spots A2, B1, and B2 are BSA blocked.

Kit Components

Aβ Peptide Panel 1 assays are available as a 4-spot multiplex kit and as single assay kits. All V-PLEX kits are provided with pre-coated plates, calibrator, detection antibodies, and reagents. V-PLEX Plus kits include additional items (controls, wash buffer, and plate seals). See below for details on the components.

See the Catalog Numbers section for a comprehensive list of all kits.

Reagents Supplied With All Kits

Table 1. Reagents that are supplied with V-PLEX and V-PLEX Plus Kits

Reagent	Storage	Catalog #	Size	Quantity Supplied 1 Plate Kit	5 Plate Kit	25 Plate Kit	Description
Diluent 35	2–8°C	R50AE-3	30 mL	1 bottle			Diluent for samples and calibrator which mimics human CSF; contains proteins and preservatives.
		R50AE-2	150 mL		1 bottle	5 bottles	
Diluent 100	2–8°C	R50AA-4	50 mL	1 bottle			Diluent for detection antibody; contains protein, blockers, and preservatives.
					1 bottle	5 bottles	
Read Buffer T (4X)	RT	R92TC-3	50 mL	1 bottle	1 bottle	5 bottles	Buffer to catalyze the electro-chemiluminescence reaction.

Kit-Specific Components

Table 2. Components that are supplied with specific kits

Plates	Storage	Part #	Size	Quantity Supplied 1 Plate Kit	5 Plate Kit	25 Plate Kit	Description
A**J3** Peptide Panel 1 Plate	2–8°C	N45197A-1	4-spot	1	5	25	96-well plate, foil sealed, with desiccant.
A**J3**40 Peptide Plate	2–8°C	N450AA-1	4-spot	1	5	25	
A**J3**38 Peptide Plate	2–8°C	N45197A-1	4-spot	1	5	25	
A**J3**42 Peptide Plate	2–8°C	N451LBA-1	4-spot	1	5	25	

Table 3. Kits are supplied with individual calibrators for each assay ordered

Calibrators	Storage	Catalog #	Size	Quantity Supplied 1 Plate Kit	5 Plate Kit	25 Plate Kit	Description
A**J3**1-40 Peptide	s;–70°C	C00OA-2	30 µL/vial	1	5	25	Synthetic peptide calibrators in diluent that mimics human CSF. Analyte concentrations are provided in the lot-specific certificate of analysis (COA).
A**J3**1-38 Peptide	s;–70°C	C00NZ-2	30 µL/vial	1	5	25	
A**J3**1-42 Peptide	s;–70°C	C01LB-2	30 µL/vial	1	5	25	

Table 4. Kits are supplied with detection antibodies for the specific kit that was ordered

SULFO-TAG Detection Antibody	Storage	Catalog #	Size	Quantity Supplied 1 Plate Kit	5 Plate Kit	25 Plate Kit	Description
Anti-A**J3** 4G8 Antibody (50X)*	2–8°C	D20RQ-2	75 µL	1			SULFO-TAG conjugated antibody specific for human and rodent Aβ peptides
		D20RQ-3	375 µL		1	5	
Anti-A**J3** 6E10 Antibody (50X)*	2–8°C	D21LB-2	75 µL	1			SULFO-TAG conjugated antibody specific for human Aβ peptides
		D21LB-3	375 µL		1	5	

*SULFO-TAG conjugated detection antibodies should be stored in the dark.

Table 5. Kits that include the Aβ40 assay are supplied with Aß40 Blocker

Blocker	Storage	Catalog #	Size	Quantity Supplied 1 Plate Kit	5 Plate Kit	25 Plate Kit	Description
Aβ40 Blocker	2–8°C	R93BJ-1	40 µL	1			Blocking reagent for measuring CSF samples containing high abundance of Aß40 peptide; not for use with serum and plasma
		R93BJ-2	200 µL		1	5	

V-PLEX Plus Kits: Additional Components

Table 6. Additional components that are supplied with V-PLEX Plus Kits

Reagents	Storage	Catalog #	Size	Quantity Supplied 1 Plate Kit	5 Plate Kit	25 Plate Kit	Description
Neurodegeneration Control 1**	s;–70°C	C41LB-1	1 vial	1 vial	5 vials	25 vials	Multi-analyte controls in diluent that mimics human CSF. The concentrations of the analytes are provided in the lot-specific COA.
Neurodegeneration Control 2**	s;–70°C	C41LB-1	1 vial	1 vial	5 vials	25 vials	
Neurodegeneration Control 3**	s;–70°C	C41LB-1	1 vial	1 vial	5 vials	25 vials	
Wash Buffer (20X)	RT	R61AA-1	100 mL	1 bottle	1 bottle	5 bottles	20-fold concentrated phosphate buffered solution with surfactant.
Plate Seals	-	-	-	3	15	75	Adhesive seals for sealing plates during incubations.

**Provided as components within Neurodegeneration Control Pack (catalog # C41LB-1)

Additional Materials and Equipment

- ☐ Appropriately sized tubes for reagent preparation
- ☐ Polypropylene microcentrifuge tubes for preparing dilutions
- ☐ Liquid handling equipment for desired throughput, capable of dispensing 10 to 150 µL/well into a 96-well microtiter plate
- ☐ Plate washing equipment: automated plate washer or multichannel pipette
- ☐ Microtiter plate shaker (rotary) capable of shaking at 500–1,000 rpm
- ☐ Phosphate-buffered saline plus 0.05% Tween-20 for plate washing or MSD Wash Buffer catalog # R61AA-1 (included in V-PLEX Plus kit)
- ☐ Adhesive plate seals (3 per plate included in V-PLEX Plus kits)
- ☐ Deionized water
- ☐ Vortex mixer

Optional Materials and Equipment

- ☐ Neurodegeneration Control Pack 1, available for separate purchase from MSD, catalog # C41LB-1 (included in V-PLEX Plus kit)
- ☐ Centrifuge (for sample preparation)

Safety

Use safe laboratory practices and wear gloves, safety glasses, and lab coats when handling kit components. Handle and dispose of all hazardous samples properly in accordance with local, state, and federal guidelines.

Additional product-specific safety information is available in the safety data sheet (SDS), which can be obtained from MSD Customer Service or at www.mesoscale.com.

Best Practices

- Do not mix or substitute reagents from different sources or different kit lots. Lot information is provided in the lot-specific COA.
- Assay incubation steps should be performed between 20-26°C to achieve the most consistent signals between runs.
- Prepare calibrators, samples, and controls in polypropylene microcentrifuge tubes; use a fresh pipette tip for each dilution; vortex after each dilution before proceeding.
- Avoid prolonged exposure of detection antibody (stock or diluted) to light. During the antibody incubation step, plates do not need to be shielded from light except for direct sunlight.
- Avoid bubbles in wells at all pipetting steps. Bubbles may lead to variable results; bubbles introduced when adding Read Buffer T may interfere with signal detection.
- Use reverse pipetting when necessary to avoid introduction of bubbles. For empty wells, pipette gently to the bottom corner.
- Plate shaking should be vigorous, with a rotary motion between 500 and 1,000 rpm. Binding reactions may reach equilibrium sooner if you use shaking at the middle of this range (~700 rpm) or above.
- When using an automated plate washer, rotate the plate 180 degrees between wash steps to improve assay precision.
- Gently tap the plate on a paper towel to remove residual fluid after washing.
- Read buffer should be at room temperature when added to the plate.
- Keep time intervals consistent between adding read buffer and reading the plate to improve inter-plate precision. Unless otherwise directed, read plate as soon as practical after adding read buffer.
- No shaking is necessary after adding read buffer.
- If an incubation step needs to be extended, avoid letting the plate dry out by keeping sample or detection antibody solution in the plate.
- Remove the plate seals prior to reading the plate.
- If assay results are above the top of the calibration curve, dilute the samples and repeat the assay.
- When running a partial plate, seal the unused sectors (see sector map in instrument and software manuals) to avoid contaminating unused wells. Remove all seals before reading. Partially used plates may be sealed and stored up to 7 days at 2–8°C in the original foil pouch with desiccant. You may adjust volumes proportionally when preparing reagents.

Reagent Preparation

Bring all reagents to room temperature. Diluted calibrator, controls, and samples should be prepared during the blocking step and used within one hour of preparation. Thorough mixing of stock and diluted kit reagents is required.

Prepare Calibrator Dilutions

MSD supplies individual Aβ peptide calibrators at a concentration that is 40-fold higher than the recommended highest standard. To prepare 7 calibrator solutions plus a zero calibrator for up to 4 replicates:

1) Prepare the highest calibrator by diluting the supplied peptide calibrator with Diluent 35. Mix well by vortexing.

   Instructions for Aβ Peptide Panel 1 multiplex kits (Figure 3):

Transfer 10 µL of Aβ 1-40 Peptide, 10 µL Aβ1-38 Peptide, and 10 µL Aβ1-42 Peptide into 370 µL of Diluent 35. Or

Instructions for Aβ singleplex assay kits (Figure 4):

Add 10 µL of the supplied peptide calibrator to 390 µL of Diluent 35.

2) Prepare the next calibrator by transferring 100 µL of the highest calibrator to 300 µL of Diluent 35. Mix well by vortexing. Repeat 4-fold serial dilutions 5 additional times to generate 7 calibrators.
3) Use Diluent 35 as the zero calibrator.

For the lot-specific concentration of each calibrator, refer to the COA supplied with the kit. You can also find a copy of the COA at www.mesoscale.com.

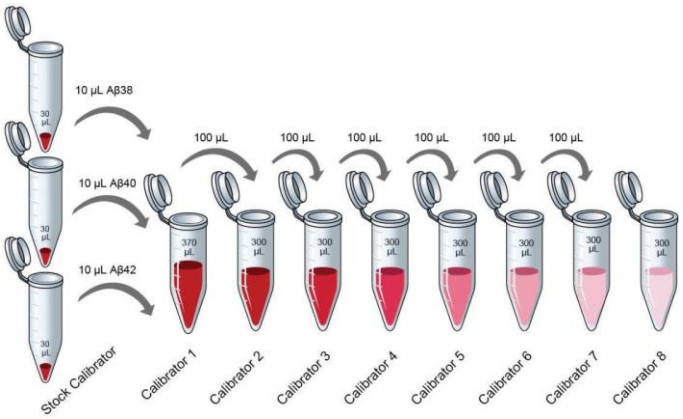

Figure 3. Preparation of calibrator solutions for AP Peptide Panel 1 multiplex kits

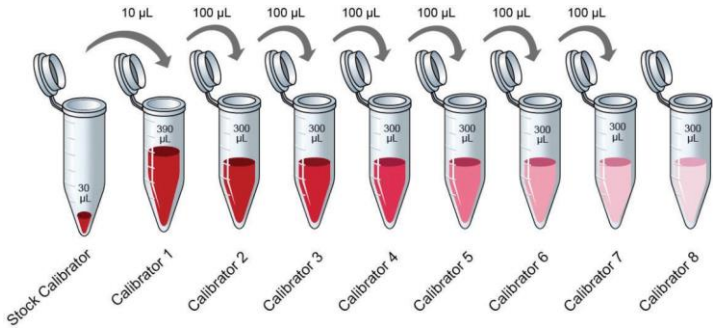

Figure 4. Preparation of calibrator solutions for AP singleplex assay kits

Sample Collection and Handling

CSF sample collection methods and pre-analytical conditions may cause variability in measured Aβ peptide levels. MSD recommends reviewing current literature and protocols such as those proposed by the Alzheimer's Disease Neuroimaging Initiative (ADNI).[10-12] Samples described herein were clarified through a single centrifugation step at 1,200 rcf for 10 minutes at 2-8°C. Samples should be used immediately or frozen in aliquots and stored at ≤-70ºC until needed. Repeated freeze–thaw of samples is not recommended. Evaluate sample stability under the selected method as needed.

Dilute Samples

Human CSF samples: MSD recommends a minimum 2-fold sample dilution; however depending on the sample set under investigation, a higher dilution factor may be needed to maximize matrix tolerance. Mix thawed sample well by vortexing, then dilute with Diluent 35. For example, to dilute 2-fold, add 60 µL of sample to 60 µL of Diluent 35. Mix diluted sample well by vortexing.

Mouse plasma samples: Mouse samples may be tested with the Aβ Peptide Panel 1 (4G8) kit only. MSD recommends a 4-fold dilution for evaluation of mouse EDTA plasma. Mix thawed samples well by vortexing, then dilute with Diluent 35. For example, to dilute 4-fold, add 30 µL of sample to 90 µL of Diluent 35.

The Aβ Peptide Panel 1 kits exhibit good dilution linearity; you may conserve CSF or plasma sample volume by using a higher sample dilution. Please see the dilution linearity section for representative data.

Prepare Controls

Three levels of multi-analyte frozen liquid controls are available for separate purchase from MSD in the Neurodegeneration Control Pack, catalog # C41LB-1. (Controls are included only in V-PLEX Plus Kits.) The controls are prepared by spiking known levels of synthetic Aβ peptides into a diluent that mimics human CSF.

Thaw controls at room temperature and mix well by vortexing. Dilute controls 2-fold in Diluent 35 and mix well by vortexing. For the lot-specific concentrations of each analyte in the control pack, refer to the supplied COA. You can also find a copy of the COA at www.mesoscale.com.

Prepare Detection Antibody Solution

MSD provides detection antibody as a 50X stock solution. The working solution is 1X. Prepare the detection antibody solution immediately prior to use.

For kits that include Aβ40 assay, the Aβ40 Blocker may be included in the working detection antibody solution at a final concentration of 1X. For sample types that are expected to have low levels of Aβ40 peptide, Aβ40 blocker may be omitted. Omission of Aβ40 blocker may result in high signals of the Aβ40 controls, close to the upper limit of quantification.

Detection Antibody Solution with Aβ40 Blocker For one plate,

combine the following:

- ☐ 60 µL of 50X SULFO-TAG Anti-Aβ 4G8 Antibody or Anti-Aβ 6E10 Antibody
- ☐ 30 µL of Aβ40 Blocker
- ☐ 2,910 µL of Diluent 100

Detection Antibody Solution without Aβ40 Blocker For one plate,

combine the following:

- ☐ 60 µL of 50X SULFO-TAG Anti-Aβ 4G8 Antibody or Anti-Aβ 6E10 Antibody
- ☐ 2,940 µL of Diluent 100

Prepare Wash Buffer

MSD provides 100 mL of Wash Buffer as a 20X stock solution in the V-PLEX Plus kit. The working solution is 1X. PBS + 0.05% Tween-20 can be used instead.

For one plate, combine:

- ☐ 15 mL of MSD Wash Buffer (20X)
- ☐ 285 mL of deionized water

1X MSD Wash Buffer can be stored at room temperature for up to two weeks.

Prepare Read Buffer T

MSD provides Read Buffer T as a 4X stock solution. The working solution is 2X. For one plate,

combine:

- ☐ 10 mL of Read Buffer T (4X)
- ☐ 10 mL of deionized water

You may keep excess diluted Read Buffer in a tightly sealed container at room temperature for up to one month.

Prepare MSD Plate

MSD plates are pre-coated with capture antibodies (Figures 1 and 2) and exposed to a proprietary stabilizing treatment to ensure the integrity and stability of the immobilized antibodies. Plates may be used as delivered; no additional preparation (e.g., pre-wetting) is required.

Protocol

Note: Follow Reagent Preparation before beginning this assay protocol. STEP 1: Add

Blocker

- ☐ Add 150 µL of Diluent 35 to each well. Seal the plate with an adhesive plate seal and incubate at room temperature with shaking for 1 hour.

STEP 2: Wash and Add Detection Antibody Solution and Sample

- ☐ Wash the plate 3 times with at least 150 µL/well of 1X MSD Wash Buffer.
- ☐ Add 25 µL of detection antibody solution to each well.
- ☐ Add 25 µL of prepared samples, calibrators or controls per well. Seal the plate with an adhesive plate seal and incubate at room temperature with shaking for 2 hours.

STEP 3: Wash and Read

- ☐ Wash the plate 3 times with at least 150 µL/well of 1X MSD Wash Buffer.
- ☐ Add 150 µL of 2X Read Buffer T to each well. Analyze the plate on an MSD instrument. Incubation in Read Buffer T is not required before reading the plate.

Validation

MSD's V-PLEX products are validated following fit-for-purpose principles[9] and MSD design control procedures. Three independently-built kit lots were included in the validation of the Aβ Peptide Panel 1 (6E10) and (4G8) kits. Accuracy and precision of calibrators and controls were determined from multiple test runs conducted over several days by multiple analysts. Assay specificity, tolerance to interferences, robustness, and stability were also evaluated. The validation methods used are described below.

- Sensitivity

The upper limit of quantification (ULOQ) and lower limit of quantification (LLOQ) were determined through measurement of samples created by spiking known amounts of calibrator into assay diluent. The accuracy and precision of these measurements was evaluated across multiple kit lots.

- Precision

Precision is presented as the coefficient of variance (CV). The typical specification for precision is a concentration CV of less than 25% for controls on both intra- and inter-day runs.

- Dilution Linearity, and Spike Recovery

Spike recovery and dilution linearity were assessed across multiple kit lots.

- Specificity

Assay specificity and tolerance to interferences were evaluated across multiple lots using peptides within the kit, and a panel of other analytes of interest.

- Robustness and Stability

The robustness of the protocol was evaluated to examine the boundaries of the selected incubation times. Assay component robustness was assessed through freeze–thaw testing and stability studies for calibrators, antibodies, and controls. The validation program includes a real–time stability study with scheduled performance evaluations of complete kits for up to 54 months from date of manufacture.

Representative data from the validation studies are presented in the following sections. The calibration curve and measured limits of detection for each lot can be found in the lot-specific COA that is included with each kit and available for download at www.mesoscale.com.

Analysis of Results

The calibration curves used to calculate analyte concentrations were established by fitting the signals from the calibrators to a 4-parameter logistic (or sigmoidal dose-response) model with a $1/Y^2$ weighting. The weighting function provides a better fit of data over a wide dynamic range, particularly at the low end of the calibration curve. Analyte concentrations were determined from the ECL signals by back-fitting to the calibration curve. These assays have a wide dynamic range (4 logs), which allows accurate quantification of samples without the need for multiple dilutions or repeated testing. The calculations to establish calibration curves and determine concentrations were carried out using the MSD DISCOVERY WORKBENCH® analysis software.

Best quantification of unknown samples will be achieved by generating a calibration curve for each plate using a minimum of two replicates at each calibrator level.

Typical Data

Calibration curve accuracy and precision were assessed for three kit lots. Representative data from one kit lot are presented below. The average intra-plate signal CVs were typically less than 8%. Calibration curves for each lot are presented in the lot-specific COA.

Figure 5. Typical calibration curves and representative data for the A/3 Peptide Panel 1 (4G8) assay

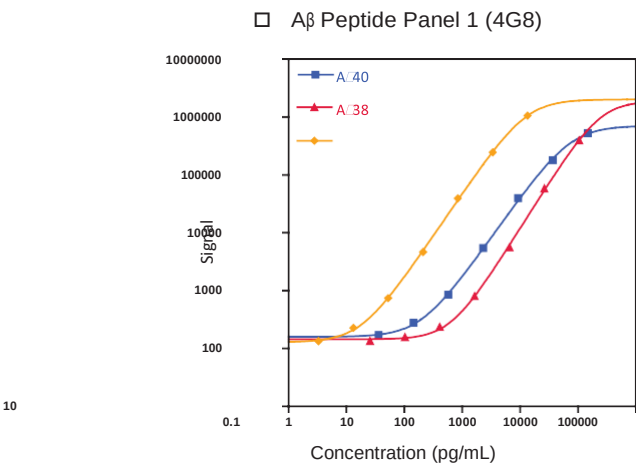

AJ340[1]		
Assigned Conc. (pg/mL)	Average Signal	%CV
14,825	528,168	5.9
3,706	179,871	6.9
927	39,760	7.4
232	5,451	7.8
57.9	850	7.5
14.9	278	8.4
3.62	171	4.4
0	148	5.9

AJ338[1]		
Assigned Conc. (pg/mL)	Average Signal	%CV
10,500	396,928	3.2
2,625	58,861	5.2
656	5,659	5.6
164	810	4.0
41.0	238	4.6
10.3	158	6.1
2.56	135	5.4
0	132	5.3

AJ342[1]		
Assigned Conc. (pg/mL)	Average Signal	%CV
1,348	1,055,597	2.8
337	246,458	3.1
84.2	39,402	4.9
21.1	4,663	5.1
5.26	747	5.6
1.32	229	8.4
0.329	134	6.4
0	110	8.2

Figure 6. Typical calibration curves and representative data for the A/3 Peptide Panel 1 (6E10) assay

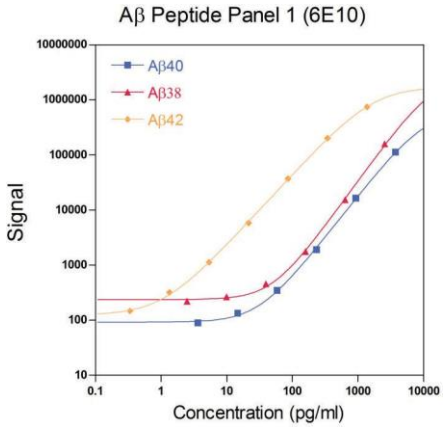

AJ340[2]		
Assigned Conc. (pg/mL)	Average Signal	%CV
14,900	391,584	5.3
3,725	113,481	6.8
931	16,502	8.4
233	1,908	8.5
58.2	352	7.5
14.6	134	4.4
3.64	90	5.3
0	77	5.0

AJ338[2]		
Assigned Conc. (pg/mL)	Average Signal	%CV
10,200	952,636	3.4
2,550	158,685	5.4
638	15,447	7.8
159	1,777	5.0
39.8	460	7.6
9.96	266	5.1
2.49	222	7.8
0	212	6.9

AJ342[2]		
Assigned Conc. (pg/mL)	Average Signal	%CV
1,380	744,788	2.3
345	201,808	2.8
86.3	37,005	3.9
21.6	5,831	4.6
5.39	1,127	3.4
1.35	319	2.9
0.337	147	4.2
0	93	7.6

[331] See the kit-specific COA for calibration curve concentrations, specifications, and quality control data.

Spot the Difference®

Sensitivity

The lower limit of detection (LLOD) is a calculated concentration corresponding to the signal 2.5 standard deviations above the background (zero calibrator). The LLODs shown below were calculated based on 50 runs across 3 kit lots for each kit product.

The ULOQ is the highest concentration at which the %CV of the calculated concentration is <20% and the percent recovery of the standard is within 80–120% of the known value.

The LLOQ is the lowest concentration at which the %CV of the calculated concentration is <20% and the percent recovery of the standard is within 80–120% of the known value.

The quantitative range of the assay lies between the LLOQ and ULOQ.

The LLOQ and ULOQ are verified for each kit lot and the results are provided in the lot-specific COA that is included with each kit and available at www.mesoscale.com.

Table 7. LLOD, LLOQ, and ULOQ for each analyte in the A/3 Peptide Panel 1 Kits

Kit Name	Analyte	Median LLOD (pg/mL)	LLOD Range (pg/mL)	LLOQ (pg/mL)	ULOQ (pg/mL)
Aβ Peptide Panel 1 (4G8)	A**J3**40	5.41	3.72–42.6	20.0	6,000
	A**J3**38	22.2	13.8–57.7	60.0	7,500
	A**J3**42	0.516	0.198–1.15	2.50	1,270
Aβ Peptide Panel 1 (6E10)	A**J3**40	9.97	7.26–12.2	50.0	7,000
	A**J3**38	16.7	7.59–24.3	60.0	8,480
	A**J3**42	0.368	0.220–0.537	3.13	1,270

Precision

Neurodegeneration Controls 1, 2, and 3 were made by spiking Aβ peptides into diluent that mimics human CSF. CSF Controls 1, 2and 3 were made by spiking peptides into human CSF. Peptides were spiked at three levels within the quantitative range of the assay to create controls 1, 2, and 3. Analyte levels were measured by five analysts using a minimum of two replicates on ?37 runs over eight months across three kit lots. Results are shown below. While the typical specification for precision is a concentration CV of less than 25% for controls on both intra- and inter-day runs, for this panel, the data indicates that for most assays the CVs are below 10%.

Average intra-plate %CV is the average %CV of the control replicates within an individual run. Inter-plate %CV is the variability of controls across ?37 runs.

Inter-lot %CV is the variability of controls across three kit lots.

Table 8. Intra-run and Inter-run %CVs in the A/3 Peptide Panel 1 Kits

Kit Name	Analyte	Control	Ave. Conc. (pg/mL)	Ave. Intra-plate %CV	Ave. Inter-plate Conc. %CV	Inter-Kit Lot Conc. %CV
Aβ Peptide Panel 1 (4G8)	Aβ40	Neurodegeneration Control 1	9,071	6.8	9.7	7.9
		Neurodegeneration Control 2	3,036	5.3	8.3	7.0
		Neurodegeneration Control 3	570	5.2	11.1	9.1
		CSF Control 1	8,963	5.1	10.7	9.6
		CSF Control 2	3,019	5.2	10.5	9.9
		CSF Control 3	1,865	5.7	9.6	7.9
	Aβ38	Neurodegeneration Control 1	2,754	4.8	7.0	4.7
		Neurodegeneration Control 2	694	4.9	9.9	8.5
		Neurodegeneration Control 3	183	5.2	17.6	18.0
		CSF Control 1	4,977	4.3	6.9	3.6
		CSF Control 2	1,321	4.5	11.7	11.4
		CSF Control 3	609	4.2	13.0	13.0
	Aβ42	Neurodegeneration Control 1	1,303	2.3	7.5	7.5
		Neurodegeneration Control 2	495	2.2	7.7	7.3
		Neurodegeneration Control 3	206	2.2	8.2	7.6
		CSF Control 1	1,804	3.5	6.8	6.5
		CSF Control 2	497	2.4	7.6	6.4
		CSF Control 3	261	2.9	7.5	6.6
Aβ Peptide Panel 1 (6E10)	Aβ40	Neurodegeneration Control 1	9,957	5.5	7.1	6.3
		Neurodegeneration Control 2	3,236	4.4	6.0	3.6
		Neurodegeneration Control 3	615	4.3	7.8	3.8
		CSF Control 1	9,415	4.4	6.9	5.5
		CSF Control 2	3,111	4.2	7.9	6.1
		CSF Control 3	1,933	4.9	8.3	4.2
	Aβ38	Neurodegeneration Control 1	3,044	4.2	7.1	3.8
		Neurodegeneration Control 2	768	3.9	6.2	1.2
		Neurodegeneration Control 3	197	4.4	9.5	7.8
		CSF Control 1	5,276	3.1	7.2	5.3
		CSF Control 2	1,471	3.6	6.8	0.6
		CSF Control 3	705	4.0	7.6	3.0
	Aβ42	Neurodegeneration Control 1	1,440	2.2	7.0	7.0
		Neurodegeneration Control 2	532	2.0	6.5	6.1
		Neurodegeneration Control 3	216	2.5	7.4	5.9
		CSF Control 1	1,925	3.0	8.4	9.2
		CSF Control 2	513	2.4	8.3	9.0
		CSF Control 3	263	2.7	8.8	8.0

Dilution Linearity

To assess linearity, CSF samples collected from individual patients according to accepted protocols[10] and mouse EDTA plasma samples were diluted 2-fold, 4-fold, and 8-fold before testing. Percent recovery at each dilution was calculated by dividing the dilution-adjusted concentration by the dilution-adjusted concentration at 2-fold dilution (for human CSF samples) or 4-fold (for mouse plasma samples). The average percent recovery shown below is based on samples within the quantitative range of the assay.

$$\%\ Recovery = \frac{(measured\ concentration \times dilution\ factor)}{(measured\ concentration\ at\ 2\text{-}fold\ dilution \times 2)} \times 100$$

Figure 7. Dilution linearity in human CSF and mouse plasma samples for the A/3 Peptide Panel 1 Kits

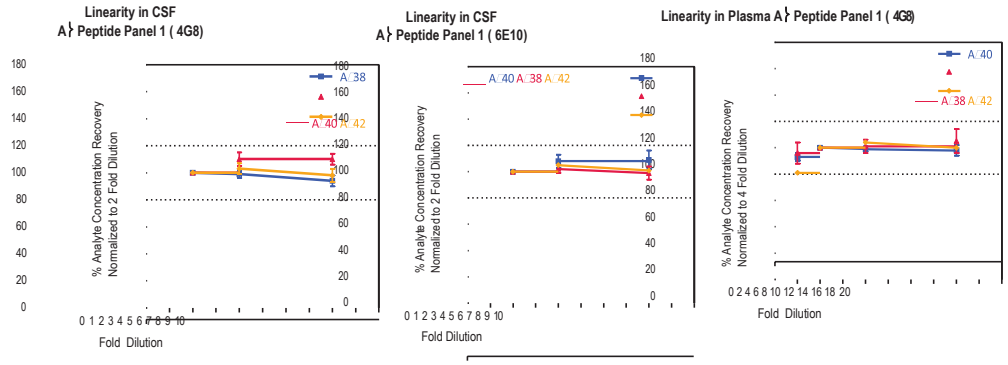

Table 9. Analyte percent recovery at various dilutions in each sample type in the A/3 Peptide Panel 1 Kits

			AJ340		AJ338		AJ342	
Kit Name	Sample Type	Fold Dilution	Average % Recovery	% Recovery Range	Average % Recovery	% Recovery Range	Average % Recovery	% Recovery Range
Aβ Peptide Panel 1 (4G8)	Human CSF (N=10)	2	100	N/A	100	N/A	100	N/A
		4	110	103–118	99	99–93	103	103–103
		8	110	105–119	94	94–86	98	103–98
	Mouse Plasma (N=10)	2	93	89–98	96	96–84	81	105–81
		4	100	N/A	100	N/A	100	N/A
		8	99	97–104	101	101–95	104	108–104
		16	98	94–104	105	105–94	100	119–100
Aβ Peptide Panel 1 (6E10)	Human CSF (N=10)	2	100	N/A	100	N/A	100	N/A
		4	108	101–114	102	102–96	105	106–105
		8	109	101–125	99	99–92	101	107–101

Spike Recovery

Spike and recovery measurements of different sample types were evaluated throughout the quantitative range of the assays. Multiple individual human CSF or mouse EDTA plasma samples were spiked with calibrators at two levels (high and low) and then diluted 2-fold (for human CSF samples) or 4-fold (for mouse plasma samples). The average % recovery for each sample type is reported along with %CV and % recovery range. The expected concentration is the sum of the measured endogenous concentration and the spiked calibrator concentration.

$$\%\ Recovery = \frac{measured\ concentration}{expected\ concentration} \times 100$$

Table 10. Spike and Recovery measurements of different sample types in the A/3 Peptide Panel 1 Kits

		Aβ40			Aβ38			Aβ42		
Kit Name	Sample Type	Average % Recovery	%CV	% Recovery Range	Average % Recovery	%CV	% Recovery Range	Average % Recovery	%CV	% Recovery Range
Aβ Peptide Panel 1 (4G8)	Human CSF (N=10)	88	11.6	70–114	96	5.2	90–112	92	11.0	79–125
	Mouse Plasma (N=10)	100	17.2	70–114	90	22.0	90–112	100	16.5	79–125
Aβ Peptide Panel 1 (6E10)	Human CSF (N=10)	95	10.9	73–131	96	6.1	85–113	95	10.7	80–132

Specificity

To assess specificity, each assay in the panel was tested individually. Cross-reactivity was less than 1.0% for all assays in the kit. Cross-reactivity was also evaluated with a panel of related Aβ peptides and other proteins of interest, including Aβ1-16, Aβ17-24, Aβ1-37, Aβ1-39, Aβ1-41, Aβ1-43, sAPPα, sAPPβ, and Tau. The A42 assay exhibits minor cross-reactivity with some related Aβ peptides: Aβ1-41 (2.6%); Aβ1-43 and Aβ1-37 (<0.75%). Given the low endogenous levels of these peptides in CSF,[13,14] this is expected to have a minimal effect on Aβ42 quantification.

$$\%\ Nonspecificity = \frac{nonspecific\ signal}{specific\ signal} \times 100$$

Figure 8. A/340, A/338, and A/342 assay specificity

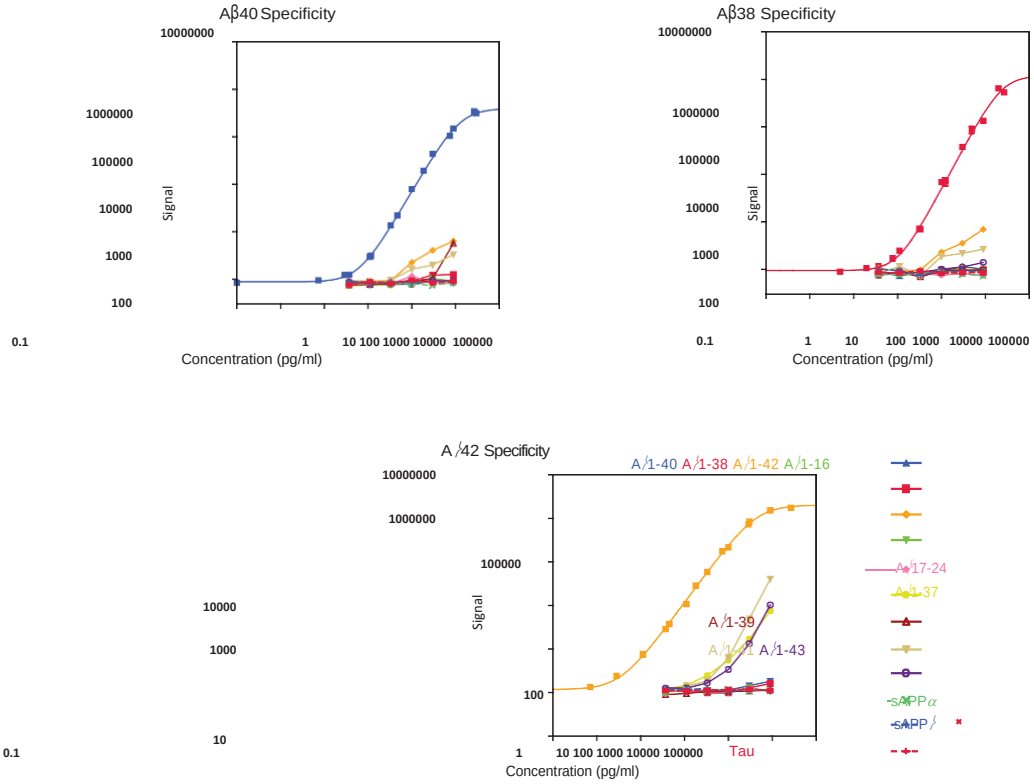

Interference

Aβ40 (top), Aβ38 (middle), or Aβ42 (bottom) peptide calibrators were co-spiked into assay diluent with various Aβ peptides and proteins of interest at or above expected endogenous levels for these analytes (Aβ40, sAPPa, and sAPP β spiked at 5 ng/mL; all other interferents spiked at 1 ng/mL). Measured Aβ levels were largely within 25% of the sample with no interferent, regardless of the spiked analyte or concentration.

Figure 9. A/340, A/338, and A/342 measured concentration with interferents

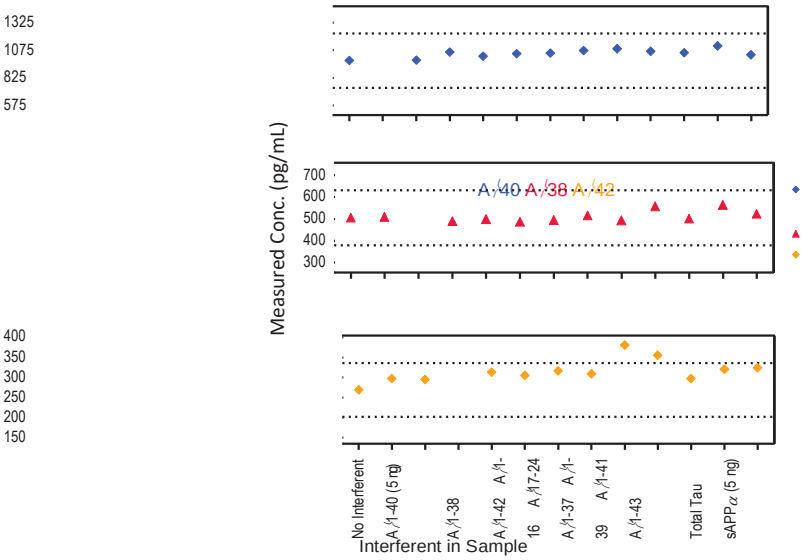

Stability

Assay kit calibrators and controls were tested for freeze–thaw stability. Results (not shown) demonstrated that calibrators and controls may go through 3 freeze/thaw cycles without significantly affecting the performance of the assay. In addition, thawed calibrators and controls are stable for ? 8 days when stored at 2–8°C or room temperature. 4G8 and 6E10 detection antibodies diluted for the assay are light stable for at least 4 hours. The kits are stable for 30 months from the date of manufacture. In addition, the validation study includes an on-going real-time stability study with scheduled performance evaluations of complete kits for up to 54 months from date of manufacture.

Tested Samples

Sample Range

Aβ peptides were measured in different sample types in order to determine the expected endogenous levels. Individual patient CSF samples were collected according to accepted protocols.[10] The commercial vendors that supplied the pooled CSF from remnant clinical samples were not able to adhere to stringent collection and handling procedures. CSF samples were diluted 2-fold prior to testing. Mouse plasma samples were diluted 4-fold prior to testing. Results for each sample set are reported below. Concentrations are corrected for sample dilution.

Table 11. Median and range of different sample types measured in the A/3 Peptide Panel 1 Kits

Kit Name	Sample Type	Statistic	AJ340	AJ338	AJ342
A} Peptide Panel 1 (4G8)	Individual Patient Human CSF (N=23)	Median (pg/mL)	4,162	1,327	264
		Range (pg/mL)	2,112–7,458	689–2,910	37–706
		% Detected	100	100	100
	Pooled Remnant Human CSF (N=12)	Median (pg/mL)	2,324	670	195
		Range (pg/mL)	58.8–8,347	ND–3,340	3.96–748
		% Detected	100	92	100
	Mouse Plasma (N=20)	Median (pg/mL)	207	55.0	25.4
		Range (pg/mL)	113–317	ND–217	11.7–32.7
		% Detected	100	15	100
A} Peptide Panel 1 (6E10)	Individual Patient Human CSF (N=26)	Median (pg/mL)	3,831	1,293	187
		Range (pg/mL)	1,300–7,187	607–3,202	25–607
		% Detected	100	100	100
	Pooled Remnant Human CSF (N=12)	Median (pg/mL)	2,225	745	178
		Range (pg/mL)	43.7–7,012	ND–3,437	3.31–691
		% Detected	100	92	100

ND = Non-detectable

Disease Samples

Well-curated normal and individual AD patient CSF samples were diluted 2-fold prior to measuring with the Aβ Peptide Panel 1 (6E10) Kit. Samples handling was consistent with accepted protocols. The table below displays median and range of the measured concentrations for each sample set. Concentrations have been corrected for sample dilution. A graphical representation is also provided for the individual normal and AD patient samples. Comparable results were obtained with the 4G8 kit.

Figure 10. Normal and AD CSF samples measured in the A/3 Peptide Panel 1 (6E10) Kit

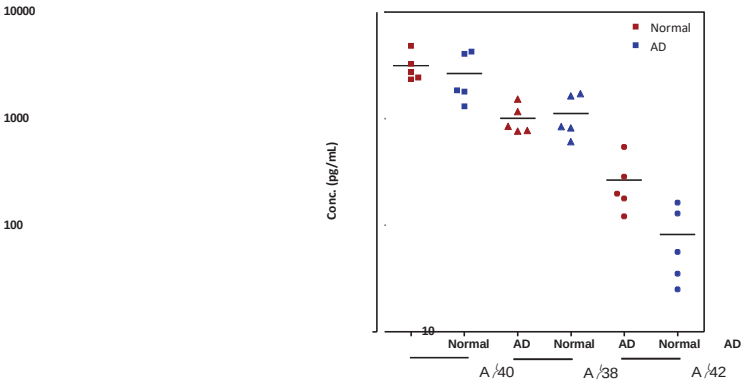

Table 12. Median and range of diseased samples measured in the A/3 Peptide Panel 1 (6E10) Kit

Kit Name	Sample Type	Statistic	AJ340	AJ338	AJ342
Aβ Peptide Panel 1 (6E10)	Normal CSF (N=5)	Median (pg/mL)	2,715	842	197
		Range (pg/mL)	2,320–4,827	761–1,515	121– 542
		% Detected	100	100	100
	AD CSF (N=5)	Median (pg/mL)	1,831	837	56
		Range (pg/mL)	43.7–4,057	418–1,635	3.31–285
		% Detected	100	100	100

Assay Components

Calibrators

The assay calibrators are made using synthetic Aβ peptides.

Antibodies

Table 13. Antibody source species

		Source Species		
Kit Detection Antibody	Analyte	MSD Capture Antibody	MSD Detection Antibody	Assay Generation
4G8	AJ340	Mouse Monoclonal	Mouse Monoclonal	A
	AJ338	Mouse Monoclonal	Mouse Monoclonal	A
	AJ342	Mouse Monoclonal	Mouse Monoclonal	B
6E10	AJ340	Mouse Monoclonal	Mouse Monoclonal	A
	AJ338	Mouse Monoclonal	Mouse Monoclonal	A
	Aβ42	Mouse Monoclonal	Mouse Monoclonal	B

References

1. Albert MS, et al. The diagnosis of mild cognitive impairment due to Alzheimer's disease: recommendations from the National Institute on Aging-Alzheimer's Association workgroups on diagnostic guidelines for Alzheimer's disease. Alzheimers Dement. 2011 May;7(3):270-9.
2. Blennow K, et al. Cerebrospinal fluid and plasma biomarkers in Alzheimer disease. Nat Rev Neurol. 2010 Mar;6(3):131-44.
3. Gabelle A, et al. Correlations between soluble α/β forms of amyloid precursor protein and Aβ38, 40, and 42 in human cerebrospinal fluid. Brain Res. 2010 Oct 21;1357:175-83.
4. Jack CR Jr, et al. Tracking pathophysiological processes in Alzheimer's disease: an updated hypothetical model of dynamic biomarkers. Lancet Neurol. 2013 Feb;12(2):207-16.
5. Karran E, et al. The amyloid cascade hypothesis for Alzheimer's disease: an appraisal for the development of therapeutics. Nat Rev Drug Discov. 2011 Aug 19;10(9):698-712.
6. Page RM, et al. Generation of Abeta38 and Abeta42 is independently and differentially affected by familial Alzheimer disease-associated presenilin mutations and gamma-secretase modulation. J Biol Chem. 2008 Jan 11;283(2):677-83.
7. Guidance for Industry Alzheimer's Disease: Developing Drugs for the Treatment of Early Stage Disease. Office of Communications, Division of Drug Information Center for Drug Evaluation and Research Food and Drug Administration February 2013.
8. Kozauer N, and Katz R. Regulatory innovation and drug development for early-stage Alzheimer's disease. N Engl J Med 2013; 368:1169-1171.
9. Lee JW, et al. Fit-for-purpose method development and validation for successful biomarker measurement. Pharm Res. 2006 Feb;23(2):312-28.
10. Alzheimer's Disease Neuroimaging Initiative Procedures Manuals. Website: http://www.adni-info.org/Scientists/ProceduresManuals.aspx.
11. Bjerke M, et al. Confounding factors influencing amyloid Beta concentration in cerebrospinal fluid. Int J Alzheimers Dis. 2010 Jul 15;pii:986310.
12. Schoonenboom NS, et al. Effects of processing and storage conditions on amyloid beta (1-42) and tau concentrations in cerebrospinal fluid: implications for use in clinical practice. Clin Chem. 2005 Jan;51(1):189-95.
13. Portelius E, et al. Distinct cerebrospinal fluid amyloid beta peptide signatures in sporadic and PSEN1 A431E-associated familial Alzheimer's disease. Mol Neurodegener. 2010; 5:2.
14. Bibl M, et al. CSF amyloid-beta-peptides in Alzheimer's disease, dementia with Lewy bodies and Parkinson's disease dementia. Brain. 2006; 2129(Pt 5):1177–1187.

Catalog Numbers

Table 14. Catalog numbers for the V-PLEX and V-PLEX Plus neurodegeneration biomarker multiplex and single assay kits*

Kit Name	V-PLEX			V-PLEX Plus*		
	1 plate kit	5 plate kit	25 plate kit	1 plate kit	5 plate kit	25 plate kit
Multiplex Kits						
A**J3** Peptide Panel 1 (4G8)	K15199E-1	K15199E-2	K15199E-4	K15199G-1	K15199G-2	K15199G-4
A**J3** Peptide Panel 1 (6E10)	K15200E-1	K15200E-2	K15200E-4	K15200G-1	K15200G-2	K15200G-4
Single Assay Kits						
A**J3**40 (4G8)	K150SJE-1	K150SJE-2	K150SJE-4	K150SJG-1	K150SJG-2	K150SJG-4
A**J3**38 (4G8)	K150SHE-1	K150SHE-2	K150SHE-4	K150SHG-1	K150SHG-2	K150SHG-4
A**J3**42 (4G8)	K150SLE-1	K150SLE-2	K150SLE-4	K150SLG-1	K150SLG-2	K150SLG-4
A**J3**40 (6E10)	K150SKE-1	K150SKE-2	K150SKE-4	K150SKG-1	K150SKG-2	K150SKG-4
A**J3**38 (6E10)	K150SIE-1	K150SIE-2	K150SIE-4	K150SIG-1	K150SIG-2	K150SIG-4
Human A**J3**42 (6E10)	K151LBE-1	K151LBE-2	K151LBE-4	K151LBG-1	K151LBG-2	K151LBG-4
Human Total Tau	K151LAE-1	K151LAE-2	K151LAE-4	K151LAG-1	K151LAG-2	K151LAG-4

*V-PLEX Plus kits include controls, plate seals, and wash buffer. See Kit Components for details.

Summary Protocol

AJ3 Peptide Panel 1 Kits

MSD provides this summary protocol for your convenience.
Please read the entire detailed protocol prior to performing the Aβ Peptide Panel 1 assays.

Sample and Reagent Preparation

- ☐ Bring all reagents to room temperature.
- ☐ Prepare calibrator solutions in Diluent 35 using the supplied calibrator.
- ☐ Dilute samples and controls in Diluent 35 before adding to the plate.
- ☐ Prepare detection antibody solution by diluting each 50X detection antibody 50-fold in Diluent 100.
- ☐ Prepare 2X Read Buffer T by diluting 4X Read Buffer T 2-fold with deionized water.

STEP 1: Add Diluent 35

- ☐ Add 150 µL/well of Diluent 35.
- ☐ Incubate at room temperature with shaking for 1 hour.

STEP 2: Wash and Add Detection Antibody Solution and Sample or Calibrator

- ☐ Wash the plate 3 times with at least 150 µL/well of 1X MSD Wash Buffer.
- ☐ Add 25 µL/well of 1X detection antibody solution.
- ☐ Add 25 µL/well of calibrator or diluted sample.
- ☐ Incubate at room temperature with shaking for 2 hours.

STEP 3: Wash and Read Plate

- ☐ Wash the plate 3 times with at least 150 µL/well of 1X MSD Wash Buffer.
- ☐ Add 150 µL/well of 2X Read Buffer T.
- ☐ Analyze the plate on the MSD instrument.

Plate Diagram

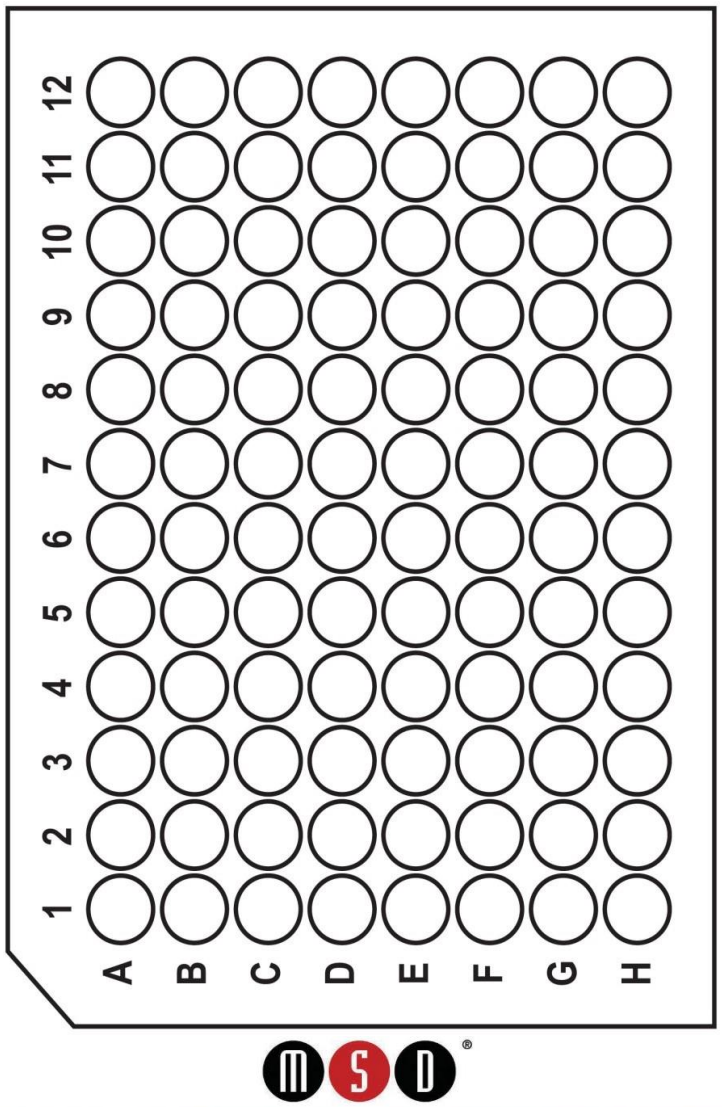

www.mesoscale.com®

Appendix G

ab83389

Glutamate Assay kit (Colorimetric)

Instructions for Use

For the rapid, sensitive and accurate measurement of Glutamate in various samples.

This product is for research use only and is not intended for diagnostic use.

Version 5 Last Updated 30 April 2015

FOR RESEARCH USE ONLY.

NOT FOR USE IN DIAGNOSTIC OR THERAPEUTIC PROCEDURES.

Table of Contents

INTRODUCTION

1. BACKGROUND

Glutamate Assay Kit (Colorimetric) (ab83389) provides a sensitive detection method of the glutamate in a variety of samples. This kit will only measure free glutamate levels but not glutamic acid found in the backbone of peptides or proteins. The glutamate enzyme mix recognizes glutamate as a specific substrate leading to proportional color development. The amount of glutamate can therefore be easily quantified by colorimetric (spectrophotometry at OD = 450 nm) method.

Glutamate, one of the two acidic proteinogenic amino acids, is also a key molecule in cellular metabolism. In humans, glutamate plays an important role both in amino acid degradation and disposal of excess or waste nitrogen. Glutamate is the most abundant swift excitatory neurotransmitter in the mammalian nervous system. It is believed to be involved in learning and memory and has appeared to be involved in diseases like amyotrophic lateral sclerosis, lathyrism, autism, some forms of mental retardation and Alzheimer's disease. Glutamic acid is also present in a wide variety of foods, and has been used as a flavour enhancer in food industry.

2. ASSAY SUMMARY

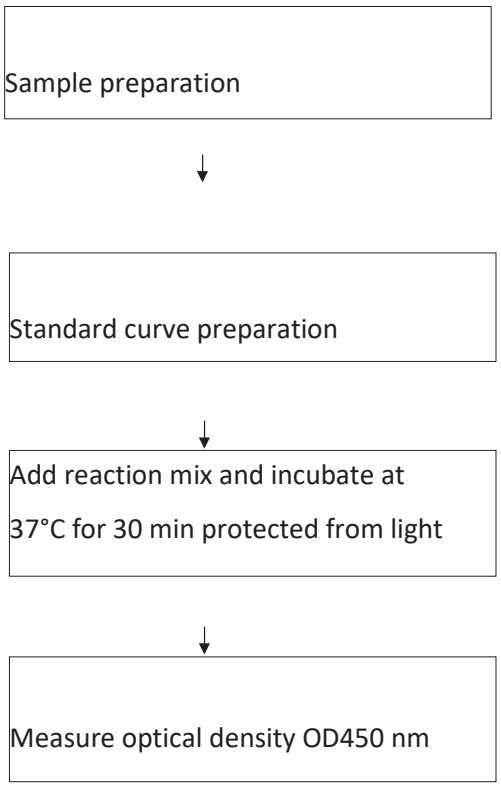

3. PRECAUTIONS

Please read these instructions carefully prior to beginning the assay.

All kit components have been formulated and quality control tested to function successfully as a kit. Modifications to the kit components or procedures may result in loss of performance.

4. STORAGE AND STABILITY

Store kit at -20ºC in the dark immediately upon receipt. Kit has a storage time of 1 year from receipt, providing components have not been reconstituted.

Refer to list of materials supplied for storage conditions of individual components. Observe the storage conditions for individual prepared components in section 5.

Aliquot components in working volumes before storing at the recommended temperature. **Reconstituted components are stable for 2 months.**

5. MATERIALS SUPPLIED

Item	Amount	Storage Condition (Before Preparation)	Storage Condition (After Preparation)
Glutamate Assay Buffer	25 mL	-20°C	-20°C
Glutamate Enzyme Mix	1 vial	-20°C	-20°C
Glutamate Developer	1 vial	-20°C	-20°C
Glutamate Standard (0.1M)	100 µL	-20°C	-20°C

6. MATERIALS REQUIRED, NOT SUPPLIED

These materials are not included in the kit, but will be required to successfully utilize this assay:

- MilliQ water or other type of double distilled water (ddH_2O)
- PBS
- Microcentrifuge
- Pipettes and pipette tips
- Colorimetric microplate reader – equipped with filter for OD450 nm
- 96 well plate: clear plates for colorimetric assay
- Orbital shaker
- Vortex
- Dounce homogenizer or pestle (if using tissue)

7. LIMITATIONS

- Assay kit intended for research use only. Not for use in diagnostic procedures.
- Do not use kit or components if it has exceeded the expiration date on the kit labels.
- Do not mix or substitute reagents or materials from other kit lots or vendors. Kits are QC tested as a set of components and performance cannot be guaranteed if utilized separately or substituted.

8. TECHNICAL HINTS

- **This kit is sold based on number of tests. A 'test' simply refers to a single assay well. The number of wells that contain sample, control or standard will vary by product. Review the protocol completely to confirm this kit meets your requirements. Please contact our Technical Support staff with any questions.**
- Keep enzymes and heat labile components and samples on ice during the assay.
- Make sure all buffers and developing solutions are at room temperature before starting the experiment.
- Avoid cross contamination of samples or reagents by changing tips between sample, standard and reagent additions.
- Avoid foaming or bubbles when mixing or reconstituting components.
- Samples generating values higher than the highest standard should be further diluted in the appropriate sample dilution buffers.
- Ensure plates are properly sealed or covered during incubation steps.
- Ensure complete removal of all solutions and buffers from tubes or plates during wash steps.
- Make sure you have the appropriate type of plate for the detection method of choice.
- Make sure the heat block/water bath and microplate reader are switched on before starting the experiment.

ASSAY PREPARATION

9. REAGENT PREPARATION

- Briefly centrifuge small vials at low speed prior to opening.

9.1 Glutamate Assay Buffer:

Ready to use as supplied. Equilibrate to room temperature before use. Store at -20°C.

9.2 Glutamate Enzyme Mix:

Reconstitute Glutamate Enzyme Mix with 220 µL Assay Buffer. Aliquot enzyme mix so that you have enough volume to perform the desired number of assays. Store at -20°C protected from light. Use within two months. Do not freeze- thaw more than 5 times. Keep on ice during the assay and protected from light.

9.3 Glutamate Developer:

Reconstitute Glutamate Developer with 820 µL of ddH_2O. Pipette up and down several times to completely dissolve the pellet into solution, do not vortex. Aliquot developer so that you have enough volume to perform the desired number of assays. Store at -20°C. Keep on ice during the assay.

9.4 Glutamate Standard (0.1M = 100 mM):

Ready to use as supplied. Aliquot standard so that you have enough volume to perform the desired number of assays. Store at -20°C. Keep on ice during the assay.

ASSAY PREPARATION

10. STANDARD PREPARATION

- Always prepare a fresh set of standards for every use.
- Diluted standard solution is unstable and must be used within 4 hours.

10.1 Prepare a 1 mM Glutamate standard by diluting 5 µL of the 0.1 M Glutamate Standard in 495 µL of Assay Buffer.

10.2 Using 1 mM standard, prepare standard curve dilution as described in the table in a microplate or microcentrifuge tubes:

Standard #	Volume of Standard (µL)	Assay Buffer (µL)	Final volume standard in well (µL)	End [glutamate] in well
1	0	150	50	0 nmol/well
2	6	144	50	2 nmol/well
3	12	138	50	4 nmol/well
4	18	132	50	6 nmol/well
5	24	126	50	8 nmol/well
6	30	120	50	10 nmol/well

Each dilution has enough amount of standard to set up duplicate reading (2 x 50 µL).

11. SAMPLE PREPARATION

General Sample information:

- We recommend performing several dilutions of your sample to ensure the readings are within the standard value range.
- We recommend that you use fresh samples. If you cannot perform the assay at the same time, we suggest that you complete the Sample Preparation step before storing the samples. Alternatively, if that is not possible, we suggest that you snap freeze cells or tissue in liquid nitrogen upon extraction and store the samples immediately at -80°C. When you are ready to test your samples, thaw them on ice. Be aware however that this might affect the stability of your samples and the readings can be lower than expected.

11.1 Cell (adherent or suspension) samples):

11.1.1 Harvest the amount of cells necessary for each assay (initial recommendation = 2 x 10^6 cells).

11.1.2 Wash cells with cold PBS.

11.1.3 Resuspend cells in 100 µL Assay Buffer.

11.1.4 Homogenize cells quickly by pipetting up and down a few times.

11.1.5 Incubate cells for 15 – 30 min on ice.

11.1.6 Centrifuge sample for 2 – 5 minutes at 4°C at top speed using a cold microcentrifuge to remove any insoluble material.

11.1.7 Collect supernatant and transfer to a clean tube.

11.1.8 Keep on ice.

11.2 Tissue samples:

11.2.1 Harvest the amount of tissue necessary for each assay (initial recommendation 10 mg).

11.2.2 Wash tissue in cold PBS.

11.2.3 Resuspend tissue in 100 µL of Assay Buffer.

ASSAY PREPARATION

11.2.4 Homogenize tissue with a Dounce homogenizer sitting on ice, with 10 – 15 passes.

11.2.5 Incubate sample for 15 – 30 min on ice.

11.2.6 Centrifuge samples for 2 – 5 minutes at 4°C at top speed using a cold microcentrifuge to remove any insoluble material.

11.2.7 Collect supernatant and transfer to a clean tube.

11.2.8 Keep on ice.

11.3 Serum and urine samples:

Serum and urine samples can be tested directly by adding sample to the microplate wells. Bring volumes up to 50 µL with Assay Buffer.

However, to find the optimal values and ensure your readings will fall within the standard values, we recommend performing several dilutions of the sample (1/2 – 1/5 – 1/10).

11.4 Food samples:

For liquid food samples (e.g., soya sauce), we recommend performing several dilutions of the sample. (1/50 – 1/100 – 1/250 – 1/500).

11.4.1 For solid food samples (e.g., tomato): chopped in small pieces (you can use a food blender to improve extraction of glutamate) and homogenize in Assay Buffer (1 g sample/mL assay buffer).

11.4.2 Incubate homogenate for a minimum of 10 minutes at room temperature.

11.4.3 Centrifuge samples for 10 minutes at 4°C at top speed using a cold microcentrifuge to remove insoluble material.

11.4.4 Collect supernatant and transfer to a clean tube. Recommended dilutions: 1/25 – 1/50 – 1/100 – 1/150

NOTE: *We suggest using different volumes of sample to ensure readings are within the Standard Curve range.*

12. ASSAY PROCEDURE and DETECTION

- **Equilibrate all materials and prepared reagents to room temperature prior to use.**
- **It is recommended to assay all standards, controls and samples in duplicate.**

12.1 Set up Reaction wells:

- Standard wells = 50 µL Standard dilutions.
- Sample wells = 2 – 50 µL samples (adjust volume to 50 µL/well with Glutamate Assay Buffer).
- Background control sample wells = 2 – 50 µL samples (adjust volume to 50 µL/well with Glutamate Assay Buffer).

12.2 Reaction Mix:

Prepare 100 µL of Reaction Mix for each reaction:

Component	Reaction Mix Samples (µL)	Background Reaction Mix (µL)
Glutamate Assay Buffer	90	92
Glutamate Developer	8	8
Glutamate Enzyme Mix	2	0

Mix enough reagents for the number of assays (samples, standards and background control) to be performed. Prepare a Master Mix of the Reaction Mix to ensure consistency. We recommend the following calculation:

X µL component x (Number samples + standards +1).

12.3 Add 100 µL of Reaction Mix into each standard and sample wells.

12.4 Add 100 µL of Background Reaction Mix into Background sample wells.

12.5 Mix and incubate at 37°C for 30 minutes protected from light.

12.6 Measure output (OD450 nm) on a microplate reader.

DATA ANALYSIS

13. CALCULATIONS

- Samples producing signals greater than that of the highest standard should be further diluted in appropriate buffer and reanalyzed, then multiplying the concentration found by the appropriate dilution factor.
- For statistical reasons, we recommend each sample should be assayed with a minimum of two replicates (duplicates).

13.1 Average the duplicate reading for each standard and sample.

13.2 Subtract the mean absorbance value of the blank (Standard #1) from all standard and sample readings. This is the corrected absorbance.

13.3 If the sample background control is significant, then subtract the sample background control from sample readings.

13.4 Plot the corrected absorbance values for each standard as a function of the final concentration of Glutamate.

13.5 Draw the best smooth curve through these points to construct the standard curve. Most plate reader software or Excel can plot these values and curve fit. Calculate the trendline equation based on your standard curve data (use the equation that provides the most accurate fit).

13.6 Extrapolate sample readings from the standard curve plotted using the following equation:

$$S_a = \left(\frac{Corrected\ absorbance - (y - intercept)}{Slope}\right)$$

13.7 Concentration of samples in the test samples is calculated as:

$$Glutamate\ Concentration = \left(\frac{S_a}{S_v}\right) * D$$

Where:

Sa = Amount of sample (nmol) from standard curve.

Sv = Volume of sample (µL) added into the well.

D = Sample dilution factor.

DATA ANALYSIS

L-Glutamic acid Molecular Weight is 147.13g/mol.

14.TYPICAL DATA

TYPICAL STANDARD CURVE – Data provided for **demonstration purposes only**. A new standard curve must be generated for each assay performed.

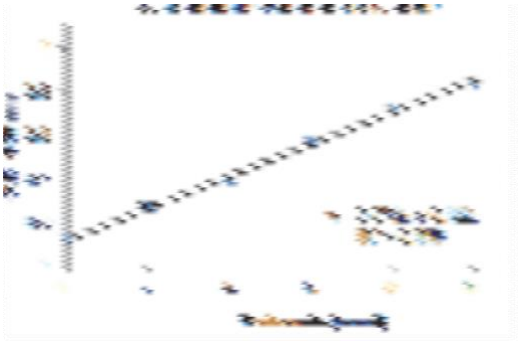

Figure 1: Typical Glutamate standard calibration curve using colorimetric reading.

DATA ANALYSIS

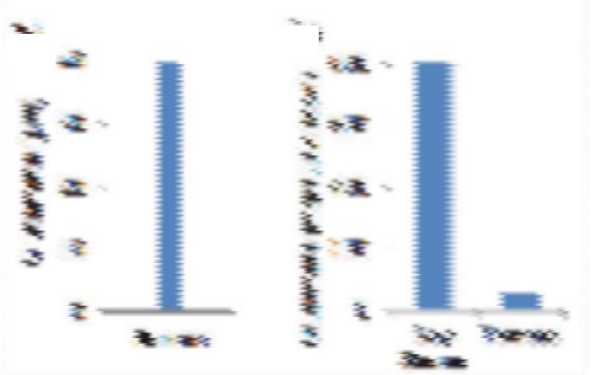

Figure 2: Glutamate concentration in various samples. Left graph shows concentration of glutamate in human serum (25 µL). Right graph should concentration of glutamate in soy sauce (25 µL, 500X diluted) and fresh tomato (25 µL, 50X diluted). Enzyme mix is inhibited by tomato homogenate. Assays were performed following the kit protocol.

15. QUICK ASSAY PROCEDURE

***NOTE**: This procedure is provided as a quick reference for experienced users. Follow the detailed procedure when performing the assay for the first time.*

- Solubilize Glutamate Enzyme Mix and Glutamate developer, thaw Glutamate Standard and Assay Buffer (aliquot if necessary); get equipment ready.
- Prepare standard curve.
- Prepare samples in duplicate (find optimal dilutions to fit standard curve readings).
- Set up plate for standard (50 µL), samples (50 µL) and background sample wells (50 µL).
- Prepare Glutamate Reaction Mix and Background Reaction Mix (number samples + standards + 1).

Component	Reaction Mix Samples (µL)	Background Reaction Mix (µL)
Glutamate Assay Buffer	90	92
Glutamate Developer	8	8
Glutamate Enzyme Mix	2	0

- Add 100 µL of Reaction Mix to standard and sample wells.
- Add 100 µL Background Reaction Mix to background sample wells.
- Incubate plate at 37°C for 30 min protected from light.
- Measure plate at OD450 nm.

16. TROUBLESHOOTING

Problem	Cause	Solution
Assay not working	Use of ice-cold buffer	Buffers must be at room temperature
	Plate read at incorrect wavelength	Check the wavelength and filter settings of instrument
	Use of a different 96-well plate	Colorimetric: Clear plates Fluorometric: black wells/clear bottom plate
Sample with erratic readings	Samples not deproteinized (if indicated on protocol)	Use PCA precipitation protocol for deproteinization
	Cells/tissue samples not homogenized completely	Use Dounce homogenizer, increase number of strokes
	Samples used after multiple free/ thaw cycles	Aliquot and freeze samples if needed to use multiple times
	Use of old or inappropriately stored samples	Use fresh samples or store at -80°C (after snap freeze in liquid nitrogen) till use
	Presence of interfering substance in the sample	Check protocol for interfering substances; deproteinize samples
Lower/ Higher readings in samples and Standards	Improperly thawed components	Thaw all components completely and mix gently before use
	Allowing reagents to sit for extended times on ice	Always thaw and prepare fresh reaction mix before use
	Incorrect incubation times or temperatures	Verify correct incubation times and temperatures in protocol

RESOURCES

Problem	Cause	Solution
Standard readings do not follow a linear pattern	Pipetting errors in standard or reaction mix	Avoid pipetting small volumes (< 5 µL) and prepare a master mix whenever possible
	Air bubbles formed in well	Pipette gently against the wall of the tubes
	Standard stock is at incorrect concentration	Always refer to dilutions described in the protocol
Unanticipated results	Measured at incorrect wavelength	Check equipment and filter setting
	Samples contain interfering substances	Troubleshoot if it interferes with the kit
	Sample readings above/ below the linear range	Concentrate/ Dilute sample so it is within the linear range

17. FAQs

Does this assay only measure free glutamate or can it also measure the amount of glutamic acid in peptides/proteins?

This kit measures free glutamate levels only and not glutamic acid in the backbone of peptides/proteins.

Does glutamine cross-react during this assay?

This assay uses enzymatic detection which reacts with glutamate and not glutamine.

What is the detection sensitivity of the assay?

The kit shows a linear standard curve up to 100 µM Glutamate.

Why there is an increase in the glutamate level in astrocytes cell culture?

Astrocytes release glutamate in a Ca^{2+}-dependent manner. It is a well- studied function required during transmitter uptake and release. The rate of release can be plotted against time and then the time when the release is minimum it can be for intracellular glutamate assay.
Otherwise, total glutamate in medium + cells can be measured.

18. INTERFERENCES

These chemicals or biological materials will cause interferences in this assay causing compromised results or complete failure:

- RIPA buffer – contains SDS which can denature proteins and affect enzyme activity

UK, EU and ROW
Email: technical@abcam.com | Tel: +44-(0)1223-696000

Austria
Email: wissenschaftlicherdienst@abcam.com | Tel: 019-288-259

France
Email: supportscientifique@abcam.com | Tel: 01-46-94-62-96

Germany
Email: wissenschaftlicherdienst@abcam.com | Tel: 030-896-779-154

Spain
Email: soportecientifico@abcam.com | Tel: 911-146-554

Switzerland
Email: technical@abcam.com
Tel (Deutsch): 0435-016-424 | Tel (Français): 0615-000-530

US and Latin America
Email: us.technical@abcam.com | Tel: 888-77-ABCAM (22226)

Canada
Email: ca.technical@abcam.com | Tel: 877-749-8807

China and Asia Pacific
Email: hk.technical@abcam.com | Tel: 108008523689 (9=�tim)

Japan
Email: technical@abcam.co.jp | Tel: +81-(0)3-6231-0940

www.abcam.com | www.abcam.cn | www.abcam.co.jp